AREA RICERCA E TRASFERIMENTO TECNOLOGICO
SETTORE DOTTORATI E CONTRATTI PER LA RICERCA
U. O. DOTTORATI DI RICERCA

PhD School of Biomedicine Neuroscience and Advanced Diagnostic
Department of Biomedicine Neuroscience and Advanced Diagnostic
SSD: BIOS-12/A

POLYMERIC POROUS SCAFFOLDS AND BIOREACTORS: FROM 3D *IN VITRO* MODELS TO TISSUE ENGINEERING APPLICATIONS

PhD STUDENT
CAMILLA CARBONE

PhD COORDINATOR
PROF. FABIO BUCCHIERI

TUTOR
PROF. FABIO BUCCHIERI

CO TUTOR
PROF. VINCENZO LA CARRUBBA

CYCLE XXXVII
YEAR OF DOCTORAL DEGREE ATTAINMENT 2024/2025

I. Introduction 4

Tissue Engineering and in vitro models 4

Cells 6

Scaffolds 8

Signals and Bioreactors 26

Use of polymeric scaffolds and bioreactors for TE applications 32

Use of polymeric scaffolds and bioreactors as 3D in vitro models 33

Clinical relevance of these devices 34

Aims and goals 36

II. Experimental section: 3D static and dynamic devices designed and characterized as *in vitro* model or for TE applications 38

Static Devices 39

Gradient pore size scaffold via TIPS for TE 39

1. Project : Effect of thermal history on pore size architecture 40

Scaffolds via TIPS as 3D breast cancer model 71

2. Project : PLLA porous scaffold as a 3D breast cancer model to investigate drug resistance 73

Dynamic Devices 90

Dynamic devices as 3D models 90

3. Project : Drug Delivery bioreactor 92

4. Project : Air-Liquid Interface (ALI) bioreactor 121

Dynamic devices for TE applications 165

5. Project: Mini Air lift bioreactor 167

III. Conclusions 202

IV. References 207

I. Introduction

Tissue Engineering and in vitro models

Tissue engineering (TE) is a multidisciplinary field that combines biology, material science, and biomedical engineering to restore, maintain, improve, or replace different biological tissues. By exploiting the interaction of three core components, cells, scaffolds and signals, TE aims to create functional constructs that mimic the biological and mechanical properties of native tissues (Lanza et al., 2000; Sarvazyan, 2020). These constructs have applications both in vivo, to guide and repair tissue damage, and in vitro for modeling physiological conditions. Autologous cells, derived from the patient, offer high biocompatibility but is challenging in availability and scalability. Allogenic and xenogenic cells address availability issues but require immunosuppressive strategies to mitigate immune rejection. Stem cells, including mesenchymal stem cells (MSCs) and induced pluripotent stem cells (iPCSs), have emerged as promising candidates due to self-renewal and differentiation potential (Marion & Mao, 2006; Singh et al., 2015). Biomaterials represent the second fundamental constituent for TE: these materials are processed to become structural bases where cells can adhere, proliferate, and form new tissue (Eldeeb et al., 2022). Ideal scaffolds should be biocompatible and biodegradable, they should possess mechanical properties that align with the target tissue (C. Yang et al., 2024). A variety of materials, including natural polymers, synthetic polymers, and composites have been explored for scaffold fabrication (Pattanayak et al., 2023; Ye et al., 2022). Signals are the third essential component for TE: bioactive molecules, growth factors, chemicals, and mechanical stimuli are used to influence cell behavior such as migration, proliferation, and differentiation. These molecules can be incorporated into scaffolds or delivered locally to enhance tissue formation (Pei et al., 2023).

By playing on these three components TE aims to regenerate tissues and organs either *in vitro* or *in vivo*. One peculiar aspect of this approach is the potential development of 3D *in vitro* models able to simulate human tissue environment, allowing researchers to study biological processes more effectively (Ganguly, 2024). For example, being able to conduct pre-clinical testing to predict and evaluate potential adverse effects of new drugs, requires a thorough assessment of their delivery efficacy. A key challenge in this process is replicating the complex physiological interactions that occur within the human body(Abolhassani et al., 2024). The physiological environment of tissues is exceptionally intricate and challenging to mimic *in vitro*. The tumor microenvironment (TME) is one

of the most complex and unique aspects of cancer biology. 3D models play a critical role in cancer research by providing a more accurate representation of the TME compared to traditional 2D cultures (Anderson & Simon, 2020). These models allow researchers to study tumor behavior, interactions between cancer cells and their surroundings, immune cells, and blood vessels in a more physiologically relevant context. This enhanced understanding of the TME can lead to the development of more effective cancer therapies and personalized treatment strategies (Jiang et al., 2020; Micalet et al., 2023).

Animal models provide a controllable experimental environment with complexes like those observed within human cells and organs. These experiments are useful for establishing adequate administration, the bioavailability of the drug, and therapeutic efficacy. Furthermore, they allow us to determine dose-limiting toxicity to detect whether toxicity can be monitored clinically. Animal tests can replicate some physiological phenomena observed in humans, but due to the difference in species, they often aren't truly representative (Hartung, 2024). In addition, there is a very current debate about the ethical problems associated with the use of animals in research. Russell and Burch in 1959 first proposed the guidelines "Principles of Human Experimental Techniques' 'which are still followed today by many regulatory bodies around the world. Three guiding principles constitute the "3 Rs" (Reduction, Refinement, Replacement) initially mentioned in this article: (1) whenever possible, methods other than using animals should be employed (2) the number of animals used should be kept to a minimum (3) procedure should be improved to minimize animal suffering. Despite animal experimentation seems to be still essential to evaluate the effects related to the administration of new drugs, the 3 Rs in animal research is a concept that authorization agencies, in the European Union and the United States, are currently more actively pushing. Thus, several organizations support the improvement of *in vitro* models for preclinical drug testing to reduce the use of animals in the drug development process (Sántha, 2020).

In vitro 3D models bridge the gap between traditional 2D cultures and animal models, offering a cost-effective, scalable, and ethical alternative for preclinical research. They provide a promising platform for high-throughput research, drug screening, disease modeling, and regenerative medicine. By replicating the complex interactions and heterogeneity of tumors, 3D models improve the predictive ability of preclinical studies and enhance the translation of research findings into clinical applications. In this thesis, various systems and devices that I have had the opportunity to work on over the past

three years of my doctoral studies will be explored. These include advancements in 3D *in vitro* models, tissue engineering scaffolds, and innovative bioreactor designs. By showcasing their potential and applications, this research aims to contribute to the fields of drug delivery, tissue engineering, and cancer research, highlighting the critical role of the microenvironment in these advanced biomedical applications.

Cells

Cells can be classified as autologous (patient's own), allogenic (from another human being), or xenogenic (animal-derived). While autologous cells are the perfect candidate for tissue engineering due to their high biocompatibility, at the same time there is the problem of obtaining the correct quantities of them, especially for older and unwell patients. This aspect gives the necessity of resorting to cell culture expansion, which can take place in some cases such as T-flasks, Petri dishes, and multi-well plates (static cell culture) or inside apparatus called bioreactors in which it is possible to obtain adynamic cell culture that better represents a natural *in vivo* environment for cells in terms of distribution of nutrients and avoid potential contamination (Vunjak-Novakovic & Freshney, 2006). Instead, allogenic and xenogenic cells overcome the problem of availability, but they are immunogenic, differently from the first type, and for this reason, a reaction from the immune system is produced, and immunosuppressive therapy is required.

There is the possibility of considering another cell classification, regarding their level of differentiation. In this context, it is possible to discuss stem cells. These kinds of cells are not specialized and they don't have a specific function (i.e., blood cells, bone cells, or cartilage cells), but they have the potential to specialize, under appropriate conditions, into any type of specific cell. Therefore, they have two important capacities:

- Self-renewal (symmetric cell division): from one single stem cell they generate a couple of identical stem cells, similar to the initial one, not differentiated.
- Differentiation: from one single stem cell they generate a couple of different stem cells, the first similar to the initial one and the second progenitor, which is more specialized than the first, but it still can differentiate more.

Three prominent stem-cell types are receiving intensive investigation for their application in TE, they are show in Fig 1.:

1. Embryonic stem (ES) cells are derived from human embryos. Embryonic stem cells (ES) have several characteristics, including the ability to self-renew and pluripotency, which is the potential to differentiate into any cell type in the human body. This flexibility represents a significant advantage for tissue engineering but, at the same time, a potential limitation because it can cause the formation of undesired or tumoral cells. In addition, despite their potential, one of the most problematic challenges is their difficult availability, the possibility of not reaching the required maturation, or the inefficient control of their differentiation (Khademhosseini et al., 2013).
2. Induced pluripotent stem cells (iPSCs) are derived by genetic reprogramming of mature somatic cells, specifically by modifying some transcription factors. One of the most important features is immune compatibility because these kinds of cells are obtained from the same human being, which is at the same time donor and receiver. Instead, a possible disadvantage is the development of efficient and safe reprogramming techniques, without which there are some risks of cell alteration (Vunjak-Novakovic & Freshney, 2006).
3. Adult stem (AS) cells come from fetal, neonatal, pediatric, or adult donor tissue. These kinds of cells overcome the problem of availability and uncontrolled differentiation and for these reasons, they represent a valid alternative, more rapid and direct than the cells previously described. Mesenchymal Stromal Cells (MSCs) are the most used adult stem cells, thanks to their capacity to differentiate into various tissues, including cartilage, bone, adipose tissue, and some types of muscle. They are particularly promising for the reconstruction of musculoskeletal and vascular tissues (Laino et al., 2006).

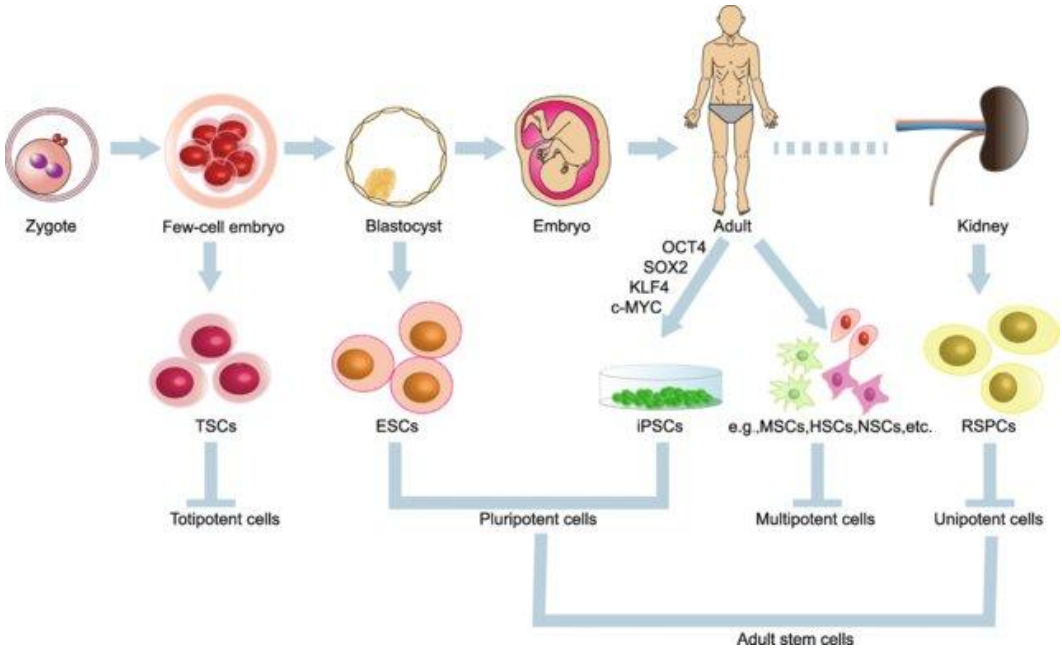

Figure 1: Stem Cell Sources and classification, Image adapted from Liu et al., Stem Cell Research & Therapy (2020), licensed under CC BY 4.0 (http://creativecommons.org/licenses/by/4.0/ (D. Liu et al., 2020)

Scaffolds

In native tissues, cells organize themselves in a 3D manner, allowing for crucial interactions across their surfaces, which facilitates essential functions. Three-dimensional *in vitro* models simulate the human tissue environment, enhancing the study of biological processes, disease progression, and drug response. TE uses these models to create constructs that can repair or replace damaged tissues. Preclinical testing of new drugs often begins with 2D culture techniques, but these fail to replicate *in vivo* conditions. Thus, animal models are also used, though ethical concerns and species differences limit their representativeness. TE offers advanced 3D culture systems that better mimic the complex physiological environment, improving drug screening and reducing the reliance on animal testing. There are various methods for developing 3D cell cultures, each with its unique advantages and applications:

- Organoids and spheroids: these are miniature versions of living tissues and organs, grown *in vitro* from stem cells or tissue samples. Organoids replicate the structure and function of real organs, making them valuable tools for studying human development, disease modeling, and drug testing. Recent advancements have improved their complexity and functionality,

allowing for more accurate disease modeling and personalized medicine applications (Bhattacharya et al., 2024; Ivascu & Kubbies, 2006; Thangam et al., 2024; Vinci et al., 2012)

- 3D Bioprinting: this cutting-edge method involves 3D printing biocompatible materials, cells, and supporting structures into functional living tissues or organs. It is increasingly used in drug discovery and research, with ongoing efforts to make the process high throughput for mainstream drug development (S. V. Murphy & Atala, 2014).
- 3D matrixes: they are three-dimensional systems with interconnected pores designed to simulate the extracellular matrix (ECM). The ECM is essential for facilitating cell communication and various functions. Both polymer-based scaffolds and hydrogels are commonly used to achieve this, with recent advancements enhancing their mechanical properties and biocompatibility(Capuana, Lopresti, et al., 2022; Choi et al., 2024; Fan et al., 2022; Radulescu et al., 2022)

The scaffold is a 3D support characterized by interconnected pores emulating the extracellular matrix (Carfì Pavia et al., 2008a) as shown in Fig. 2. The ECM is made up of a complex mixture of proteins and polysaccharides to give the tissues their properties, it is typically composed of collagen, fibrin, elastin, hyaluronic acid, fibrin, proteoglycans, growth factors, and cytokines (Naahidi et al., 2017).

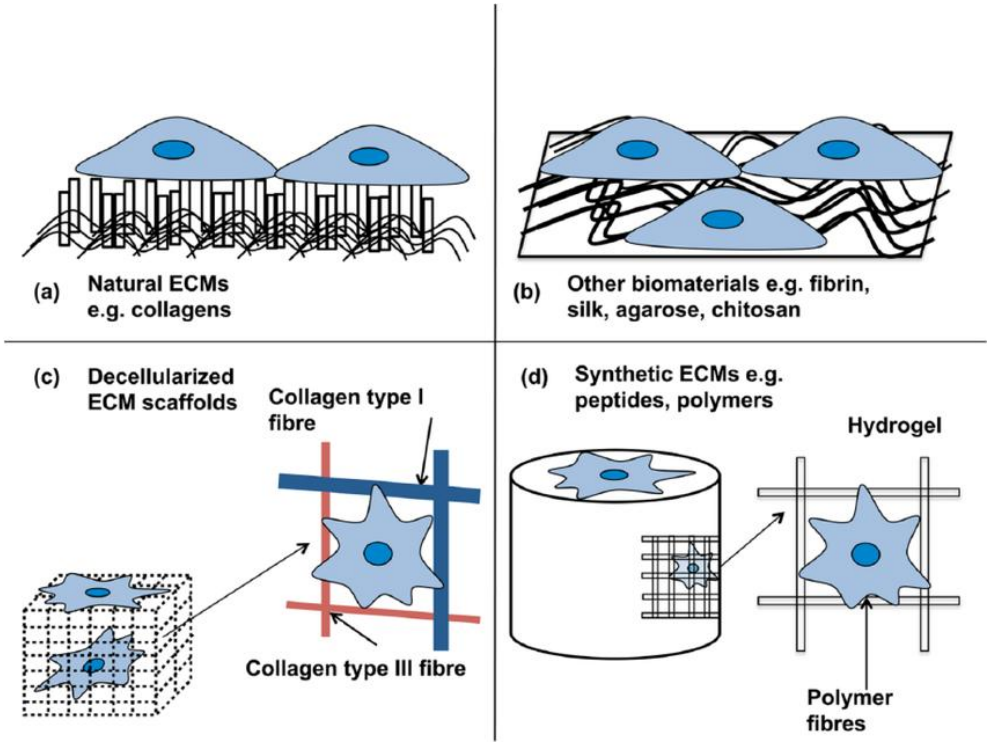

Figure 2: Different types of ECM scaffolds available to use for tissue engineering applications. Image from Kular et al. "The extracellular matrix: Structure, composition, age-related differences, tools for analysis and applications for tissue engineering", Journal of Tissue Engineering (2014). Licensed under CC BY-NC (http://creativecommons.org/licenses/by-nc/4.0/). No modifications were made (Kular et al., 2014)

The scaffolds can incorporate small molecules and growth factors providing a bioactive system that promotes cell adhesion, proliferation, and differentiation intending to recreate their physiological environment.

When designing a scaffold for tissue engineering, specific characteristics must be considered: first of all, biocompatibility. A system is defined as biocompatible when it has the ability not to cause a significant or prolonged inflammatory response in the host. The cells can adhere, function, and migrate to the surface through the scaffold to avoid an inflammatory response so severe that it reduces healing (Ratner, 2011). Once a biomaterial is implanted, the body reacts with inflammation, wound healing, and immunological reactions (Al-Zyoud et al., 2023). Biocompatibility can also be influenced by other factors such as the doctor's intervention, the subject's age, sex, and genetic background.

Pore scaffold architecture, including pore size, shape, and density is of principal importance in cellular behavior. Generally, high porosity and large pores are associated with increased proliferation,

differentiation, and gene expression. The structure must have high porosity and pores must be interconnected. Another important feature is the average pore size, they must be large enough to allow cells to migrate into the structure, but also small enough to have a high specific surface area. The pore size and inter-porous connectivity affect the surface and therefore the drug release kinetics and affect the ability of cells to penetrate and proliferate on the surface of the scaffold(Rambhia & Ma, 2015).

The scaffold must be biodegradable to allow cells to produce their extracellular matrix. The bioproducts of this degradation should also be non-toxic and able to exit the body without interference with other organs. The degradation rate of the scaffolds is important because it is linked to the vitality of the tissues. If the scaffold degrades too fast, the tissue that forms may be defective on the contrary, if the degradation is too slow (Zhou et al., 2023). The new tissue will not be able to grow at its best. Degradation comes on the surface and into the bulk. A scaffold's surface degradation is characterized by a steady reduction in the scaffold's size without any alteration to its mechanical properties (Chew et al., 2016). The scaffold's size and mechanical qualities rapidly degrade at a critical stage of surface deterioration. The loss of material occurs throughout the volume of the scaffold during bulk deterioration. As a result, mechanical strength drops off during bulk degradation and is influenced by the rate of degradation. Natural polymers primarily degrade on their surfaces because most of the scaffolds are typically too large for enzymes to access. This means that the degradation process mainly occurs at the outer layers of the material, where enzymes and other biological agents can interact with the polymer. On the other hand, synthetic polymers can degrade by surface, bulk, or both, depending on their composition. Surface degradation happens when the outer layer of the polymer breaks down, while bulk degradation occurs throughout the entire material. Some synthetic polymers are designed to degrade in a controlled manner, allowing for applications in drug delivery systems and other biomedical uses (X. Zhang et al., 2024).

.

Biomaterials for polymeric scaffolds

Polymeric biomaterials, represented in Fig. 3, whether natural or synthetic, are primarily designed to be biologically compatible with the human body. They play a crucial role in supporting, enhancing, restoring, or replacing the biological functions of damaged tissues and organs.

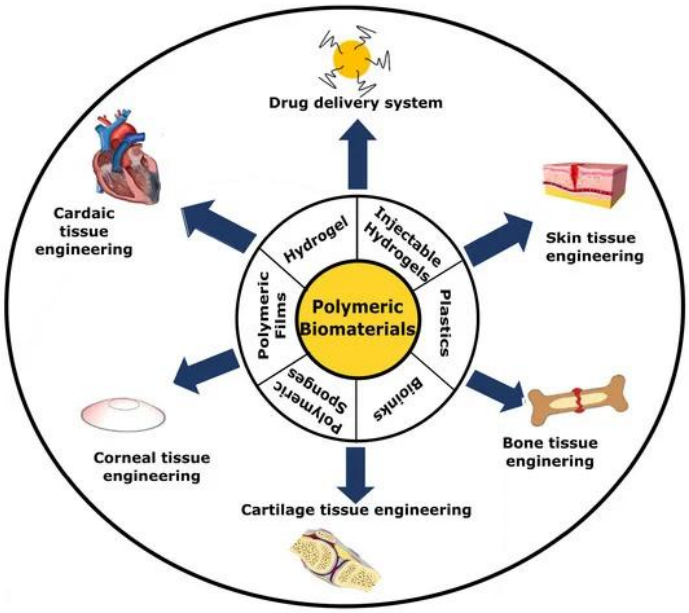

Figure 3: Image adapted from Kalirajan et al. Polymers (2021), licensed under CC BY 4.0 (https://creativecommons.org/licenses/by/4.0/). Available at https://www.mdpi.com/2073-4360/13/17/3015 (Kalirajan et al., 2021)

Given their continuous interaction with tissues, blood, and other bodily fluids, biocompatibility is a critical attribute of these materials. It refers to the ability of a material to perform an appropriate host response in a specific application. Over the years, the definition has evolved to include various aspects of interaction between biomaterials and biological systems. Initially, it was defined as the ability of a material to be in contact with a living system without producing a harmful effect (Ratner, 2011). More recently, it has been expanded to include the material's ability to bring the most appropriate beneficial cellular or tissue response in a specific situation (Al-Zyoud et al., 2023).

Natural Biomaterials

Natural biomaterials are generally enzyme-biodegradable and biocompatible (Garcia-Garcia et al., 2024; S. Liu et al., 2023). Their primary benefit is containing bio-functional chemicals that facilitate cell adhesion, proliferation, and differentiation. However, there are drawbacks: enzymatic degradation may be difficult to manage in terms of degradation rate. Since enzymatic activity varies between hosts, so does the degradation rate. Therefore, determining the lifespan of natural polymers

in vivo can be challenging. Additionally, natural polymers often lack mechanical strength. These materials are derived from natural sources and can be categorized into two primary types: polysaccharides and proteins. Polysaccharides are complex carbohydrates composed of sugar molecules. Key examples of polysaccharide-based biomaterials include alginate, hyaluronic acid, starch, and agarose.

- Alginate: Derived from brown seaweed, alginate is commonly used in wound dressings and drug delivery systems due to its excellent gel-forming abilities and biocompatibility. It is particularly valued for its ability to create hydrogels that can encapsulate cells and drugs, providing a conducive environment for cell growth and controlled release of therapeutics (Sahoo & Biswal, 2021).

- Starch: Sourced from plants, starch is utilized in biodegradable plastics and as a scaffold material in tissue engineering. Its biocompatibility and ease of modification make it a versatile choice for creating materials that support cell adhesion and growth (Roslan et al., n.d.).

- Agarose is a polysaccharide with hydroxyl groups, making it water-soluble; its chains form a thermally reversible gel at low temperatures, becoming water-soluble at high temperatures. By adjusting the concentration of agarose, various properties of the gel can be changed, including strength and permeability. For example, low concentrations result in a mechanically weak and extremely porous entangled structure. These types of hydrogel are widely studied for tissue culture systems as they allow cells and tissues to grow in a three-dimensional solution. Chondrocytes, the main cartilage cell type, can be maintained in culture for two to six weeks using agarose gels. These results support the use of agarose gels for cartilage healing and potential studies as a matrix for nerve regeneration(Zarrintaj et al., 2018).

- Hyaluronic acid is a common glycosaminoglycan in the extracellular matrix of tissues, promoting early inflammation, which is essential for wound healing. It is a desirable option for biomedical applications because it is non-immunogenic and has no adhesiveness. At low concentrations, it has a random spiral shape that becomes tangled as its concentration increases. However, one disadvantage is that hyaluronidase and other enzymes rapidly break

it down. Hyaluronic acid is often more stable when made into a hydrogel (Garcia-Garcia et al., 2024).

Protein-based biomaterials are another crucial category, incorporating materials such as collagen, silk, fibrin, and elastin.

- Collagen, in its triple helix form, consists of three intertwined polypeptide chains, with adhesion domains that allow for a desirable surface area for cell attachment. It has some disadvantages, including considerable variability due to the variety of types, a tendency to break down rapidly, and enzymatic biodegradability, which limits its mechanical qualities. However, it promotes natural blood clotting, which is beneficial for wound healing. These qualities make it suitable for use as a scaffold for epithelial cells such as fibroblasts and keratinocytes (Parenteau-Bareil et al., 2010).

- Silk: Derived from silkworms, silk protein has gained attention for its mechanical strength and biocompatibility. It is used to create durable scaffolds that support cell proliferation and differentiation, making it suitable for bone and ligament tissue engineering (Tandon et al., 2020).

- Fibrin: Formed from fibrinogen during the blood clotting process, fibrin is used in tissue engineering and regenerative medicine to create scaffolds that mimic the natural wound healing environment. Its ability to support cell attachment and migration is particularly beneficial in creating constructs for vascular and skin regeneration (Noori et al., 2017).

- Elastin: Found in elastic tissues such as skin and blood vessels, elastin provides elasticity and resilience. It is used in biomaterials to develop flexible scaffolds that can withstand dynamic physiological conditions, promoting tissue repair and regeneration. Some examples of natural polymers include agarose, hyaluronic acid, and chitosan (Rodriguez-Cabello et al., 2021).

Synthetic Biomaterials

A major advantage of synthetic polymers is their ability to be tailored to suit specific functions and exhibit controllable properties. Among the most used synthetic biomaterials, there are polyesters capable of satisfying necessary criteria such as biocompatibility, processability, and controlled degradation. The rate of degradation can be controlled by adjusting the molecular weight, copolymerization ratio, and polydispersity of the polymers. Synthetic materials allow for the creation of 3D microenvironments with adjustable characteristics, including mechanical properties, degradation rate, and porosity. Despite these advantages, synthetic polymers have low intrinsic bioactivity and produce acidic products. Therefore, it is essential to modify them with biological or chemical substances to achieve adequate cellular responses. Examples of these materials are Poly(lactic acid) (PLA), Poly(L-lactic acid) (PLLA), Poly(D-lactic acid) (PLDA) and Poly(lactic-co-glycolic acid) (PLGA).

- Poly(lactic acid) (PLA): it is a biodegradable polymer derived from renewable resources like corn starch or sugarcane. Its biocompatibility and biodegradability make it an important material in TE and biomedical applications. PLA can be processed into various forms, including fibers, films, and foams, providing versatility in its applications. It degrades into lactic acid, a natural metabolite, which is safe for the body. However, the hydrophobic nature of PLA can limit cell attachment and proliferation. To enhance its cellular interactions, PLA is often blended with other materials or modified with bioactive molecules (Grémare et al., 2018).

- Poly(L-lactic acid) (PLLA): PLLA is a stereoisomer of PLA with a pendant methyl group that lowers the melting temperature to 170-180°C and increases its hydrophobicity. This structural difference slows down the degradation process, making PLLA suitable for long-term applications. PLLA can absorb proteins and promote cell adhesion, making it an excellent choice for scaffolds. It supports a variety of cell types, such as nerve stem cells, which have shown signs of neurite development on PLLA fibers for potential neuronal regeneration. Human bladder smooth muscle cells have also demonstrated normal metabolic activity and

proliferation when seeded on PLLA scaffolds (Conoscenti, Schneider, et al., 2017; Hu et al., 2010; F. Yang et al., 2004).

- Poly(D-lactic acid) (PLDA) is another stereoisomer of PLA, composed of D-lactic acid units. Similar to PLLA, PLDA is biodegradable and biocompatible, but it degrades at a different rate and has different mechanical properties compared to PLLA1. PLDA can be used in similar applications as PLLA, such as tissue engineering and drug delivery systems (Cifuentes et al., 2021).

- Poly(glycolic acid) (PGA): PGA is a widely used polyester known for its rapid degradation and hydrophilicity, which can result in an abrupt loss of mechanical strength. Glycolic acid can lower the pH of surrounding tissue in large amounts, potentially causing irritation and tissue damage. Despite this, PGA has been widely used to create scaffolds for different cell growth types. For instance, glycosaminoglycan sulfate expression in bovine chondrocytes on PGA scaffolds was 25% higher than in natural cartilage, with similar *in vitro* and *in vivo* results. Myofibroblasts and endothelial cells have also been successfully cultured on PGA matrices, producing collagen and elastic filaments, indicating potential applications in heart valve manufacturing (Benatti et al., 2019; Low et al., 2020).

- Poly(lactic-co-glycolic acid) (PLGA): PLGA is an amorphous copolymer of PLA and PGA, known for its tunable degradation rates and mechanical properties. It commonly degrades via bulk ester hydrolysis, and adjusting the ratio of lactic acid to glycolic acid can control the degradation rate. However, the mechanical and degrading properties of PLGA are not linearly proportional to its copolymer composition. Research has shown that PLGA scaffolds can support the growth of various cell types, such as fibroblasts, which can regenerate an extracellular matrix (Jin et al., 2021).

Composite Materials

Composite materials combine natural and synthetic materials to leverage the advantages of both. These materials are designed to enhance biological capabilities, mechanical properties, and overall

performance in biomedical applications. For instance, synthetic and natural polymers have been mixed to create scaffolds with improved biological and mechanical properties, while ceramics have been incorporated into polymer-based scaffolds to enhance their strength and functionality.

- Hydroxyapatite (HA), for example, is a naturally occurring mineral form of calcium apatite, similar to the composition of human bone. When combined with Poly(L-lactic acid) (PLLA), the resulting composite material exhibits enhanced mechanical properties and improved osteoconductivity, making it ideal for bone tissue engineering applications. The HA provides the necessary bioactivity for bone growth, while the PLLA offers controlled degradation and mechanical support (Ngo et al., 2022).

- Carbon Nanotube (CNT)-Polymer Composites: Carbon nanotubes (CNTs) are known for their exceptional mechanical strength, electrical conductivity, and thermal stability. When incorporated into polymer matrices, such as PLA or PLLA, the resulting composites exhibit improved mechanical properties and electrical conductivity. These composites are used in applications such as neural interfaces, biosensors, and orthopedic implants, where enhanced mechanical strength and electrical properties are beneficial (MacDonald et al., 2005).

- Silk Fibroin-Chitosan Composites: Silk fibroin is a natural protein derived from silk, known for its biocompatibility, biodegradability, and excellent mechanical properties. Chitosan is a natural polysaccharide derived from chitin, with antimicrobial properties and biocompatibility. When combined, silk fibroin and chitosan create a composite material with enhanced mechanical properties, antimicrobial activity, and biocompatibility1. These composites are used in wound healing, tissue engineering, and drug delivery systems (Faheed, 2024).

Scaffold production techniques

Several techniques were used to create efficient biomimetic micro- and nanostructured biomaterials with the desired degree of porosity, pore size, pore interconnectivity, and mechanical properties that better mimic osteochondral tissue. Conventional methods are shown in Fig. 4. In the following pages,

some of the most used of them will be analyzed, exposing their advantages and disadvantages, such as:

- Solvent casting/Particulate leaching
- Emulsion Freeze-Drying
- Gas Foaming
- 3D printing
- Fuse deposition modeling
- Electrospinning

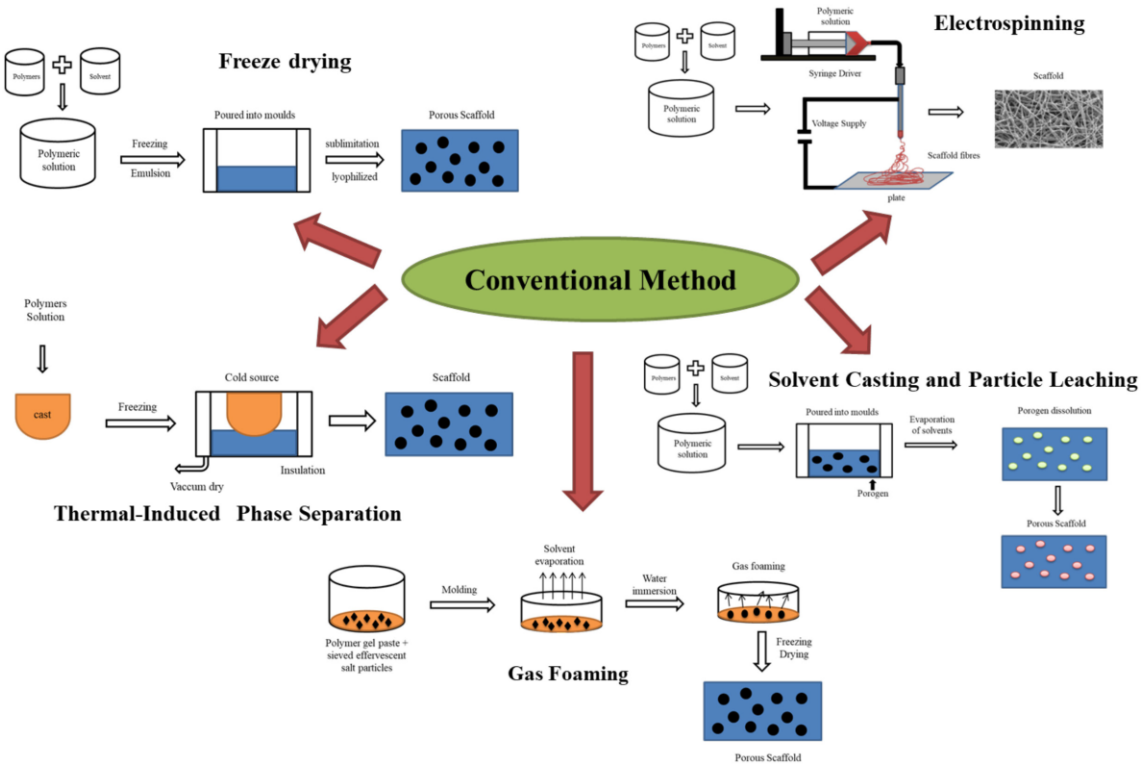

Figure 4: Image adapted from Kumar and Jacob, Journal of Applied Biology & Biotechnology (2022), licensed under CC BY 4.0 (https://creativecommons.org/licenses/by/4.0/). Available at: https://www.frontiersin.org/journals/bioengineering-and-biotechnology/articles/10.3389/fbioe.2023.1186351/full [60(Kumar & Jacob, 2022)

- **Solvent Casting/Particulate Leaching**

The solvent casting technique consists of a simple, easy, and inexpensive technique. The chosen polymer is dissolved into a specific organic solvent in a mold. Then, after the polymeric solution preparation, the final step is the removal of the solvent by air-drying, vacuum-drying, or freeze-

drying. The commonly used solvents are toxic, and for this reason, the risk of traces in the final scaffolds is relevant. Consequently, this technique is combined with particulate leaching, which involves using solid porogen particles (salt, wax, or sugar). Due to this combination, the polymeric solution is poured into a mold containing the porogen particles (with the desired dimensions), the solvent is removed, and then the particles are leached with water. In this way, obtaining a final porous scaffold with a specific dimension is possible. Generally, the final porosity is around 94-95% and the maximum pore size obtained is 500 μm [41]. The most common disadvantages of this technique are the difficulty of obtaining a high degree of porosity, and the necessity to remove the toxic solvent without leaving some traces that can cause damage to cells and operators. In addition, the choice of the porogen amount added is fundamental because a low amount of particles can generate isolated pores, while if the amount added is too high, a final structure with voids will be formed (Janik & Marzec, 2015)

- **Emulsion Freeze-Drying**

With emulsion freeze-drying, the polymer is dissolved in the solvent and mixed with water to create an emulsion. The emulsion is quickly cooled and frozen, for example, in liquid nitrogen, to maintain the structure that was in the liquid phase. Subsequently, the frozen solvent is removed by freeze-drying under a vacuum, basing the process on the conversion of the ice into the gas phase. In addition, it is possible to manage the final structure, by changing the freezing rate; a high rate produces small pores. The benefits are linked to the possibility of obtaining a high level of porosity (> 90%), the removal of toxic solvents, and the non-necessity of high temperatures and leaching processes. Instead, the problems are the emulsion instability, the small size of the pores, and the porosity, which is often irregular. This technique, for example, was used to produce 3D structures with different polymers, like silk protein, PGA, PLLA, and PLGA (Janik & Marzec, 2015).

One of the examples reported in the literature for OC regeneration shows a polymer collagen matrix in which hydroxyapatite particles (HAp) are gradually distributed with different concentrations. The different distribution of HAp gives the scaffold a gradient variation of mechanical features, mimicking better the cartilage-bone interface (Parisi et al., 2020). Another possibility involves the fabrication of a 3D structure based on chitosan, PCL, and CS, showing suitable features in terms of porosity and pore size (L. Chen et al., 2023)

- **Gas Foaming**

The gas foaming technique uses carbon dioxide or nitrogen at high pressure as a porogen, removing the use of organic solvents and high temperature, which can cause damage to the surrounding cells and tissue. The technique involves dissolving a high quantity of gas in a polymeric matrix to saturate the polymer. Subsequently, the dissolved gas becomes unstable because of rapid depressurization, and the nucleation and growth of bubbles start, generating a distinct phase. To minimize the free energy of the system, the gas molecules become a cluster, and the nucleation of pores starts. As a consequence of this nucleation, the polymer volume increases, but the density decreases (Lu et al., 2013).

An example reported in scientific literature involves the use of PGA and PLA. In particular, solid samples of this polymer are first produced by compression molding at high temperatures. Then, samples are saturated with CO2 by exposure to high-pressure CO2 gas for a few days, before reducing the solubility of the gas in the polymer. After depressurization, the nucleation and growth of gas bubbles dispersed throughout a polymer occur, and the final bubble dimension will determine the final pore size. Moreover, with regulation of the time and velocity of depressurization, it is possible to control the pore size. The problem with this scaffold fabrication technique is the difficulty of controlling it adequately, and this aspect can be considered a problem for correct cellular proliferation and interconnection because the pores could be closed during foaming. Moreover, the possibility of high pressure could block the cellular inclusion on scaffolds. With this technique, it is possible to produce a scaffold with a porosity of 93% and a maximum pore size of 100 μm (C. Liu et al., 2007; Mabrouk et al., 2020; Subia et al., 2010)

34

- **CAD Based Techniques**

These techniques represent an advanced technique of scaffold fabrication. Due to these, it is possible to design and customize the 3D structure concerning the specific feature required of the host tissue to be regenerated with the help of computer-aided design (CAD). The starting point of this technique consists of the design of the scaffold with the help of design software. Then, the designed and customized model is converted into a series of cross-sections, and, finally, the production of the 3D scaffold occurs using a stratification method such as fused deposition modeling (FDM), selective laser sintering (SLS), 3D printing, or stereolithography (SLA). This technique produces scaffolds

with more specific and customized porosity, architecture, geometry, and interconnectivity, generating biomimetic structures. These benefits are, however, offset by the high cost of this method and the limited range of polymer materials that can be used. (Subia et al., 2010). 3D Bioprinting represents one of this century's most promising alternative scaffold fabrication techniques, offering the possibility to realize biocompatible and customized scaffolds for tissue regeneration. With this technique, it is possible to classify a first procedure in which the printing materials, or ink, are used to create an acellular 3D structure, subsequently populated with cells. Instead, when live cells are seeded and included in the biomaterial, before printing, it is usually necessary to speak about bioink. The benefits are also associated with some limitations, such as the high costs of technology and the development of suitable and printable biomaterials.

- **Electrospinning**

This technique's ability to create scaffolds with primary structural features suitable for cell development and subsequent tissue organization is one of its main benefits. In addition to being able to manage posture geometry, it can manufacture ultrafine fibers with a unique orientation, a high aspect ratio, a large surface area, and a special orientation. These traits are advantageous for improved cell development both *in vitro* and *in vivo* because they have a direct impact on cell adhesion, cell expression, and oxygen and nutrient transportation. This offers a spatial context where new tissue can grow and function physiologically (Haider et al., 2020; Lu et al., 2013).

- **Phase Separation**

Phase separation is a broadly used technique for scaffold fabrication due to its possibility to customize the mechanical properties and pore sizes of the produced scaffolds concerning the specific requirements of tissue to restore. This kind of technique exploits the thermodynamic demixing of a binary (polymer-solvent) or ternary (polymer-solvent-nonsolvent) polymer solution, due to the reduction of solvent power, to obtain two phases: a polymer-rich phase and a solvent-rich phase. Consequently, the solidification of the polymer-rich phase will generate a solid matrix, while the solvent-rich phase will generate pores after the solvent removal (Capuana et al., 2021). Depending on the type of mechanism that induces the phase separation, it is possible to classify:

- Diffusion-Induced Phase Separation (DIPS): the addition of a nonsolvent to the polymer solution, induces phase separation.
- Chemically Induced Phase Separation (CIPS): this kind of phase separation occurs during polymerization due to the decreasing entropy of mixing caused by the growth of the molecular weight of the polymer (Luo et al., 2011).
- Thermally Induced Phase Separation (TIPS): the variation of temperature-induced phase separation (Capuana et al., 2021) More details about this mechanism will be discussed in the next few paragraphs.

TIPS

As mentioned in the previous paragraphs, Thermally Induced Phase Separation (TIPS) is one of the most common scaffold techniques used to obtain a porous and well-interconnected 3D structure. This represents the technique on which this thesis project will focus attention because it is easy to reproduce, low-cost, and represents a method for producing polymer scaffolds with porosity over 90% (Capuana et al., 2021). TIPS eliminates the need for a porogen leaching step, simplifying the fabrication process while maintaining versatility. It involves controlled cooling of a polymer solution, inducing phase separation into a polymer-rich and polymer-lean phase under the binodal curve, followed by solidification under the spinodal curve. This behavior is mapped onto a temperature-composition phase diagram, aiding in the visualization of the demixing and solidification mechanisms, as reported in Fig. 5.

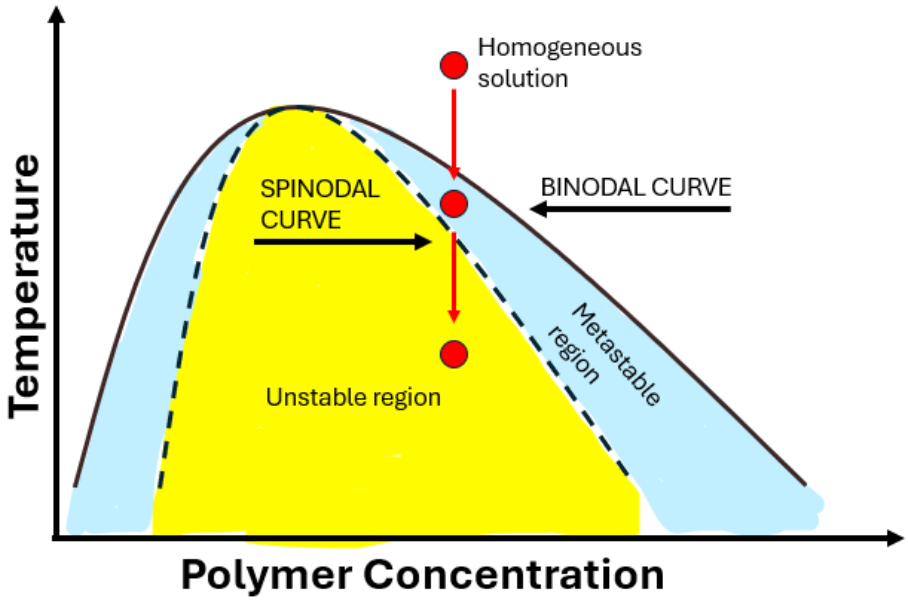

*Figure 5: Phase diagram illustrating the relationship between polymer concentration and temperature, highlighting the binodal and spinodal curves. The **binodal curve** (solid line) separates the homogeneous solution from the phase-separated regions, distinguishing the **metastable region** (light blue) from the **unstable region** (yellow). The **spinodal curve** (dashed line) defines the boundary where spontaneous demixing occurs, leading to phase separation without nucleation. The red dots indicate key points in the phase transition process, with an arrow showing the transition from a homogeneous state to the unstable region.*

Above the upper curve, called the binodal curve, the polymer solution is in the homogeneous phase (monophasic). The point where the binodal and spinodal curves meet is the critical point. When the temperature decreases at a constant concentration, the polymer solution reaches the binodal curve, and demixing occurs, generating two phases. The region between the binodal and spinodal curves is the metastable region in which nucleation and growth mechanisms take place. The starting concentration plays a crucial role in determining the final morphology. If the initial concentration is to the left of the critical point, nucleation of the polymer-rich phase occurs, producing a dense phase. In contrast, if the initial concentration lies to the right of the critical point, the nucleation of the solvent-rich phase generates the desired polymer network (Nam & Park, 1999; Zeinali et al., 2022). The behavior of the solution in TIPS depends significantly on whether a binary or ternary system is used. In binary systems, only a polymer and a solvent are present. These systems rely primarily on temperature and polymer concentration to induce phase separation, resulting in easy but less versatile scaffold morphology. Ternary systems, which include a polymer, solvent, and non-solvent, allow for finer control over phase separation. The addition of a non-solvent reduces the polymer's solubility,

modulating pore size and interconnectivity. This flexibility makes ternary systems more suitable for diverse tissue engineering applications. Furthermore, ternary systems exhibit unique phase separation pathways, with more complex spinodal and binodal curves and metastable regions. In this thesis a ternary solution made by Poly-L-lactic acid at 4%, 1.4 Dioxane and water (La Carrubba et al., 2008) was used to produce all the scaffolds presented.

The pore distribution, shape, and size are the results of a balance between different parameters:

- Polymer concentration
- Polymer molecular weight
- Solvent/non-solvent ratio
- Cooling rate

Polymer Concentration

When the polymer concentration increases and all other parameters are the same, the pore dimension decreases. This is related to a major nucleation of the system, and for this reason, pores are smaller. For example, Hua et al. reports in a scientific study about a PLLA/Dioxane/Water system, with an 87/13 solvent/non-solvent weight ratio how, after 10 minutes with a quenching temperature of 30° C, the pore sizes are reduced (Hua et al., 2001). This confirms the dependence between polymer concentration and pore size.

Polymer Molecular Weight

The molecular weight of polymers is a key parameter in controlling the final morphology of scaffolds produced via Thermally Induced Phase Separation (TIPS). It directly influences the viscosity of the polymer solution, thereby affecting both the separation process and the stability of the formed structures. At the same polymer concentration, higher molecular-weight polymers result in a more regular and organized scaffold morphology due to increased viscosity, which slows down phase separation and stabilizes the structure. Conversely, lower molecular-weight polymers yield a less viscous polymer-rich phase. This reduced viscosity may lead to instability, causing dispersed phases to coalesce and form irregular morphologies. For instance, Chen et al. (J. S. Chen et al., 2010)

demonstrated that scaffolds fabricated with higher molecular weight PLLA exhibited significantly improved organization compared to those made with lower molecular weight PLLA, highlighting the importance of viscosity in maintaining structural integrity during TIPS.

Solvent/Non-solvent Ratio

This represents another key parameter for the TIPS technique. The choice of the correct solvent/non-solvent ratio is fundamental to obtaining scaffolds with the properties required for tissue regeneration. Especially, the addition of non-solvent reduces the solubility of the polymer in the solution, promoting phase separation and modulating pore sizes and interconnection. Indeed, if the amount of the non-solvent increases (reduction of the solvent/non-solvent ratio), a macroporous structure is promoted with an increase in pore sizes because the interaction with the polymer is weakened. In contrast, a microporous structure is created when the ratio is increased (more solvent is used), reducing pore dimensions.

Cooling Rate

The influence of the quenching route depends on two variables: temperature and time. In particular, changing the demixing temperature and time is one of the best ways to customize the final scaffold morphology in terms of the pore sizes, distribution, and interconnectivity. The following image (Fig. 6) shows how the scaffold pore sizes change while demixing time varies in the metastable region. Starting at 25°C the system is more nucleated and almost independent of time. At 30°C, the pores, after the nucleation, start to grow, becoming larger until saturation. Moreover, at 35°C the trend is similar to one at 30°C but with a major growth and pore size (Conoscenti et al., 2017).

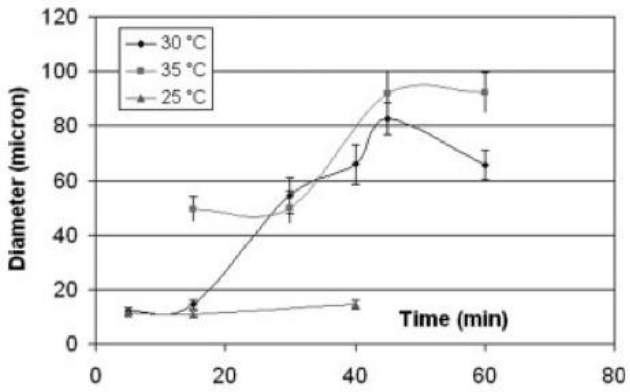

Figure 6: Image adapted from Conoscenti al., Archives in Chemical Research (2017 (Conoscenti, et al., 2017)), ***Copyright:*** *© 2017 Conoscenti G, This is an open-access article distributed under the terms of the Creative Commons Attribution License, which permits unrestricted use, distribution, and reproduction in any medium, provided the original author and source are credited.*

Signals and Bioreactors

The second pillar of tissue engineering (TE) consists of mechanical and physical signals, as well as biochemical signals like growth factors and transcription factors. Growth factors (GFs) are proteins that play a critical role in regulating cellular activities, including proliferation, differentiation, migration, and adhesion. These factors, such as bone morphogenic proteins (BMPs), vascular endothelial growth factor (VEGF), and fibroblast growth factor (FGF), are naturally produced by cells (Y. Zhang & Habibovic, 2022).

Different types of effects essential for injury healing and tissue regeneration can be classified as follows:

- Chemotactic effect: Initiating cell migration.
- Mitogenic effect: Stimulating cell division.
- Morphogenic effect: Inducing cellular differentiation.
- Apoptotic effect: Triggering programmed cell death.
- Metabolic effect: Modulating cellular metabolic activity.
- Combination of effects: Integration of the above effects.

One significant advantage of engineered tissues is their capability to release growth factors directly to the injury site, promoting healing with various delivery methods, such as using carriers, depending on the optimal concentration of growth factors needed. Transcription factors (TFs) are proteins that control cellular transcription, the process of converting genetic information from DNA to mRNA.

These factors are crucial in cell development, particularly in managing differentiation and consequently in tissue regeneration.

Bioreactors can play a fundamental role in delivering these signals to cell cultures (Castro et al., 2020; Parrish et al., 2018). These devices create controlled environments for cell growth, ensuring sterility and providing necessary conditions while allowing easy monitoring of growth parameters. Initially used in microorganism fermentation, bioreactors now incorporate sensors to monitor environmental parameters, such as pH, temperature, and oxygen levels, in real-time. Dynamic cultures facilitated by bioreactors improve mass transport efficiency and enhance cell proliferation and differentiation (Lim et al., 2022a; Meneses et al., 2020; Selden & Fuller, 2018).

Types of Bioreactors

Bioreactors are essential in tissue engineering for creating controlled environments that mimic physiological conditions (J. Zhao et al., 2016a). Their design must address the following considerations:

- Ensuring uniform cellular distribution within scaffolds to avoid overgrowth or necrosis.

- Maintaining precise control of pH, temperature, oxygen levels, shear stress, and pressure for optimal cell growth.

- Delivering oxygen, nutrients, and growth factors efficiently while removing metabolic waste to prevent necrosis, especially in dense tissue constructs.

- Supporting the application of mechanical, physical, and biochemical signals, such as growth factors and transcription factors, to guide cell behavior and differentiation.

- Simplifying assembly and disassembly to reduce handling time and contamination risks.

- Biocompatible materials that can withstand sterilization processes like autoclaving. Disposable bioreactors offer a convenient alternative for specific applications.

Additional features include transparency for visual monitoring, compact designs for incubator use, and flexible tubing for ease of assembly. Ensuring fluid systems have tight seals is crucial for leak prevention.

Bioreactors are categorized based on their mechanisms for enhancing mass transport, nutrient delivery, and signal application to engineered tissues (Lim et al., 2022a; Martin et al., 2004; J. Zhao et al., 2016a). Below are the primary types:

- Spinner Flask Bioreactors

These consist of chambers containing scaffolds suspended in culture medium, which is mixed using a magnetic stir bar as shown in Fig. 7. The stirring ensures media mixing and reduces mass transport limitations at the scaffold surface. However, shear stress caused by mixing can lead to cell detachment or affect cell viability. Spinner flasks are simple and cost-effective but offer limited control over oxygen gradients and internal scaffold conditions.

Figure 7: Spinner Flask bioreactor. Illustration courtesy of Sara Pecorella. Used with permission. Special thanks for the valuable contribution to this project

- Rotating Wall Bioreactors

Rotating wall bioreactors, represented in Fig.8, feature scaffolds positioned between concentric cylinders. The outer cylinder rotates to generate a low-shear, laminar flow of the culture medium, which supports the suspension of scaffolds and reduces cell detachment. Despite these advantages, they often fail to ensure uniform oxygen and nutrient delivery to the scaffold core.

Figure 8: Rotating wall bioreactor. Illustration courtesy of Sara Pecorella. Used with permission. Special thanks for the valuable contribution to this project

- Wave-Wall Bioreactors

These systems create undulating movements in the culture medium, preventing stagnant layers and improving nutrient distribution as depicted in Fig. 9. However, the mechanical shear forces generated by the wave motion can detach cells or cause stress-related changes, limiting their use for sensitive cell types.

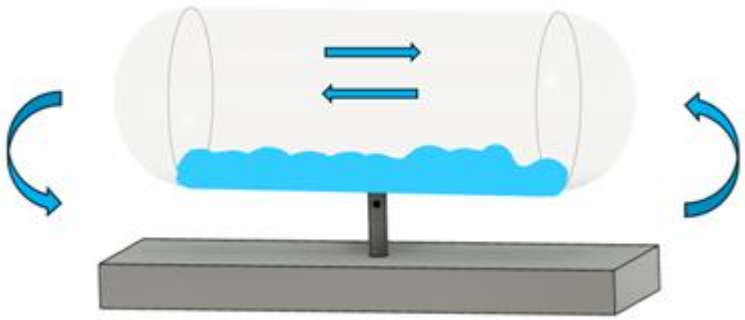

Figure 9: Wave-Wall bioreactor. Illustration courtesy of Sara Pecorella. Used with permission. Special thanks for the valuable contribution to this project

- Dynamic Loading Bioreactors

These systems apply mechanical stimuli, such as compression, tension, or vibration, to cell-seeded scaffolds. By mimicking the physiological forces experienced by tissues *in vivo*, dynamic loading bioreactors enhance tissue maturation and mechanical strength. They also allow researchers to study the effects of specific mechanical cues on cell behavior and tissue growth.

- Perfusion Bioreactors

Perfusion bioreactors are among the most advanced systems for tissue engineering (Beşkardeş et al., 2018; Engel et al., 123 C.E.; Lombardo et al., 2021; Parrish et al., 2018; F. Zhao & Ma, 2005). They directly circulate culture medium through or around scaffolds, addressing mass transport challenges and enhancing cell growth at the scaffold core. Perfusion bioreactors are highly effective for maintaining nutrient and oxygen gradients and facilitating waste removal, making them particularly suitable for large-scale tissue constructs.

- Direct Perfusion Systems

In these systems, the scaffold is integrated directly into the flow path, forcing culture medium through the scaffold pores as shown in Fig. 10. This approach reduces internal mass transfer constraints, ensuring optimal nutrient delivery and oxygenation throughout the scaffold. Direct perfusion systems are ideal for dense tissues where central regions are prone to necrosis.

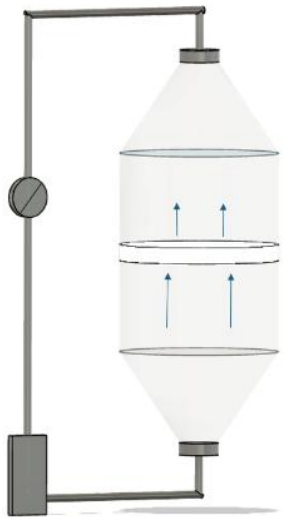

Figure 10: direct perfusion system. Illustration courtesy of Sara Pecorella. Used with permission. Special thanks for the valuable contribution to this project

- Indirect Perfusion Systems

These systems circulate medium around the scaffold without forcing it through the pore structure as depicted in Fig.11. While this reduces the risk of scaffold deformation or mechanical damage, it is less effective for nutrient delivery to the scaffold's core, making it suitable for tissues with lower cell density or less metabolic demand.

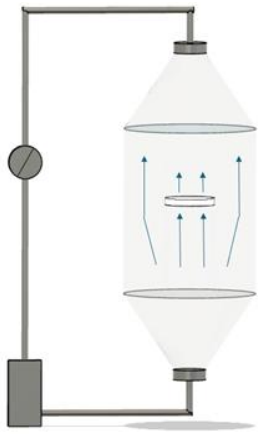

Figure 11: indirect perfusion system Illustration courtesy of Sara Pecorella. Used with permission. Special thanks for the valuable contribution to this project

The evolution of bioreactor technology has revolutionized tissue engineering by addressing critical challenges in nutrient delivery, environmental control, and signal application. While simpler systems like spinner flasks and rotating wall bioreactors remain widely used for basic studies, advanced designs such as perfusion and microfluidic bioreactors provide unparalleled precision and scalability. Among these, perfusion systems stand out for their ability to sustain large, dense tissue constructs, making them indispensable tools in both research and clinical applications.

Use of polymeric scaffolds and bioreactors for TE applications

Tissue engineering (TE) is revolutionizing the medical field by combining scaffolds and bioreactors to restore, maintain, or enhance tissue functions. Scaffolds are three-dimensional frameworks that play an essential role in providing structural support for cell attachment, proliferation, and differentiation. They are designed to mimic the natural extracellular matrix (ECM), thus facilitating the organization of cells into functional tissues (Jafari et al., 2017).

The integration of bioreactors in TE applications further amplifies the potential of these scaffolds. Bioreactors create a controlled environment that encourages cell growth and differentiation, ensuring that cells receive the necessary nutrients and oxygen. By providing mechanical stimulation and regulating nutrient supply, bioreactors significantly enhance the success of scaffolds in TE.

Considering the example of bone tissue engineering, the combination of hydroxyapatite (HA) with poly(L-lactic acid) (PLLA) scaffolds has shown promising results (Roseti et al., 2017). This composite material not only improves osteoconductivity but also provides the mechanical strength required for bone regeneration. The use of perfusion bioreactors in this context has the potential to ensure a constant supply of nutrients and mechanical stimuli, promoting the formation of bone-like structures.

In cartilage tissue engineering, scaffolds made of poly(glycolic acid) (PGA) combined with collagen are utilized to create cartilage-like tissues (Jafari et al., 2017). By employing spinner flasks and rotating wall bioreactors, the culture conditions are maintained to facilitate the formation of essential extracellular matrix components, which are critical for cartilage regeneration.

For cardiovascular tissue engineering, PLGA scaffolds have demonstrated their utility in engineering heart valves (Ma et al., 2018). Dynamic loading bioreactors, which apply mechanical forces that mimic physiological conditions, significantly enhance the maturation and functionality of the engineered tissues, making them suitable for clinical applications.

In synthesis, TE offers innovative solutions for restoring and enhancing tissue function. The synergy between advanced scaffold materials and bioreactor systems has opened the way for significant breakthroughs in the development of functional tissues. By mimicking the natural extracellular matrix and creating controlled environments for cell growth, these technologies demonstrate immense potential across various applications, from bone and cartilage regeneration to cardiovascular tissue repair. As research continues to refine scaffold designs and optimize bioreactor systems, the promise of tissue engineering to address complex medical challenges and improve patient outcomes becomes ever more real.

Use of polymeric scaffolds and bioreactors as 3D in vitro models

The potential of scaffolds and bioreactors extends beyond tissue engineering applications to the creation of three-dimensional (3D) *in vitro* models. These models offer a more accurate representation of the *in vivo* environment compared to traditional two-dimensional (2D) cell cultures, thus providing valuable insights into cell behavior, disease mechanisms, and drug testing (Antonelli, 2023; Caballero et al., 2022; Imamura et al., 2015).

In cancer research, for example, 3D models using scaffolds and bioreactors can closely mimic the tumor microenvironment. This setup allows researchers to study tumor growth, invasion, and response to therapies more effectively. Microfluidic bioreactors, with their precise control over the microenvironment, facilitate high-throughput screening of anticancer drugs, thereby accelerating the development of new treatments (Engrácia et al., 2023; Yamada & Cukierman, 2007).

Neurodegenerative disease research also benefits from 3D models. By using collagen scaffolds and perfusion bioreactors, researchers can simulate the brain's microenvironment, providing crucial insights into disease mechanisms and potential treatments. These models enable the study of neuronal interactions and the effects of neuroprotective agents in a setting that closely resembles the human brain (A. R. Murphy et al., 2017).

Liver models are another area where the combination of scaffolds and bioreactors shows great promise. Silk fibroin-chitosan composite scaffolds, when combined with dynamic loading bioreactors, can replicate the liver's complex architecture and function. These 3D models provide a reliable platform for evaluating drug metabolism and toxicity, offering significant advantages over traditional 2D cultures (Krishani et al., 2023).

Clinical relevance of these devices

The clinical relevance of combining scaffolds and bioreactors is intense, offering the potential to transform regenerative medicine and personalized therapy. By providing more accurate models of human tissues and organs, these devices can significantly improve the development and testing of new treatments, ultimately leading to better patient outcomes.

In regenerative medicine, for instance, the combination of scaffolds and bioreactors enables the engineering of functional tissues and organs that can repair or replace damaged tissues in patients. Engineered bone grafts using HA-PLLA composites, for example, can be used to treat bone defects and fractures, providing a viable alternative to traditional bone grafts.

Drug testing and development also benefit from 3D *in vitro* models created using scaffolds and bioreactors. These models offer a more accurate platform for drug testing, reducing reliance on animal models and improving the prediction of drug efficacy and toxicity in humans.

Personalized medicine will benefit immensely from these advancements. The development of patient-specific tissue models, manufactured using scaffolds and bioreactors, lays the foundations for personalized drug testing and tailored treatment planning. These innovations allow for the recreation of patient-specific physiological conditions, which are crucial for the accurate testing of medical treatments. By closely mimicking the biological environment of human tissues, these models enable researchers to observe how different treatments interact with cells in a controlled, but realistic setting. This approach not only enhances the precision of preclinical studies but also reduces the dependence on animal testing, aligning with ethical standards and improving the efficiency of the drug development process. Furthermore, the ability to customize these models to reflect the unique characteristics of individual patients holds the promise of truly personalized therapies, tailored to the specific needs and responses of each person, thereby maximizing therapeutic efficacy and minimizing adverse effects.

Aims and goals

The primary aim of this thesis is to develop and evaluate innovative 3D static and dynamic devices that replicate physiological conditions for two different research line: tissue engineering (TE) applications and 3D *in vitro* models. A key aspect of this work is the strategic use of a single biomaterial, poly(L-lactic acid) (PLLA), chosen for its suitability for thermally induced phase separation (TIPS) and its remarkable versatility. By leveraging different fabrication techniques and post-processing strategies, PLLA can be finely tuned to achieve diverse structural, mechanical, and biological properties. This adaptability allows its use in a wide range of applications, from highly porous scaffolds for tissue engineering to reinforced composite structures with enhanced performance.

To achieve this goal, the research focuses on the following objectives:

1. Develop and optimize static devices based on PLLA scaffolds, created via TIPS, for osteochondral TE applications and 3D cancer models. The choice of PLLA is crucial due to its:
    - Excellent biocompatibility and biodegradability, making it ideal for TE applications.
    - Porosity control through TIPS, allowing for the design of scaffolds with tunable mechanical and biological properties.
    - Potential for composite formulations, enabling the integration of bioactive molecules or secondary materials to enhance functionality.
2. Design and evaluate dynamic bioreactors, including drug delivery and air-liquid interface (ALI) systems, to enhance tissue growth by providing mechanical stimulation, nutrient distribution, and waste removal. These bioreactors complement the PLLA-based scaffolds, offering a more physiologically relevant microenvironment for tissue maturation.
3. Harness the synergy between TIPS and 3D printing to prototype customized and scalable tissue engineering devices. By integrating these two fabrication techniques, this work enables:
    - The rapid development and testing of novel scaffold designs.
    - The adaptation of biomaterials to different tissue engineering needs.
    - The creation of hybrid structures, where TIPS-derived porous scaffolds can be reinforced or combined with 3D-printed frameworks for enhanced mechanical stability.

4. Validate the developed models in relevant biological applications, particularly for tissue engineering and drug prescreening studies, providing new tools for more accurate preclinical testing and personalized medicine approaches.

By combining PLLA's versatility, the integration of TIPS with 3D printing, and the development of dynamic bioreactors, this thesis contributes to advancing *in vitro* tissue models, improving biomaterial applications, and enabling next-generation TE strategies.

II. Experimental section: 3D static and dynamic devices designed and characterized as *in vitro* model or for TE applications

The experimental section of this thesis is organized into different projects, that resemble distinct research works. These projects, developed in parallel during the whole PhD period, focus on the design, production, and application of scaffolds and bioreactor systems. Some results presented in this section have already been published in peer-reviewed journals, highlighting their scientific relevance and impact. In this thesis, I have only included the aspects of those publications that are directly related to my personal contributions and work. Each project includes a dedicated introduction, which outlines the specific context and objectives. This is followed by a detailed materials and methods section, describing the experimental setup, protocols, and techniques employed. The results and discussion section provides an in-depth analysis of the findings, interpreting their implications in the context of tissue engineering or 3D in vitro models. Finally, each project concludes with a summary of its outcomes and their relevance to the overarching aims of the thesis.

Despite the distinctive focus of each project, the work presented in this thesis is unified by several key elements. The use of Thermally Induced Phase Separation (TIPS) to fabricate scaffolds from poly(L-lactic acid) (PLLA) represents a central aspect of the experimental framework. This biomaterial was selected for its biocompatibility, biodegradability, and superior mechanical properties compared to hydrogels. Its adaptability, achieved by modifying pore size or incorporating fillers such as hydroxyapatite, enables the replication of a wide variety of tissues. Another unifying aspect of the experimental work is the development and prototyping of innovative bioreactor systems, designed to provide precise and controlled stimuli, including perfusion and air-liquid interfaces. These bioreactors aim to mimic physiological conditions, thereby enhancing tissue growth and maturation or enabling advanced drug prescreening applications.
The experimental work described in this thesis aims to demonstrate how the synergy between scaffold and bioreactor can lead tissue engineering toward the creation of functional tissues suitable for regeneration or repair. It further seeks to establish innovative 3D models for studying disease mechanisms, testing new drugs, and reducing reliance on animal experiments. Finally, it lays the

groundwork for personalized therapies by offering the possibility of recreating patient-specific tissues for tailored treatment strategies in the future.
This section integrates fundamental research with applied science, emphasizing how the combination of TIPS-fabricated PLLA scaffolds and bioreactor systems can address critical challenges in regenerative medicine, preclinical research, and personalized medicine.

Static Devices

Gradient pore size scaffold via TIPS for TE

The ECM's molecular composition and structure vary by tissue, influencing mechanical properties like stiffness, measured by Young's modulus. For instance, neural tissues have a low modulus (1-4 kPa), while hard tissues like bone and cartilage have higher values (1000-20000 kPa) (Davis et al., 2021). Osteochondral tissue, comprising cartilage and subchondral bone, exemplifies this complexity with its zonal differences in cell distribution, ECM composition, and collagen arrangement. The challenge in regenerating avascular cartilage, unlike vascularized bone, underscores the need for scaffolds that emulate these characteristics(Browe et al., 2022; B. Zhang et al., 2020).
To address this challenge, gradient pore size scaffolds fabricated via Thermally Induced Phase Separation (TIPS) offer a promising strategy. Unlike uniform porous structures, gradient scaffolds enable zonal differentiation by providing distinct microenvironments within the same construct. This approach is especially relevant for osteochondral tissue engineering, where cartilage requires higher porosity for cell migration and nutrient diffusion, while the underlying bone demands greater mechanical strength.
Gradient scaffolds offer significant advantages. They enable zonal differentiation, providing distinct microenvironments that promote specific cellular behaviors in different zones. In the cartilage zone, higher porosity supports enhanced cell migration and nutrient diffusion, which are crucial processes for tissue regeneration. Conversely, the bone zone benefits from reduced porosity, providing the necessary mechanical strength for the underlying structure.
By integrating these advantages, gradient pore size scaffolds can better mimic the natural ECM, potentially leading to improved outcomes in tissue engineering and regenerative medicine.

1. *Project : Effect of thermal history on pore size architecture*

1.1 Introduction

This project focuses on designing scaffolds that replicate the anatomical and physicochemical features of cartilage, calcified cartilage, and subchondral bone, emphasizing gradient pore size, porosity, and interconnectivity. Porosity is crucial for cell infiltration and nutrient transport but must balance mechanical properties. Large pores enhance oxygenation and growth but increase degradation rates if they are too large, while small pores improve cell adhesion. Gradient pore size scaffolds offer smoother transitions between tissue layers, reducing interface instability and improving load transfer.

Material choice for scaffolds depends on application requirements, focusing on biocompatibility, biodegradability, and appropriate mechanical properties. Polymers, particularly Poly-L-lactic acid (PLLA), are favored for their manageable biodegradation rates and ability to mimic native mechanical properties. This study utilizes PLLA to create scaffolds with gradient pore sizes for repairing osteochondral defects, employing the Thermally Induced Phase Separation (TIPS) technique.

TIPS involves cooling a polymer solution to induce phase separation, creating a porous structure. By varying cooling rates, immersion times, polymer concentration, and solvent ratios, scaffolds with well-interconnected structures and varied pore sizes were produced. This study also used a MATLAB toolbox to predict temperature profiles during scaffold production. Several scaffolds were produced and characterized morphologically, topographically, and structurally using tools like Micro-Computed Tomography (μ-CT), Scanning Electron Microscopy (SEM), and Differential Scanning Calorimetry (DSC). MATLAB and Image J software were used for detailed analysis of pore size distribution and porosity.

1.2 Materials and methods

Solution preparation

Scaffolds were prepared from a ternary solution consisting of Poly-L-Lactic Acid (PLLA), 1-4 dioxane, and deionized water. The specific materials used included PLLA (Resomer, L 209 S from Evonik Industries, Essen, Germany), 1-4 dioxane (Sigma-Aldrich, Munich, Germany), and deionized water.

1. Approximately 50 g of 1-4 dioxane was measured and poured into a dedicated graduated beaker under a fume hood due to its toxicity.
2. The precise amount of dioxane was confirmed using a digital precision balance.
3. The weight ratio of dioxane to water was set at 87/13. The unknown water amount was calculated using the proportion in Eq. 1

$$m_{DIOX} : \%_{DIOX} = m_{H2O} : \%_{H2O}$$

Equation 1

The polymer (PLLA) constituted 4% of the entire solution, while the solvent and non-solvent together made up 96%.

4. The polymer mass (mPLLA) was calculated using the proportion reported in Eq. 2:

$$m_{SOL} : \%_{SOL} = m_{PLLA} : \%_{PLLA}$$

Equation 2

where m_{SOL} is the sum of dioxane and water.

5. PLLA was dissolved in the solvent mixture using magnetic stirring at 180°C and 300-400 rpm as shown in Fig.12.

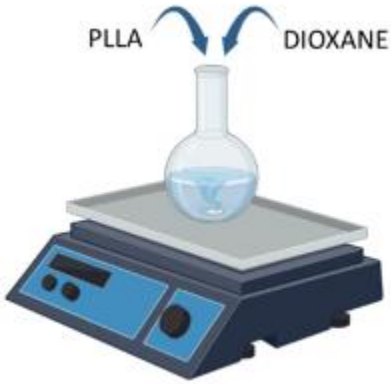

Figure 12: Experimental setup for the preparation of the polymeric solution used in scaffold fabrication. The system includes controlled temperature conditions and continuous stirring to ensure homogeneous mixing before phase separation.

6. Once the polymer-solvent system was clear, the temperature was set to 45°C, and deionized water was added dropwise to the PLLA/1-4 dioxane mixture, as explained in Fig. 13. This order of addition is strategic to avoid dissolution problems due to the higher affinity between dioxane and water rather than the polymer.

Figure 13: Solution preparation scheme: Water addition dropwise

7. After the water addition was complete, the temperature was raised to 180°C to achieve a homogeneous ternary solution.
8. Finally, the temperature decreased to 60°C, and the solution was stored in a stove at this point.

Scaffolds Preparation

Scaffolds with a specific cylindrical geometry were prepared using the Thermally Induced Phase Separation (TIPS) technique. The required geometry was ensured by using a cylindrical High-Density Polyethylene (HDPE) sample holder, with the following dimensions:

- Outer Diameter (OD): 2.06 cm
- Inside Diameter (ID): 1.77 cm
- Wall Thickness: 0.145 cm
- Height: 2.77 cm
- Lid Thickness: 1.32 cm (to isolate the internal system)

The ternary solution, initially maintained at 60°C, was poured into the sample holder, and the lid was secured quickly. The sample holder was then placed in a thermostatic bath set to a specific temperature within the metastable region for 45 minutes to promote phase separation. Following this, it was directly immersed in an ethyl alcohol bath at -20°C for 15 minutes to freeze the scaffold's structure.

Scaffolds were produced under three different thermal histories, altering only the thermostatic bath temperature while keeping the quench temperature and immersion times constant:

1. 25°C
2. 30°C
3. 35°C

For each thermal history, scaffolds were produced in four combinations based on the presence or absence of a Teflon shell coating system in the baths:

1. **N-N (No Teflon-No Teflon)**: No Teflon shell in both baths.
2. **N-T (No Teflon-Teflon)**: Teflon shell only in the quench bath.
3. **T-T (Teflon-Teflon)**: Teflon shell in both baths.
4. **T-N (Teflon-No Teflon)**: Teflon shell only in the thermostatic bath.

A total of twelve scaffolds were produced. After quenching, the frozen sample holders were immersed in deionized water for 5 minutes. The mold was then opened, the scaffold extracted and immersed again in deionized water under a fume hood to remove traces of dioxane.

Washing and Drying

Post-production, the scaffolds were placed in a washing system overnight to completely remove dioxane residues. Each scaffold combination was etched differently with a scalpel for easy identification. The washing system connected to a silicone tube and a deionized water tank. When the tank valve opened, water filled the scaffold sites, and dioxane residues were collected in a separate waste tank. After the overnight wash, dioxane residues were removed, and the scaffolds were dried in a vacuum oven at 45°C.

The scaffolds obtained, exemplified in Fig. 14, underwent morphological and structural analysis using various techniques.

Figure 14: Cylindrical Scaffold obtained ant the end of TIPS protocol, 1,5 cm diameter 2,5 cm height

Scanning Electron Microscope (SEM)

The SEM technique employs an electron beam that interacts with the sample's atoms, generating signals to produce high-resolution images that reveal external morphology, chemical composition, crystalline structure, and pore size distribution.
The SEM system comprises several components: an electron gun with a tungsten filament cathode, which generates the electron beam. The electron beam is then focused and directed onto the sample using electromagnetic lenses. The interaction between the electron beam and the sample's surface and subsurface layers produces emitted electrons, which are collected to form images.
Key types of emitted electrons include:

- **Auger Electrons**: Low-energy electrons providing chemical composition information.
- **Secondary Electrons**: Low-energy electrons used for topographical analysis.
- **Continuous X-Rays**: Used to measure sample mass thickness.
- **Characteristic X-Rays**: Identify elemental composition by generating unique spectral peaks.

The obtained images offer insights into the sample's topography, morphology, composition, and crystallographic information. The surface morphology of PLLA scaffolds was analyzed using the FEI Quanta 200 FEG SEM at the University of Palermo, operating at 10 kV. Prior to analysis, scaffolds were sectioned, mounted on aluminum stubs, and coated with a gold layer to enhance conductivity.

Micro-Computed Tomography (μ-CT)

Micro-CT (μ-CT) is a 3D imaging technique using X-rays to analyze samples non-destructively. Unlike medical CT, μ-CT offers higher resolution, with the sample rotating while the X-ray source and detector remain fixed. This method captures X-ray projection images at different rotation angles, reconstructing them into a 3D virtual model.

μ-CT enables the analysis of internal features such as porosity, structural thickness, volume fraction, and density. The morphology of PLLA scaffolds was assessed using a Skyscan 1272 (Bruker) μ-CT scanner at the ATeN Center, University of Palermo. Scans were conducted using 40 kV X-rays at 250 mA, with the specimen rotating 180° in 0.1° increments, producing high-resolution images with a pixel size of 3.75 μm. Images were processed using Bruker's software for noise reduction and 3D visualization.

Differential Scanning Calorimetry (DSC)

DSC is used to analyze the thermal properties of materials by measuring heat flow during heating or cooling cycles. The DSC instrument compares the heat flow between a sample and a reference. The temperature difference (DT) signal is converted to calorimetric data such as melting point, melting energy, and specific heat.

Thermal properties of PLLA scaffolds were analyzed using the DSC131 evo (Setaram Instrumentation, France). Scaffolds were sectioned, punched, and placed in aluminum crucibles as shown in Fig. 15. The analysis involved heating from room temperature to 220°C at a rate of

10°C/min under nitrogen flow. The melting enthalpy (ΔHm) and melting temperature (Tm) were determined from the resulting data.

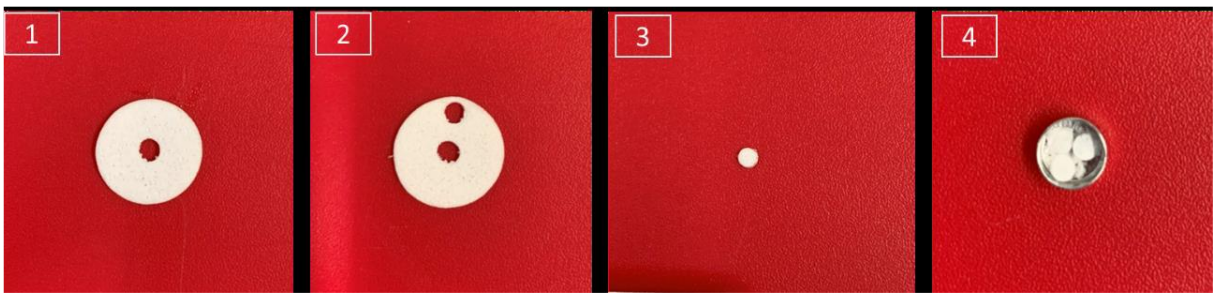

Figure 15: Sample prparation for DSC analysis: from the initial cylinder, circled section were cutted with a blade. From these sections samples were extracted by punching as follow 1) punching at the center ; 2) punchin at the border; 3) punched sample $) samples ready for analysis

Mathematical Modelling: Thermal Transient

The thermal transient of three thermal histories was modeled using the Partial Differential Equation (PDE) Toolbox in MATLAB:

1. Thermostatic bath at 25°C for 45 minutes, then quench at -20°C for 15 minutes.
2. Thermostatic bath at 30°C for 45 minutes, then quench at -20°C for 15 minutes.
3. Thermostatic bath at 35°C for 45 minutes, then quench at -20°C for 15 minutes.

Finite Element Analysis (FEM) was used to determine temperature distribution over time for the cylindrical sample holder and Teflon shell, if present. FEM, effective for complex geometries and materials, solves the heat equation for thermal conductivity. The technique uses domain discretization, applying specific equations to each element, and assembles them into a global system. Boundary conditions, such as fixed temperatures, are applied to this system. Numerical methods then solve the system, providing data on temperature fields, gradients, and heat fluxes.

The analysis assumed a Biot number approaching infinity (Bi→∞), indicating negligible temperature differences between the wall and the external environment. The conduction-dominant heat transfer was modeled using Eq. 3:

$$\rho c_p \frac{\partial T}{\partial t} - \nabla \cdot (k \nabla T) = Q$$

Equation 3

where ρ is density, c_p is specific heat, k is thermal conductivity, $\frac{\partial T}{\partial t}$ is the temperature rate change, $\nabla \cdot (k\nabla T)$ is the thermal conductivity divergence, and Q is internal heat generation.

The MATLAB script used functions like createpde, multicylinder, generateMesh, and pdemesh for creating and plotting the model's mesh. Thermal properties were assigned using thermalProperties, with initial and boundary conditions set via thermalIC and thermalBC. The thermal transient was solved with solve, and the temperature values were organized into a matrix, "Tradius".
The modeling provided temperature trends versus radius for both baths, generating 24 temperature-time profiles. These were used to create temperature-time graphs at different radial values, focusing on the outer and inner radii (Rborder and Rcenter). The temperature difference (ΔTCB) between the center and border was calculated for all cases and time intervals.

Pore Size Analysis: *ImageJ and MATLAB*

SEM images were analyzed with ImageJ to measure average pore size. Since pixel dimensions vary with magnification, a conversion to metric units (micrometers) was necessary:

- Open the image in ImageJ.
- Use the Line Tool to draw across the scalebar.
- Select Analyze > Set Scale to calibrate the scalebar in pixels.
- Enter the known distance and unit (e.g., 1 mm).

Forty measurements per image were manually recorded to estimate average pore diameter. Pore size distributions for the scaffold's center, middle zone, and border were plotted using Origin 2023b.

A MATLAB script was also used for pore size and distribution analysis. The script:

- Converted images to grayscale.
- Divided the image into regions using multithresh.
- Converted the image to binary with imquantize, representing pores with black pixels.
- Visualized segmented images using label2rgb.

The final part of the script removed background noise, identified pores, measured average diameter, and plotted pore size distribution.

1.3 Results

After producing the scaffolds, the first morphological analysis was conducted using Scanning Electron Microscopy (SEM) for the three thermal histories. SEM images in tiff format were used to calculate pore sizes and distribution with ImageJ and MATLAB software. These measurements were then plotted using Origin Pro to visualize pore dimension distributions. However, SEM analysis is limited to examining the sample's surface, and sample preparation may cause surface damage. Therefore, a second, non-invasive analysis using micro-Computed Tomography (μ-CT) was performed to verify the SEM results and provide a comprehensive view of scaffold morphology.

Morphological Analysis

A. **First Thermal History (25°C-45'/-20°C-15') Fig. 16:**

SEM and μ-CT images showed that N-N and T-N scaffolds had smaller pores compared to N-T and T-T scaffolds. A continuous pore size gradient from the center to the border was less evident than other thermal histories.

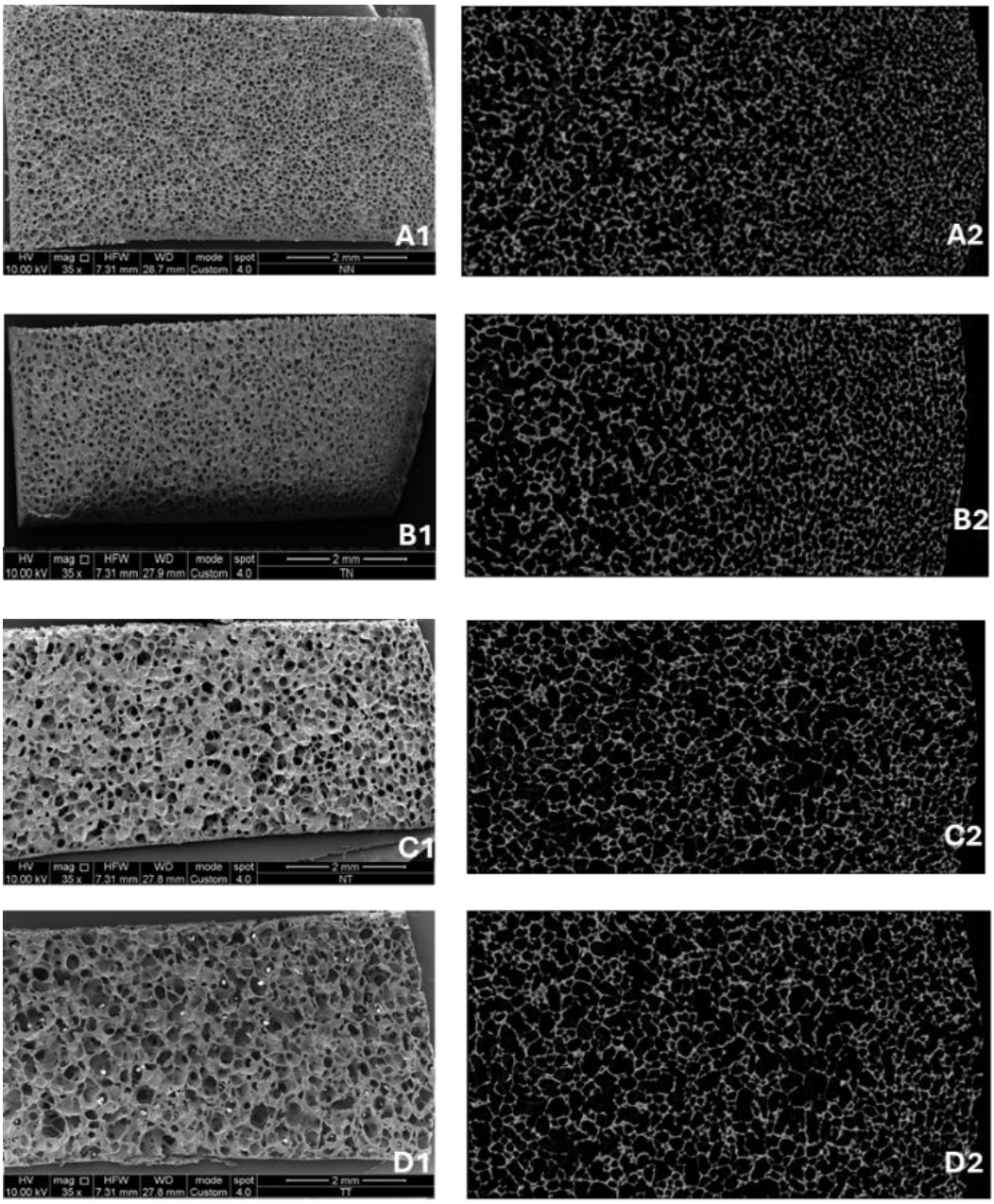

Figure 16: SEM and µ-CT images (center-border) of PLLA scaffolds at 25°C. A1) N-N (SEM); A2) N-N (µ-CT); B1) T-N (SEM); B2) T-N (µ-CT); C1) N-T (SEM); C2) N-T (µ-CT); D1) T-T (SEM); D2) T-T (µ-CT).

B. **Second Thermal History (30°C-45'/-20°C-15') Fig. 17:**

SEM and µ-CT analysis revealed a more pronounced continuous gradient in pore size for N-N and T-N scaffolds. Scaffolds with Teflon shell in the quench (N-T and T-T) displayed more regular and homogeneous morphology with larger pores.

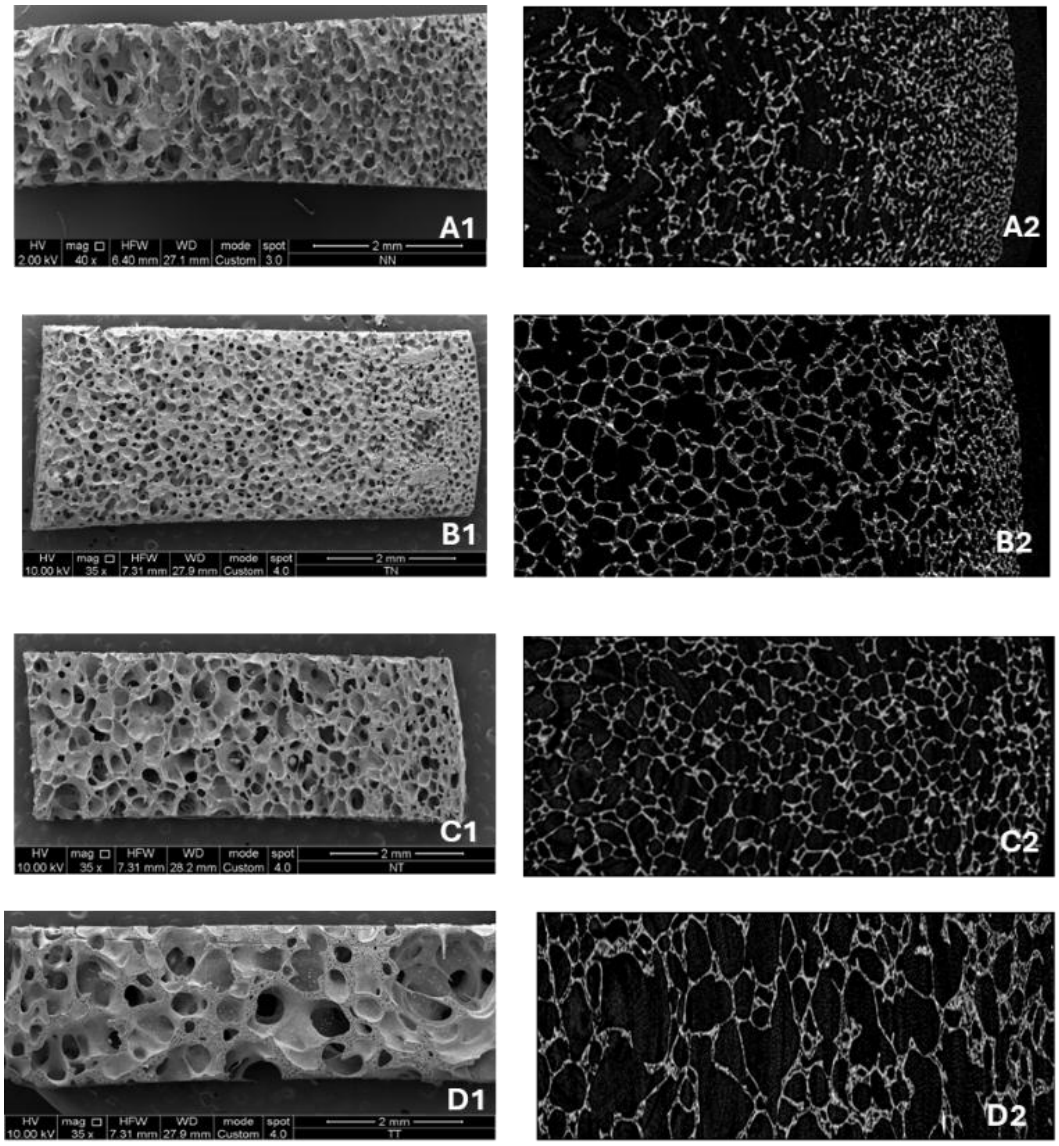

Figure 17: SEM and µ-CT images (center-border) of PLLA scaffolds at 30°C. A1) N-N (SEM); A2) N-N (µ-CT); B1) T-N (SEM); B2) T-N (µ-CT); C1) N-T (SEM); C2) N-T (µ-CT); D1) T-T (SEM); D2) T-T (µ-CT).

C. **Third Thermal History (35°C-45'/-20°C-15') Fig. 18:**

All scaffold combinations exhibited more homogeneous morphology, including those with previously described gradient porous structures.

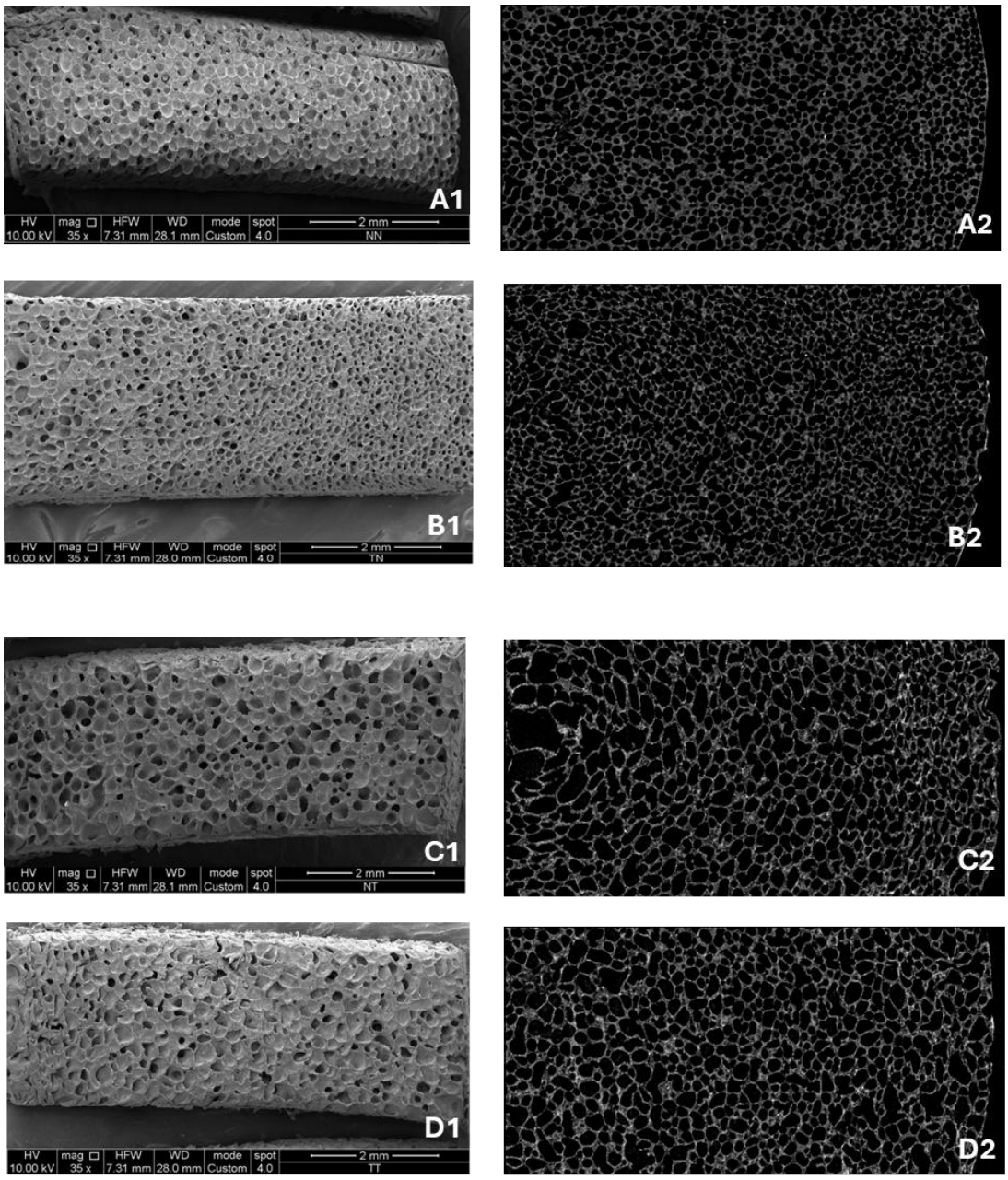

18: SEM and µ-CT images (center-border) of PLLA scaffolds at 35°C. A1) N-N (SEM); A2) N-N (µ-CT); B1) T-N (SEM); B2) T-N (µ-CT); C1) N-T (SEM); C2) N-T (µ-CT); D1) T-T (SEM); D2) T-T (µ-CT).

SEM and µ-CT images of scaffolds for each thermal history highlight differences in pore size and distribution between center and border regions.

Pore Size Analysis

SEM images were magnified 100x in the center, middle zone, and border of the sample to calculate pore sizes. Two reference case studies, N-N and T-T scaffolds prepared at 30°C, are represented in the Fig. 19

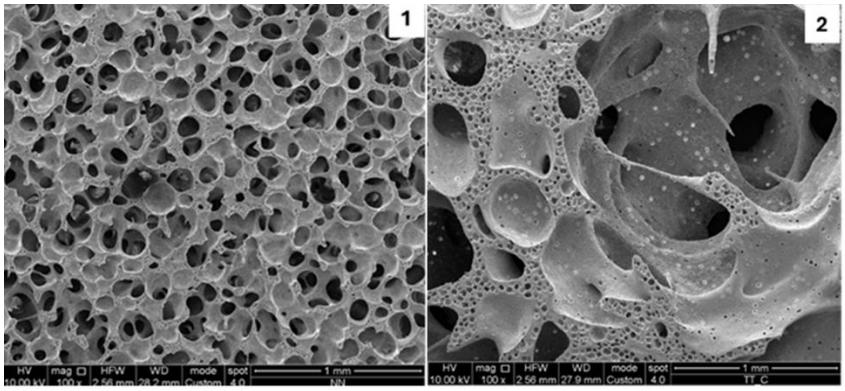

Figure 19: SEM image (100 x) of scaffolds. 1) N-N$_{_CENTER}$; 2) T-T$_{_CENTER}$ In addition, in Tables 1,2, and 3 the standard deviation was also reported for each calculated average value. The statistical difference between the average values of the border (B) and center (C) was reported in the last column.

Average pore sizes, calculated using SEM images analyzed in ImageJ and MATLAB, are reported in below (Tab. 1, Tab.2, Tab 3) for each thermal history. For each SEM image were measured at least 40 pores for all conditions but the T-T case in which there are larger and less pore so the measurement were 15. After measuring a t-Test was carried out in order to verify if the average pore dimensions between the center and the border of the scaffold were statistically different or not. In the first case a successful pore gradient was considered, whereas in the second case the whole structure was assumed as homogeneous

Table 1: Scaffold pore sizes prepared at 25°C calculated with ImageJ and MATLAB. Statistical significance for pore size differences was assessed using an independent t-test. A result of 'yes' in the last column indicates a statistically significant difference ($p < 0.05$) between the center and border pore sizes, while 'no' signifies no significant difference ($p \geq 0.05$)

Scaffold Type	Average diameter (**µm**) ImageJ			Average diameter (**µm**) Matlab			Border-Centre Pore Size differences
	C	**M**	**B**	**C**	**M**	**B**	
N-N	91 ± 22	77 ± 19	59 ± 20	85 ± 16	72 ± 13	55 ± 15	yes
T-N	88 ± 15	77 ± 19	75 ± 18	82 ± 20	71 ± 25	71 ± 14	yes
N-T	166 ± 43	131 ± 41	125 ± 40	161 ± 39	128 ± 42	122 ± 32	yes
T-T	157 ± 37	149 ± 42	146 ± 43	153 ± 51	144 ± 53	140 ± 39	no

Table 2: Scaffold pore sizes prepared at 30°C, calculated with ImageJ and MATLAB. Statistical significance for pore size differences was assessed using an independent t-test. A result of 'yes' in the last column indicates a statistically significant difference ($p < 0.05$) between the center and border pore sizes, while 'no' signifies no significant difference ($p \geq 0.05$)

Scaffold Type	Average diameter (**µm**) ImageJ			Average diameter (**µm**) Matlab			Border-Centre Pore Size differences
	C	**M**	**B**	**C**	**M**	**B**	
N-N	161±32	142 ± 19	112 ± 25	157 ± 24	133 ± 19	105 ± 16	yes
T-N	138 ± 34	127 ± 35	109 ± 26	131 ± 31	120 ± 36	102 ± 20	yes
N-T	179 ± 65	179 ± 62	171 ± 72	172 ± 47	171 ± 51	163 ± 50	no
T-T	326 ± 127	376 ± 131	273 ± 74	301 ± 90	324 ± 131	264 ± 99	no

Table 3: Scaffold pore sizes prepared at 35°C, calculated with ImageJ and MATLAB. Statistical significance for pore size differences was assessed using an independent t-test. A result of 'yes' in the last column indicates a statistically significant difference ($p < 0.05$) between the center and border pore sizes, while 'no' signifies no significant difference ($p \geq 0.05$)

Scaffold Type	Average diameter (**µm**) ImageJ			Average diameter (**µm**) Matlab			Border-Centre Pore Size differences
	C	**M**	**B**	**C**	**M**	**B**	
N-N	149 ± 29	144 ± 36	110 ± 28	144 ± 30	137 ± 49	103 ± 35	yes
T-N	168 ± 46	140 ± 27	132 ± 43	159 ± 37	135 ± 29	124 ± 23	yes
N-T	215 ± 59	212 ± 59	186 ±. 59	204 ± 39	201 ± 43	181 ± 55	yes
T-T	175 ± 87	175 ± 35	178 ± 22	171 ± 46	169 ± 46	171 ± 43	no

When examining the thermal history of the case studies at 30°C, it becomes apparent that the T-T scaffold features larger and more uniform pores. This trait extends to T-T scaffolds across other thermal histories as well. In contrast, the N-N scaffold exhibits the most pronounced pore size gradient, with increases of 55%, 50%, and 40% from border to center for thermal histories at 25°C, 30°C, and 35°C, respectively. T-N scaffolds tend to display a less pronounced gradient in pore structure.

Following qualitative and quantitative analyses, it was determined that for each thermal history, N-N and T-N conditions result in more significant pore size gradients. Meanwhile, N-T and T-T scaffolds are characterized by more homogeneous pore sizes. MATLAB modeling was utilized to uncover the underlying reasons for these observations. Initial temperature profiles within the samples were plotted against the radius, as shown in Figs (20-21) at various iteration times for the first thermostatic bath and the quench process.

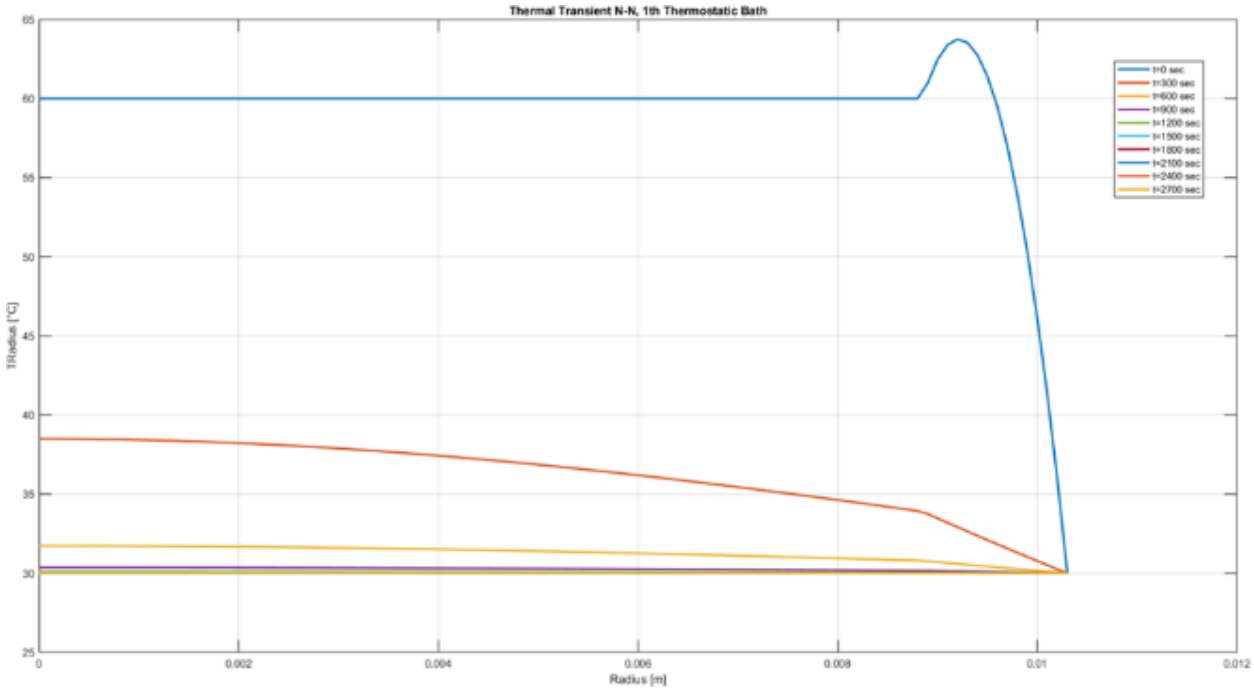

Figure 20 Temperature evolution across the radius of the N-N scaffold (30°C) during the first thermostatic bath. The graph shows temperature transients at different time points (every 300s), illustrating the cooling dynamics within the scaffold matrix.

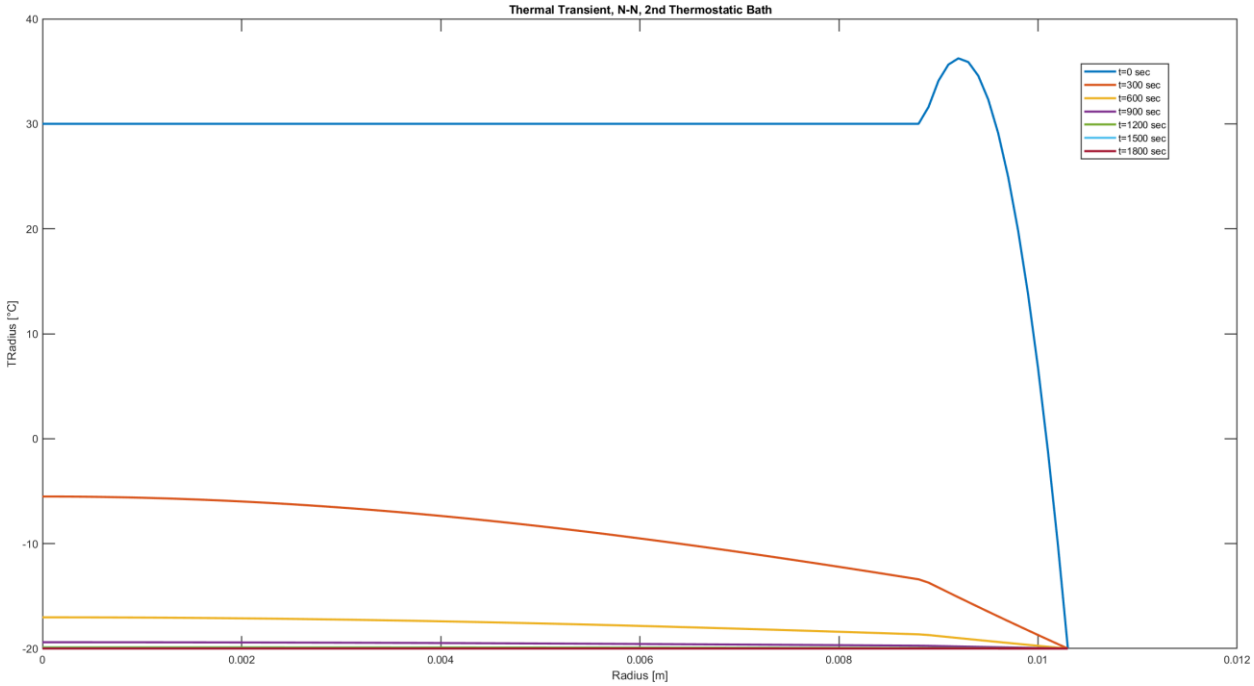

Figure 21: Temperature evolution across the radius of the N-N scaffold (30°C) during the second thermostatic bath. The graph highlights thermal transients at different time points (every 300s), showing the temperature stabilization phase after quenching

In the first simulation, the temperature drops below 40°C within 5 minutes (300 seconds) and reaches 30°C in approximately 10 minutes (600 seconds). During the quenching process, the temperature starts at 30°C and decreases to -20°C in about 10 minutes.

A similar mathematical simulation was conducted for the T-T scaffold, as illustrated in Figs 22-23.

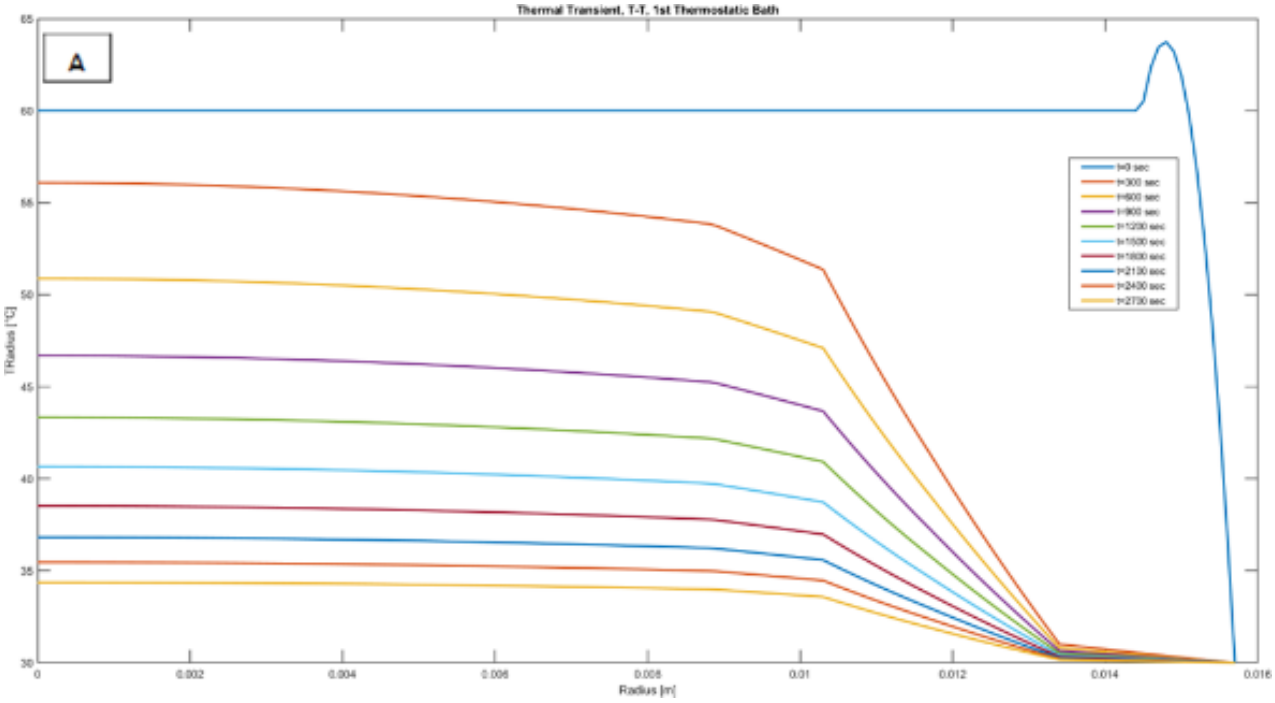

Figure 22: Temperature evolution across the radius of the T-T scaffold (30°C) during the first thermostatic bath. The graph indicates the slower cooling process compared to N-N scaffolds due to the presence of the Teflon shell

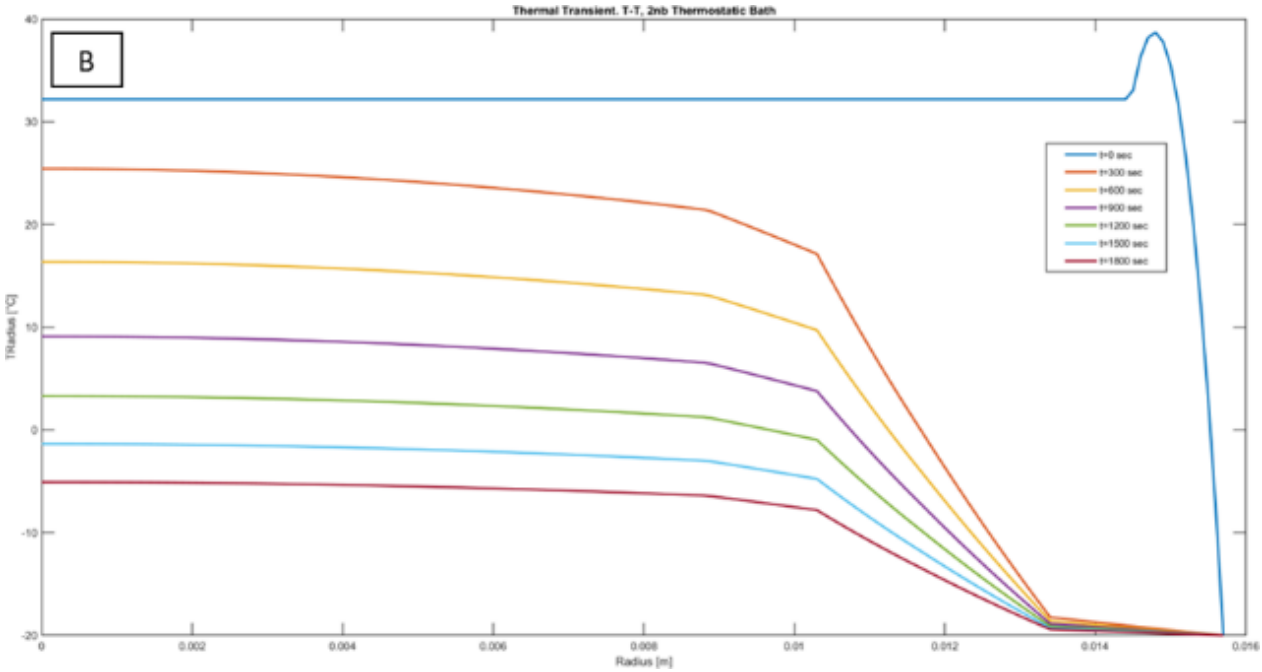

Figure 23: Temperature evolution across the radius of the T-T scaffold (30°C) during the second thermostatic bath. The presence of the Teflon shell results in a delayed thermal transient, influencing the final temperature distribution;

In the T-T simulation, the presence of the Teflon shell resulted in a slower temperature decrease in both thermostatic baths. The additional thermal transients are documented in the appendices. To accurately correlate with the morphological images, it was essential to examine temperature versus time at various radial positions. The focus was on the temperatures at the outer and inner radii of the sample at different times, consistent with the MATLAB simulations, as illustrated in Figs 24-25.

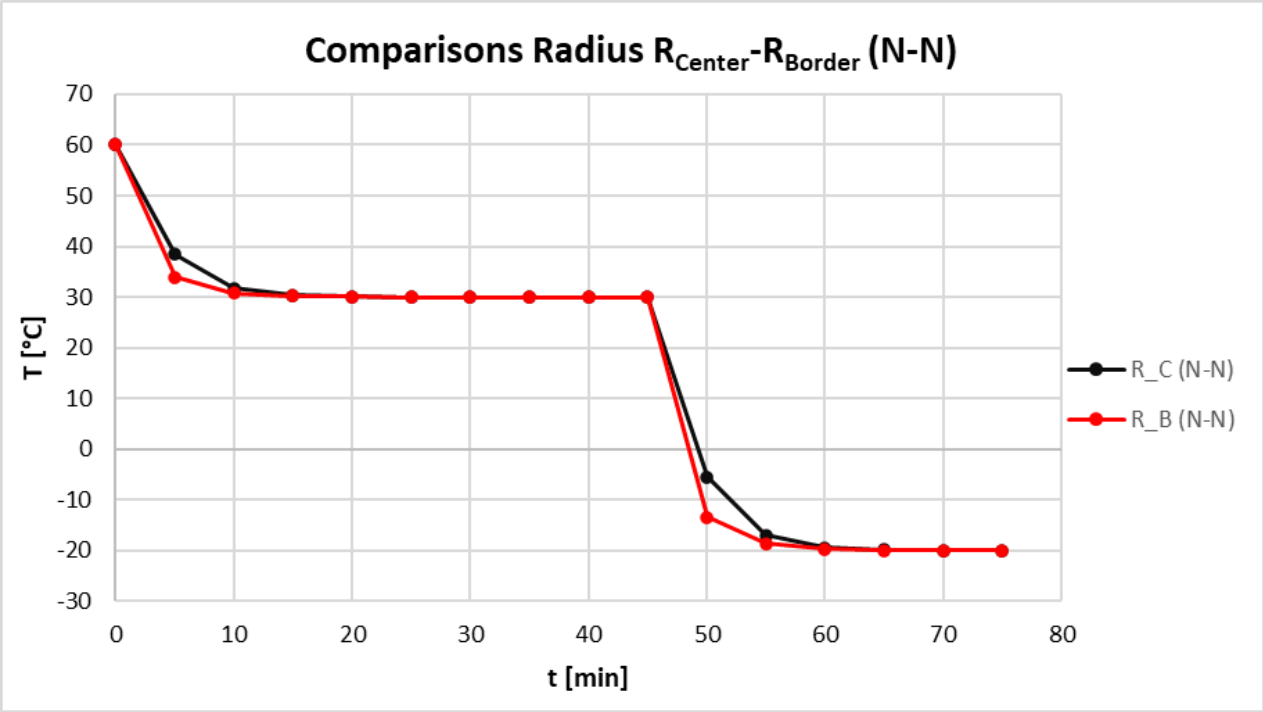

Figure 24: Tempertature-time curves for N-N: Temperature evolution at two distinct radial positions: the outer radius (R_C) and the inner radius (R_B) of the sample. The temperature is plotted against time in minutes, depicting the cooling behavior of the system. The graph reveals two notable temperature drops, occurring around 5 minutes and 47 minutes respectively, followed by periods of temperature stabilization.

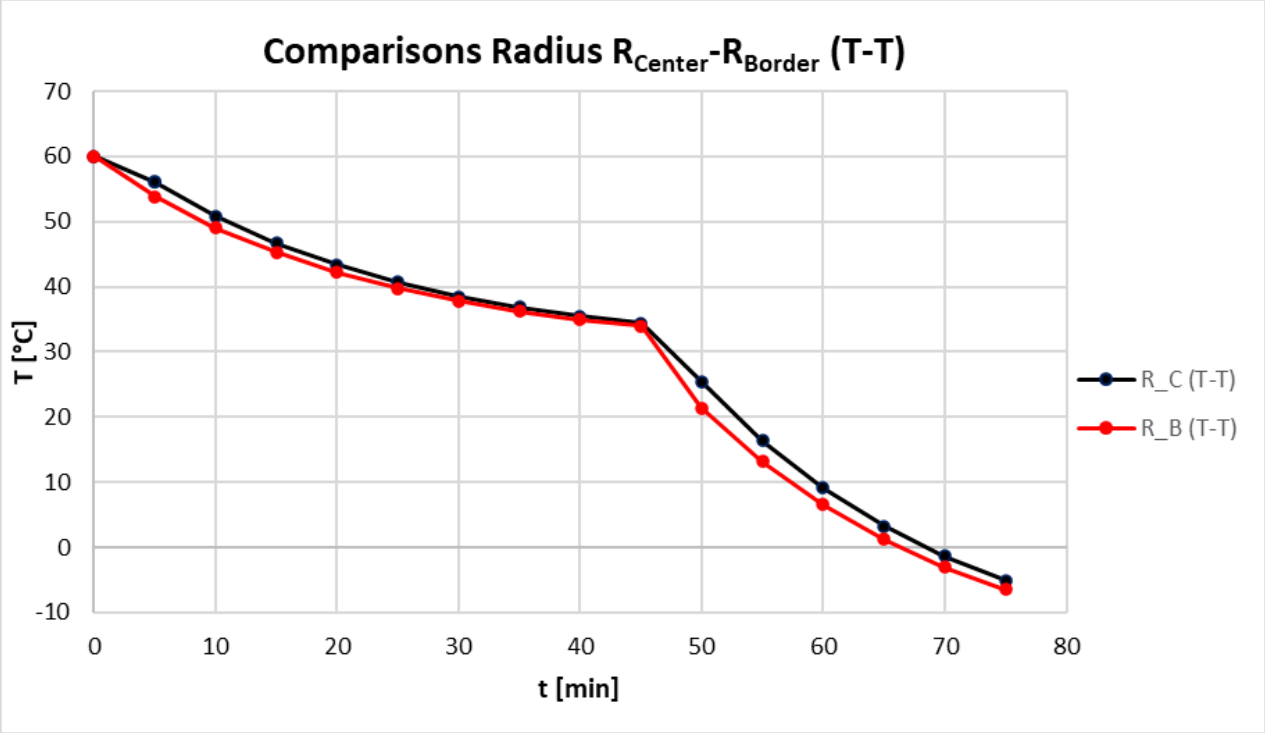

Figure 25: Tempertature-time curves for T-T Temperature evolution at two distinct radial positions: the outer radius (R_C) and the inner radius (R_B) of the sample. The temperature is plotted against time in minutes, depicting the cooling behavior of the system. The graph reveals none severe temperature drops.

After the calculation of the T-t curves for each thermal history, the differences between center and border temperature (ΔTCB), were calculated. The results are resumed in the following tables (Tab. 4,5 and 6) for the three thermal histories.

Table 4: ΔT_{CB} for scaffolds prepared at 25°C

	ΔT_{CB}				
Scaffold Type	5 min	45 min	50 min	60 min	75 min
N-N	5.3	0	7.15	0.31	0
T-N	2.61	0.44	7.54	0.32	0
N-T	5.3	0	3.46	2.23	1.14
T-T	2.61	0.44	3.65	2.35	1.21

Table 5: ΔT_{CB} for scaffolds prepared at 30°C.

	ΔT_{CB}				
Scaffold Type	5 min	45 min	50 min	60 min	75 min
N-N	4.55	0	7.891	0.33	0
T-N	2.24	0.38	8.218	0.34	0
N-T	4.55	0	3.83	2.464	1.27
T-T	2.24	0.38	3.99	2.57	1.32

Table 6: ΔT_{CB} for scaffolds prepared at 35°C.

	ΔT_{CB}				
Scaffold Type	5 min	45 min	50 min	60 min	75 min
N-N	3.84	0	8.64	0.36	0
T-N	1.87	0.32	8.91	0.36	0
N-T	3.84	0	4.21	2.71	1.384
T-T	1.87	0.32	4.35	2.791	1.428

The trends of ΔTCB for the studies cases (N-N and T-T at 30°C) is below reported in Figs. 26-27.

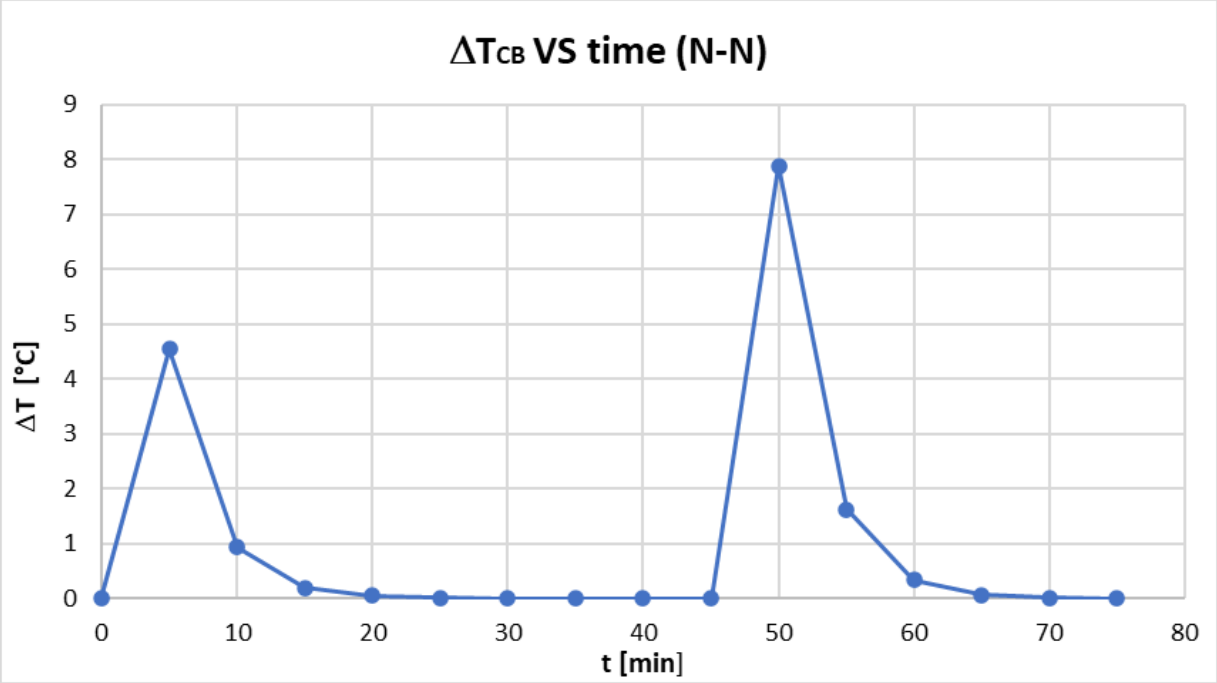

Figure 26: Trend of ΔTCB for T-T scaffolds, prepared at 30°C Exhibits significant fluctuations with notable ΔTCB peaks at 5 minutes (4.55°C) and 50 minutes (7.891°C), indicating periods of rapid temperature change followed by stabilization to 0°C at 45 minutes and 75 minutes.

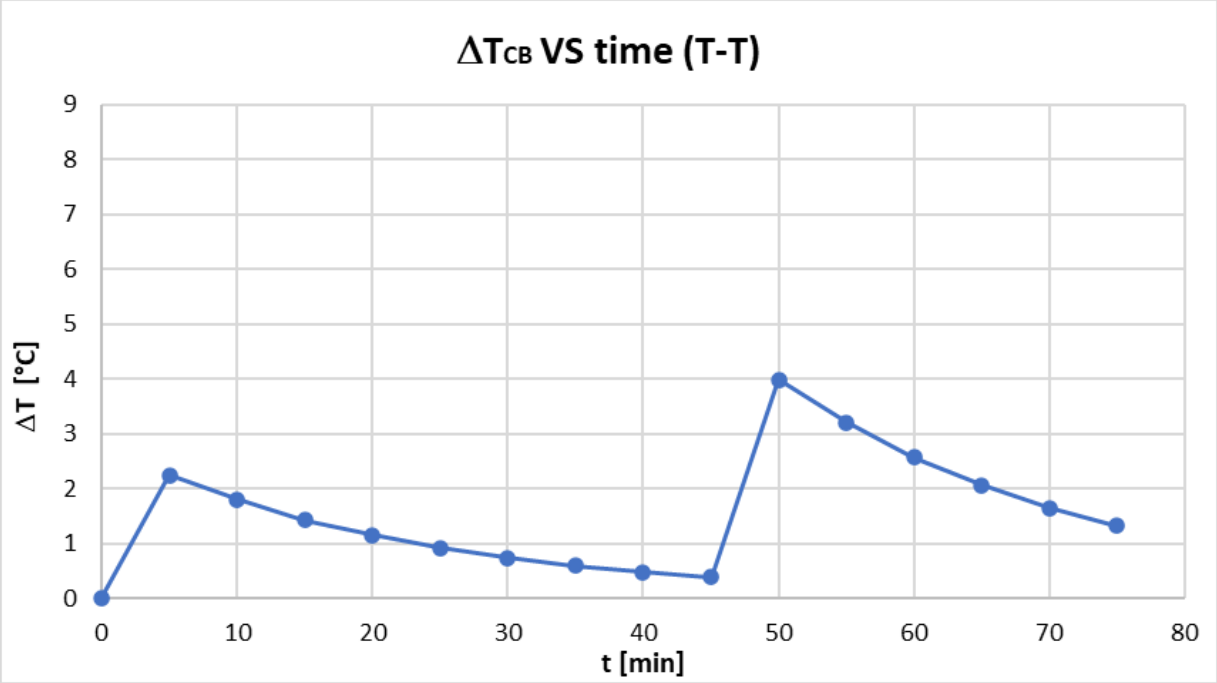

Figure 27: Trend of ΔTCB for T-T scaffolds, prepared at 30°C. Moderated thermal response with lower ΔTCB values. Peaks are observed at 5 minutes (2.24°C) and 50 minutes (3.99°C), with stabilization at 0.38°C at 45 minutes and 1,32°C at 75 minutes.

It is apparent that the greatest center-border temperature difference occurs between 45 and 50 minutes, coinciding with the onset of the quench process. Consequently, we carried out the mathematical simulation of the thermal transient again, increasing the discretization time (every two minutes) to better evaluate the temperature differences between the border and the center. This produced new ΔTCB tables and trends. These results are reported in Figs. 28-29.

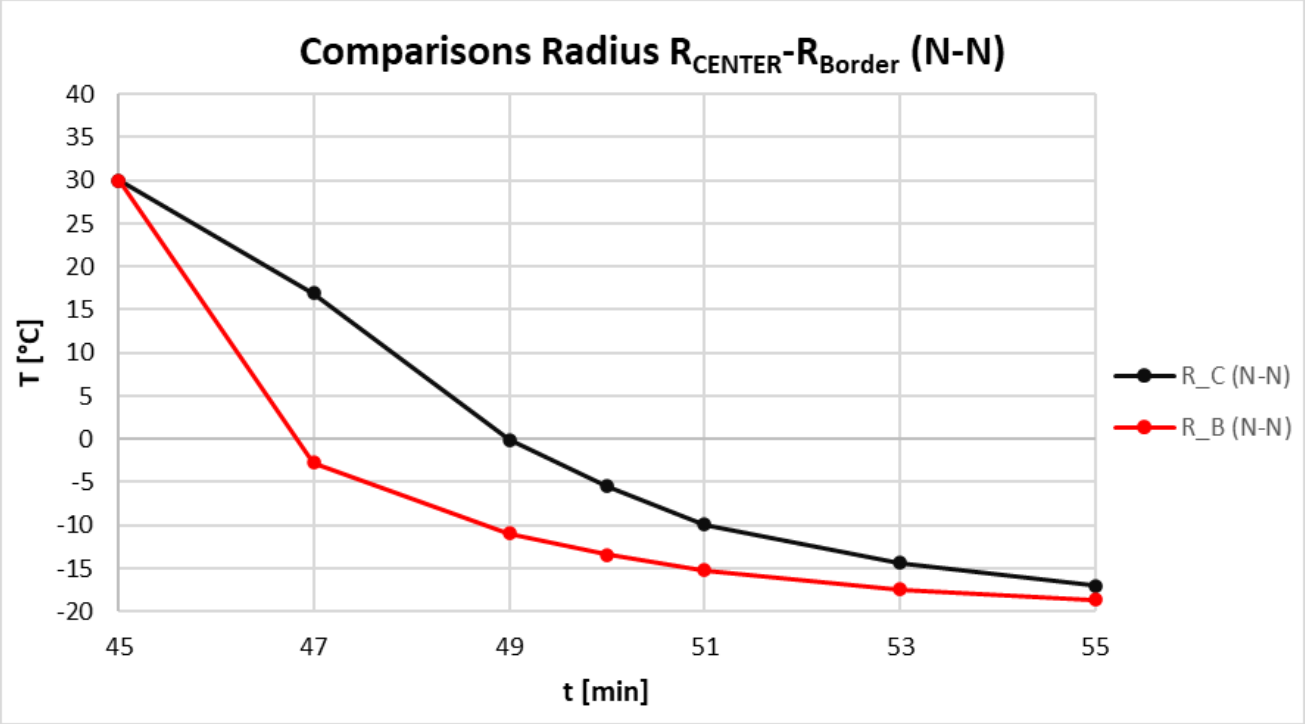

Figure 28: MATLAB-generated thermal transient simulation for N-N scaffolds. The model validates experimental observations, showing the influence of thermal history on scaffold cooling behavior and final temperature distribution (range time 45-55 minutes).

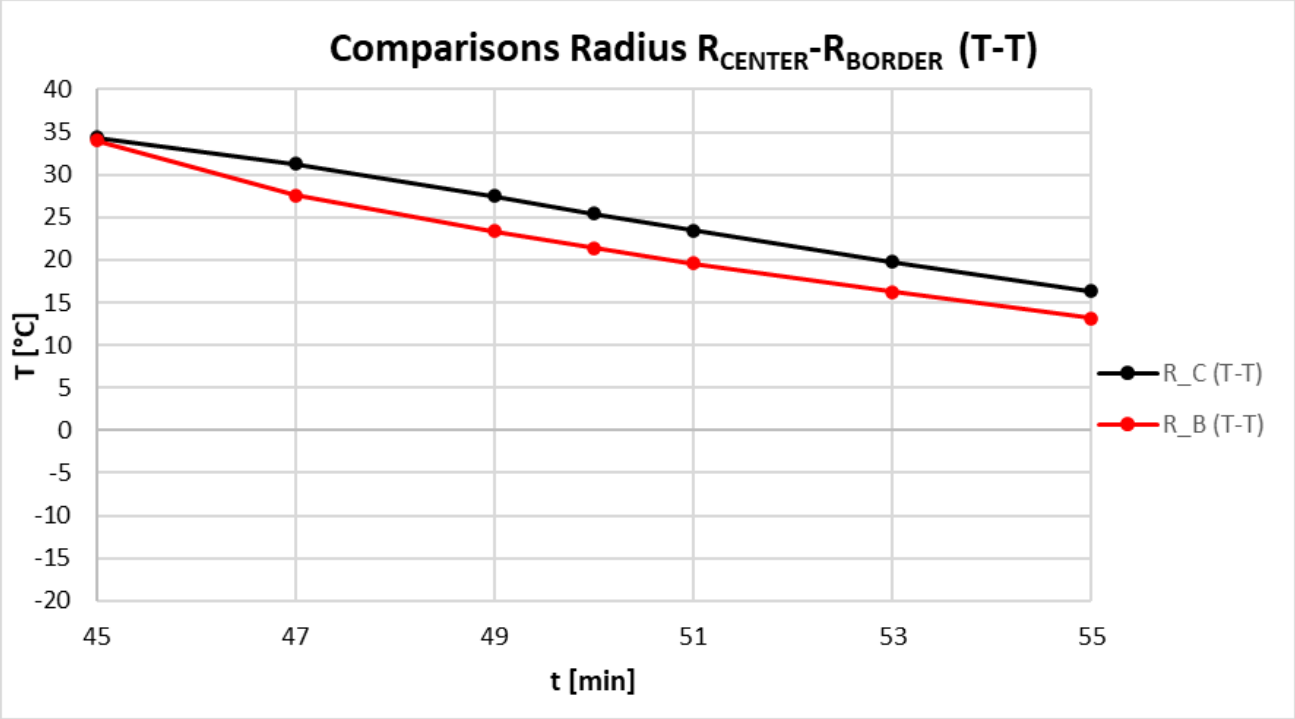

Figure 29: MATLAB-generated thermal transient simulation for T-T scaffolds. The model validates experimental observations, showing the influence of thermal history on scaffold cooling behavior and final temperature distribution (range time 45-55 minutes).

For both case studies, the temperature difference between the center and border (ΔTCB) was calculated and reported in Figs. 30-31.

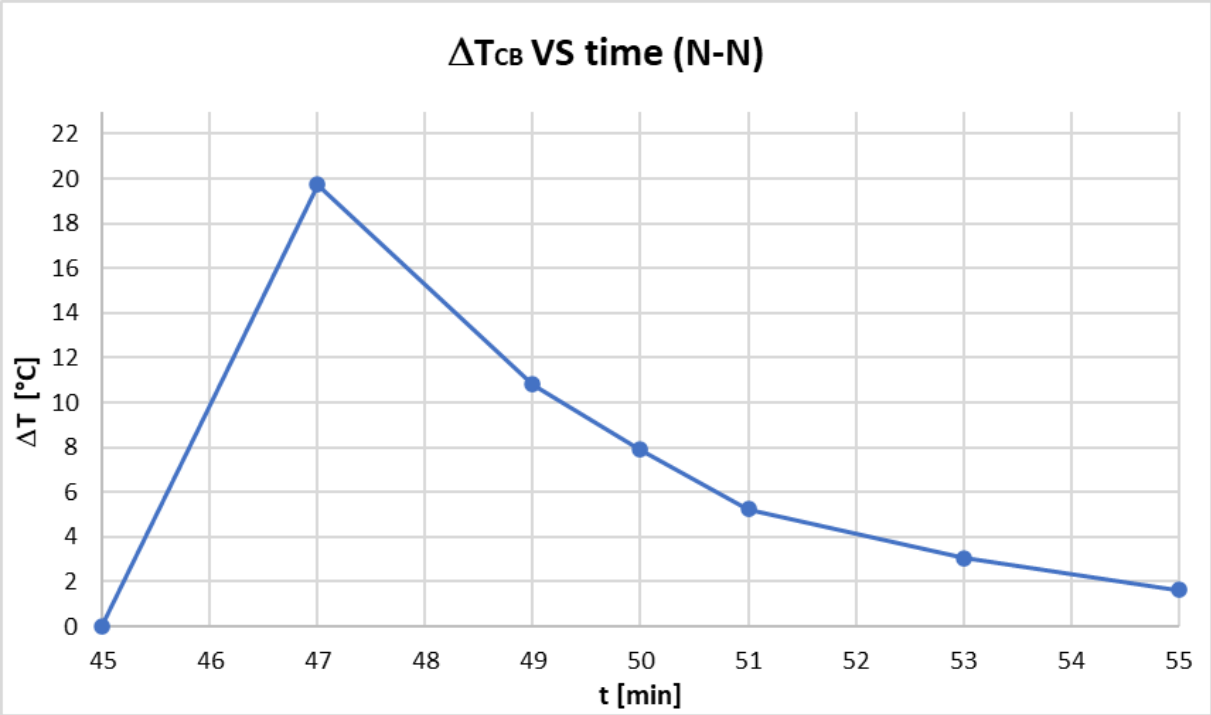

Figure 30: trend of the temperature center-border difference (ΔTCB) for N-N scaffolds over the 45-55 minute range, prepared at 30°C. The graph illustrates the thermal gradient evolution, highlighting critical temperature variations between the scaffold core and periphery during the quenching process

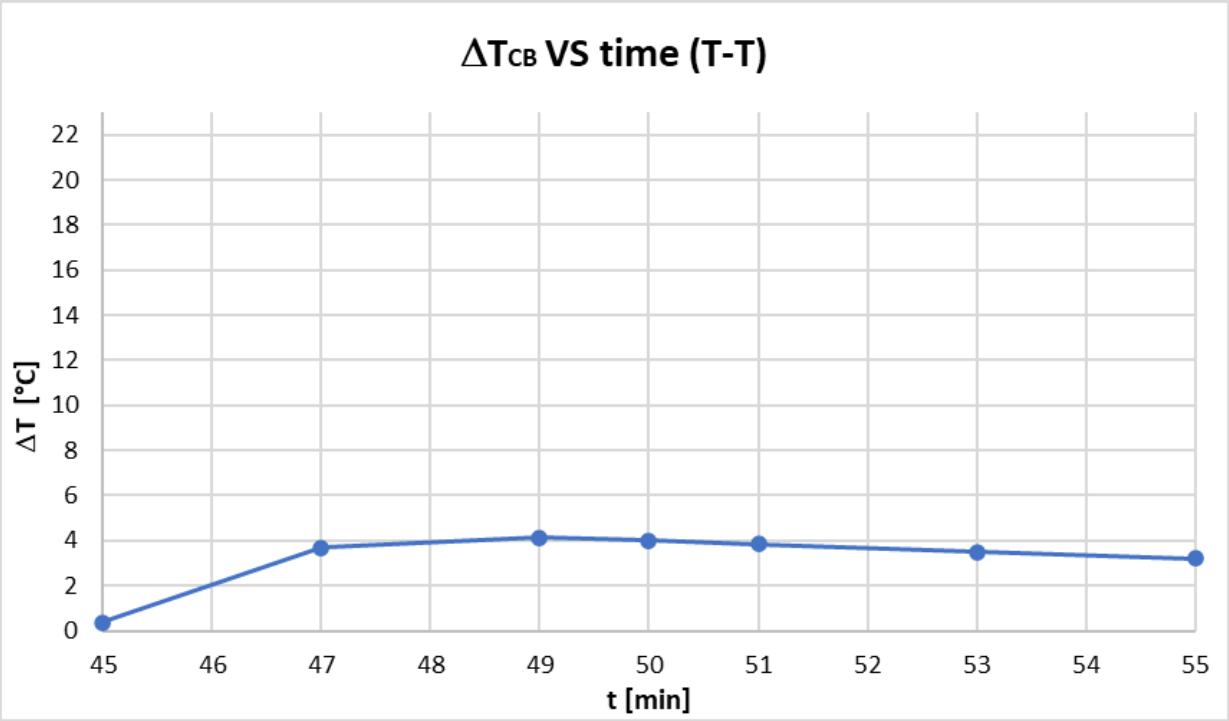

Figure 31 : trend of the temperature center-border difference (ΔTCB) for T-T scaffolds over the 45-55 minute range, prepared at 30°C. The graph illustrates the thermal gradient evolution, highlighting critical temperature variations between the scaffold core and periphery during the quenching process

The ΔTCB for the three thermal histories is summarized in Tab. 7, Tab. 8 and Tab. 9.

Table 7: ΔT_{CB} for scaffolds prepared at 30°C

Scaffold Type	5 min	45 min	47 min	49 min	51 min	75 min
N-N	5.3	0	17.81	9.80	5.23	0
T-N	2.61	0.44	18.79	10.32	5.51	0
N-T	5.3	0	3.17	3.58	3.31	1.14
T-T	2.61	0.44	3.35	3.77	3.5	1.21

Table 8: ΔT_{CB} for scaffolds prepared at 30°C

Scaffold Type	5 min	45 min	47 min	49 min	51 min	75 min
N-N	4.55	0	19.73	10.83	5.25	0
T-N	2.24	0.38	20.57	11.27	5.99	0
N-T	4.55	0	3.53	3.96	3.68	1.27
T-T	2.24	0.38	3.68	4.13	3.83	1.32

Table 9: ΔT_{CB} for scaffolds prepared at 35°C

Scaffold Type	5 min	45 min	47 min	49 min	51 min	75 min
N-N	3.84	0	21.65	11.85	6.29	0
T-N	1.87	0.32	22.38	12.23	6.49	0
N-T	3.84	0	3.88	4.36	4.03	1.35
T-T	1.87	0.32	4.01	4.5	4.17	1.43

From this further discretization, we can observe how ΔTCB increases significantly in the first minutes of the quench for conditions without quench insulation (e.g., *-N). ΔTCB also increases with higher demixing temperatures: for instance, in the N-N case, it increased from 17.81°C for the first thermal history (25°C) to 19.73°C for the second one (30°C), reaching 21.65°C for the third thermal history (35°C).

Regarding ΔTCB, T-T and N-T scaffolds exhibited smaller temperature gradients. They remained in the metastable region for a prolonged period, cooling slowly with similar temperatures at the border and center. Thus, during quenching, the pores had more time to grow uniformly. Larger pores in T-T samples may be attributed to the solution not reaching the set temperature but a higher one. For example, the T-T solution of the second thermal history, after 45 minutes, reached approximately 35°C, whereas the N-T solution reached the set temperature of 30°C. This observation aligns with literature data indicating that higher demixing temperatures result in larger average pore sizes. In fact, scaffolds prepared at 35°C showed bigger pores than those prepared at 30°C.

The N-T scaffold, prepared at 30°C, quickly reached the set temperature and maintained the same temperature profile at the center and border during the quench process, resulting in a more homogeneous morphology.

Crystallization Analysis

Focusing on the second bath Fig.30 for the N-N case, it is evident that the cooling rate of the border is significantly faster than that of the center. A plausible explanation for the smaller border pores in N-N scaffolds is a different crystallization process. DSC analysis revealed that the melting enthalpy (ΔH) differed between the border and center:

- N-N scaffold: ΔH_border = 54.399 J/g, ΔH_center = 66.746 J/g.
- T-T scaffold: ΔH_border = 62.893 J/g, ΔH_center = 62.893 J/g.

This difference in melting enthalpy could be linked to varying degrees of crystallization. A higher crystallization rate is associated with lower melting enthalpy. In the T-T scaffold, the border and center cooling rates were almost the same, resulting in no significant difference in crystallization degree. Consequently, the ΔH values for T-T scaffolds were nearly identical, as reported in Tab. 10, indicating uniform crystallization kinetics and the absence of a pore gradient.

Table 10: DSC values for the scaffold 30°-45'

Sample	**ΔH_melt [J/g]**	**T_melt [°C]**
N-N_Center	66.746	180.036
N-N_Border	54.399	180.404
T-N_Center	64.482	180.122
T-N_Border	60.975	180.487
N-T_Center	67.781	179.063
N-T_Border	63.574	179.374
T-T_Center	63.879	180.172
T-T_Border	62.893	180.866

Taking Tab. 10 as a reference, the maximum difference in melting enthalpy, indicating crystallization, was observed in N-N scaffolds, correlating with the greater difference in pore sizes from border to

center. T-N and N-T samples showed smaller differences in melting enthalpy, resulting in less defined pore size gradients. The T-T samples exhibited nearly identical enthalpies between center and border, suggesting uniform crystallization kinetics and the absence of pore gradients.

1.4 Discussion

This study focused on the development of PLLA scaffolds with gradient pore sizes for osteochondral tissue regeneration, employing the Thermally Induced Phase Separation (TIPS) method. The results highlight the significance of thermal history and the quenching process in controlling the final morphology of the scaffolds in terms of pore size.

SEM and μ-CT analysis confirmed that pore size distributions varied significantly with thermal history. Scaffolds prepared with Teflon insulation (T-T) exhibited more uniform pores, whereas non-Teflon scaffolds (N-N and T-N) showed pronounced gradient pore structures, particularly in the N-N case, where the largest center-border pore size differences were observed. These findings are consistent with the work of La Carrubba et al. (2018) (La Carrubba & Brucato, 2018), who noted the impact of thermal conditions on pore homogeneity in polymer scaffolds.

The MATLAB simulations of the thermal transient behavior revealed that scaffolds without Teflon insulation (N-N) had the most significant temperature differences between the center and border, particularly during the quenching process. This temperature gradient likely explains the observed differences in pore formation, with faster cooling rates in the border region leading to smaller pores. This aligns with findings from Chinnasami et al. (2018) (Chinnasami et al., 2018), where rapid cooling rates induced by phase separation resulted in smaller and more irregular pores.

In terms of crystallization, DSC analysis revealed that N-N scaffolds exhibited the largest difference in melting enthalpy between the center and border, which correlated with their pronounced pore size gradient. The uniform crystallization kinetics observed in T-T scaffolds may explain the more homogeneous pore structures in these samples, supporting earlier studies by Huang et al. (2014) (Huang et al., 2014), who highlighted the role of controlled crystallization in achieving uniform pore morphology.

The findings also demonstrate the importance of temperature control during the phase separation process in determining pore size and distribution. The second bath, particularly during the 45–55 minute quenching period, played a crucial role in the formation of pore gradients, especially in the N-N scaffolds. These observations were consistent with the work of La Carrubba et al. (2008) (La

Carrubba et al., 2008) who showed that slow cooling facilitated the formation of larger, more homogeneous pores in PLLA scaffolds.

1.5 Conclusion

This research explored the development of scaffolds with gradient pore sizes for osteochondral tissue regeneration by using TIPS tecnique. Osteochondral tissue, an anisotropic structure composed of cartilage and bone, plays a critical role in supporting joint function. Damage to this tissue can lead to pain and impaired mobility, which are often challenging to treat. Tissue engineering offers a promising alternative by employing biomaterials designed to facilitate osteochondral tissue regeneration.

In this research, poly(L-lactic acid) (PLLA) scaffolds were fabricated using the Thermally Induced Phase Separation (TIPS) technique. TIPS relies on liquid-liquid phase separation to create a porous structure, with the pore size a critical factor for cellular growth being adjustable by modifying the process temperature and duration.

This study investigated various strategies to produce PLLA-based scaffolds with gradient pore sizes with low cost tecnique. Scaffolds were prepared under different thermal histories and parameter combinations. Across all three thermal histories, the first bath was found to be the primary determinant of pore dimensions, while the second bath (quenching stage) was critical for inducing a pore gradient in samples without a Teflon shell during the 45–55-minute range. Conversely, samples with a Teflon shell exhibited a more uniform pore morphology.

Thermal transient analysis, combined with morphological characterization, established a correlation between the applied thermal conditions and the final scaffold structure.

For future advancements, the model could be refined by incorporating the temperature dependence of physical properties such as density, specific heat, and thermal conductivity, which were assumed constant in this reasearch. Furthermore, the results could be validated through mechanical and biological testing. Mechanical evaluations, such as compression tests, would assess the scaffolds' stiffness, toughness, and strength key mechanical properties of osteochondral tissue. From a biological perspective, scaffolds could be seeded with osteoblasts and chondrocytes to evaluate cell adhesion, proliferation, and viability. These studies would help identify the most suitable scaffolds for osteochondral tissue regeneration, particularly in terms of pore size and gradient configuration.

Scaffolds via TIPS as 3D breast cancer model

Breast cancer (BC) is the most prevalent malignant tumor among women globally, accounting for 36% of oncological patients (Smolarz et al., 2022). In 2020, over 2.3 million new cases and 685,000 deaths were reported, with projections indicating over 3 million new cases and 1 million deaths annually by 2040 (Arnold et al., 2022). In Italy alone, 53,000 new cases were reported in 2019, representing the most diagnosed cancer in women (Nardin et al., 2020). The complexity of breast cancer, patient variability, and tumor cell heterogeneity pose significant challenges in finding efficient treatments (Notarbartolo et al., 2004; Poma et al., 2007). Traditional cancer research has relied on animal models, offering insights into tumor genesis and advancements in the field. However, animal models pose ethical concerns, cost issues, and limitations in capturing human breast cancer diversity (Kolahi Azar et al., 2024; Mather, 2012). A major challenge in cancer research is chemotherapy resistance, which often leads to treatment failure. Multidrug resistance (MDR) involves tumor cells developing resistance to various drugs through multiple mechanisms, preventing effective intracellular concentrations of chemotherapeutic agents. Contributing factors include genetic instability, increased DNA repair, epithelial-mesenchymal transition, inhibition of apoptosis, and overexpression of detoxifying enzymes and drug targets. (Gu et al., 2023) (Poma et al., 2024).
2D culture models, where cells are maintained in designed culture media on glass or plastic surfaces, have limitations in accurately replicating cellular and extracellular interactions (Antonelli, 2023; Kapałczyńska et al., 2018). These models often fail to mimic tumor cell biology and drug responses accurately, leading to the development of advanced 3D cell culture models (J. Bin Kim et al., 2004) 3D *in vitro* models offer significant advantages for biomedical research and drug development by better mimicking the human tumor microenvironment compared to 2D cultures. They provide a realistic system for studying disease processes and drug effects, closely resembling *in vivo* conditions. These models enhance our understanding of cancer immunology, cell interactions, and drug responses (Ahmad, 2019; Caballero et al., 2022) revolutionizing breast cancer research and drug testing (Lombardo et al., 2019; Sztankovics et al., 2023). 3D models replicate tissue microenvironments more accurately than 2D cultures, are cost-effective, reproducible, and include human cancer and immune cells with growth factors and biomolecules (Li et al., 2021; Nguyen et al., 2016). Various 3D systems, such as 3D printing and hydrogels, offer different benefits and limitations. 3D printing creates complex support structures for studying tumors in physiological environments (Barcena et

al., 2024; Bhuskute et al., 2022)while hydrogels provide tunable mechanical features and store growth factors (Carfì Pavia et al., 2008a; Prince et al., 2022; Schmid et al., 2020; Xin & Naficy, 2022). Polymeric porous scaffolds, essential in this field, mimic the intricate extracellular matrix (ECM) of breast cancer tissue. These scaffolds offer tunable properties for cell adhesion, migration, and drug response, advancing breast cancer research and treatment development (Sharma et al., 2023).

Below, two studies will be presented that aim to enhance breast cancer research through the use of *in vitro* 3D models.

2. *Project : PLLA porous scaffold as a 3D breast cancer model to investigate drug resistance*

This project has been published in Journal of Biomedical Materials Research A, 2024, where I am the 1st author. The results presented in this thesis derive from my own experimental work and data analysis.

2.1 Introduction

This study addresses the challenge of chemotherapy resistance in breast cancer, which often leads to treatment failure. Multidrug resistance (MDR) involves tumor cells developing resistance to various drugs through mechanisms such as genetic instability, increased DNA repair, epithelial-mesenchymal transition, inhibition of apoptosis, and overexpression of detoxifying enzymes and drug targets. The MDR phenotype often involves overexpression of the MDR1 gene, encoding P-gp efflux pumps (Poma et al., 2021), and remains a significant cause of cancer recurrence and metastasis, highlighting the need for advanced tumor models for better understanding and new therapies (Bucci-Muñoz et al., 2023) (Poma et al., 2024). Traditional cancer research has relied on animal models, offering insights into tumor genesis and advancements in the field (Mondal et al., 2022; Moran-Alvarez et al., 2023; Tosca et al., 2023). However, animal models pose ethical concerns, cost issues, and limitations in capturing human breast cancer diversity (Arnason, 2020; Lakshmanan et al., 2022). These ethical issues and limitations have led to increased use of *in vitro* models, which are more ethical, cost-effective, and allow for controlled experiments To better understand these mechanisms and develop more effective treatments, advanced tumor models are necessary.

This research utilized Poly-L-Lactic Acid (PLLA) porous scaffolds produced by Thermally Induced Phase Separation (TIPS) as a 3D model to establish three distinct breast cancer cell lines: triple-negative breast cancer (MDA-MB-231), ER+ adenocarcinoma (MCF-7), and its multidrug-resistant variant (MCF-7R). PLLA, an FDA-approved polymer for biomedical applications, was chosen for its widespread use and longer degradation time compared to hydrogels. By cultivating these cell lines on PLLA scaffolds, we aimed to create an in vitro microenvironment closely resembling physiological tumor conditions. This innovative approach enables the assessment of cellular interactions, drug response, and molecular mechanisms in a setting that more accurately mimics the human tumor microenvironment. Specifically, we investigated the response of these cell lines to doxorubicin, a commonly used chemotherapeutic agent, and explored the underlying mechanisms of drug resistance.

By utilizing PLLA porous scaffolds, this study seeks to bridge the gap between traditional monolayer cell cultures and in vivo models. The application of 3D cultures provides a more physiologically relevant system for studying disease processes and drug effects, potentially leading to the development of more effective treatments for breast cancer.

In particular, this research project was conducted during my PhD with the support of Prof. Monica Notarbartolo's team composed by Prof. Paola Poma, Dr. Salvatrice Rigogliuso and Dr. Manuela Labbozzetta (University of Palermo)

.

2.2 Materials and Methods

Solution preparation

The solution preparation is completely described in the "2.1.1 Effect of thermal history on pore size architecture", Materials and Methods section.

Scaffold production and characterization

Scaffolds were produced by TIPS starting from a ternary solution based on Poly-Left-Lactic Acid (PLLA, Resomer, L 209 S, Evonik Industries, Essen, Germany), 1,4-dioxane (Sigma-Aldrich, Munich, Germany) and water as described in previous work (Carfì Pavia et al., 2008b).

Briefly, the polymer was dissolved into 1,4 dioxane with a concentration of 4% (wt/wt). Its complete dissolution was achieved by stirring at a temperature of 180 °C for 30 minutes. Then distilled water was added dropwise with a constant dioxane to water weight ratio of 87/13 and still complete dissolution was achieved by stirring at a temperature of 180 °C. When the solution resulted homogeneous it was kept at 60°C until its usage. The solution (initially at 60°C) was poured into a High-Density Polyethylene (HDPE) cylindrical sample holder with an inner diameter of 17.6 mm and a height of 35.7 mm. The sample holder was first immersed into a thermostatic water bath (TWB) set to 20°C (demixing temperature) for a defined demixing time of 15 minutes. Subsequently, the holder was covered by a Polytetrafluoroethylene (PTFE) coating, a thermal resistance to control the cooling rate and immersed into an ethyl alcohol bath (EAB) at -20°C for at least 15 min to suddenly cool down the solution, thus preserving its porous architecture (Lombardo et al., 2019).

At the end of this process, cylindrical scaffolds were obtained and washed in distilled water, drop by drop overnight, to completely remove the dioxane from the inner parts of the matrix. Scaffolds were then placed at 45° C and under vacuum for 3 hours. When they were completely dry, slices of 2 mm were cut by a scalpel, from which little cylinders were extracted using a biopsy punch; these cylinder scaffolds (3,5 mm in diameter and 2 mm in height) were used for the subsequent phases.

The overall morphology of PLLA scaffolds was examined using Scanning Electron Microscopy (SEM, QUANTA 200F, FEI Company Philips, Thermo Fisher, Waltham, MA, USA) with an accelerating voltage of 10 kV. Prior to analysis, samples were cut into small slices and positioned on an aluminum stub coated with conductive carbon tabs.

Pore sizes and distribution were determined from SEM micrographs starting from a MATLAB script found in the literature made by Rabbani et al. (Arash Rabbani, 2023). After defining the spatial resolution and the number of intensity levels of the image segmentation, the script converts the image to a greyscale. The image is divided into multiple regions based on different intensity levels, creating a depth map and subsequently a binary segmentation. At this point the script can estimate the average pore distribution.

Porosity was evaluated through pycnometry. By measuring the change in pressure resulting from the introduction of helium, the real volume of a solid sample can be accurately determined using the principles of gas displacement. Three samples were cut starting from a big cylindrical scaffold and their apparent volumes were calculated. To completely fill the instrument chamber, the samples were inserted simultaneously into a gas pycnometer (Pycnomatic ATC, Thermo Fisher Scientific, Waltham, MA, USA) and the real volume was determined. The porosity of the samples was determined comparing the entire real volume to the sum of apparent volumes of the scaffolds through the following Eq. 4:

$$Porosity\ \% = 1 - \left(\frac{V_{measured}}{V_{apparent}}\right) * 100$$

Equation 4

Cell lines and 2D culture conditions

A human breast adenocarcinoma cell line MCF-7 and a triple-negative breast cancer (TNBC) cell line MDA-MB-231 were obtained from ATCC (respectively HTB-22™ and HTB-26™, Rockville, MD, USA). MCF-7R cells were established treating wild-type cells with gradually increasing concentrations of doxorubicin (Sigma D15-15). The IC_{50} value of doxorubicin in MCF-7R is approximately 50 times higher than the original IC_{50}. Unlike MCF-7, MCF-7R lacks ERα expression, is estrogen-insensitive, and overexpresses P-gp; in addition is characterized by a constitutive activation of the NF-κB pathway, and by the overexpression of some targets of this transcription factor such as Inhibitor of Apoptosis Proteins (IAPs) which determine its resistance to drug-induced cell death. All cell lines were cultured in Dulbecco's Modified Eagle Medium (DMEM) (HyClone Europe Ltd, Cramlington, UK). All media were further supplemented with 10% heat-inactivated fetal calf serum, 2 mM L-glutamine, 100 units/ml penicillin, and 100 µg/ml streptomycin (all reagents were from HyClone Europe). All cell lines were cultured in a humidified atmosphere of 5% CO_2 at 37˚C. Cells with a narrow range of passage numbers were used for all experiments. The cultures, maintained as monolayers in complete medium, were routinely tested for Mycoplasma infection and then, when they reached the 80%-90% confluence, they were enzymatically recovered with trypsin and used in the experiments described below.

Evaluation of 3D growth on scaffolds

The scaffolds were sterilized in 70% ethanol for 8 h, washed 2 times 3 minutes each in Phosphate Buffered Saline (PBS), and soaked in Dulbecco's modified Eagle's-high glucose medium (DMEM, Sigma Aldrich, Italy) 30 min before the seeding. The seeding on scaffolds was carried out in 6-multiwell plates, one for each cell line. The samples were divided into groups of five per well to select the most suitable growth time for the experiments (24 hours, 5 days, 10 days, and 15 days); two scaffolds were used for SEM morphological analysis and three were transferred in a 96- well to perform cell viability analysis using MTS assay. The cells were seeded with a density of 4 × 10^4 cells/scaffold in 10 µL of cell suspension. Subsequently, the plates were incubated in a humidified atmosphere of 5% CO_2 at 37˚C, for one hour; finally, complete culture medium was added to fully cover the scaffolds. For each experiment, unseeded scaffolds were used as controls. At different time points, a commercial solution (MTS: Promega Corporation Madison, WI, USA) containing 3- (4,5-dimethylthiazol-2-yl) -5- (3-carboxymethoxyphenyl) - 2- (4-sulfophenyl) -2H-tetrazolium (MTS)

and phenazine ethosulfate was added. The plates were incubated in a humidified atmosphere at 37°C in 5% CO_2 for 2 hours, and the bio-reduction of the MTS dye was evaluated by measuring the absorbance of each well at 490 nm using a microplate reader (iMark Microplate Reader; BioRad Laboratories, Inc., Hercules, CA, USA). MTS assay was performed in triplicate, for each chosen time point. A cell-free scaffold was used as a blank. All tests were performed in triplicate. The growth trend was expressed showing absorbance values (mean ± SE) versus the different time points.

SEM was carried out to observe cell morphologies during growth. To do so scaffolds were firstly transferred to a 96 multiwell plate and were washed with complete 1X DPBS 3 times, for 3 minutes each. Cells were fixated using 4% glutaraldehyde (Sigma Aldrich) for 30 minutes at 4 °C. Samples were rinsed with complete 1X DPBS 2 times, for 3 minutes each. Dehydration was then carried at room temperature, in solutions of ethanol at increasing concentration (15%, 30%, 50%, 75%, 100%, 3 minutes each). After the last step, the ethanol evaporated at room temperature until the samples were completely dry. Subsequently, the scaffolds were cut into two halves using a scalpel and each half was placed on the stubs with inverted faces, to be able to observe both surfaces. Finally, they were sputter coated for 120 s in argon atmosphere (Sputtering Scancoat Six, Edwards, Crawley, UK) and observed.

Live–Dead Assay

One milliliter of PBS containing Ca++ and Mg++ was mixed with 5 µL of fluorescein diacetate (FDA) stock solution (5 mg/mL in acetone) and 1 µL of propidium iodide (PI) stock solution (2 mg/mL in PBS). The FDA dye stains living cells in green, while the PI dye marks dead cells in red. A total of 50 µL of this staining solution was applied to each sample. Samples were observed from the outer surface and subsequently cut by a scalpel in order to observe the cross section. , and the sample (either a seeded scaffold segment or coverslip) was immersed in it. The imaging was conducted with a LEICA (modello) and LAS software Version: 4.1.0. at 1 day and 5 days.

Viability inhibition after doxorubicin treatment

For the cell proliferation assay in 2D, cell lines were seeded at 5×10^3 cells/well in 96-well plates and incubated overnight at 37°C. The medium was replaced with fresh complete medium supplemented with Doxorubicin at several concentrations. After 72 hours of treatment, 16 µl of MTS

reagent was added. The plates were incubated in a humidified atmosphere at 37°C in 5% CO_2 for 2 hours, and the bioreduction of the MTS dye was evaluated by measuring the absorbance of each well at 490 nm using a microplate reader (iMark Microplate Reader; BioRad Laboratories, Inc., Hercules, CA, USA). All tests were performed in triplicate. After 5 days of 3D culture, the samples were incubated in a 96-well plate in a complete culture medium supplemented with Doxorubicin at the indicated concentrations. After 3 or 6 days of incubation, MTS assay was carried out as described before. Cell growth inhibition was expressed as a percentage (mean ± SE) of absorbance compared to control cells for MDA-MB-231, MCF-7 and MCF-7R. SEM morphological analysis was carried out as described before.

Realtime PCR

Gene expression was evaluated on cell lines MCF-7 and MCF-7R seeded on PLLA scaffold. Total cellular RNA was isolated after their lysis using a TRIzol reagent (Invitrogen Life Technologies, Carlsbad, CA, USA). For each sample, the same amount of total RNA (500 ng) was reverse-transcribed using a High-Capacity cDNA Reverse Transcription Kit (Applied Biosystems, USA) following the protocol provided by the manufacturer. BrightGreen 2X qPCR MasterMix (Applied Biological Materials Inc. Richmond, BC V6V 2J5 Canada) was employed to analyze the obtained cDNA for quantitative real-time PCR (qRT-PCR) in triplicates. The qRT-PCR was performed using the primers: β-ActinF CGGGAAATCGTGCGTGACAT and β-ActinR GGACTCCATGCCCAGGAAGG; P-glycoproteinF GCCTGGCAGCTGGAAGACAAATACACAAAATT and P-glycoproteinR CAGACAGCAGCTGACAGTCCAAGAACAGGACT. The running of the samples and data collection were performed on a StepOne AB Real Time PCR system (Applied Biosystems Life Technologies Inc., Foster City, CA, USA). β-Actin was used as an internal standard.

Statistical analysis

The results obtained are reported as mean ± standard error (SE). Statistical analysis was performed by analysis of variance (one-way ANOVA) followed by Tukey's test. STATISTICS ver. 10 (StatSoft Inc. 2011) was used as the analysis software.

2.3 Results

Scaffolds morphology and porosity

As can be noticed in Figs. 32(A-C) SEM micrographs revealed a porous structure characterized by interconnected pores, essential for ensuring adequate nutrition supply, cell migration, and matrix colonization.

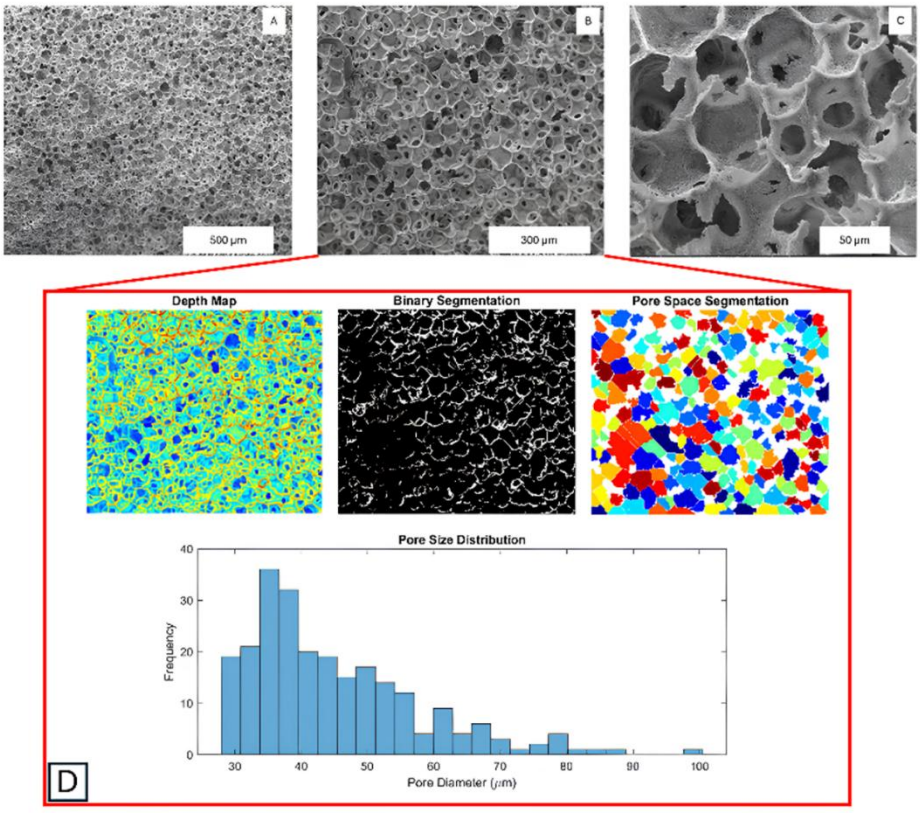

Figure 32: A, B and C Morphological characterization by SEM of the porous 3D scaffolds (TIPS parameter 20°C 15 min TWB and -20°C 15 min EAB. A) Magnification 150x, scale bar 500 µm. B) Magnification 300x, scale bar 300 µm C) Magnification 1200x

scale bar 50 µm D) MATLAB results: depth map, binary segmentation, pore space segmentation and pore size distribution in micrometers. Reproduced from Carbone et al., 2024 (Carbone et al., 2024)

As shown in Fig. 32 the MATLAB code provides a depth map, a binary segmentation, and a colored pore space segmentation from which it can be extracted the pore sizes distribution. The average pore size estimated was 44.8 µm, with a pore size distribution (Fig. 32D) that ranges mainly between 30 µm and 80 µm.

The scaffolds were also analyzed through pycnometry. Tab. 11 shows the porosity obtained and our structures are characterized by an ideal overall porosity for cell culture (Loh & Choong, 2013) .

Table 11: apparent volume, measured volume and porosity Reproduced from Carbone et al., 2024 (Carbone et al., 2024)

Total apparent volume [cc]	2.448
Real volume measured [cc]	0.154
Overall porosity %	93.7 %

3D growth curves and morphological analysis of cells

MDA-MB-231 growth curve had already been shown in previous work (Lombardo et al., 2019). The data obtained through the MTS assay, performed in triplicate after 1, 5, 10 and 14 days, allowed us to construct 3D growth curves shown in Fig.33A for MCF-7 and MCF-7R cell lines.

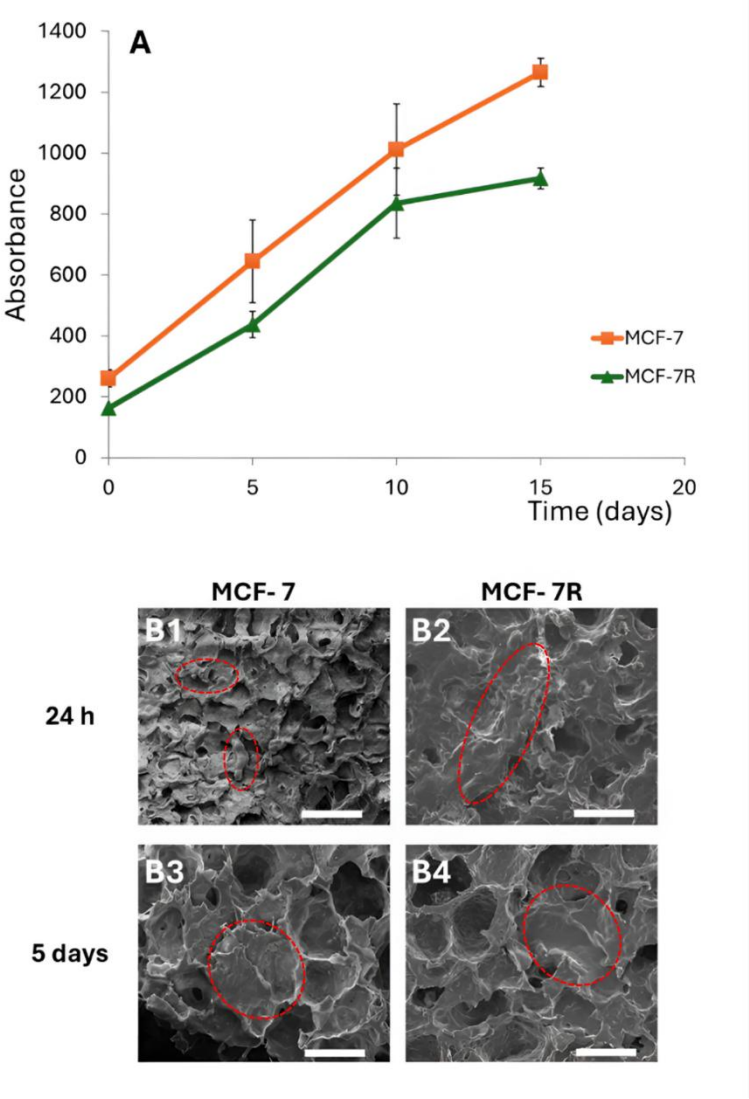

Figure 33: A) absorbance values from MTS assay for MCF-7 and MCF-7R at 1,5,10 and 14 days, N=3 replicates were used B1) SEM micrograph of MCF-7 cells at 24 h magnification 600x scale bar 100 µm. B2) SEM micrograph of MCF-7R cells at 24 h magnification 600x scale bar 100 µm. B3) SEM micrograph. of MCF-7 cells at 5 days magnification 600x scale bar 100 µm B4) SEM micrograph of MCF-7R cells at 5days magnification 600x scale bar 100 µm. Reproduced from Carbone et al., 2024 (Carbone et al., 2024)

Both curves depicted in Fig. 33A show that cells are able to proliferate on the scaffold over time, as previously observed for the MDA-MB-231 cell line(Lombardo et al., 2019). Furthermore, Figs 33 (B1-B4) show how both cell lines after 5 days are able to create a compact layer on the polymer matrix. For that reason 5 days were chosen as starting time for doxorubicin treatment.

Breast cancer cells acquired chemoresistance in 3D culture

A live/dead assay was performed to assess cells' health prior to treatment (at 1 and 5 days of culture). Live/dead staining, reported in Fig.34 indicated that the majority of the cells survived and colonized the scaffold over 5 days, they adhered to the surface but were also able to migrate into matrix.

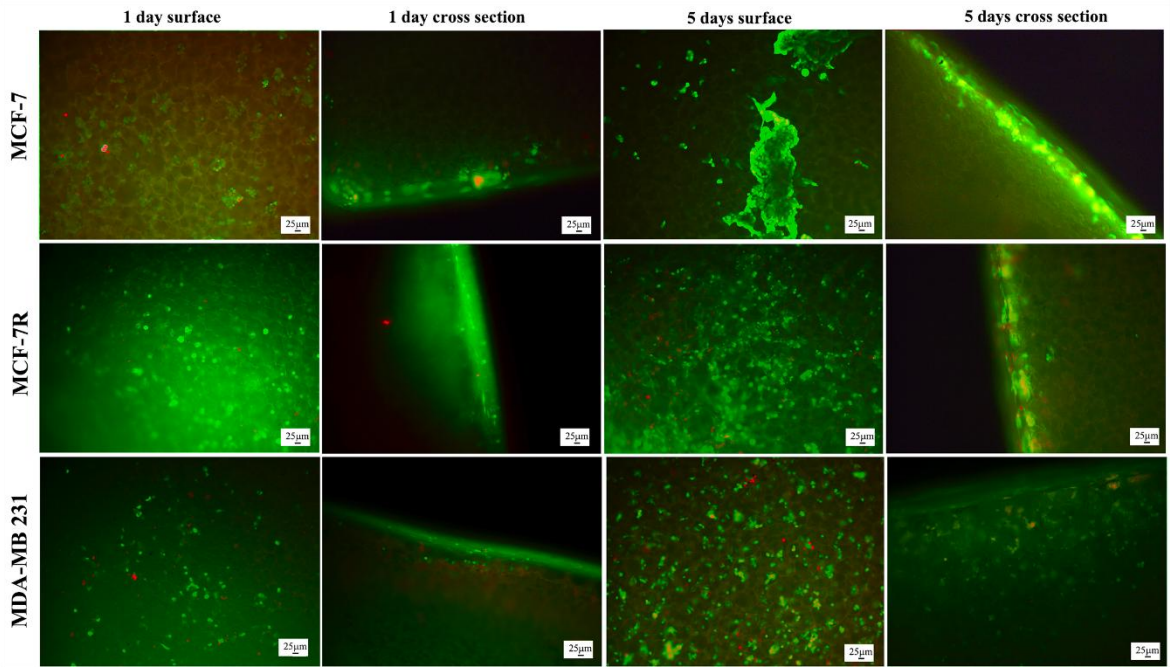

Figure 34: live dead assay for three BC cell lines: MDA-MB 231, MCF-7 e MCF-7R at 1 day and 5 days, surface and cross section. Reproduced from Carbone et al., 2024 (Carbone et al., 2024)

An increase in cell density could be observed after 5 days compared to 1 day of culturing. Most cells attached to the outer surface, but several cells can also be observed in the inner scaffold regions. To examine the inner regions, the scaffolds were cut with a blade before capturing microscopic images. This process resulted in the death of some cells, which were subsequently stained red.

The cytotoxicity of doxorubicin was evaluated in the three BC cell lines seeded on PLLA scaffold, by MTS assay. The graphs in Fig. 35 A1, highlights a noticeable difference in the MDA-MB 231 cell line cultivated in 3D and in 2D: an increasing drug concentration was necessary in the treated 3D system to reach the IC_{50} that rises from 54.5 ng/ml in 2D to 445 ng/ml in 3D.

Regarding the MCF-7 cell line, Fig. 35 A2 shows a very similar trend, with an IC_{50} of 0.75 µg/ml in 2D that rises to 7.45 µg/ml in 3D culture.

Cellular morphology undergoes significant alteration before and after reaching the IC_{50} threshold. MDA-MB-231 cells lose their typical clustered structure (Fig. 35 B1-B2). Regarding the MCF-7 cells, from Fig. 35 B3-B4 it can be noticed that the original layer appears to be disrupted after a doxorubicin treatment at a concentration higher than the IC_{50} value.

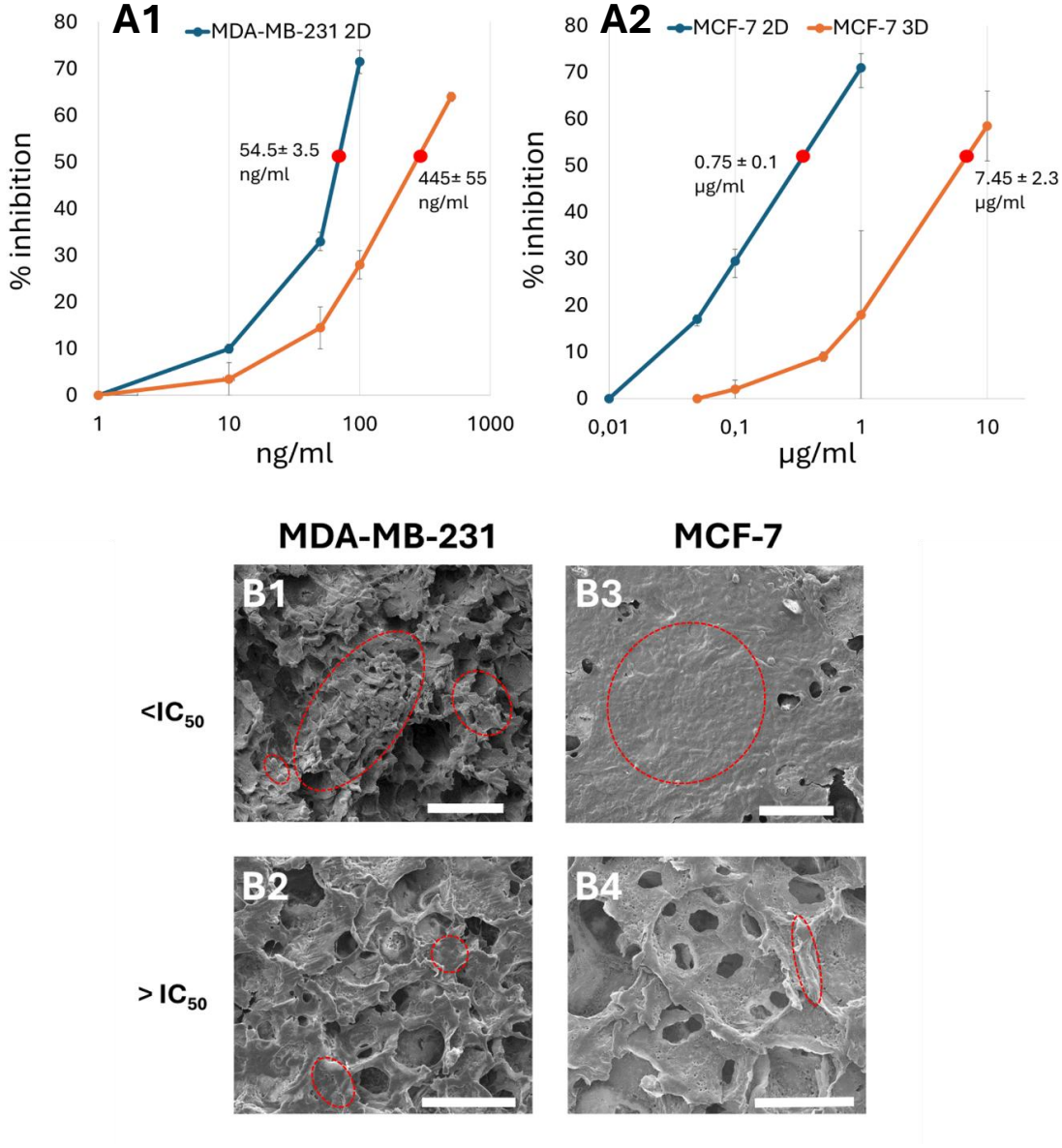

Figure 35: A1) % of growth inhibition from MTS assay for MDA-MB-231 cultivated in 2D (blue) and 3D (orange) for different doxorubicin concentrations, IC50 values are shown in both curves as red dots N=3 replicates were used.; A2) % of growth inhibition from MTS assay for MCF-7 cultivated in 2D (blue) and 3D (orange) for different doxorubicin concentrations, IC50 values are shown in both curves as red dots . N=3 replicates were used B1) SEM micrographs on healthy MDA-MB-231 cells grown in 3D, scale bar 100 µm magnification 600x, B2) SEM micrographs on MDA-MB-231 cells grown in 3D and treated with a doxorubicin

concentration higher then IC_{50} value, scale bar 100µm magnification 800x; B3)SEM micrographs on healthy MCF-7 cells grown in 3D scale bar 100 µm magnification 600x; B4) SEM micrographs on MCF-7 cells grown in 3D and treated with a doxorubicin concentration higher then IC_{50} value, scale bar 100µm magnification 800x Reproduced from Carbone et al., 2024 (Carbone et al., 2024);

A very different behavior was observed for MCF-7R cell line. Firstly, in 2D cultures the IC_{50} value increases from 0.75 to 39 µg/ml with respect to the corresponding sensitive line. Going to 3D cultures, after 3 days from the treatment, the growth inhibition doesn't even reach the IC_{50} value (as witnessed by the orange dashed line in Fig. 36 A, despite the high concentrations tested (about 200 µg/ml).

A significantly longer exposure time (6 days), reported in Fig 36 was necessary to reach a detectable IC_{50} value equal to 165 µg/ml. These data suggest that MCF-7R cells, grown in 3D, acquire a stronger chemoresistance with respect to sensible line, leading one to suppose that they assume a spatial conformation that closely resembles the *in vivo* state.

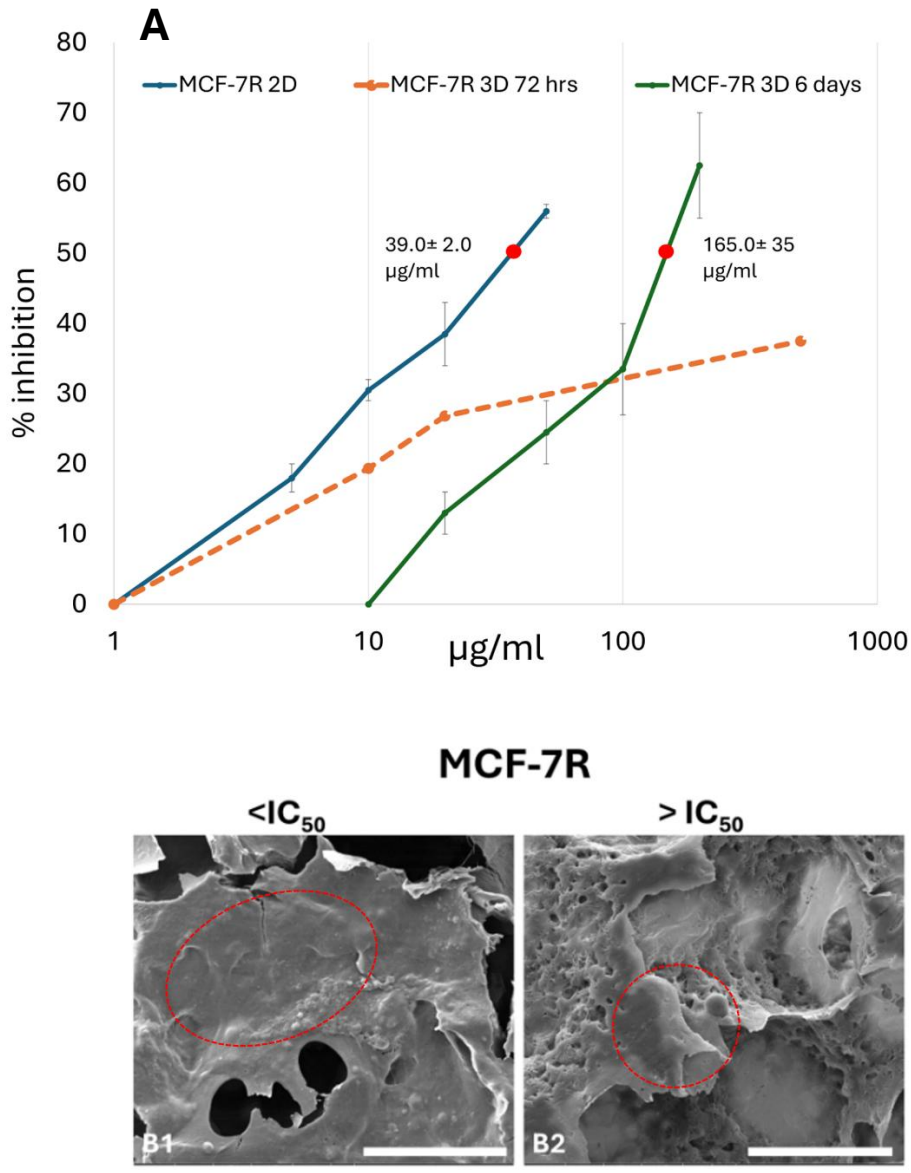

Figure 36: A) MCF-7R cells growth inhibition % after being treated with doxorubicin in 2D (blue) in 3D for 3 days (dashed orange) and in 3D for 6 days (grey) N=3 replicates were used ; B1) SEM micrographs on healthy MCF-7R cells grown in 3D, scale bar 40 µm magnification 2400x, B2) SEM micrographs on MCF-7R cells grown in 3D and treated with a doxorubicin concentration higher then IC_{50} value, scale bar 40µm magnification 2400x

Also, in this case different cells morphologies can be noticed when the cells are treated with a higher or lower concentration respect to the IC_{50} value. MCF-7R cells lose their typical epithelial behavior (Fig. 36 B1), and as shown in Fig. 36 B2 the original layer appears to be disrupted.

Is 3D culture chemoresistance associated with increased drug efflux?

P-glycoprotein (P-gp) efflux pump expression was analyzed at both transcriptional and protein level to evaluate if the penetration of doxorubicin was inhibited in 3D cultures by its overexpression. The doxorubicin sensitive line (MCF-7 cells) was chosen as control for this investigation as it lacks expression of P-gp. Fig. 37 A clearly shows a notable increase in P-gp mRNA levels in the 3D culture, compared to that of the same 2D cells. However, these levels are clearly modest if compared to those of P-gp of the resistant 2D cell line (MCF-7R) characterized by a significant relative overexpression of the efflux pump (Fig. 37 B). These results demonstrate that MCF-7 cells express high levels of P-gp mRNA when they grow in 3D, whereas they don't express it in 2D monolayers. However, this is not reflected in increased protein expression (too low to be shown).

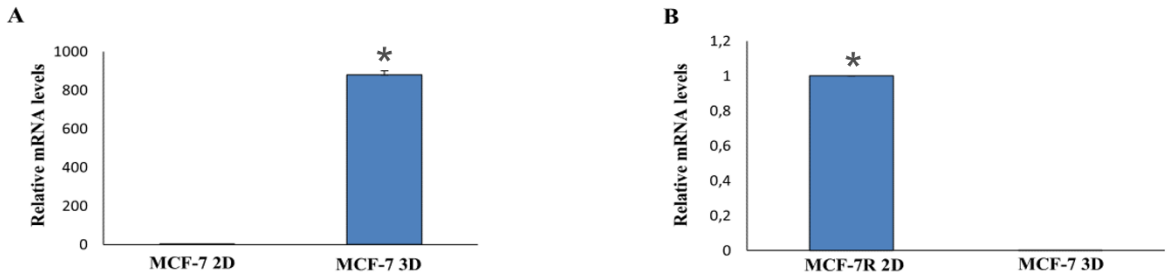

Figure 37: ***Expression of P-glycoprotein in 3D MCF-7 cell line by qRT-PCR****. A. Evaluation of P-gp mRNA expression levels in 3D MCF-7 cell line compared to those of the same 2D cell line. B. Evaluation of P-gp mRNA expression levels in 3D MCF-7 cell line compared to those of the MCF-7R cell line. For each condition, N=3 technical replicates were used. Data are expressed as mean ± standard error of two experiments. * = p<0.01. Reproduced from Carbone et al., 2024 (Carbone et al., 2024)*

2.4 Discussion

In recent years the discussion on the use of animals for pre-clinical testing has involved the entire scientific community which has looked for alternative tests to evaluate drug efficacy *in vitro*. In fact, in the USA a law allowing the FDA not to require animal models for the authorization of new drugs has already been approved (Wadman, 2023). On the other hand, it is known that 2D monolayer cultures are unsuitable for the study of anti-tumor molecules.

Since drug resistance in cancer cells challenges modern oncology, the exploration of innovative therapeutic strategies becomes necessary. Recent studies have highlighted the importance of understanding the molecular mechanism behind drug resistance, including genetic mutations, efflux pumps, altered signaling pathways and microenvironmental influences (Poma et al., 2024). Research aims to enhance the success of cancer treatments and increase patient survival rate. With this study we demonstrate that 3D scaffold-based models are able to provide a tumor microenvironment that better mimic the *in vivo* conditions offering a cost effective, scalable, and more ethical alternative for preclinical research (Garg et al., 2024; Tratar et al., 2018).

In this project, we show the results by 3D cultures obtained with PLLA scaffolds. On these supports, we seeded three different breast cancer cell lines: triple negative breast cancer, MDA-MB-231, MCF-7 and its multidrug resistance variant, MCF-7R. The obtained data showed that the scaffolds seem to produce a microenvironment for tumor cell growth *in vitro* that closely mimics *in vivo* conditions. The results align with previous studies that utilized devices for 3D growth of the same cell lines, showing consistent findings in terms of growth and morphology (Liverani et al., 2017, 2019).

As a matter of fact, for MDA-MB-231 and MCF-7 cells the IC_{50} values increases of about one order of magnitude when compared to 2D cultures. In the case of MCF7-R cell line, a longer exposure time (6 days) is needed to obtain an IC_{50} . The findings are consistent with earlier studies regarding chemotherapeutic drugs such as doxorubicin (Alwahsh et al., 2024; Jaiswal & Mandal, 2024).

It is possible to hypothesize that genotypic/phenotypic changes occur in cells growing in 3D models; such changes become more evident for cells characterized by multidrug resistance. This hypothesis is supported by data in the literature which indicate how 3D growth induces alterations in the cell cycle and variations in gene expression and in the levels of some proteins, implicated in the increase in aggression and in the development of the resistant phenotype (Ding et al., 2018). In agreement with this hypothesis, our data indicate an increase in P-gp mRNA expression levels in MCF-7 cells grown in 3D, compared to the 2D model, demonstrating that the 3D environment of the scaffold favors the development of a resistant phenotype, thus supporting the higher concentration of doxorubicin needed to reach the IC_{50}. 3D environment alters probably in a limited and transient manner the expression of the P-gp, but only at transcriptional level in sensitive cells. Conversely,

MDR cellular variant, not only exhibits higher levels of mRNA, but is also characterized by an overexpression of the protein.

Furthermore, data in the literature indicate that various cytoskeleton modifications are also associated with MDR phenotype and have been used as prognostic factors (Bichat et al., 1997). In this regard ongoing research of the authors shows that the growth of sensitive MCF-7 cells on the scaffold promotes the expression of vimentin, which is normally not expressed in such cells under 2D conditions. Vimentin plays a fundamental role in the ability of cells to invade the surrounding matrix, inducing the formation of metastases.

Overall, the presented data strengthens the hypothesis that the 3D growth onto the employed porous scaffolds favors the development of the resistant phenotype, indicating them as an excellent support for the study of this phenomenon.

2.5 Conclusion

Understanding MDR is very crucial in cancer research and novel advanced 3D models are necessary to study tumor microenvironment. This study highlights the potential of PLLA porous scaffolds produced by TIPS as perfect candidate to accomplish this objective, particularly in demonstrating significant differences in drug response and cellular behavior when compared to traditional 2D cultures. In fact, IC_{50} values for doxorubicin are markedly higher in 3D indicating an increasing resistance. Specifically for MDA-MB-231 this value rises from 54.5 ng/ml in 2D to 445 ng/ml in 3D; for MCF-7 cell line the IC_{50} of 0.75 μg/ml in 2D increases to 7.45 μg/ml in 3D culture; the MDR line MCF-7R demonstrates this trend even more pronounced with a doubled treatment time that was necessary to reach the IC_{50} equal to 165 μg/ml compared to 39 μg/ml in 2D. SEM micrographs reveal complex cellular architectures, cell clusters typical of MDA-MB-231 and compact layer for the MCF-7 sensible and resistant, that look like disrupted upon treatment with concentration higher than their respective IC_{50}. We investigated the molecular mechanism of resistance by comparing P-gp mRNA expression in 2D and 3D MCF-7 cells and we showed that 3D cultures express higher levels respect to 2D although this did not translate into a corresponding increase in protein levels. This suggests a transcriptional but not translational response to the 3D environment, in fact the MCF-7R exhibits much higher levels of both mRNA and protein indicating that 3D microenvironment may induce a temporary and limited increase in P-gp expression in sensitive cells but not comparable to the MDR

variants. In conclusion our study demonstrates that PLLA scaffold via TIPS offer a robust 3D system that enhance breast cancer understanding. This approach has the potential to bridge the gap between traditional monolayer culture and animal models leading to more effective and personalized treatment. Future perspective should include deeper investigation into molecular mechanism behind the observed drug resistance and further evaluation of PLLA 3D models potential for preclinical drug testing and development.

Dynamic Devices

Dynamic devices as 3D models

Three-dimensional (3D) culture systems, such as polymeric networks called scaffolds or hydrogels, demonstrate a superior ability to simulate the *in vivo* microenvironment compared to two-dimensional (2D) cultures (Abbasi et al., 2020). They replicate the specific 3D conditions in terms of composition and structure of the extracellular matrix (ECM), providing relevant signals and stimuli, and reflecting cell behavior more accurately (Yamada & Cukierman, 2007). The ECM plays a crucial role in cell adhesion, migration, differentiation, and survival, thus its accurate representation in *in vitro* models is vital.

Despite their advantages, static 3D models have limitations such as inadequate nutrient and oxygen diffusion throughout the scaffold, which can lead to necrotic regions (Pampaloni et al., 2007). These limitations can significantly hinder the accurate simulation of the tumor microenvironment and the effectiveness of drug testing.

To address these shortcomings, tissue engineering scaffolds have been integrated with bioreactor principles, creating dynamic biomimetic environments (Martin et al., 2004) . Dynamic 3D culture systems, facilitated by bioreactors, provide continuous nutrient and oxygen supply and efficient waste removal, which are crucial for maintaining cell viability and function. These systems mimic the physiological conditions more accurately than static models.

Bioreactors are advanced devices that utilize mechanical methods to influence biological processes, thereby enhancing cell culture conditions. Perfusion flow bioreactors are particularly advantageous as they improve cell seeding processes and distribution within scaffolds. This results in better oxygenation and nutrient delivery throughout the scaffold, closely replicating the *in vivo* environment (Lombardo et al., 2021). Perfusion bioreactors can significantly enhance the viability and functionality of cultured cells by providing a dynamic environment that promotes uniform cell growth and nutrient distribution.

Dynamic culture conditions enable a more realistic simulation of the tumor microenvironment, which is essential for accurate drug screening and therapeutic testing. By continually refreshing the culture medium and maintaining proper fluid dynamics, dynamic systems can prevent the formation of necrotic cores and ensure consistent cell behavior across the scaffold.

In summary, dynamic 3D culture systems, particularly those utilizing perfusion bioreactors, offer a significant improvement over static models. They provide an enhanced simulation of the *in vivo* conditions, leading to more accurate and reliable preclinical testing results.

3. *Project : Drug Delivery bioreactor*

3.1 Introduction

The development of new drugs is widely recognized as a high-cost and time-consuming process due to the numerous stages involved. These costs, in terms of both time and money, place a significant burden on healthcare systems as they are ultimately reflected in pharmaceutical expenses. Innovative strategies to optimize this process include research on advanced pre-clinical models. For instance, the use of animals as human surrogates has been criticized for its limited accuracy in predicting human drug responses and its ethical implications(Shanks et al., 2009). Despite these concerns, animal testing continues to be employed due to the current lack of viable alternatives.

Traditional two-dimensional (2D) cell cultures remain a standard in preliminary drug studies, particularly in cancer research, due to their simplicity and well-established protocols (Antoni et al., 2015). These *in vitro* tumor models are critical tools for pre-screening drugs and evaluating therapeutic efficacy. However, 2D models often fail to replicate the dynamic and complex biophysical properties of the tumor microenvironment (Langhans, 2018). The physiological tumor microenvironment is inherently three-dimensional (3D), which influences cell behavior in ways that 2D systems cannot emulate.

Three-dimensional (3D) culture systems, such as polymeric scaffolds or hydrogels, have emerged as superior models, better mimicking the *in vivo* microenvironment compared to 2D. These systems replicate the structural and compositional characteristics of the extracellular matrix (ECM), providing essential biochemical and biomechanical cues that influence cell behavior (Yamada & Cukierman, 2007). The ECM plays a critical role in regulating cell adhesion, migration, differentiation, and survival, making its accurate representation crucial in *in vitro* models.

Despite their advantages, static 3D models face challenges, such as limited nutrient and oxygen diffusion, which can result in necrotic regions within the scaffold (Pampaloni et al., 2007). To address these limitations, researchers have integrated tissue engineering scaffolds with bioreactor technologies to create dynamic biomimetic environments (Martin et al., 2004).

Bioreactors are devices that enhance cell culture conditions by providing continuous nutrient and oxygen supply while efficiently removing waste products. Among these, perfusion flow bioreactors offer notable advantages, such as improved cell seeding efficiency and uniform distribution within

scaffolds, enhancing oxygenation and better replicating *in vivo* conditions (Lombardo et al., 2021) For instance, Lombardo et al. demonstrated the utility of a dual-flow bioreactor in achieving improved cell distribution and scaffold integration (Lombardo et al., 2021). Similarly, bioreactors have been used during the cell seeding phase to ensure uniform cell distribution and viability.

This study introduces a novel and compact system inspired by the prototype "dual-flow" bioreactor described by Lombardo et al. (Lombardo et al., 2021). The primary objective was to minimize manual operations and reduce system size without compromising the ability to regulate radial flow through the scaffold matrix. The prototype was redesigned from a vertical to a horizontal orientation, maintaining internal flow through the scaffold lumen while replacing the secondary flow with a static fluid layer using basal media. A new main chamber was developed using 3D printing technology. Key parameters, such as scaffold morphology, permeability, fluid velocity, and pressure dynamics, were systematically analyzed.

To control radial flow, a pressure drop was induced by an external mechanical stimulus. The study utilized porous scaffolds fabricated through Thermally Induced Phase Separation (TIPS) and combined these with principles of fluid dynamics and 3D cell culture to develop an optimized system for drug delivery research and pre-screening applications. This system aims to provide a 3D model for *in vitro* testing while reducing costs, time consumption, and ethical concerns associated with animal models. The bioreactor's fluid dynamics were tested and demonstrated its ability to regulate perfusion flows through hollow cylindrical porous scaffolds. Additionally, the system successfully supported dynamic cell seeding and culture within the 3D matrix, maximizing efficiency and producing promising results.

3.2 Materials and methods

Scaffold Synthesis and Characterization

Scaffolds were synthesized using the Thermally Induced Phase Separation (TIPS) technique, a widely used method for creating porous structures with controlled morphology. The starting solution comprised Poly-L-Lactic Acid (PLLA) dissolved in 1,4-dioxane at a concentration of 4% (wt/wt). Complete dissolution was achieved by stirring the mixture at 180°C until a homogeneous solution

was formed. Deionized water was then added dropwise under continuous stirring to achieve a dioxane-to-water weight ratio of 87/13 (wt/wt), ensuring precise control over phase separation conditions.

To create scaffolds with a hollow cylindrical geometry, the solution was poured into a custom-fabricated aluminum sample holder. The holder was designed with an external diameter of 3.5 cm, an external height of 4 cm, an internal cavity diameter of 1 cm, and an internal cavity height of 2.8 cm. A tightly fitted aluminum lid sealed the holder, preventing contamination and ensuring consistent processing conditions. A 0.2 cm hole in the lid allowed the insertion of a stainless-steel rod, which was positioned to form the inner lumen of the scaffold. This design ensured reproducibility in scaffold geometry and lumen formation.

The filled sample holder was then rapidly cooled by immersion in a thermostatic water bath, inducing phase separation. Two scaffold types with distinct pore sizes were created by varying the bath temperature and immersion duration:

- **Type 0-10:** Cooling at 0°C for 10 minutes, resulting in smaller, denser pores.
- **Type 25-15:** Cooling at 25°C for 15 minutes, yielding larger, more open pores.

After phase separation, the sample holder was submerged in an ethylene glycol bath maintained at -20°C to freeze the scaffold structure further. For Type 0-10 scaffolds, the immersion time was 15 minutes, while Type 25-15 scaffolds were frozen for 30 minutes. To ensure uniform pore architecture in Type 25-15 scaffolds, the holder was enclosed in a Teflon jacket during the freezing step, reducing temperature gradients across the sample.

The scaffolds were carefully extracted from the holders, and the stainless-steel rod was gently removed to preserve the lumen integrity. To remove residual solvents, the scaffolds were washed overnight in deionized water at room temperature. Subsequently, they were dried in a vacuum oven at 40°C for a minimum of 4 hours, a process that ensured complete solvent removal while maintaining the structural stability of the scaffolds.

Morphological Analysis

The morphology of the scaffolds was examined using a Scanning Electron Microscope (SEM, Phenom Pro-X, Netherlands) operated at 10 kV. To prepare samples for SEM analysis, scaffolds were cross-sectioned into 3 mm pieces using a scalpel, mounted on aluminum stubs with conductive carbon

adhesive tabs, and sputter-coated with a 4 nm layer of gold under an argon atmosphere (Sputtering Scancoat Six, Edwards). This preparation ensured optimal imaging quality and minimized charging effects during analysis.

Porosity Measurement

The porosity of scaffolds was assessed using a helium pycnometer, which measures the real volume of solids through gas displacement. For each scaffold type, three samples were analyzed to determine the mean real volume ($Vmes$), which was compared to the total apparent volume ($Vapp$) of the scaffold trio. The apparent volume was calculated as the difference between the volume of the external cylinder and the inner cavity using the Eq. 5:

$$V_{app} = V_{C_{ext}} - V_{C_{int}}$$

Equation 5

Porosity (P) was calculated using the following formula reported in Eq. 6:

$$P(\%) = \left(1 - \frac{V_{mes}}{V_{app}}\right) \times 100$$

Equation 6

This analysis provided insights into the impact of cooling conditions on scaffold pore structure and overall porosity.

Bioreactor Design and Setup

The original bioreactor design utilized vertical orientation, which was effective but required considerable space and manual handling. To improve usability and integration with laboratory equipment, the design was miniaturized and modified to a horizontal configuration. This redesign

reduced the overall dimensions while maintaining functionality, making it compatible with standard incubators.
The bioreactor chamber was 3D-printed using biocompatible resin, with internal dimensions of 5 cm × 3 cm × 2 cm and a wall thickness of 3 mm. The chamber included precision-machined holes (0.5 cm internal diameter) on opposing side walls to accommodate tubing connections for fluid flow. This design ensured a tight seal, preventing leaks and maintaining sterile conditions during experiments.

For the dynamic testing setup the scaffold was securely placed inside the bioreactor chamber, and the tubing system was connected to a New Era Syringe Pump (model NE-1000). This pump was equipped with a microcontroller, allowing precise regulation of flow rates across a wide range (0.1–10 ml/min). The compact dimensions of the pump (22.86 cm × 14.61 cm × 11.43 cm) facilitated its integration into the bioreactor setup, enabling continuous operation within an incubator.
During testing, deionized water was pumped through the scaffold lumen at flow rates of 0.5 ml/min and 1 ml/min. Radial flow across the scaffold was assessed by collecting the outflow over 10 minutes, measuring the volume with a precision scale. By subtracting the measured outflow from the nominal flow rate, the radial flow rate was calculated. This setup enabled accurate evaluation of the scaffold's permeability under dynamic conditions.

Bioreactor Characterization: Perfusion Tests with Toluidine Blue

To qualitatively evaluate radial perfusion, static tests were performed using a toluidine blue solution (0.1% v/v in deionized water). The scaffold was inserted into the bioreactor chamber filled with the dye solution, and tests were conducted at three time intervals: 15, 30, and 60 minutes.
At the end of each test, the scaffold was removed, sectioned, and visually inspected to assess the distribution and intensity of staining within the cross-sectional area. This analysis provided insights into the scaffold's perfusion efficiency and the uniformity of dye penetration.

Bioreactor Characterization : Radial Flow Analysis

Dynamic radial flow tests were conducted under varying flow rates and configurations to characterize scaffold performance. The following setups were tested:

- **0-0.5:** 0°C scaffold, 0.5 ml/min flow rate.
- **0-1:** 0°C scaffold, 1 ml/min flow rate.
- **25-0.5:** 25°C scaffold, 0.5 ml/min flow rate.
- **25-1:** 25°C scaffold, 1 ml/min flow rate.

Radial flow was calculated as the difference between the nominal flow rate imposed by the syringe pump and the measured outflow. Measurements were repeated for five samples per setup to ensure statistical reliability. Different height (0 , 5 cm , 10 cm , 15 cm and 20 cm) of the terminal tube were tested too ad shown in Fig 38.

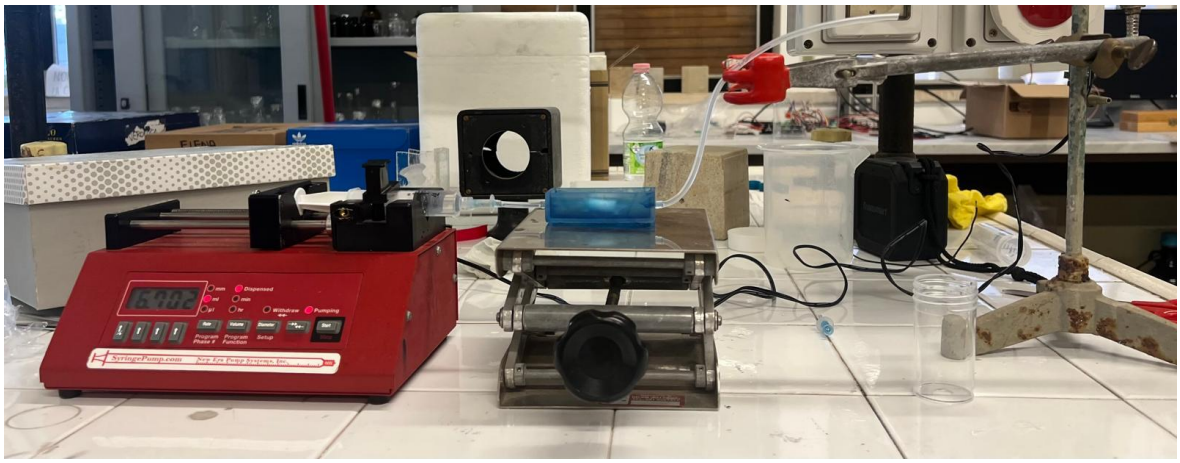

Figure 38: Schematic representation of the experimental setup for scaffold perfusion under dynamic conditions. The system consists of a syringe pump, connectors, microfluidic tubes, and a closing component, ensuring uniform flow distribution

Bioreactor Characterization **:** *Pressure and Permeability*

Two pressure sensors were placed before and after the scaffold to measure the pressure drop (ΔP). Permeability (K) was calculated using Darcy's law (Eq. 7) for cylindrical geometries:

$$K = \frac{Q\mu \ln\left(\frac{R_{ext}}{R_{int}}\right)}{2\pi h_s (P_{ext} - P_{int})}$$

Equation 7

where h_s is the scaffold height, R_{ext} and R_{int} are the external and internal scaffold radii, μ is the fluid viscosity, and $P_{ext} - P_{int}$ is the pressure drop. Bernoulli's equation was applied to analyze the effects of pressure, height, and velocity within the bioreactor. It states that the total energy in a steady,

incompressible flow system is conserved. For this study, the pressures at the upper (P1∗) and lower (P2∗) sides of the scaffold were derived from uPS1 and uPS2 suing Bernoulli's equation Eq. 8.

$$\frac{uPS}{\rho} + \frac{1}{2}\rho v_1^2 + \rho g z_1 = P^* + \frac{1}{2}\rho v_2^2 + \rho g z_2 + h_{fd}$$

Equation 8

where v_i is the fluid velocity (m/s), z_i is the static height (m), g is gravitational acceleration ($\frac{m}{s^2}$), ρ is the fluid density ($\frac{kg}{m^3}$), and h_{fd} is the distributed pressure loss.

Since the velocities and height differences were negligible between the considered points, Eq. 8 simplifies to Eq 9:

$$u_{PS} = P^* + \rho g h$$

Equation 9

Where:

P* is the scaffold pressure, ρ is the fluid density, g is the gravitational acceleration, and h is the height.

Reynolds Number

The Reynolds number (Re) was calculated as reported in Eq. 10:

$$Re = \frac{Dv\rho}{\mu}$$

Equation 10

Where:

- D is the pipe diameter,
- v is the fluid velocity,
- ρ is the fluid density,

- μ is the fluid viscosity.

The Reynolds number is a dimensionless parameter that quantifies the ratio of inertial forces to viscous forces within the fluid. It is used to characterize flow regimes

- When Re<2000 the flow is typically laminar, indicating smooth and orderly fluid motion.
- When Re>3500, the flow transitions to turbulent, characterized by chaotic fluid movement.

In this study, the Reynolds number is essential for determining whether the flow conditions within the scaffold are conducive to uniform perfusion or prone to mixing effects. Low Re values are typically preferred for maintaining consistent nutrient delivery and waste removal in bioreactors

Concentrated ad distributed Pressure Losses

Localized head losses were calculated as reported in Eq. 11:

$$\Delta P = \frac{\beta}{2} \rho v^2$$

Equation 11

Where:

- β is a geometry-dependent constant,
- ρ is the fluid density, and
- v is the fluid velocity.

Localized head losses represent the energy dissipation that occurs when the fluid encounters abrupt changes in the flow path, such as contractions, expansions, or bends. These losses are critical in the design of bioreactors, as they influence the efficiency of fluid delivery and the maintenance of desired pressure gradients within the scaffold. Accurate accounting of ΔP ensures that the flow remains optimized for uniform cell seeding and nutrient distribution.

The distributed losses (h_{fd} Eq. 12) depend on the tube length, diameter, velocity, and the Reynolds number

$$h_{fd} = f\left(\frac{L}{D}\right)\left(\frac{\rho v^2}{2}\right)$$

Equation 12

Here, f is the Darcy-Weisbach friction factor, L is the length of the tube (m), D is its diameter (m), ρ is the fluid density (kg/m^3), and v is the fluid velocity (m/s). The friction factor f depends on the flow regime, as determined by the Reynolds number.

Nanoparticles as drug carriers

It has been decided to use the scaffolds at 25°C to test the gold nanoparticles as drug nanocarriers. The scaffolds tested with nanoparticles were first validated using the same setup, but only with water and at two terminal tube heights (0 cm and 10 cm). During these tests pressure sensors were re-implemented to investigate potential pore blockages caused by the nanoparticles themselves.

Biological Tests

The prototype was selected for both cell seeding and maintaining cultures under dynamic conditions to compare with standardized static conditions.

In this case, five tubular scaffolds were used. Dynamic seedings were performed as follow: 2.5 * 10^6 cells (MDA-MB-231) were dispersed in 5 ml of culture medium, inserted into a syringe, and flowed into the system at a rate of 0.125 ml/min Fig.39. After the seeding process, the system was placed in an incubator and maintained in culture for 48 hours under two different conditions. Specifically, two scaffolds were maintained under dynamic culture with continuous radial perfusion of 2 ml/day (named DD1 and DD2 as they were seeded and maintained dynamically). The other two scaffolds, used as controls, were maintained statically (DS1 and DS2 as they were seeded dynamically but maintained statically). A final scaffold was seeded passively and maintained under static conditions (SS). The cells were pre-labeled with a fluorescent organic compound containing an isocyanate group to make them visible under a fluorescence microscope.

For static maintenance, the system was placed inside an incubator for 48 hours; for dynamic maintenance, the system was reconnected to the syringe pump, and the scaffold was supplied with

fresh medium at a rate of 2 ml/day. The other samples, as mentioned, were maintained under completely static conditions for the same duration.

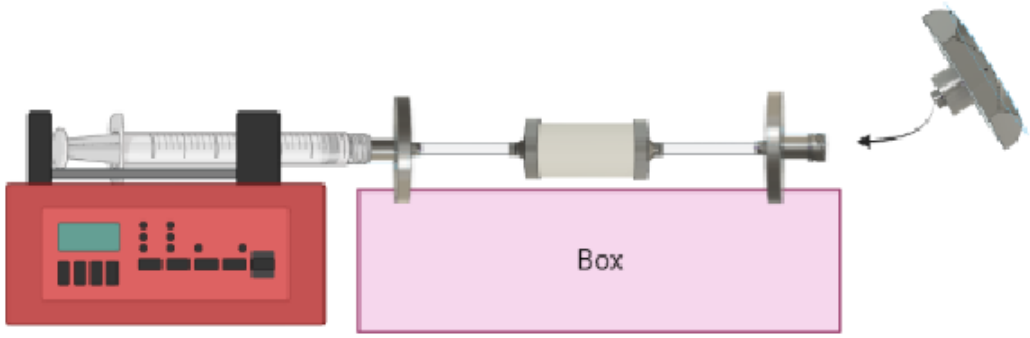

Figure 39: Illustration of the dynamic seeding system used for cell culture. The setup includes a syringe pump to inject cells into the scaffold, which is maintained under controlled flow conditions for optimized cell adhesion and growth

At the end of the described process, with the help of a blade, the retrieved scaffolds were cut into three parts: the initial part (syringe side), the central part, and the final part for each type of sample as shown in Fig. 40

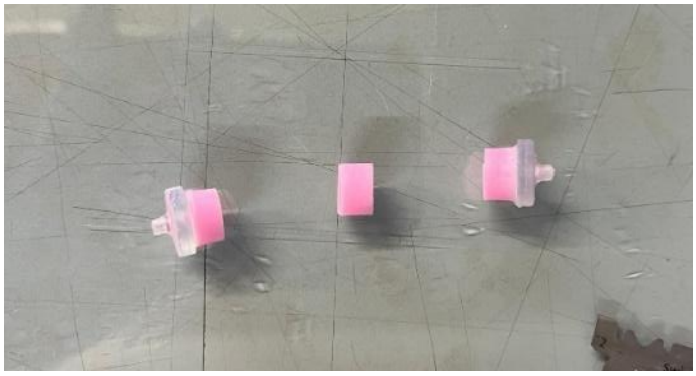

Figure 40: Scaffold after dynamic seeding and culture, sectioned into three parts, from the left: (1) Syringe side, (2) Central region, and (3) Final part. Each section was analyzed separately to assess cell distribution and growth

Once the different parts were separated, as seen in Fig. 40, they were fixed with formaldehyde (3.7%) for 15 minutes. Subsequently, the samples underwent three washing cycles with PBS to remove any residues.

Before sectioning with a cryostat, the samples were placed in suitable cassettes and embedded in OCT compound, which were then placed for at least 4 hours at -80°C. This is shown in Fig 41.

Figure 41: Scaffold sample embedded in OCT compound before cryostat sectioning. The sample was placed in cassettes and frozen at -80°C for at least 4 hours to ensure structural preservation before slicing.

The cryostat (Fig. 42) is an instrument that allows precise cuts to be made with a blade mounted on an advancing carriage. Once the sample is placed in the adjustable sample holder, the blade angle must be adjusted to achieve the optimal cutting angle for the desired test. The cutting thickness can also be set.

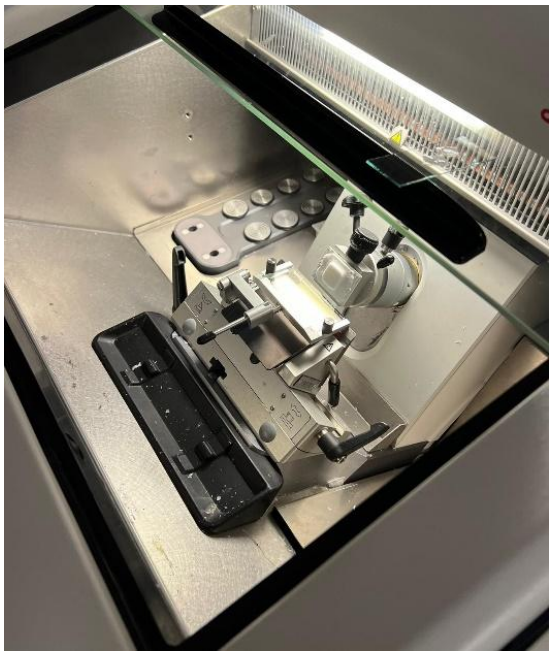

Figure 42: Cryostat used for sectioning OCT-embedded scaffolds. The instrument allows for precise control of cutting thickness and blade angle, ensuring high-quality thin sections for microscopy analysis.

The sections obtained with the cryostat were observed under a fluorescence microscope, which allowed for a detailed examination of the cell distribution within the scaffold and the identification of any differences among the various samples.

3.3 Results

Morphology and Porosity of PLLA Scaffolds

To assess the structural characteristics of the PLLA scaffolds, slices measuring 0.5 cm were precisely sectioned from various regions of each scaffold type. These slices were analyzed using scanning electron microscopy (SEM), enabling detailed observation of cross-sectional morphologies.
The SEM images (Fig.43) reveal that both types of scaffolds exhibit a regular and homogeneous structure from the lumen to the outer surface. Upon closer inspection at higher magnifications, significant differences in pore size were observed between the two scaffold types. The 25-15 scaffold

features larger pores, ranging between 50–100 µm, while the scaffold prepared at 0° displays smaller pores in the range of 15–25 µm.

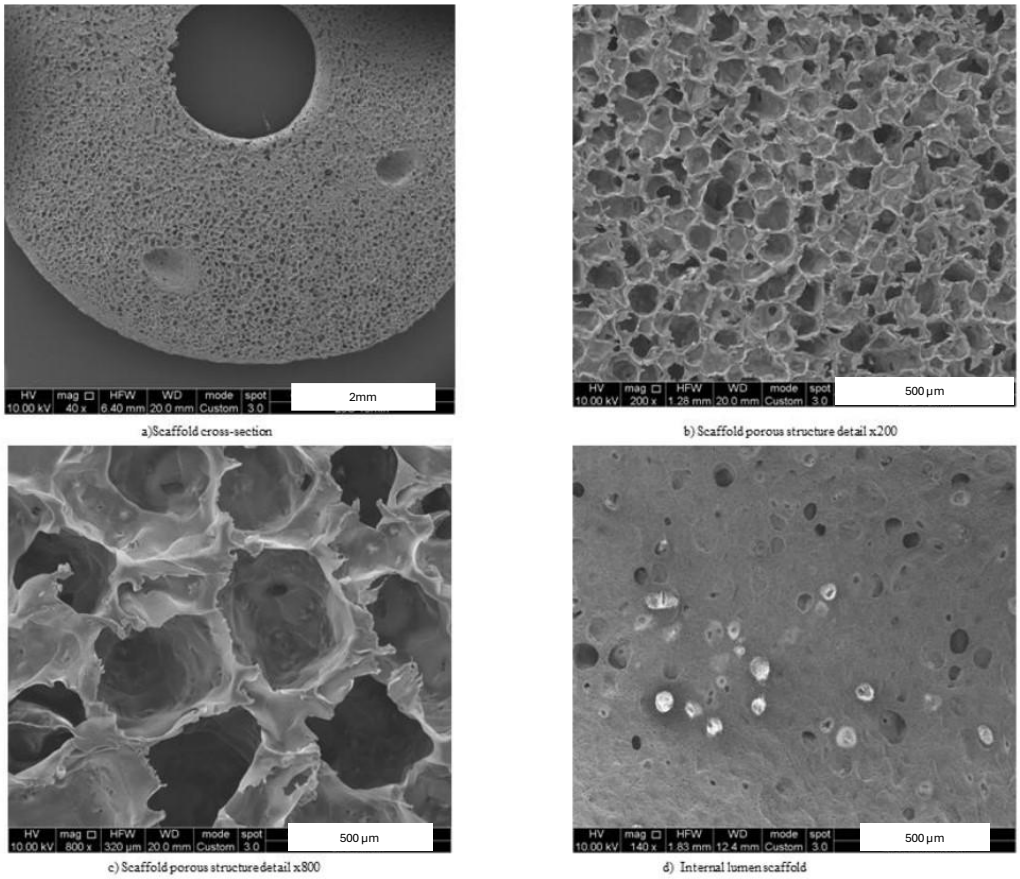

Figure 43: SEM images of PLLA scaffolds showing cross-sectional morphology. (a) General structure, (b) porous matrix at 200x magnification, (c) porous matrix at 800x magnification, and (d) internal lumen. The images highlight differences in pore size between scaffolds prepared at different temperatures.

Moreover, the scaffolds exhibit an open and interconnected pore structure extending from the outer surface to the inner lumen. This structural feature is crucial for facilitating cell colonization and migration, as well as ensuring efficient oxygen and nutrient transport, which are essential for long-term cell viability.

Table 12

0°	Scaffold 1	Scaffold 2	Scaffold 3
Height [cm]	1.8	1.8	1.6
Inner diameter [cm]	0.2	0.2	0.2
Outer diameter [cm]	0.8	0.8	0.8
Apparent volume [cc]	0.847	0.847	0.754
Total Apparent volume [cc]	2.449		
Measured volume [cc]	0.154		

Table 13

25°	Scaffold 1	Scaffold 2	Scaffold 3
Height [cm]	1.7	1.65	1.5
Inner diameter [cm]	0.2	0.2	0.2
Outer diameter [cm]	0.8	0.8	0.8
Apparent volume [cc]	0.8	0.771	0.707
Total Apparent volume [cc]	2.284		
Measured volume [cc]	0.157		

Porosity measurements, conducted as the protocol detailed in the Materials and Methods section, demonstrated that both scaffold types possess a porosity exceeding 93%, regardless of pore size (Tab 12 and Tab 13). This high level of porosity enhances the scaffold's ability to support biological processes.

Bioreactor 3D Printing : Design and Fabrication

The application of 3D printing technology provided significant cost advantages compared to commercially available luer-lock connectors. Using Fusion360 software, connectors were designed with precision to ensure leak-free coupling with tubing systems.

Key design parameters included:

- Internal diameter (ID): 1.45 mm
- Outer diameter (OD) of the tube: 1.59 mm

These dimensions were optimized to guarantee compatibility and prevent fluid leakage, demonstrating the versatility and precision of 3D printing in creating custom bioreactor components.

Radial Flow Evaluation Diffusion and perfusion

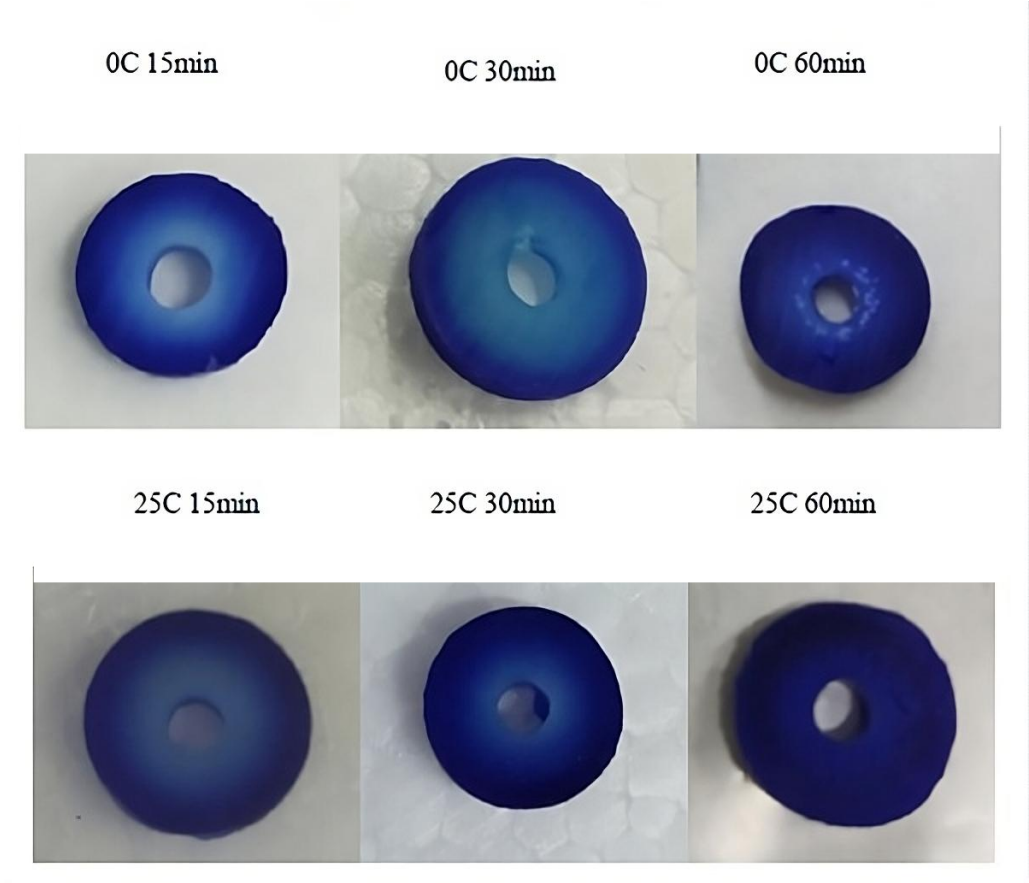

Figure 44: Static diffusion tests of nutrient permeation through scaffolds. Dye diffusion analysis shows slower penetration in 0°C scaffolds compared to 25°C scaffolds, attributed to differences in pore size."

As can be seen from these results (Fig.44) the diffusion of the dye from the outside to the inside is slower for 0° C scaffolds. This behavior is probably due to smaller pore size of 0°C scaffold with respect to the 25°C. But still, the static diffusion of nutrients and oxygen through the scaffold is guaranteed.

The study evaluated perfusion and radial flow behavior across varying flow rate conditions. The flow rate ranges are summarized in Tab. 14.

Table 14

Qrad	Minimum [µl/min]	Maximum [µl/min]
Scaffold 0°C	21.8	90.16
Scaffold 25°C	31.7	146.93

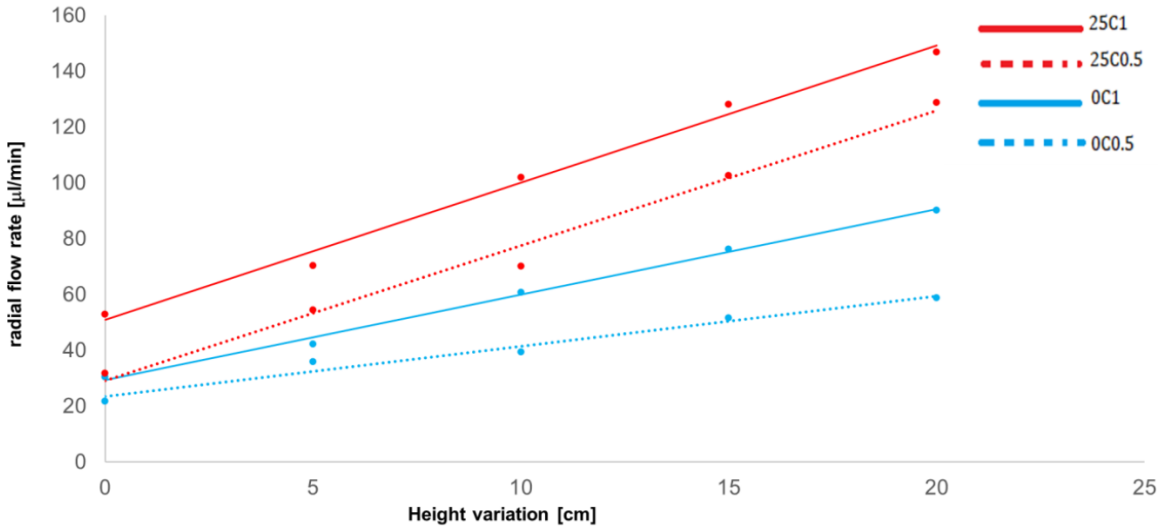

Figure 45: radial flow rate µl/min respect to terminal height variation, two scaffold type (0 and 25) , two inlet flow rate (0,5 an 1 ml/min)

Fig. 45 illustrates the variation in radial flow rate as a function of the end tube height. As anticipated, the radial flow rate increases with greater height due to a rise in internal pressure. This is attributed to the pressure differential between the external atmospheric pressure and the pressure within the scaffold lumen.

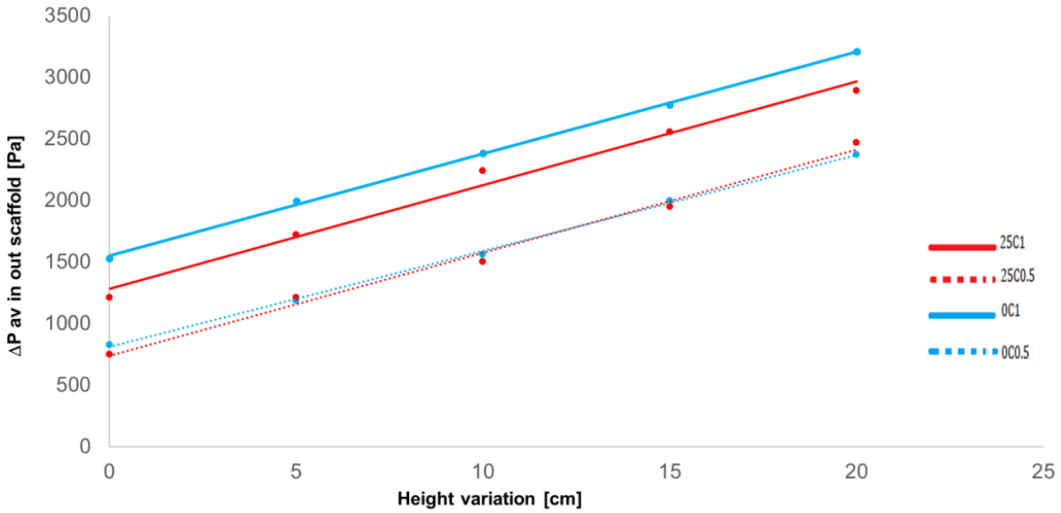

Figure 46: pressure drops respect to terminal height variation, two scaffold type (0 and 25) , two inlet flow rate (0,5 an 1 ml/min)

Further validation is presented in Fig. 46-47 , which correlates the pressure gradient (ΔP) between the scaffold's inner lumen and outer surface with the terminal heigh and radial flow rate. The analysis reveals that at a lower inner flow rate (0.5 mL/min):

- Scaffolds prepared at 25 °C (25C0.5) exhibit a higher radial flow rate as ΔP increases.
- This trend, while present at 1 mL/min, is less pronounced.

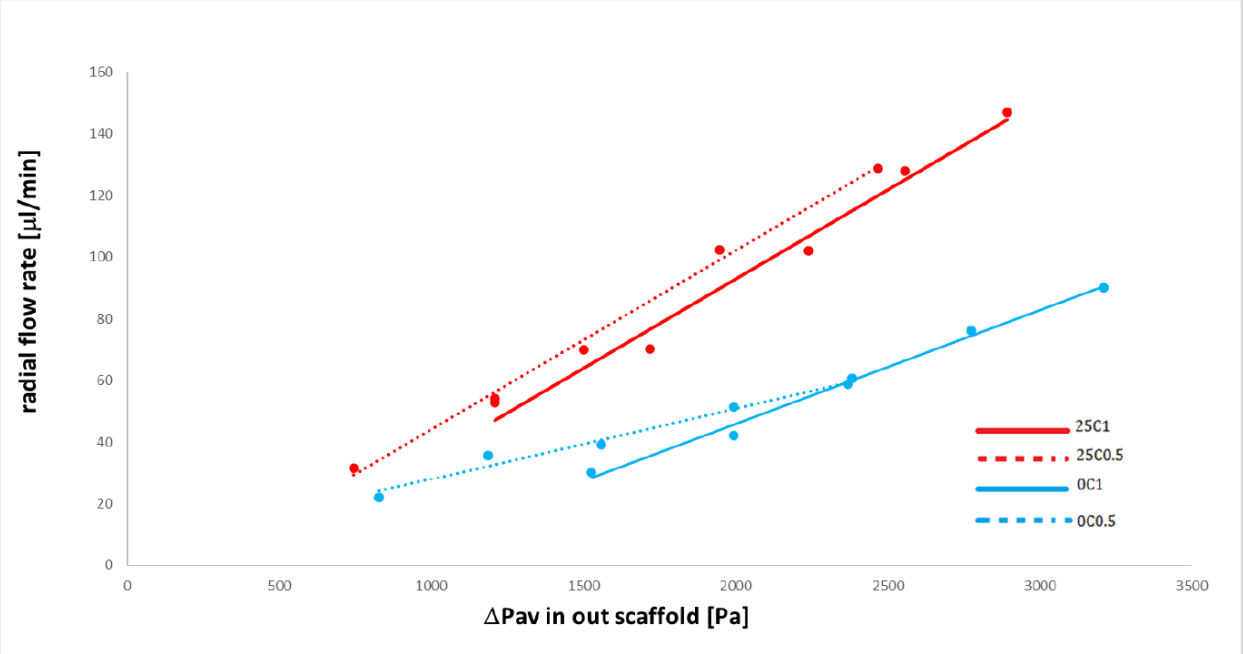

Figure 47: radial flow rate µl/min respect to pressure drops, two scaffold type (0 and 25) , two inlet flow rate (0,5 an 1 ml/min)

The findings suggest that the pore size of the scaffold strongly influences the radial flow rate, given that both scaffold types share similar porosity values.

Permeability Results

To further investigate the relationship between pore size and radial flow, permeability values were calculated based on experimental data. Results, summarized in Tab 15 Fig.48, highlight that:

- 25C scaffolds, with their larger pore sizes, exhibit higher permeability values.
- 0C scaffolds, having smaller pores, demonstrate correspondingly lower permeability values.

Table 15: permeability values for both scaffold type (25 and 0°C)

k_0° [$m2$]	k_25° [$m2$]
$6{,}33*10^{-15}$	$1.15*10^{-14}$

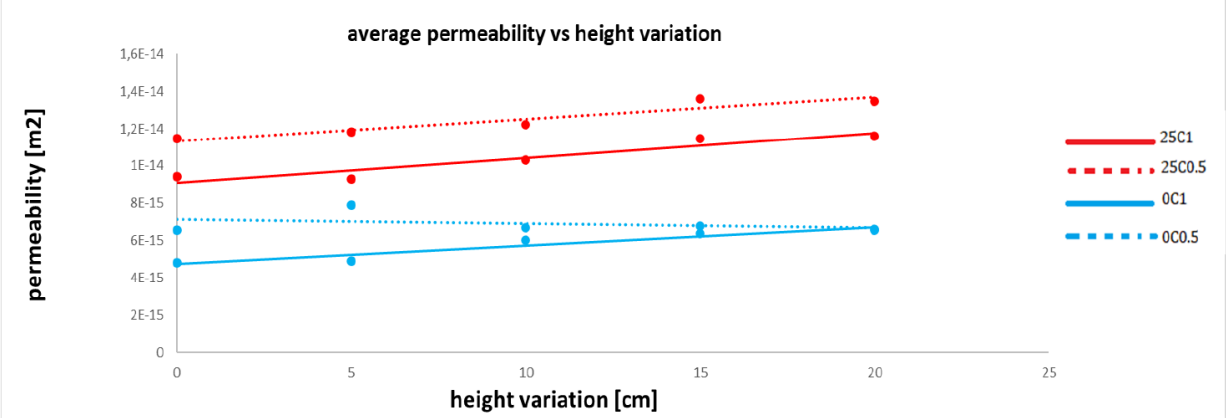

Figure 48: permeabilty values vs terminal height variation Red lines are associated with scaffold produced at 25°C while Blue lines are used for 0°C. Dotted lines are used for flow rates of 0.5 ml/min while continuous lines are used for 1 ml/min

While theoretically the lines for each scaffold type should overlap and remain horizontal, slight deviations were observed, likely due to experimental errors in measuring flow rate and pressure. Average permeability values were computed (Fig. 49) across varying test heights, with error bars confirming that larger pores contribute to greater permeability.

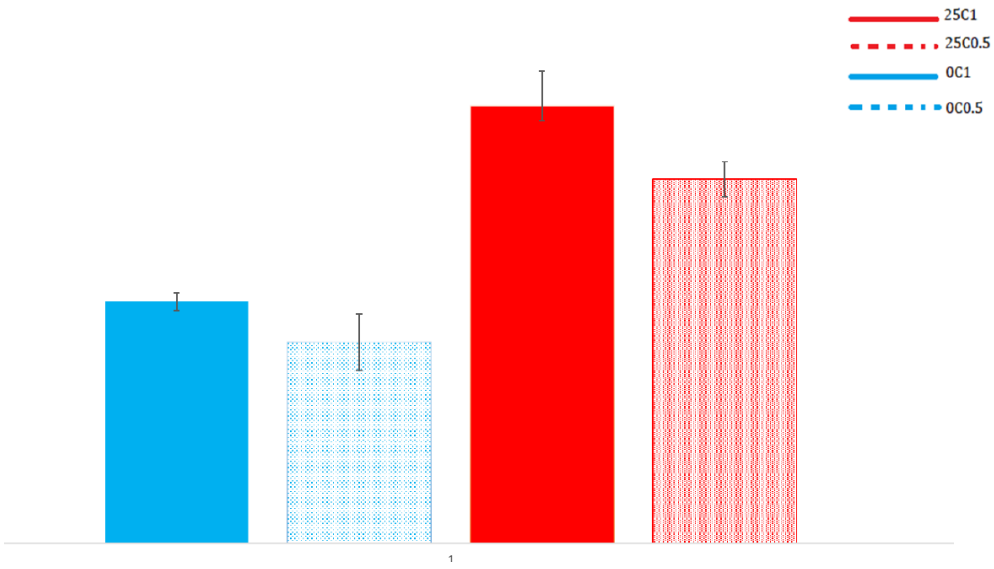

Figure 49: permeability results: , two scaffold type (0 and 25) , two inlet flow rate (0,5 an 1 ml/min) Red lines are associated with scaffold produced at 25°C while Blue lines are used for 0°C. Dotted lines are used for flow rates of 0.5 ml/min while continuous lines are used for 1 ml/min

The results align with existing literature, such as the study by which demonstrated that increasing scaffold porosity enhances permeability in collagen matrices (Al-Munajjed et al., 2008). This relationship arises because higher porosity provides increased space for fluid flow through the matrix. Similarly, findings from (Pennella et al., 2013) corroborate the observed results. Using semi-empirical models like Kozeny's equation Eq. 13:

$$k = \frac{1}{ck} \cdot \left(\frac{\epsilon^3}{s^2}\right)$$

Equation 13

where:

- ϵ = effective porosity,
- s = specific surface area, and
- c_k = Kozeny's constant (dependent on pore geometry),

it is evident that permeability scales with both porosity and pore size. This theoretical framework reinforces the experimental observations, highlighting the critical role of pore geometry in scaffold design.

Nanoparticles Radial Flow Rate Testing

Preliminary water tests by varying the height of the system's final tube are shown in Fig. 50.

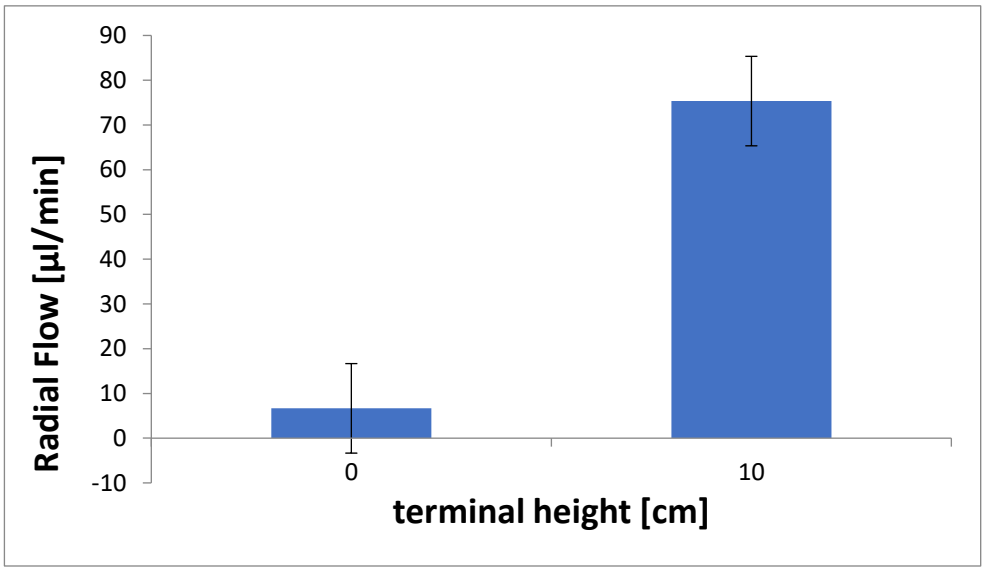

Figure 50: Final Tube Height Graph of radial flow rate vs. final tube height for different scaffold configurations. The results demonstrate how scaffold structure affects fluid dynamics, with higher terminal heights increasing flow rates

As illustrated and expected from previous results, the radial flow rates through the scaffold's porous matrix are significantly influenced by the resistance caused by the fluid outlet height. Radial flow rates at a height of 0 cm, where the fluid outlet is at the same height as the system, are generally very low and, in one case, even negative (indicating inward rather than outward flow). When the outlet tube is placed at a 10 cm height difference, there is a substantial increase in flow rates, reaching an average of about 110 µl/min.

After validating the system's radial flow rate, nanoparticle tests were conducted. Gold nanoparticles were chosen for their potential as drug carriers, enabling localized and prolonged drug delivery directly in situ. As described earlier, a suspension containing gold nanoparticles, was flowed through the internal lumen with the terminal tube at 10 cm. Fig. 51 shows the scaffold's appearance immediately after the test, with the pink coloration indicating that the particles permeated the porous matrix.

Figure 51: Scaffold inside the bioreactor immediately after nanoparticle perfusion tests. The pink coloration indicates the successful diffusion of gold nanoparticles into the porous matrix

As shown in the Tab. 16, the experimental radial flow rate was calculated from the average of three tests conducted with different scaffolds.

Table 16: Radial Flow Rate and Standard Deviation, Nanoparticle Tests

	Radial Flow (µl/min)	Standard Deviation
h=10 cm	103,76	61,72

The obtained result was satisfactory, with an average radial flow rate of 103.76 µl/min, comparable to the previously calculated flow rate with just water. However, it is essential to highlight the high percentage uncertainty calculated, corresponding to nearly 50% of the total value. Previous tests with only water yielded a total radial flow rate of 110 µl/min with a standard deviation of ±20 (less than 20%). This high variability was hypothesized to be due to partial pore occlusion by nanoparticle aggregates. To verify this hypothesis, a system capable of monitoring and recording fluid pressure within the system was implemented.

Pressure Sensor Tests with Nanoparticles

The tests were repeated, as described in the materials and methods section, implementing a pressure sensor. This time, the pressure resulting from a 10 cm height difference between the system and the outlet tube was directly investigated. The tests were conducted first with water and then with a gold nanoparticle suspension. The recorded signals are shown in the graphs in Fig. 52.

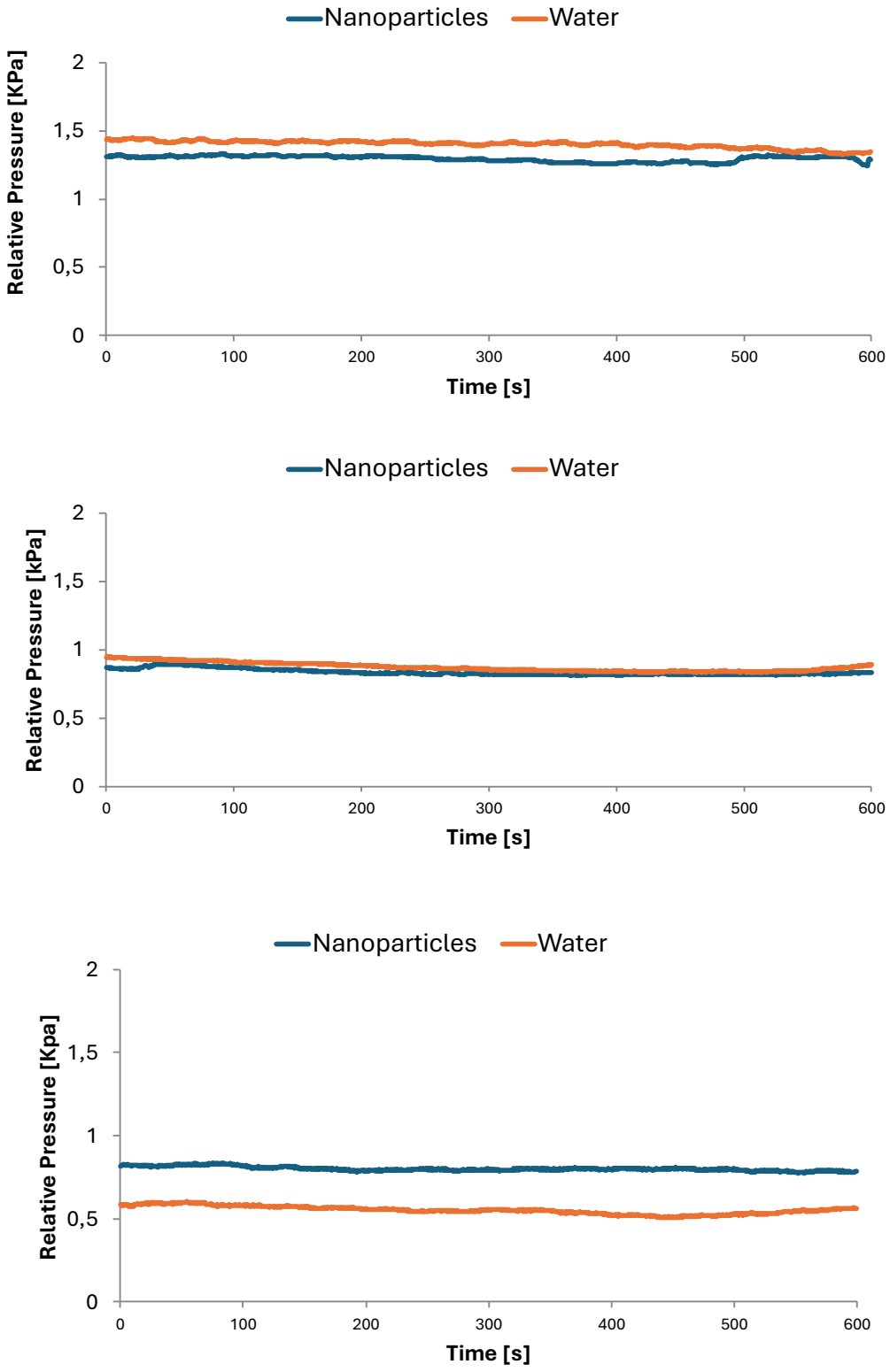

Figure 52: Pressure variation over time inside scaffolds perfused with water and nanoparticle suspensions. The pressure profiles show no significant clogging, indicating that nanoparticles traversed the porous matrix without obstructing flow

Observing the graphs, it is evident that for each tested scaffold, the two recorded signals (water and nanoparticle suspension) are closely aligned, with a maximum difference of 248 Pa. Additionally, the nanoparticle pressure signal remained stable throughout the test; if pore occlusion occurred, one would expect this signal to vary over time. Therefore, it can be concluded that the nanoparticles could traverse the porous matrix without affecting the system's operation during the tested period (10 min). It can be hypothesized that the observed variability in the obtained radial flow rates is attributable to the different permeability of each scaffold, which significantly impacts the flow rate.

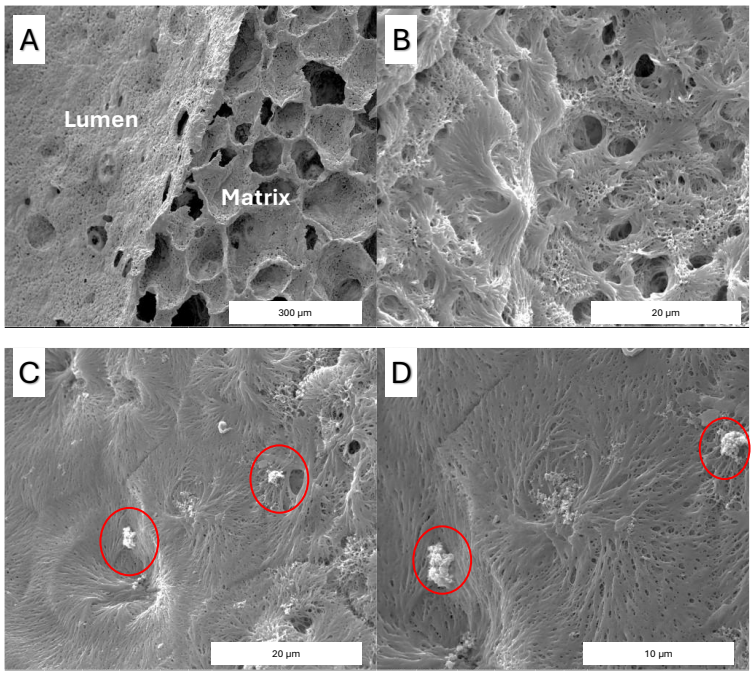

Figure 53: SEM analysis of control scaffolds (A-B) and scaffolds perfused with nanoparticles (C-D). Nanoparticles are visible as small aggregates (circled in red), demonstrating successful retention within the scaffold matrix

In Fig. 53 A-B, the control samples that were not flowed with nanoparticles can be observed. Specifically, Fig. A shows, through a longitudinal section of the sample, both the matrix and the lumen; Fig. B shows the control of the internal lumen. In images C and D, it is possible to identify two clusters of nanoparticles adhered to the lumen at different magnifications (circled in red).

Biological seeding and growth Tests in Dynamic Conditions

The previous device required cell growth within the scaffold under static conditions, wherein the medium permeated the matrix solely by diffusion. The biological tests in this thesis investigated the possibility of achieving cell growth under dynamic conditions, where the medium continuously and forcibly perfused the polymeric matrix containing the cells. This growth mode is implemented in the system by simply connecting it to a syringe pump and closing the final end. This way, the culture medium is forcibly directed towards the matrix. After 48 hours of growth, cross-sections of the scaffold were obtained and observed under a fluorescence microscope (Fig. 54).

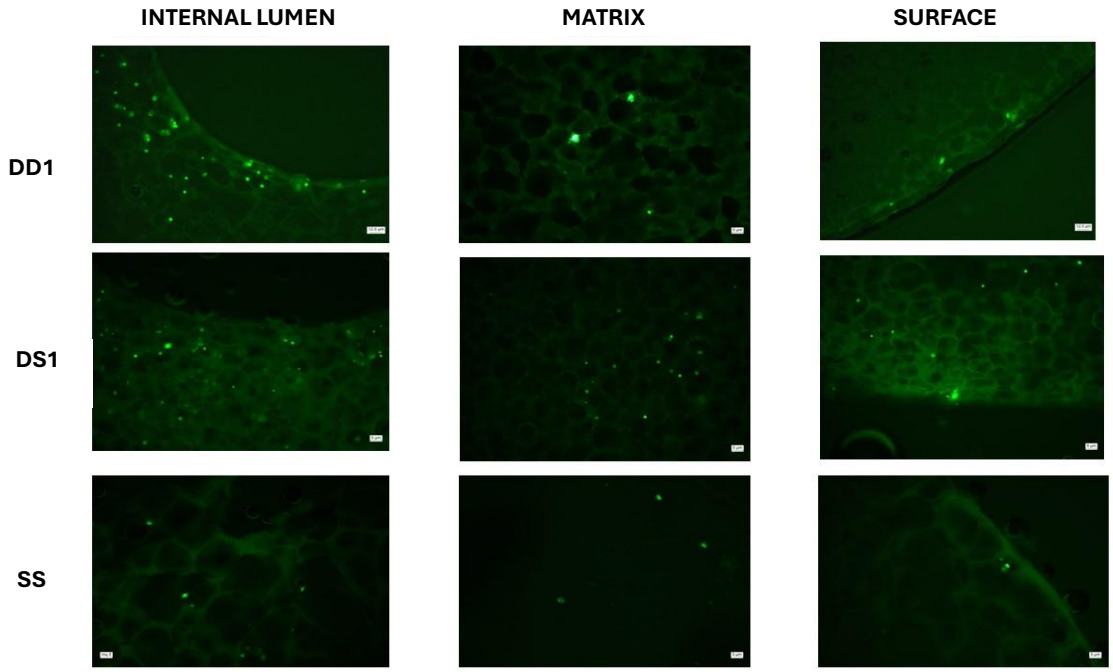

Figure 54: Cell viability assessment via fluorescence staining after 48 hours in dynamic culture. Green fluorescence represents live cells, and red fluorescence marks dead cells. DD1: Scaffold with Dynamic Seeding and Dynamic Maintenance, DS1: Scaffold with Dynamic Seeding and Static Maintenance, SS: Scaffold with Static Seeding and Static Maintenance

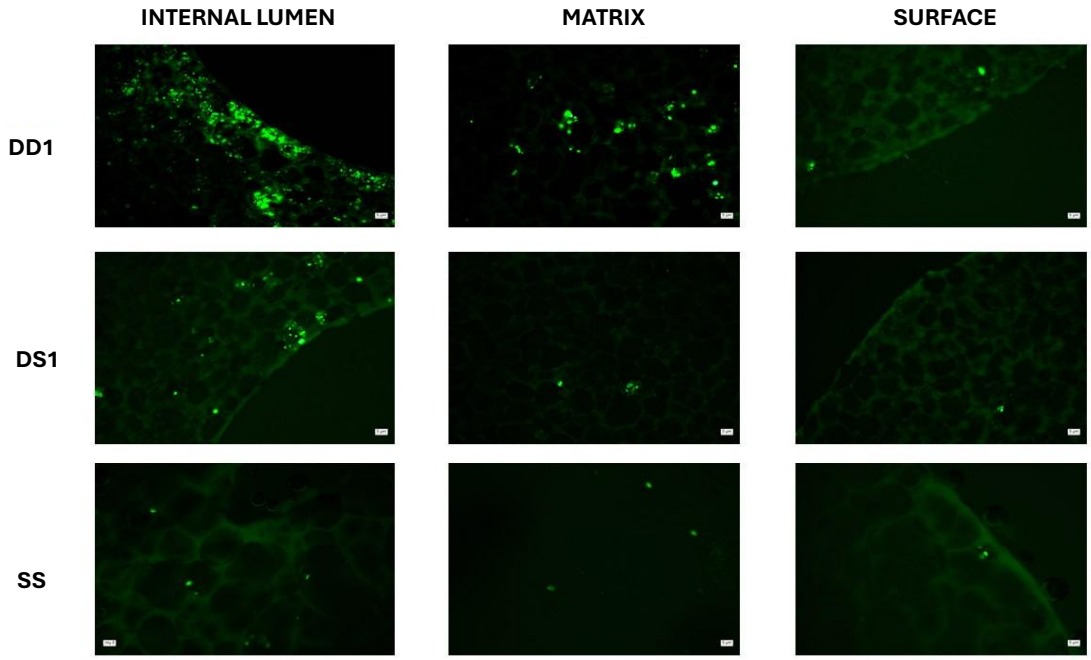

Figure 55: Cell viability assessment via fluorescence staining after 48 hours in dynamic culture. Green fluorescence represents live cells, and red fluorescence marks dead cells. DD2: Scaffold with Dynamic Seeding and Static Maintenance, DS2: Scaffold with Dynamic Seeding and Static Maintenance, SS: Scaffold with Static Seeding and Static Maintenance

As seen in Figs. 54-55, a higher number of cells are observed in the scaffolds maintained under dynamic conditions. In these scaffolds, a more uniform distribution and higher number of cells, particularly at the internal lumen level, were observed. This indicates that cells are immediately deposited as they flow into the internal lumen. This type of maintenance more accurately simulates *in vivo* conditions. Conversely, the SS scaffold shows a significantly lower number of cells across all scaffold portions.

In summary, while static models stand out for their simplicity, controlling experimental conditions might not replicate the dynamic *in vivo* environment. Conversely, dynamic models strive to realistically mimic physiological conditions using fluid flows and mechanical forces. Ultimately, the choice between static and dynamic models depends on the objectives to be achieved.

3.4 Discussion

This study aimed to develop and optimize a compact bioreactor system for *in vitro* 3D cell culture using PLLA scaffolds fabricated through Thermally Induced Phase Separation (TIPS) and perfusion conditions as dynamic culturing. The results demonstrate the feasibility of using this system to regulate radial flow, improve cell seeding efficiency, and support dynamic culture conditions, addressing key limitations in traditional static 3D models.

The SEM analysis confirmed that both scaffold types (0°C and 25°C) exhibited a homogeneous and interconnected porous structure, which is crucial for cell infiltration and nutrient transport. However, significant differences in pore size were observed, with 25°C scaffolds displaying larger pores (50–100 μm) compared to 0°C scaffolds (15–25 μm). Despite these differences, both scaffold types maintained a high porosity (>93%), aligning with prior studies emphasizing the importance of porosity in supporting biological processes and fluid dynamics (Nasrollahzadeh & Pioletti, 2016; Sarparast et al., 2020).

Perfusion and radial flow analyses revealed that scaffold pore size significantly influenced flow rates. The 25°C scaffolds, with larger pores, exhibited higher radial flow rates and permeability values ($\approx 1.15*10^{-14}$ m²) compared to the 0°C scaffolds ($6.33*10^{-15}$ m²). These findings align with existing literature, which suggests that increased pore size enhances permeability and fluid transport (Nasrollahzadeh & Pioletti, 2016). Additionally, variations in radial flow rate with terminal height and pressure differentials confirmed that scaffold design directly affects perfusion efficiency, it has been demonstrated the ability to control a radial flow in the range 10-140 μl/min depending on the scaffold pore size and terminal tube height variation.

Gold nanoparticle perfusion tests further validated the bioreactor's ability to allow drug delivery applications. The observed radial flow rates (103.76 μl/min) closely matched the values obtained with water alone (110 μl/min), suggesting that nanoparticles effectively permeated the scaffold without significant occlusion. Pressure sensor analysis confirmed stable pressure signals, indicating minimal interference due to nanoparticles aggregation. These findings highlight the system's potential for controlled drug delivery studies, aligning with prior research showing that increased scaffold permeability improves nanoparticle transport (Fiume et al., 2021; Lombardo et al., 2021).

Cell seeding and growth experiments under dynamic conditions demonstrated improved cell distribution and viability compared to static models. Fluorescence microscopy revealed that scaffolds maintained under continuous perfusion exhibited higher cell densities, particularly within the internal

lumen. This result underscores the importance of dynamic culture conditions in replicating in vivo environments, where fluid flow influences nutrient distribution and cell behavior. Previous studies have demonstrated that dynamic culture conditions enhance cell penetration and reduce superficial growth compared to static conditions. Penderecka et al. (2020) implemented dynamic culture conditions in a 3D breast cancer model, demonstrating improved cell viability, scaffold penetration, and co-localization compared to static culture (Penderecka et al., 2020). Similarly, Nanou et al. (2022) investigated 3D scaffold cultures of metastatic breast cancer cells and found that dynamic conditions influenced proliferation and tumor-like characteristics (Nanou et al., 2022).

The successful integration of a bioreactor system with TIPS-fabricated scaffolds provides a promising platform for advanced drug screening and tissue engineering applications. By enabling controlled perfusion and dynamic cell culture, this system addresses key limitations of traditional static 3D models. Future work should focus on optimizing flow parameters, incorporating real-time monitoring systems, and expanding nanoparticle testing to assess long-term scaffold performance.

Overall, this study demonstrates the potential of a compact, cost-effective bioreactor system to enhance in vitro 3D models, bridging the gap between conventional cell cultures and physiologically relevant microenvironments.

3.5 Conclusion

This study successfully developed and optimized a compact bioreactor system for in vitro 3D cell culture using PLLA scaffolds fabricated via Thermally Induced Phase Separation (TIPS) and perfusion for dynamic culturing. The results demonstrated the feasibility of regulating radial flow, improving cell seeding efficiency, and supporting dynamic culture conditions, addressing key limitations of traditional static 3D models.

The SEM analysis confirmed that both scaffold types (0°C and 25°C) exhibited homogeneous and interconnected porous structures, crucial for cell infiltration and nutrient transport. Significant differences in pore size were observed, with larger pores in the 25°C scaffolds leading to higher radial flow rates and permeability values. Gold nanoparticle perfusion tests validated the bioreactor's capability for controlled drug delivery applications.

Cell seeding and growth experiments under dynamic conditions showed improved cell distribution and viability compared to static models, emphasizing the importance of dynamic culture in replicating

in vivo environments. The integration of a bioreactor system with TIPS-fabricated scaffolds provides a promising platform for advanced drug screening and tissue engineering applications.

Future research should focus on optimizing flow parameters, incorporating real-time monitoring systems, and expanding nanoparticle testing to assess long-term scaffold performance. This compact, cost-effective bioreactor system enhances in vitro 3D models, bridging the gap between conventional cell cultures and physiologically relevant microenvironments.

4. *Project : Air-Liquid Interface (ALI) bioreactor*

4.1 Introduction

Respiratory system diseases affect one or more organs involved in breathing. The prevalence of chronic respiratory diseases among adults is approximately 7.0%, with asthma accounting for 3.4%, chronic obstructive pulmonary disease (COPD) for 2.6%, and a combination of the two for 1% (Soriano et al., 2017). Breathing, a vital process through which oxygen is transported into the body and carbon dioxide is expelled, can be impaired by numerous conditions ranging from inflammations like laryngitis, pharyngitis, and bronchitis to more severe illnesses like bronchial asthma, whooping cough, pneumonia, or bronchopneumonia, potentially leading to respiratory failure. Moreover, challenges such as COVID-19 and the effects of cigarette smoking underscore the need for *in vitro* tissue models for preliminary diagnostic testing (de Marco et al., 2013). The fluid dynamics of respiratory airways are influenced by their geometric properties, including diameter and length. Assuming the airways are cylindrical with radius RR and length LL, and that airflow is steady and parallel to the conduit axis, the wall shear stress (σ) can be estimated based on the pressure drop (q) along the airway using the Eq 14:

$$\sigma = f(R, L, q)\sigma = f(R, L, q)$$

Equation 14

This relationship highlights the dependence of shear stress on airway geometry and airflow parameters, both of which are critical for understanding respiratory mechanics and replicating physiological conditions *in vitro* (Viegi et al., 2020). Understanding airflow dynamics is essential for replicating respiratory tissue function *in vitro*. During rest, an adult exchanges approximately:

- **0.5 L of air per breath** (approximately 400 mL for females).
- **12 breaths per minute**, resulting in a ventilation rate of about **6 L per minute**.

These values represent the tidal volume and typical respiratory rate in adults (Xie et al., 2020).

Airflow through the respiratory tract is driven by pressure gradients between the external environment and the alveoli. These gradients decrease progressively through the bronchial generations, with the highest pressure drops observed in the second and third bronchial branches. The ninth bronchial generation marks a significant reduction in pressure gradients. Figure 3 (hypothetical reference) illustrates the pressure drop across various bronchial generations, emphasizing the non-uniform distribution of resistance within the airway tree (Burney et al., 2015).

This project aims to develop a three-dimensional (3D) model of bronchial mucosa by integrating anatomical, biological, and engineering knowledge. Through an extensive literature review, relevant anatomical dimensions were determined. Within the lungs, the bronchi repeatedly branch, progressively decreasing in diameter. Each branch differs in dimensions (diameter and length), cartilage composition, mechanical properties, airflow parameters (rate, pressure, velocity), and wall shear stress affecting the inner mucosa. Parameters like volumetric airflow during a resting adult's inhalation were also gathered from the literature, as these are critical for designing constructs that replicate native tissues both geometrically and physically (Halldin et al., 2015).

The main goal is to be able to seed mucosa biopsies into polymeric scaffolds and then insert them into the bioreactor. The scaffolds were synthesized using thermally induced phase separation (TIPS) from a ternary solution (polymer, solvent, and antisolvent) consisting of 4% Poly-L-lactic acid (PLLA), dioxane, and water in an 87/13 ratio. PLLA was chosen due to its FDA-approved biocompatibility, widespread biomedical applications, mechanical properties, and biodegradable nature. The ternary solution was poured into a custom-made metallic mold designed to produce a tubular scaffold featuring a lumen that mimics the shape and dimensions of a third-generation bronchus. These scaffolds were morphologically analyzed using scanning electron microscopy (SEM) to evaluate pore size and interconnectivity, ensuring optimal conditions for cellular growth and proliferation within the matrix (Viegi et al., 2020; Xie et al., 2020).

A key feature of respiratory tissue is the air-liquid interface (ALI), which was faithfully replicated in this model. The scaffold was connected to a peristaltic pump via silicone tubing and inserted into a bioreactor—a construct that provides dynamic conditions for the growth of neo-tissue within the porous matrix. The bioreactor’s main chamber, along with the connectors used to integrate the scaffold with silicone tubes, was 3D-printed using stereolithography (SLA). The system was designed

to allow the culture medium surrounding the scaffold to pass exclusively through the porous matrix. Airflow through the scaffold's lumen was controlled using a soap-film device to characterize the pump's output at different voltages, achieving an optimal balance between air and culture medium (Barnes, 2008; O'byrne & Postma, 1999).

The bioreactor was designed, developed, and fluid-dynamically characterized to serve as a robust candidate for creating the 3D *in vitro* model of bronchial mucosa. This system is easily sterilizable, with assembly procedures optimized for accessibility by any operator.

4.2 Materials and Methods

Scaffold Fabrication

The ternary solution was poured into a custom-designed metal sample holder. The holder consisted of a cylindrical structure with a 1 cm diameter central cavity, matching the external diameter of the scaffold. To create the lumen, a 0.7 cm diameter metallic rod was inserted into the center of the holder. The assembled holder is depicted schematically in Fig. 56.

Figure 56: Mold setup for scaffold production. The polymer solution was poured into the mold, which was then sealed and subjected to a controlled thermal process to induce phase separation and scaffold formation.

Once the solution was poured, the holder was sealed with a metal lid secured using screws and bolts. Phase separation of the polymer from the solvent was induced using a series of thermostatic baths.The sample holder was immersed sequentially in baths set at 0°C and -20°C, each for 10 minutes.

The pore morphology of the scaffold, influenced by the phase separation process, was characterized post-fabrication.

Washing and Drying of the Scaffold

After the thermal processing, the scaffold was extracted from the holder using tweezers and subjected to a dropwise washing system to remove residual dioxane. This process was carried out overnight to ensure thorough solvent removal.
The washing system comprised a distilled water reservoir connected via silicone tubing to a scaffold-containing chamber. The chamber ensured a watertight seal. Clean water flowed into the scaffold chamber, while dioxane-contaminated water was collected in a second reservoir for disposal.
After washing, the scaffold was dried in a vacuum oven at 45°C to ensure complete solvent removal and scaffold stabilization.

Scaffold Morphological Analysis via Scanning Electron Microscopy (SEM)

The scaffold's morphology, including pore size, porosity, and interconnectivity, was analyzed using a Quanta 200F SEM (Thermo Fisher, USA). Before analysis, the scaffold samples were fragmented into smaller pieces, mounted on aluminum stubs with conductive carbon tape, and coated with a ~4 nm gold layer using an argon atmosphere sputter coater. SEM provided detailed insights into the scaffold's microstructure, including external morphology and chemical composition.

Bioreactor Design and Prototyping

The bioreactor was designed to replicate the dynamic physiological conditions necessary for engineering respiratory mucosa tissues *in vitro*. The main chamber of the bioreactor was modeled using Autodesk Fusion software to ensure key requirements:

- Maintaining an Air-Liquid Interface (ALI).
- Sterile assembly.
- Dimensions suitable for an incubator.
- Adequate capacity for culture medium.
- Maximum system sealing.

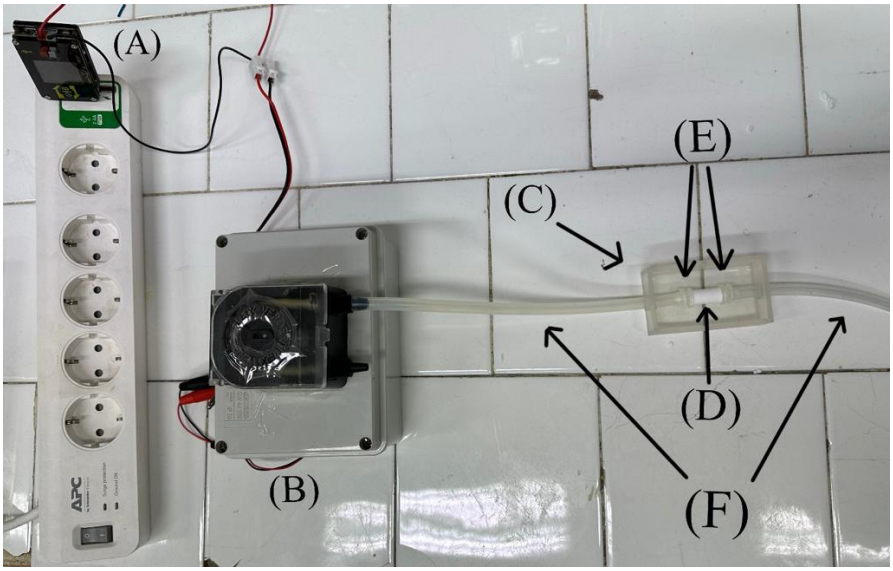

Figure 57 : Components of the bioreactor system. (A) Power supply, (B) Peristaltic pump, (C) Main chamber, (D) Scaffold, (E) Connectors, (F) Silicone tubing. The system was designed to maintain sterile conditions and facilitate controlled fluid flow through the scaffold.

As shown in Fig. 57 the rectangular chamber housed the scaffold and culture medium. Silicone tubing connected to the scaffold's ends ensured no medium entered the lumen. Custom connectors, designed via Autodesk Fusion and manufactured using stereolithographic (SLA) 3D printing, provided a tight seal between the scaffold and tubing.

Airflow Characterization

To complete the experimental setup, a peristaltic pump was used to generate airflow through the scaffold's inner lumen, simulating the physiological conditions of inhalation. The pump was characterized in terms of airflow rates at various applied voltages.

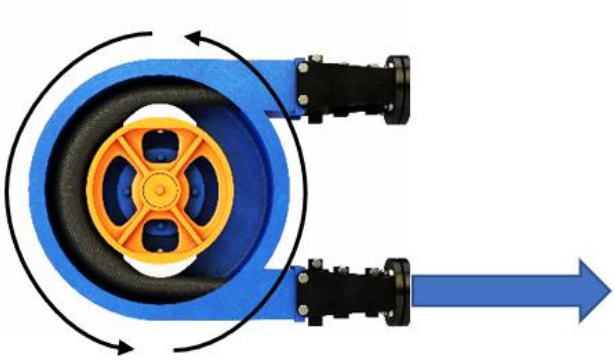

Figure 58: Schematic representation of the peristaltic pump used for controlled airflow generation. The pump operates via peristalsis, where rotating rollers compress a flexible tube to create a continuous fluid flow. The flow rate is determined by the rotor speed and applied voltage.

The peristaltic pump Fig. 58 operates on the principle of peristalsis, where rollers mounted on a rotor compress a flexible tube, creating a pushing motion that propels air forward. The speed of the rotor's rotation, measured in revolutions per minute (RPM), determines the output airflow rate. The pump was connected to a power supply, allowing for precise voltage modifications (Fig.59) .

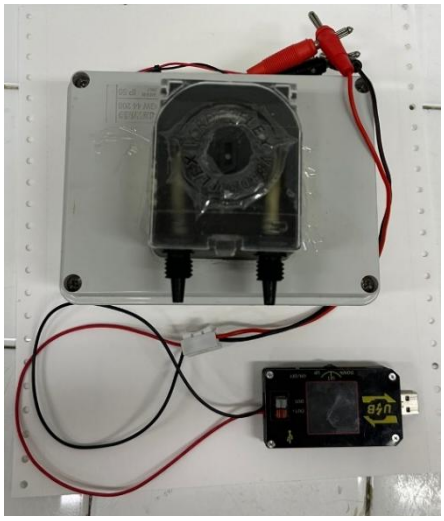

Figure 59: Peristaltic pump connected to a power supply. The voltage can be adjusted to regulate airflow rates through the scaffold lumen, mimicking physiological inhalation conditions.

To measure airflow rates, a soap-film apparatus was used (Fig. 60). This device consisted of a tubular glass column with a small reservoir of a soap-water mixture at its base.

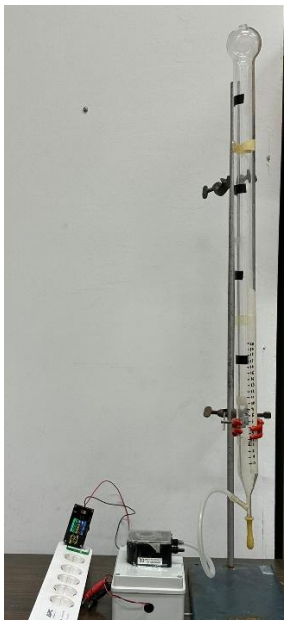

Figure 60: Soap-film apparatus for airflow measurement. The movement of the soap film in a calibrated glass tube allows for precise volumetric flow rate calculations

When air was supplied by the pump, a bubble formed and rose through the column, adopting a meniscus shape. By knowing the internal diameter of the column and measuring the time taken for the meniscus to travel a known distance, the volumetric airflow rate could be calculated as the volume of air per unit of time. The peristaltic pump was characterized at the following voltages:

- 4V
- 6V
- 8V
- 10V
- 11V

For each voltage setting, the measurements were repeated three times to ensure accuracy and reproducibility.

Static Diffusion Tests

The scaffold, along with its attached connectors, was placed inside a glass tube filled with ethanol 70 %. Vacuum was applied to remove any air trapped within the porous structure, facilitating complete hydration. To assess liquid diffusion through the scaffold's porous matrix under static conditions, the following procedure was followed:

1. The hydrated scaffold was immersed in a container filled with toluidine blue dye solution, ensuring liquid penetration occurred solely through the lateral surface of the scaffold.
2. Dyed water was added around the scaffold as shown in Fig. 61.

3. Tests were conducted for durations of:
    - 10 minutes.
    - 20 minutes.
    - 30 minutes.
    - 40 minutes.

Figure 61: Scaffold placed in a toluidine blue solution for static diffusion tests. The experiment evaluates liquid penetration through the porous matrix under controlled conditions.

After each interval, the scaffold was removed and transversely sectioned using a scalpel. The cross-section was analyzed to evaluate the extent and uniformity of dye penetration into the scaffold.

Radial Flow Rate: Theoretical Evaluation

To analyze the system's fluid dynamics, Bernoulli's equation was applied to calculate pressure within the scaffold. Subsequently, Darcy's law was used to estimate the radial flow rate of fluid through the porous matrix.

The experimental system setup is illustrated in Fig. 62, comprising:

1. A peristaltic pump.
2. Silicone tubing.
3. A main chamber containing the scaffold.
4. An outlet silicone tube for discharge.

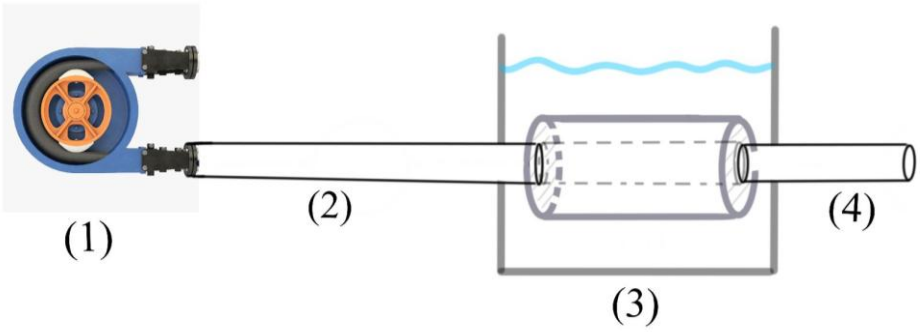

Figure 62: Schematic representation of the experimental system to evaluate radial flow rates at atmospheric pressures.

Fig. 63 highlights the measurement points for pressure calculations. *P*1 represents the pressure downstream of the scaffold, while *P*atm corresponds to atmospheric pressure, as the discharge terminal is open to the external environment.

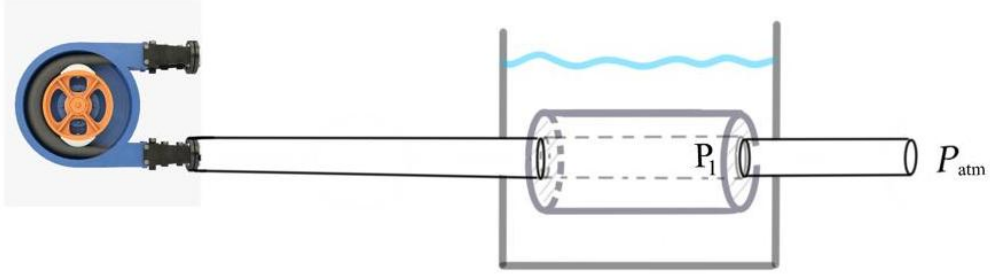

Figure 63: Experimental set up to evaluate P1 with Benoulli's law

$$\frac{P_1}{\rho} + \frac{1}{2}v_1^2 + gz_1 = \frac{P_{atm}}{\rho} + \frac{1}{2}v_2^2 + gz_2 + h_{fd}$$

Equation 15

Using the real form of Bernoulli's equation (Eq. 15) where:

- *v*1,*v*2: air velocities downstream of the scaffold and at the terminal.
- *z*1,*z*2: elevations of the two points.
- *h*fd: distributed losses due to the outlet's geometry.

Distributed losses (*h*fd) depend on the conduit's internal diameter, length, air velocity, and the Reynolds number (*Re*) reported in Eq. 16
:

$$Re = \frac{\rho v D}{\mu}$$

Equation 16

Where:

- ρ: air density.
- μ: air viscosity.
- *D*: characteristic diameter.
- *v*: air velocity.

Using this information, Bernoulli's equation was solved to calculate *P*1. Considering the system at the same elevation, by evaluating the distributed losses and knowing the velocities (which are uniform at every point in the system due to the characterized flow rates), it was possible to solve Eq 17 to determine the unknown pressure *P*1.

$$P_1 = P_{atm} + (h_{fd} * \rho)$$

Equation 17

Once *P*1 was determined, Darcy's law Eq. 18 was applied to estimate the radial flow rate *Q* through the porous scaffold:

$$Q = k * \frac{2\,\pi\,h_s\,\Delta P}{\mu\,ln\frac{r_{ext}}{r_{int}}}$$

Equation 18

Where:

- *k*: scaffold permeability.
- Δ*P*=*P*ext−*P*int: pressure gradient between the scaffold's internal lumen and external surface.
- *hs*: scaffold height.
- *r*ext, *r*int: external and internal radii of the scaffold.
- μ: fluid viscosity.

The external pressure (*P*ext) was derived as the sum of atmospheric pressure and hydrostatic pressure (ρgh) due to the liquid column above the scaffold. The radial flow rate was calculated for different airflows generated by the pump at the following voltages:

- 5V
- 8V
- 11V

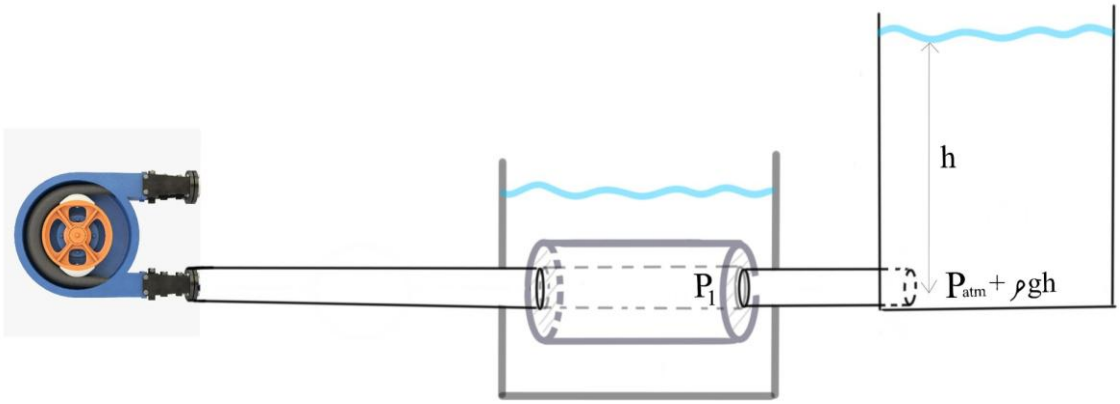

Figure 64 Schematic representation of the experimental system to evaluate radial flow rates at 5 cm terminal water column

Compared to the previous configuration, a 5 cm water column was applied at the discharge terminal as shown in Fig. 64. The presence of this column, with a specific height *h*, introduces additional hydrostatic pressure that must be added to the atmospheric pressure in the previously applied Bernoulli's equation.

Empirical pressure and radial flow

Pressure measurements at the scaffold ends were obtained using uPS pressure sensors (Fig. 65) and a four-channel sensor collector (Fig. 66) controlled by the uProcess™ software.

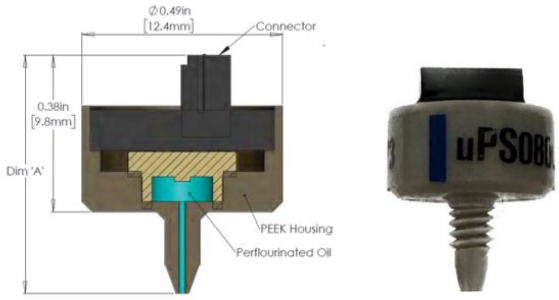

Figure 65: Pressure sensor used for monitoring scaffold permeability. The sensor was positioned upstream and downstream to measure pressure variations due to fluid flow through the scaffold

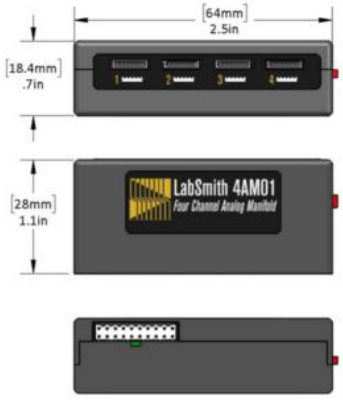

Figure 66: Four-channel data acquisition system used for real-time pressure monitoring. The system recorded pressure values upstream and downstream of the scaffold to evaluate flow resistance

Two sensors were positioned upstream and downstream of the scaffold. The configuration of the experimental setup is shown in Fig. 67.

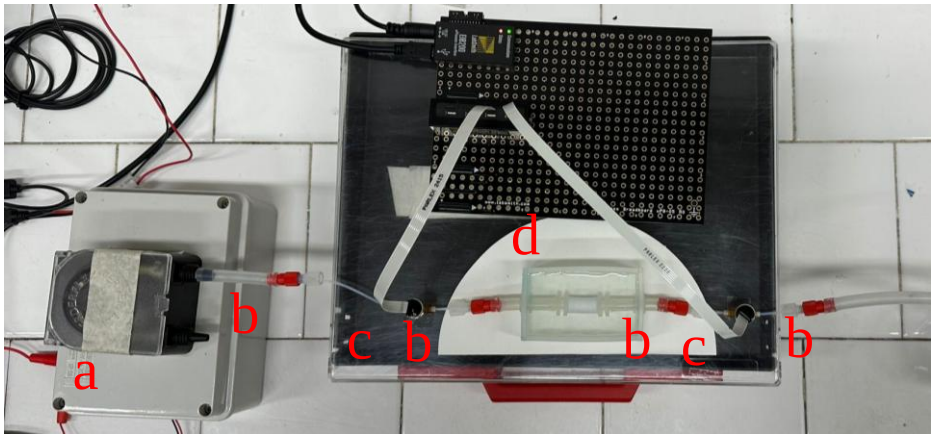

Figure 67: Pressure sensors real experimental set up :a) peristaltic pump; b) silicon tubing; c) pressure sensor; d) main chamber with the scaffold

The uPS are designed for accurate pressure monitoring. In this project, two sensors were used: one upstream of the scaffold and one downstream. This configuration allowed, thanks to the use of the real Bernoulli's law, the evaluation of the pressure values at the ends of the scaffold.
The schematic of the system arrangement is depicted in Fig. 68, showing the key components:
Peristaltic pump.

Connecting silicone tubes.

Upstream sensor (uPS1).

Main chamber with scaffold.

Downstream sensor (uPS2).

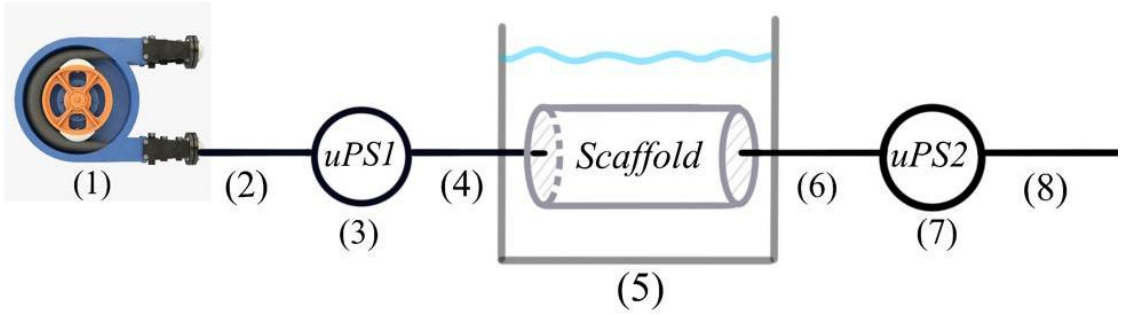

Figure 68: Pressure sensors schematic experimental set up

The following components are depicted in order: the peristaltic pump (1), a system of connecting tubes (2), the first sensor (uPS1) (3), additional connecting tubes (4), the main chamber/scaffold system (5), another connection system (6), the second sensor (uPS2) (7), and the final set of connecting tubes (8). To obtain more precise pressure measurements for both sensors, experiments were conducted with an analysis duration of 5 minutes. The values obtained during this period were averaged and used to evaluate the pressure at both ends of the scaffold. The subsequent schematic (Fig. 69) indicates the points where the pressures are measured: PS1 and PS2 represent the pressure values recorded by the sensors, while P1 and P2 are the unknown pressures at the ends of the scaffold (lumen side) to be calculated using Bernoulli's equation.

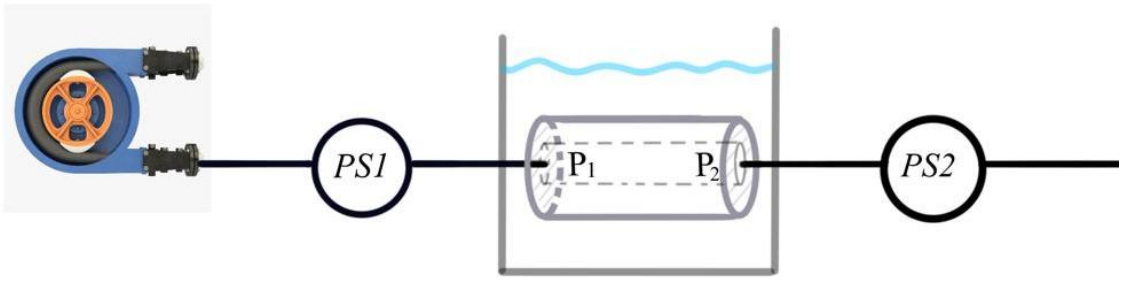

Figure 69: Pressure evaluation scheme using Bernoulli's equation. PS1 and PS2 indicate pressure values recorded by sensors, while P1 and P2 represent calculated pressures at the scaffold's inlet and outlet.

The real Bernoulli's law was used separately twice (5) (6), once using uPS1 and once using uPS2, respectively for the calculation of P1 and P2 at the two ends of the scaffold (Eq. 19-20)

$$\frac{PS1}{\rho} + \frac{1}{2}v_{s1}^2 + gz_{s1} = \frac{P_1}{\rho} + \frac{1}{2}v_1^2 + gz_1 + h_f$$

Equation 19

$$\frac{PS2}{\rho} + \frac{1}{2}v_{s2}^2 + gz_{s2} = \frac{P_2}{\rho} + \frac{1}{2}v_2^2 + gz_2 + h_f$$

Equation 20

With vs1 and vs2 being the air velocities in the sensors, v1 and v2 being the velocities at the ends of the scaffold, and hf representing the contribution of both concentrated and distributed pressure losses. The pressure losses were evaluated for each duct (distributed) and for each constriction and/or enlargement (concentrated). Concentrated pressure losses depend on the fluid velocity (v) and the parameter k, a factor that accounts for the geometric variation of the duct. Considering the system placed at the same height from the ground, evaluating the concentrated and distributed pressure losses, and knowing the velocities in each duct, it was possible to solve the equation as P1 and P2 are the only unknowns in equations (5) and (6). The volumetric flow rate, set by the peristaltic pump, is known, which allows for determining the air velocities within the tubes connecting the pump to the scaffold and the scaffold to the outlet terminal. Knowing these pressures (P1 and P2) allows for obtaining an averaged pressure value within the inner lumen; therefore, it was possible to use relation (4) to derive the radial flow rate.

This setup was also studied with a liquid head of 5 cm above the discharge terminal (Fig. 70)

Figure 70: Bioreactor system assembled for airflow experiments. The design maintains an air-liquid interface, ensuring proper oxygenation while preventing liquid overflow, in red the 5 cm liquid head above the terminal

Dynamic Perfusion Tests

The experimental setup (Fig. 71) for the evaluation of radial flow rate includes the use of:

- Bioreactor
- Peristaltic pump
- Incubator
- Water reservoi
- Collection container
- Control container

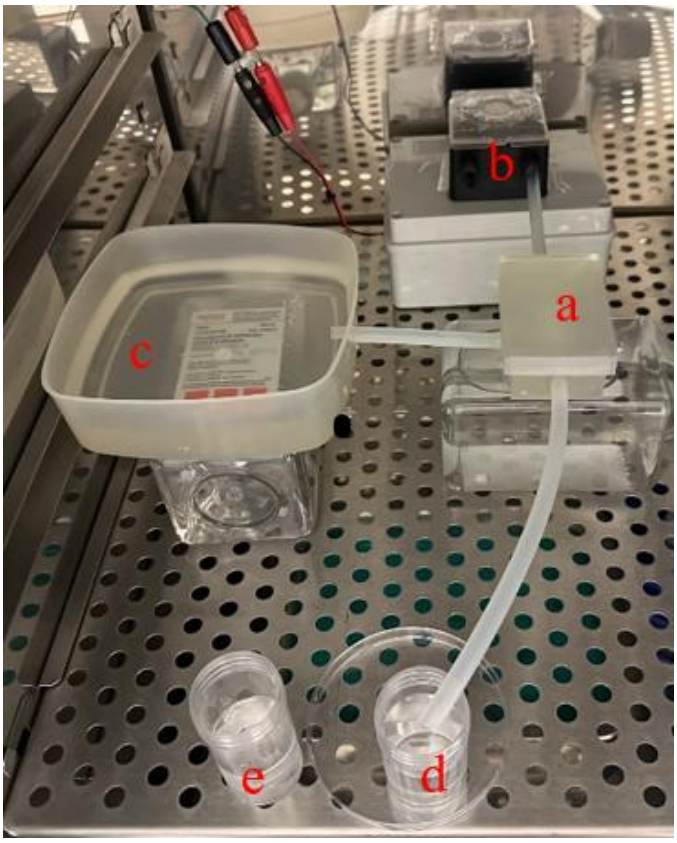

Figure 71: Experimental set up for dynamic perfusion : (a) bioreactor mai chamber, (b) peristaltic pump, (c) water resevoir, (d) eluted resevoir, (e) evaporation control resevoir

The bioreactor, including a hydrated scaffold, was assembled inside an incubator and connected to the previously characterized peristaltic pump. Dynamic tests were conducted by varying the voltage of the power supply connected to the pump. The voltages used were:

- 5V
- 8V
- 11V

Each test lasted for 5 hours. The liquid permeating the scaffold was collected in a container and then weighed on an analytical balance. The amount of water expelled from the system per unit of time corresponds to the radial flow rate.

To avoid experimental uncertainties due to solvent evaporation, a second (identical) container was placed inside the incubator as a control. The weight of the control container was measured before and

after the experiment to evaluate the amount of water evaporated during the test. This value was then used as a correction factor in determining the weight of the eluate.

The experimental tests were conducted in line with the previously described analyses under two experimental conditions: with the discharge terminal exposed to atmospheric pressure or with the discharge terminal in the collection tank, with 5 cm of water above (Fig. 72).

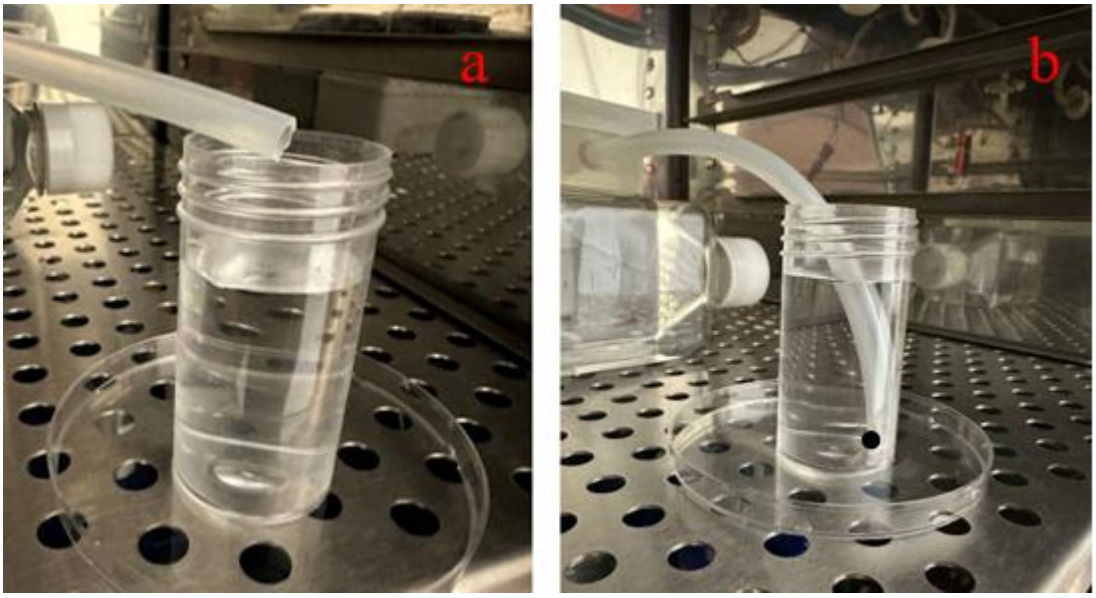

Figure 72: different experimental set up a) atmospheric pressure b) under 5 cm of H2O

4.3 Results

Scaffold characterizaiton

The prepared scaffolds have a hollow cylindrical geometry (Fig.73) with an outer diameter of 1 cm, an inner diameter of 0.6 cm, and a length of 2 cm.

Figure 73: Scaffold Geometry before and after refining the circular bases

Upon extraction from the sample holder, the bases of the cylinder appear irregular. Therefore, after the drying process is complete, a scalpel is used to standardize the cylindrical shape and ensure a uniform length of 2 cm (Fig. 74).

Figure 74: Scaffold dimensions respect to 50 cents coin.

SEM (Scanning Electron Microscopy) analyses were conducted to assess the morphology and pore size of the scaffolds. The scaffold was sectioned transversely to examine the cross-section and longitudinally to observe the internal lumen. The porous matrix visible in the cross-section is shown in Fig. 75.

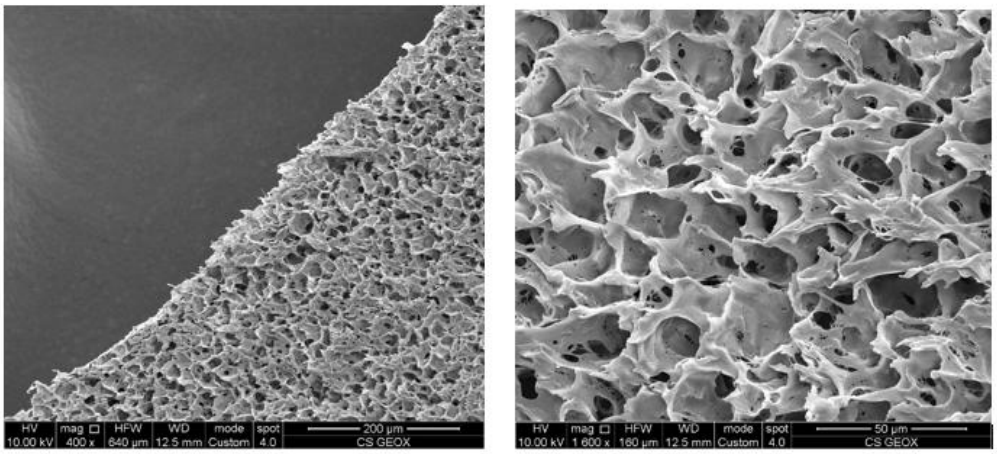

Figure 75: SEM Analysis of the Scaffold Cross Section. On the left: magnification 400x scale bar 200 µm; on the right magnification 1600x scale bar 50 µm

The pore sizes range from 15 to 25 micrometers, displaying an architecture with fully open and interconnected pores. This morphology is ideal for allowing the culture medium to reach the scaffold's lumen, where the cells are located. Fig. 76 shows the internal lumen of the scaffold.

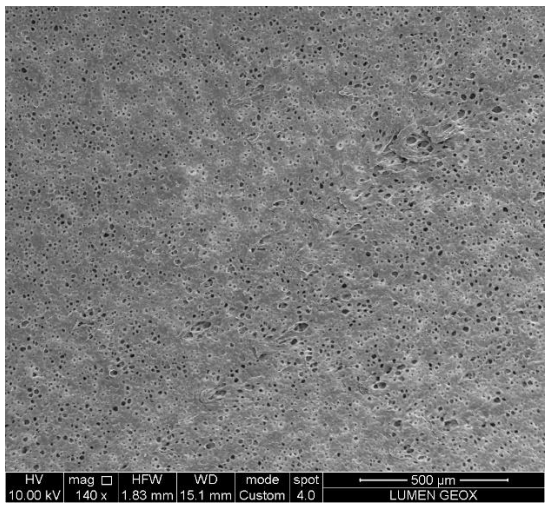

Figure 76: internal lumen pore architecture (SEM) (mag 140x ; scale bar 500µm)

On the luminal surface of the scaffold, the presence of pores is evident, which are fundamental for facilitating communication between the exterior and interior environments of the scaffold. These

pores exhibit distinct morphological characteristics compared to those observed in the cross-section. In the lumen, the pores are smaller, allowing cells to proliferate without penetrating into the pore structures. Importantly, these pores enable the perfusion of culture medium through the cross-section, delivering essential nutrients to the cells. However, they effectively prevent cellular migration into the scaffold's bulk, maintaining the scaffold's structural integrity and functional efficacy.

Bioreactor design Optimization

The selection of the final prototype of the bioreactor resulted from an in-depth design phase of the main chamber and connectors. Prototyping these components was crucial to meet the previously mentioned requirements that the bioreactor must possess. Below are the development phases of this design. The initial design phases of the bioreactor included the creation of various models, as shown in Fig. 77.

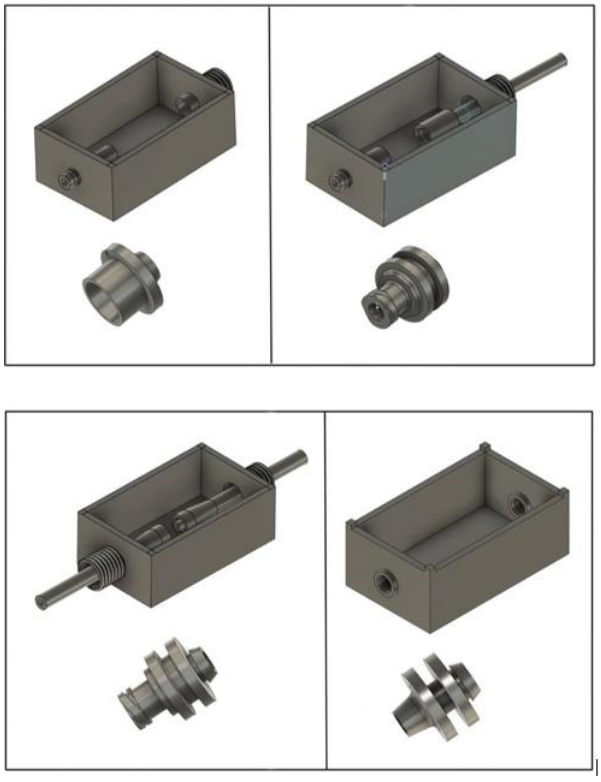

Figure 77: different bioreactor and connectors prototype designs created on Fusion 360

The selection of the final prototype resulted from an in-depth analysis of various components obtained through 3D printing. Among the various prototypes, two were particularly noteworthy. The first prototype features a main chamber with a rectangular base geometry. The dimensions of the chamber, which is designed to contain the scaffold and the cell culture medium, are:

• a = 70 mm (base length) • b = 40 mm (base width) • c = 25 mm (height)

These dimensions are illustrated in the following figure (Fig. 78).

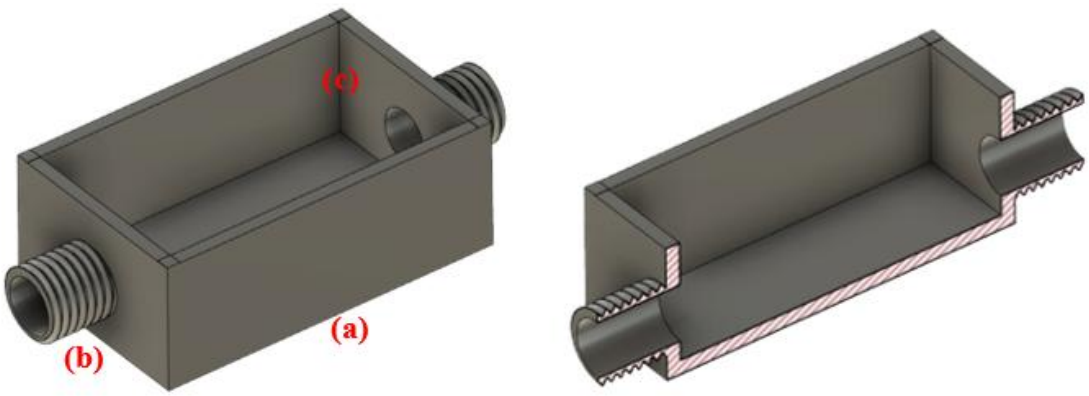

Figure 78: definitive geometry, prototype of the main chamber

The side walls contain openings through which rods pass. These rods are hollow and can be screwed into the scaffold, which is previously placed inside the chamber. It was necessary to add two threads externally to the chamber to ensure the tightening of the hollow rods and the integrity of the system. This tightening was achieved with the assistance of two Pyrex caps provided with a rubber ring seal (Fig. 79).

Figure 79: Pyrex caps

The cap features a hole through which the hollow rod passes, and an internal thread that mates with the bioreactor.

The hollow rod (Fig. 80) has a thread (male lock) at its end, allowing it to connect with the connector attached to the scaffold. This configuration enables the direction of airflow into the internal lumen of the scaffold.

Figure 80: hollow rod design and cross section

The connector, shown in Fig. 81, has been designed to enable coupling to the system by screwing into the hollow rods.

Figure 81: connector design

One side of the connector features a female thread that screws into the rod, while the other side has a fitting that inserts into the internal lumen of the scaffold. This fitting ensures optimal coupling with the scaffold. To guarantee maximum sealing in this coupling (connector-scaffold), glue is applied.

Grooves were added to the connector to allow for a secure grip with pliers, facilitating assembly under sterile conditions. Additionally, an internal channel was incorporated to allow airflow. The next image shows the connectors glued to the scaffold (Fig. 82).

Figure 82: real dimensions of scaffold glued with connectors

In the following image (Fig. 83), the CAD models of the coupling between the connector and the hollow rod can be observed.

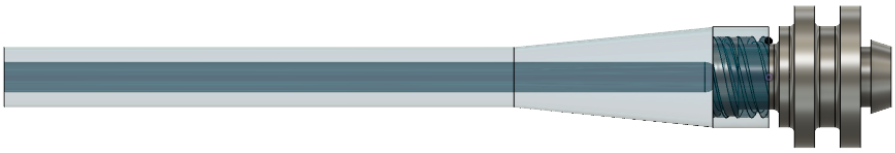

Figure 83: CAD of the Coupling between the Hollow Rod and Connector

The hollow rod is inserted into the hole of the Pyrex cap, screwed into the scaffold, and then secured by screwing the cap onto the main chamber. The system is symmetric, so the same operations are performed on the opposite side. This configuration is shown in the following image (Fig. 84).

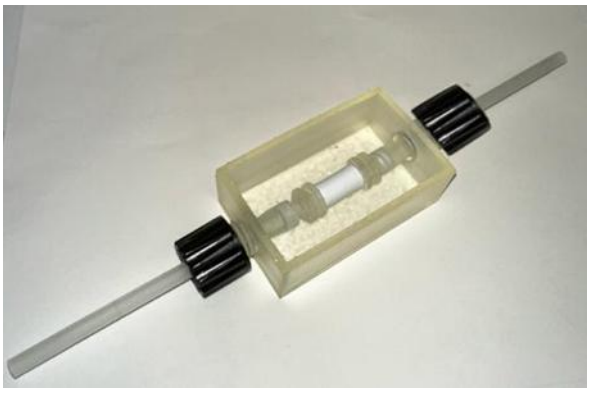

Figure 84: bioreactor assembly

One of the two rods is connected upstream to a peristaltic pump, which generates airflow into the scaffold's lumen. However, the coupling between the hollow rod and the connector does not guarantee a perfect seal, prompting the development of a different design to address this issue.

Alternative Prototype Design

A detailed analysis was conducted on another prototype (Fig. 85). This design resulted from the optimization and simplification of the previously described system. During the design phase, the threads were removed from the connectors, and the hollow rods were replaced with silicone tubes.

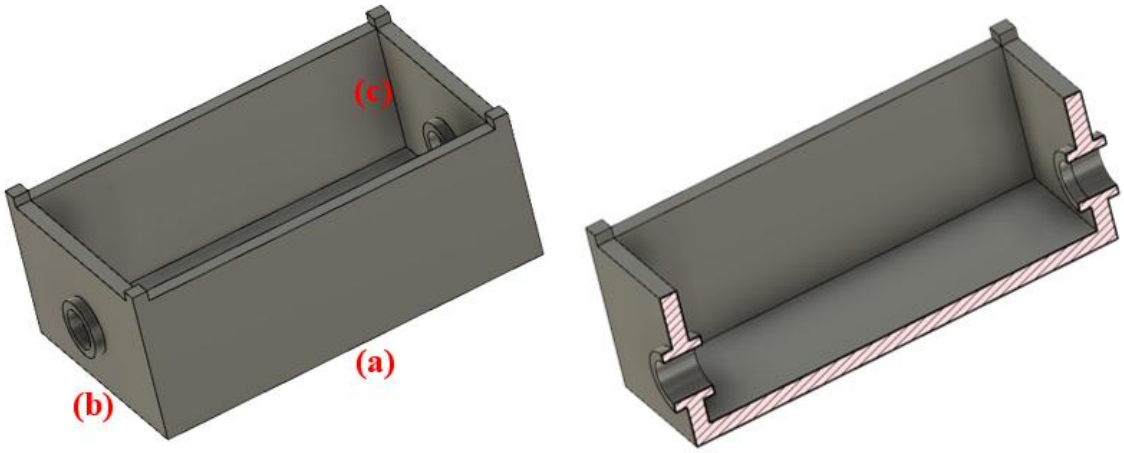

Figure 85: Geometry and Characteristic Dimensions (a, b, c) of the Main Chamber

The main chamber of the bioreactor was modified by removing the external threads while maintaining the previously mentioned dimensions (a, b, c). The new design features two holes through which silicone tubes pass. The diameter of these holes is 7.7 mm, slightly smaller than the tube diameter (8 mm) to ensure an effective fit that prevents leakage of the culture medium. This coupling is illustrated in the next image (Fig. 86).

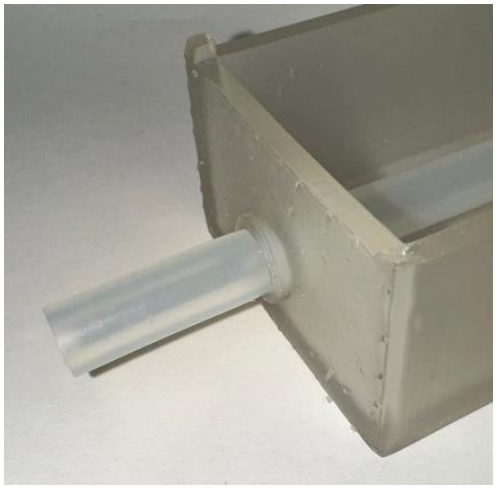

Figure 86: Coupling between the Main Chamber and Silicone Tube

The connectors glued to the scaffold no longer have threads but feature simple fittings on both the scaffold side and the tube side, as shown in Fig. 87.

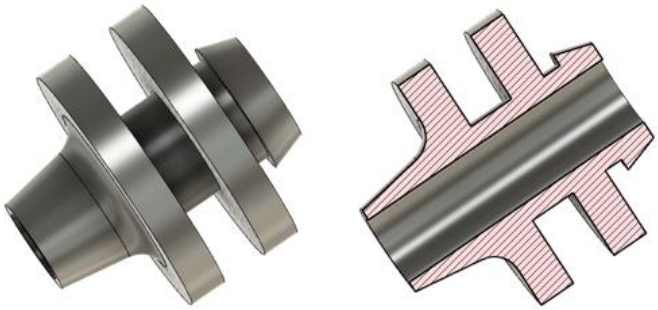

Figure 87: CAD of the Connectors

The silicone tube fits snugly over the connector, expanding during insertion to ensure a tight seal (Fig. 88).

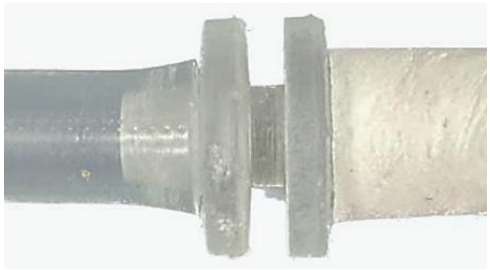

Figure 88: silicon tube-connector coupling

The presence of grooves, which facilitate the handling of the scaffold under sterile conditions, remains unchanged. The assembly (Fig. 89) involves inserting the silicone tube into the hole in the chamber and attaching the tube to the connector glued to the scaffold. This system is symmetric, so the same operation can be performed on the opposite side. One of the two tubes is connected to a peristaltic pump, which ensures airflow throughout the entire circuit, passing through the first tube, then the scaffold, and finally the second tube, which serves as the discharge outlet.

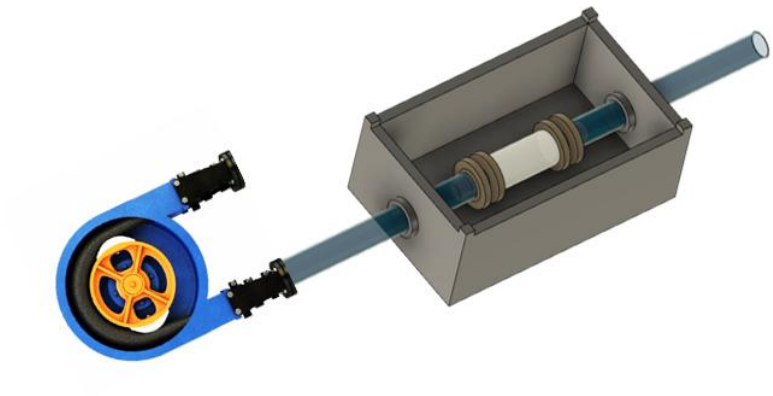

Figure 89: Peristaltic pump and bioreactor set up

In the following image (Fig. 90), the longitudinal section of the system can be appreciated, showing the airflow path generated by the pump. Externally, the scaffold is surrounded by culture medium (or water in preliminary tests).

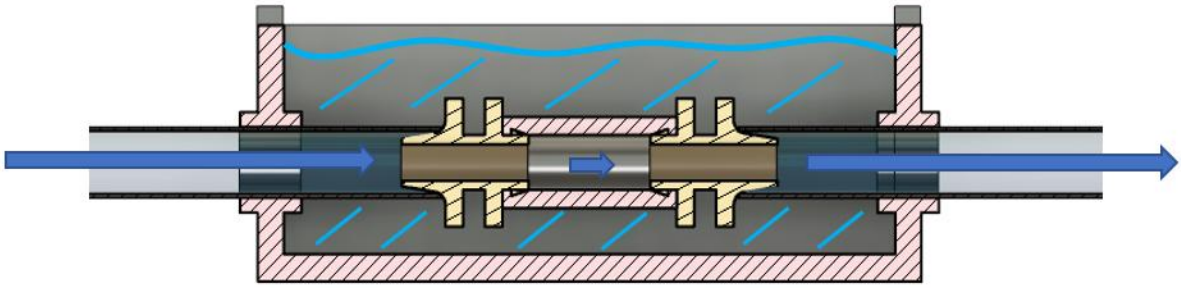

Figure 90: Bioreactor Operation Diagram, cross section

A lid was necessary to design the system to place the bioreactor in an incubator while maintaining the chamber's sterility. The chamber has raised edges at the four corners, allowing the lid to rest without creating an airtight seal, which would be fatal for any cell culture, and preventing condensation problems. The lid's geometry mirrors that of the main chamber (Fig. 91).

Figure 91: Main Chamber with its Lid

The system's simplification was appropriate to facilitate assembly operations under sterile conditions. Additionally, using silicone tubes ensured maximum sealing compared to the previous prototype, where the coupling between the connector and hollow tube, both 3D printed using stereolithography with the same material (clear resin V4), did not provide optimal sealing. The coupling of components printed with the same resin did not guarantee maximum sealing for the bioreactor prototypes requiring such tightening.

Prototyping the Seeding Tool

Since the connectors cannot be glued after seeding, a seeding protocol was needed that included the connectors already glued to the scaffold. To facilitate the biopsy insertion, tools were designed to spread the biopsy evenly throughout the scaffold's lumen.

Figure 92: Cell Seeding Tools: (a) Cell Collection, (b) Seeding into the Lumen

The previous image (Fig. 92) shows: (a) The rod through which the biopsy can be collected, and (b) the rod that allows it to be seeded into the scaffold. The first rod (a) has a tip geometry that facilitates biopsy collection, while the second rod (b) has a spherical head that enables the cells to be "spread"

within the scaffold's internal lumen. The rod lengths (5 cm) and the tip sizes (2-3 mm) were chosen to allow easy maneuvering and insertion through the connector. The following image schematically represents the method through which the cells are inserted into the scaffold (Fig. 93).

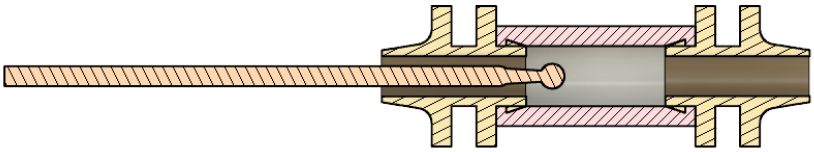

Figure 93: Seeding scheme

The aim of this project is to evaluate the radial flow of medium through the scaffold. The pressure difference between the inside and outside of the scaffold induces a radial flow through the matrix, which was assessed following variations in the pump voltage. Several experimental setups were studied to achieve a balance between the diffusion of medium from the outside into the lumen and the opposition mediated by the air flow.

Characterization of the Bioreactor: Static Diffusion Tests

The static condition was imposed by the absence of the peristaltic pump. The system depicted in the following image (Fig. 94) shows a schematic of the experimental setup in which the scaffold is immersed in water with added dye under static conditions.

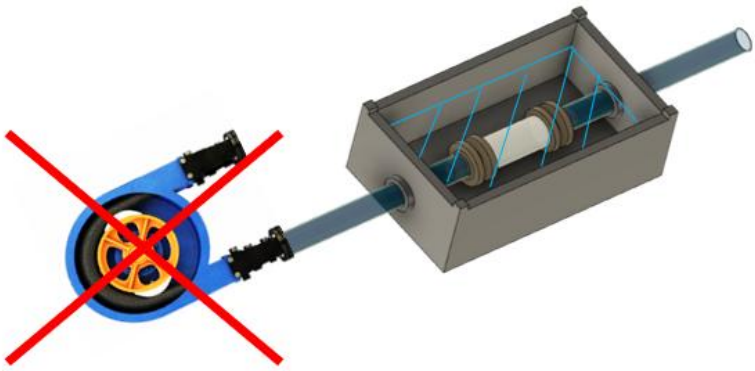

Figure 94: Schematic of Diffusion under Static Conditions

In the absence of the peristaltic pump, the pressure in the scaffold's internal lumen equals atmospheric pressure since both ends of the silicone tubes are open. Conversely, the pressure outside the scaffold is higher than atmospheric pressure due to the additional hydrostatic pressure component generated by the water above (ρgh with h being the fluid head above the scaffold). Consequently, the liquid permeates through the scaffold walls and flows into the lumen. The following image (Fig. 95) shows how the dye diffuses depending on immersion times, through a cross-section of the scaffold.

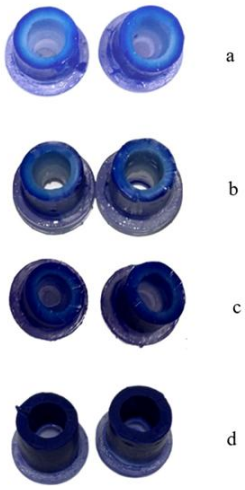

Figure 95: Diffusion Tests under Static Conditions at: a) 10 min, b) 20 min, c) 30 min, d) 40 min

It can be observed that for short times (a = 10 min), the water with dye does not diffuse to the scaffold's internal lumen, which remains white. For longer times (d = 40 min), the dye permeates through the entire thickness of the scaffold, fully coloring the section. Figure 56d shows that for times equal to or greater than 40 minutes, the fluid diffuses through the entire thickness of the scaffold, spilling into the internal lumen. This is not optimal for the presence and survival of the respiratory mucosa cells seeded, as they must constantly experience the airflow generated by the pump and derive nourishment from the scaffold bulk, where an optimal balance is sought to avoid such fluid overflow.

Characterization of the Bioreactor Airflow Rates

The airflow rates obtained from the pump characterization were evaluated in m^3/s .

The trend is rather linear, as represented in the graph in Fig. 96. The voltage is shown on the x-axis, and the corresponding airflow rates are displayed on the y-axis.

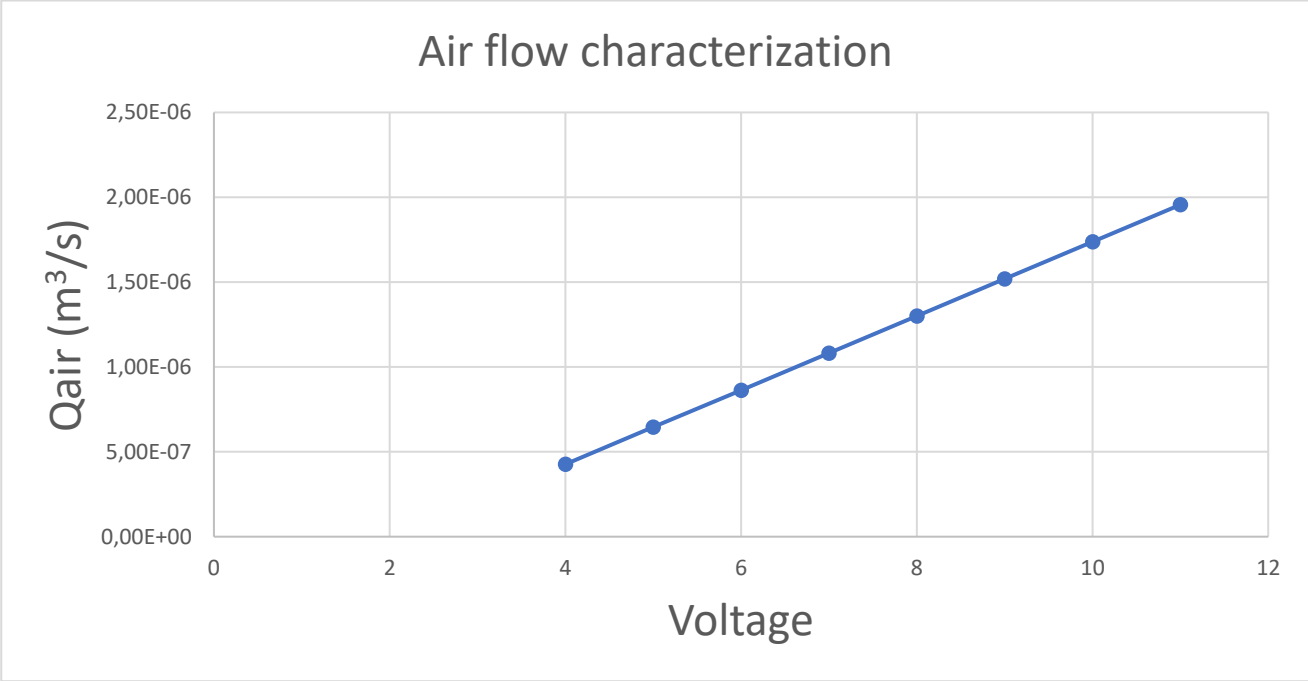

Figure 96: Power Supply Voltage vs. Airflow Rate in m^3/s

Theoretical Evaluation of Radial Flow Rate

The culture medium must penetrate the porous matrix of the scaffold to ensure nourishment for the cells. To this end, a balance must be maintained under steady conditions between the external pressure and the pressure inside the scaffold lumen. An initial approach to studying the system's fluid dynamics was purely modeling-based: Bernoulli's equation (3) was used to determine the internal pressure immediately downstream of the scaffold. This pressure value allowed us to derive the radial flow rate through the porous matrix using Darcy's law.

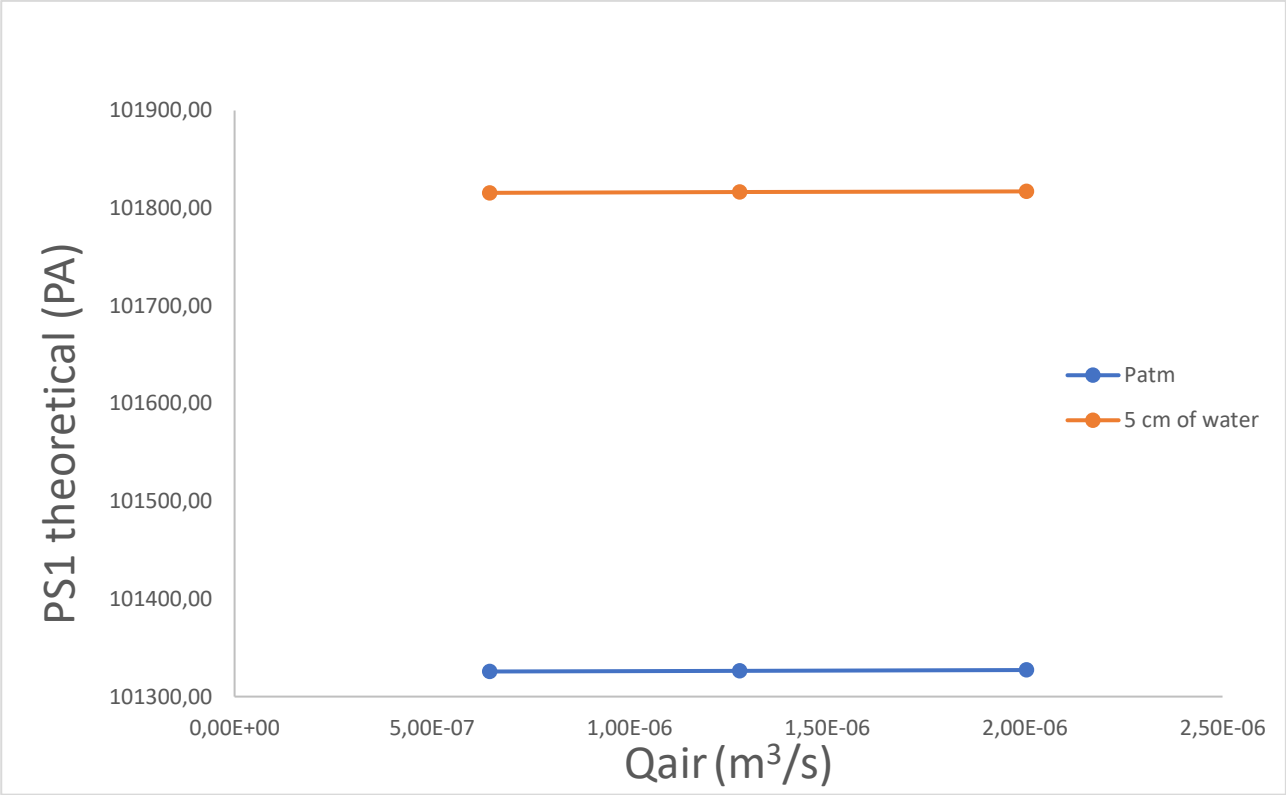

Figure 97: Airflow Rate vs. Theoretical Pressure

The previous graph (Fig. 97) shows the variations in pressure downstream of the scaffold as the airflow rate (Q_air) through the scaffold changes. Two cases were analyzed: one where the outlet is at atmospheric pressure (blue curve) and another where it is under a liquid head of 5 cm (orange curve). In both cases, the variation in airflow does not significantly affect the pressure value.

The graph in Fig. 98 shows the theoretical radial flow rates as a function of the airflow rate for the two cases described above. It illustrates the difference in behavior when the system has the outlet at atmospheric pressure or under a liquid head.

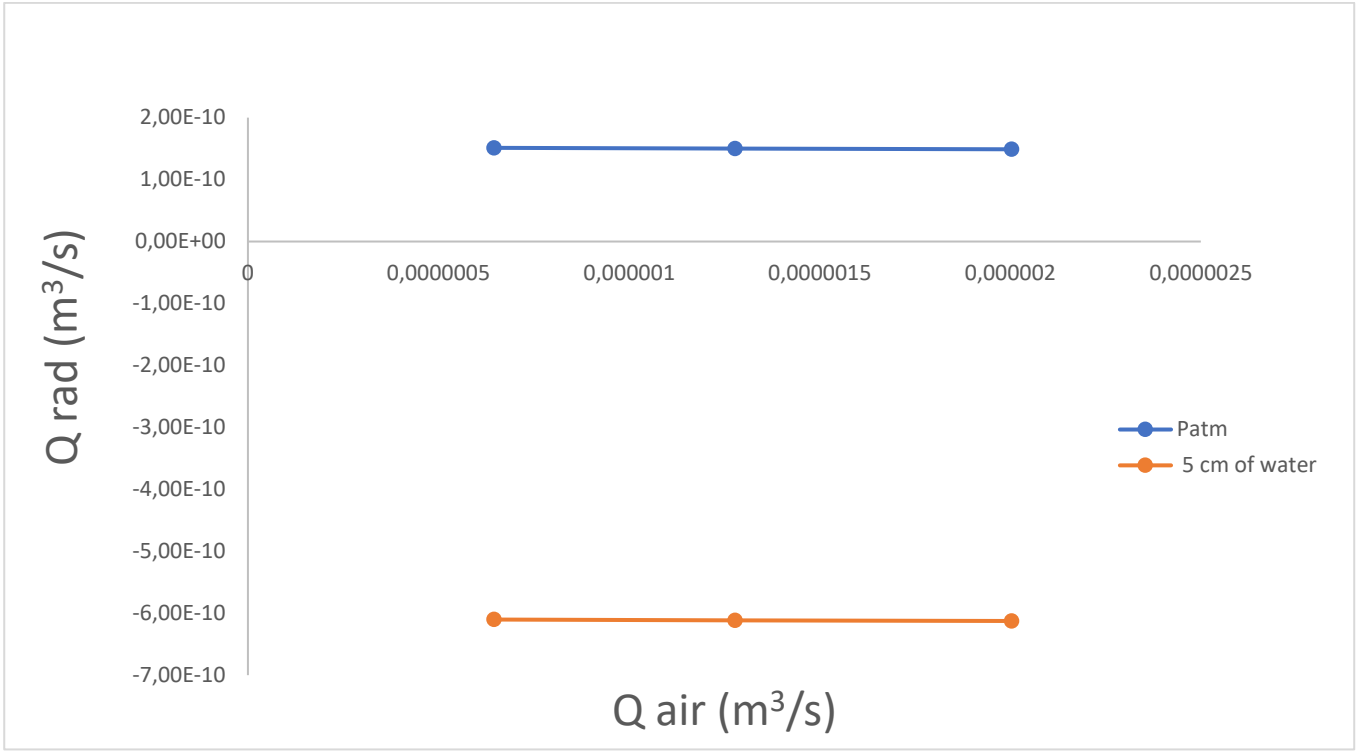

Figure 98: Airflow Rate vs. Radial Flow Rate (Theoretical Analysis)

It is observed that when the outlet is at atmospheric pressure (blue curve), there is a fluid flow from the outside to the internal lumen of the scaffold. This scenario is undesirable, as the mucosal cells should be exposed only to air at the internal lumen level. When a liquid head is present (orange curve), the direction of radial flow reverses due to a negative pressure gradient between the inside and outside of the scaffold. The presence of the liquid head increases the internal pressure of the scaffold above the external pressure, explaining the negative radial flow rate. This indicates a theoretical reversal of the radial flow direction, now occurring from the inside to the outside.

Experimental Evaluation of Radial Flow Rate

The theoretical determination of radial flow rates revealed that they occur due to a very small pressure difference (ΔP of a few tens of Pascals). Therefore, the dynamic equilibrium generated can be subject to changes due to minimal variations in the experimental setup. Given this, the previously described modeling analysis, which considered only the internal pressure calculated downstream of the scaffold,

was deemed insufficient. An experimental analysis was conducted to more accurately evaluate the pressures at the ends of the scaffold, obtaining a more reliable pressure value. This analysis used pressure sensors placed as close as possible to the ends of the scaffold. New values were obtained at different airflow rates for both configurations previously analyzed. These values (PS1 upstream pressure and PS2 downstream pressure) were averaged and used again in Darcy's relation. The recorded pressure trends are shown in the following Figs. 99-100.

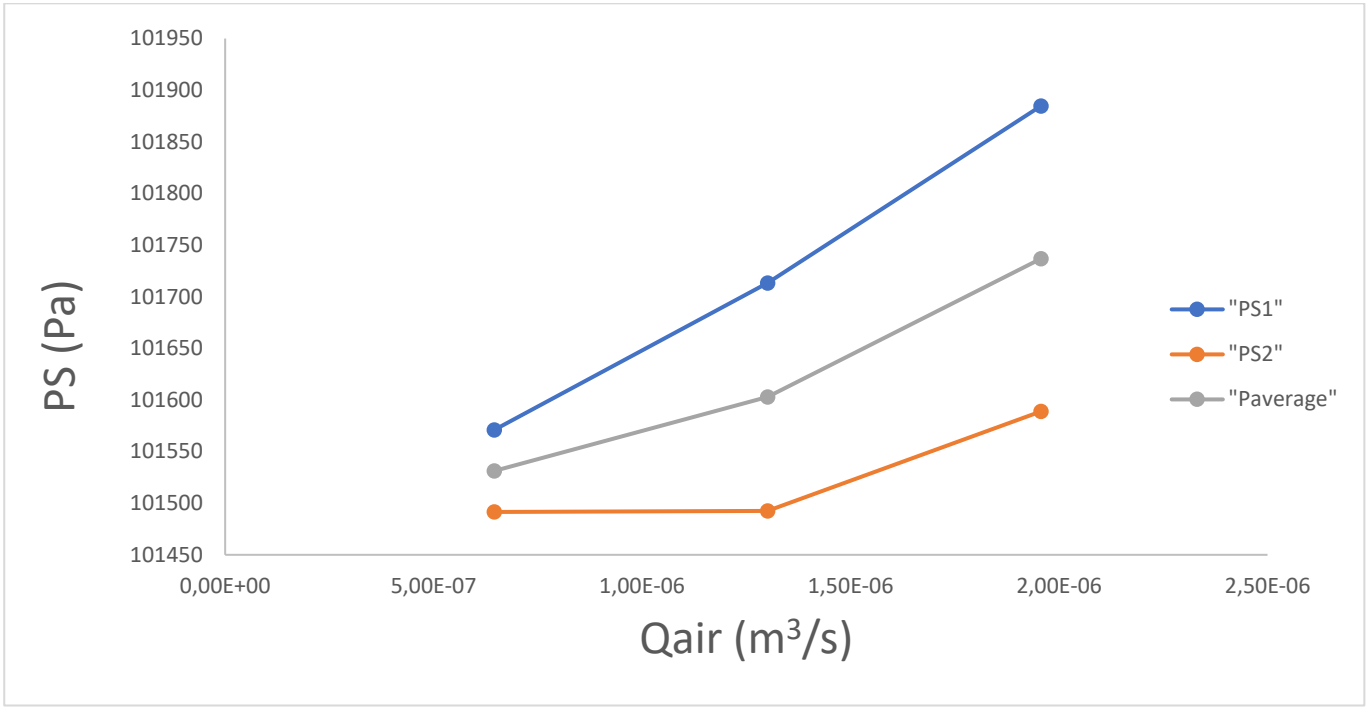

Figure 99: Sensor-Read Pressure vs. Airflow Rate (Outlet at Atmospheric Pressure

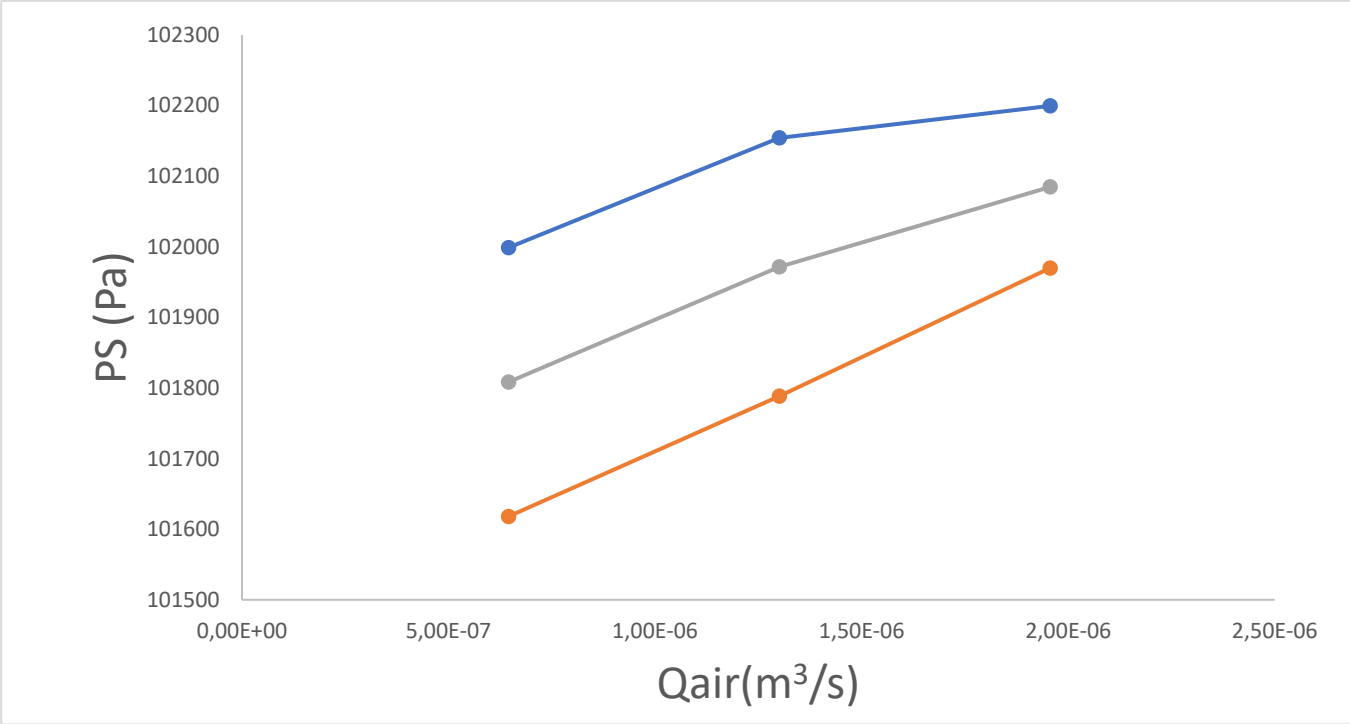

Figure 100: Sensor Pressure detected vs air flow rate (under 5 cm of water)

Fig. 99represents the variation in pressures read by the sensors when the outlet is at atmospheric pressure: their trend increases with increasing airflow rate. Fig. 100 shows the variation in the same pressures when a liquid head is applied to the outlet. The trend is similarly increasing, with higher average pressure values compared to the previous case. Unlike the theoretical analysis, where the pressure trend is fairly constant with varying Q_air, the experimental analysis showed a much more marked pressure dependence on airflow rate.

The next figure (Fig. 101) shows how the radial flow rate, derived from Darcy's relation, varies with the airflow rate. These trends indicate a progressive decrease in radial flow rate correlated with the described increase in internal pressure. Notably, in this case, a radial flow from the inside to the outside is observed, at least theoretically, under both conditions.

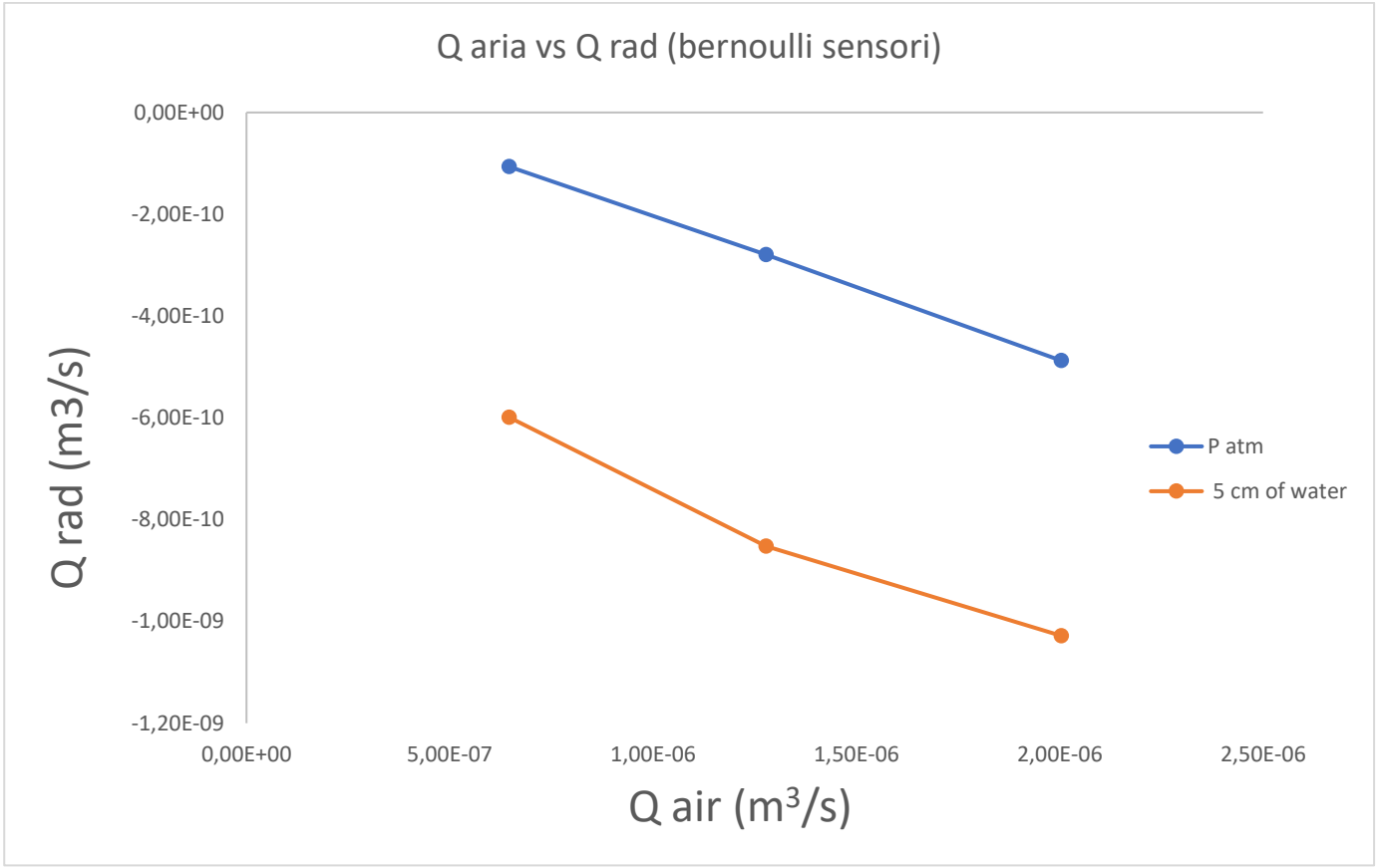

Figure 101: Airflow Rate vs. Radial Flow Rate (Experimental Analysis)

The subsequent graphs (Fig. 102-103) compare the radial flow rates evaluated through the theoretical model (2) and the experimental model (5 and 6) in the two configurations: outlet at atmospheric pressure (Fig. 102) and with a liquid head (Fig. 103).

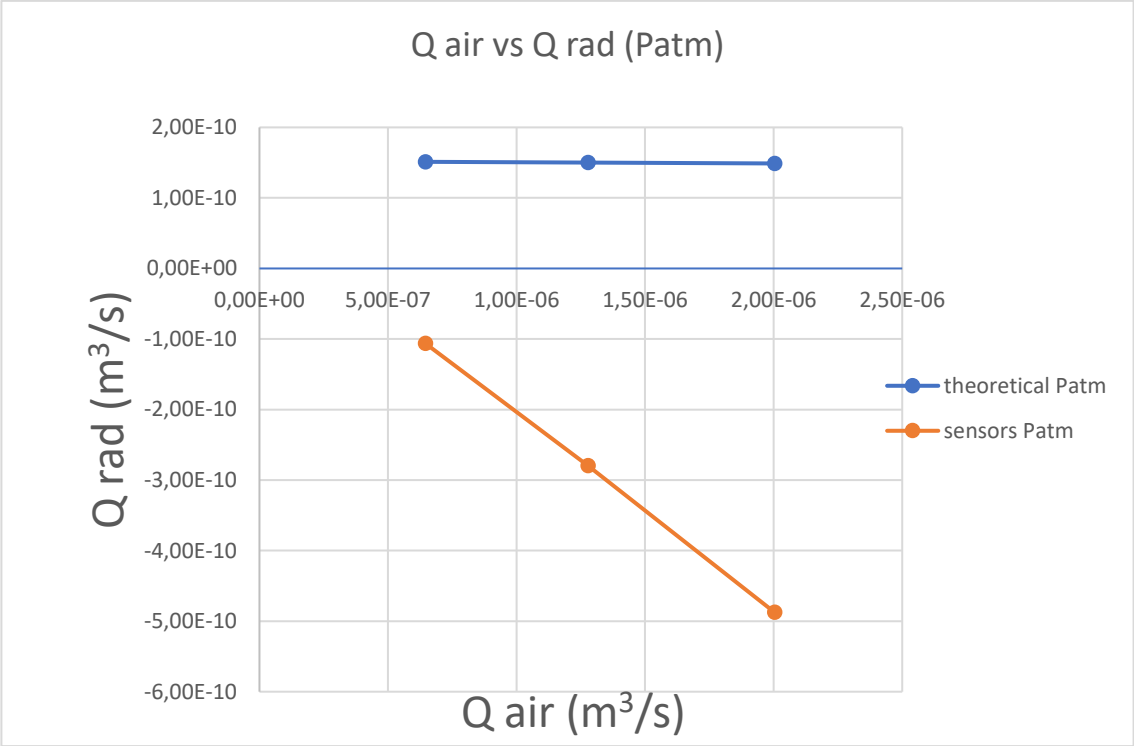

Figure 102: Airflow Rate vs. Radial Flow Rate (Outlet at Atmospheric Pressure)

As mentioned, the purely theoretical evaluation shows positive radial flow rates; this would result in the culture medium spilling into the scaffold's internal lumen. This circumstance, as previously discussed, is to be avoided. The experimental tests, however, show that the radial flow rate is always less than zero. The following graph shows the radial flow rate as a function of the airflow rate when the outlet is under a 5 cm liquid head.

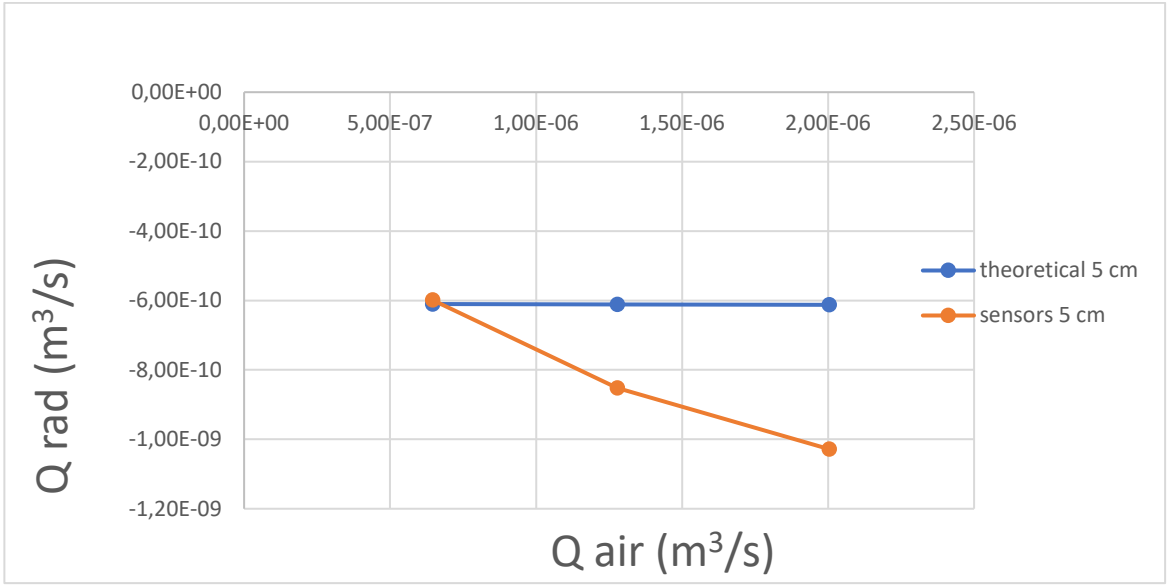

Figure 103: Airflow Rate vs. Radial Flow Rate (Outlet under 5 cm Liquid Head)

In both cases, theoretical and experimental, the radial flow rates are negative. In this case, the dependence of the radial flow rate on the airflow rate is evident. The condition closest to the desired one, i.e., permeation through the porous matrix without the culture medium spilling into the lumen, is undoubtedly that observed using pressure sensors where the outlet is at atmospheric pressure (Fig. 106, blue curve). It shows that when the system has an open outlet and low airflow rates, the radial flow rate is closer to zero, but not positive.

Dynamic Diffusion Tests

The experimental measurement of the radial flow rate presented several challenges, mainly due to the difficulty of accurately assessing the small quantities of liquid leaking through the internal lumen. Dealing with liquid flow rates on the order of microliters per minute, the solution was to conduct experiments over several hours to obtain a measurable quantity of liquid without encountering uncertainties due to the intrinsic sensitivity of the used balance.

To address this, several precautions were taken. The long duration of these tests could lower the liquid head above the scaffold, causing issues:

Pressure Gradient Variation: The variation in the head height (h) affects the hydrostatic pressure contribution (ρgh), altering the pressure gradient between the inside and outside of the scaffold.

Partial Submersion: The scaffold might be partially submerged and partially exposed to air, rendering diffusion tests ineffective since fluid flow through the entire external surface of the scaffold is necessary. To maintain a constant head level, a second, larger container than the bioreactor was used. A lateral connector was inserted, connecting the bioreactor chamber to the external tank via a silicone tube (Fig. 104).

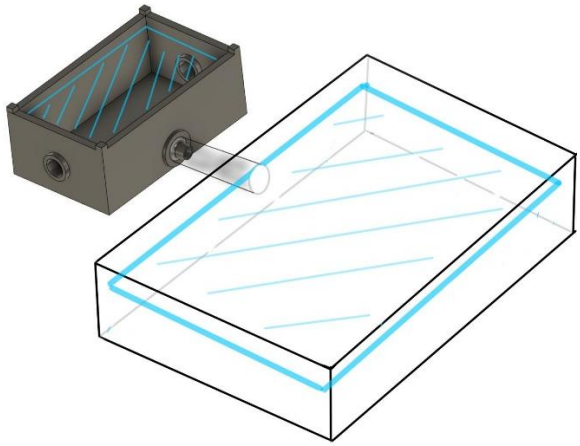

Figure 104: Schematic of the Connection between the Bioreactor Main Chamber and External Tank

Using the principle of communicating vessels, the water level in the additional tank matches that in the bioreactor's main chamber, allowing constant head tests above the scaffold.

The following image (Fig. 105) shows the radial flow rate Q (µl/min) obtained with the outlet at atmospheric pressure and under a liquid head, relative to the airflow rate Q_air (ml/min) generated by the pump.

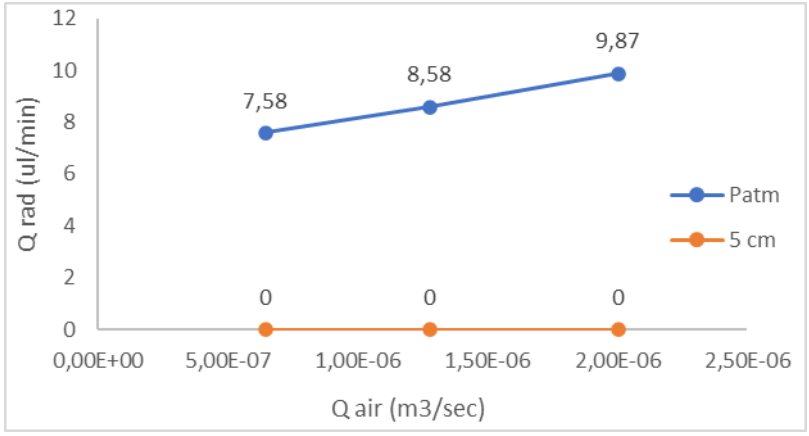

Figure 105: air flow vs empirical radial flow at atmospheric pressure (blu) and wit 5 cm of water (orange)

When the outlet was positioned under a water head (orange curve), no eluate was recorded at all tested airflow rates, allowing the estimation of the radial flow rate to be null. This result is consistent with previous analyses. Surprisingly, with the outlet open to the atmosphere (blue curve), eluate was detected, indicating a flow from the exterior to the interior lumen that remained constant despite varying airflow rates. Although this finding aligns with purely modeling analyses, it contrasts with pressure sensor analyses. A possible explanation could be the presence of non-homogeneous regions in the scaffold, leading to micro-leaks within the porous matrix. Another potential explanation could be the experimental conditions within the incubator, which are easily perturbed in terms of humidity and temperature. Therefore, modifications to the experimental setup and an increase in statistical analysis by examining more samples will be necessary to achieve more accurate measurements. Nonetheless, it is reassuring that the experimentally measured magnitudes are consistent with the predicted ones.

4.4 Discussion

In this study, a bioreactor for cultivating respiratory mucosa tissue was designed, prototyped, and characterized, demonstrating its potential in simulating *in vitro* bronchial mucosa conditions under both static and dynamic environments. This system offers significant advantages over traditional two-dimensional models by introducing controlled airflow and radial culture medium flow, closely mimicking in vivo conditions. Our findings align with previous research emphasizing the importance of bioreactors in tissue engineering to maintain physiological conditions necessary for cell growth and differentiation (Lim et al., 2022b)

The primary objective of this bioreactor design was to replicate the physiological conditions of bronchial tissue, necessitating precise regulation of both air and culture medium flow. Airflow rates, controlled via a peristaltic pump, exhibited a linear relationship with voltage input, allowing for flexible adjustments to optimize the environment for cell growth and tissue simulation. However, discrepancies arose between theoretical and experimental radial flow rates. Theoretical analyses suggested minimal internal pressure differences, potentially leading to undesirable radial flow from the scaffold's exterior to its interior under static conditions. Conversely, experimental observations under atmospheric pressure indicated that radial flow rates remained constant across varying airflow rates. These inconsistencies may result from experimental limitations, such as micro-leaks within the scaffold matrix or environmental factors like humidity and temperature, which can influence fluid dynamics. Similar challenges have been reported in previous studies on lung tissue bioreactors, highlighting the need for precise control over airflow and pressure gradients (Panoskaltsis-Mortari, 2015)

Static diffusion tests provided valuable insights into scaffold permeability, revealing that diffusion of the culture medium into the internal lumen increased over time, supporting the necessity of a pressure difference to achieve efficient nutrient flow to the cells. However, theoretical radial flow rates under liquid head conditions demonstrated reversed flow direction, which is undesirable as it could lead to leakage of culture medium into the internal lumen, potentially disrupting cellular nutrient intake and metabolic processes. While theoretically undesirable, our experimental data under atmospheric pressure showed minimal and constant radial flow, suggesting that the scaffold's structure may exhibit areas of non-uniform porosity, contributing to uneven diffusion and potential micro-leakages. Variations in scaffold permeability are a known issue in tissue engineering, as scaffold architecture significantly impacts nutrient transport and cellular behavior (Ndongo Sonfack et al., 2024)

Several challenges were encountered during the experimental phase, particularly in controlling and measuring low-volume flow rates in the microliter range. These small flow rates are susceptible to fluctuations due to environmental factors such as temperature, humidity, and the experimental apparatus setup. Maintaining a constant water head level in the external tank to stabilize the pressure gradient further emphasized the system's sensitivity. Despite these challenges, our measurements provided consistent results with theoretical predictions, suggesting that with refined experimental setups and better statistical sampling, more accurate results can be achieved. Advances in bioreactor

automation and real-time monitoring systems, such as those proposed by Lim et al. (2021), could help mitigate these issues by ensuring better control over experimental variables (Lim et al., 2022b)
In future studies, it is essential to refine the bioreactor design to minimize scaffold micro-leakages and ensure homogeneity in permeability across the matrix. Additionally, improving the accuracy of low-flow rate measurements will enhance understanding of the dynamic behavior of nutrient flow through the scaffold. Further studies on the effect of scaffold material and porosity on flow rates will contribute significantly to optimizing bioreactor performance (J. Zhao et al., 2016b).
The system presented in this study shows great promise as a tool for studying respiratory system diseases, such as cystic fibrosis, chronic obstructive pulmonary disease (COPD), and asthma. The ability to simulate both airflow and nutrient dynamics inside a three-dimensional scaffold opens new opportunities for drug testing, disease modeling, and tissue regeneration. Similar approaches have been explored for oral and craniofacial tissue engineering, where bioreactors have played a crucial role in optimizing tissue maturation and functionality (Huri et al., 2015)
Further optimization of scaffold material and structure could improve the system's physiological relevance, enabling better modeling of bronchial mucosa and its response to disease or therapeutic interventions. The integration of patient-specific bioreactor designs, as suggested in recent literature, could enhance personalized medicine approaches in respiratory research (Yu et al., 2020)
While the bioreactor design presented in this study provides valuable insights into the flow dynamics of air and culture medium, further refinements are needed to achieve a more reliable and reproducible system. Continued advancements in scaffold materials, experimental controls, and fluid dynamic modeling will pave the way for more accurate and effective in vitro models for respiratory tissue research.

4.5 Conclusion

This study has demonstrated the feasibility of a bioreactor system that closely mimics *in vivo* bronchial mucosa conditions, providing a controlled environment for airflow and nutrient flow. The findings highlight the system's potential for advancing respiratory tissue engineering by offering a more physiologically relevant platform than traditional two-dimensional models. Despite challenges related to scaffold permeability, micro-leakages, and flow rate control, our results suggest that these limitations can be mitigated through further refinement of experimental setups and bioreactor design.

Future work should focus on optimizing scaffold architecture to ensure uniform permeability, improving measurement accuracy for low-volume fluid dynamics, and integrating automated control systems for enhanced reproducibility. Additionally, expanding the application of this bioreactor model to study disease mechanisms, drug responses, and regenerative therapies could significantly contribute to the field of respiratory medicine. Continued advancements in biomaterials and bioreactor technologies will be crucial in realizing the full potential of in vitro respiratory tissue models for clinical and pharmaceutical applications.

Dynamic devices for TE applications

Bioreactors play a pivotal role in Tissue Engineering providing a controlled environment that closely mimics *in vivo* conditions, thus promoting cell growth and tissue formation. These bioreactors facilitate the systematic study of cellular responses to mechanical and biochemical cues, which is essential for developing functional tissue constructs.

The application of dynamic devices in tissue engineering has been extensively studied over the past two decades. For instance, perfusion systems have been employed to enhance the formation of bioengineered autologous cardiac muscle grafts by providing mechanical stretch regimens(Wang et al., 2021) . Similarly, rotating wall vessels (RWVs) have been used to grow three-dimensional cartilage constructs by simulating microgravity conditions. These bioreactors create a microgravity environment that allows neural cells to grow in three dimensions, closely mimicking the natural environment of the brain and spinal cord (Palladino et al., 2024).

Dynamic bioreactors offer several advantages over static culture systems. Continuous medium circulation ensures uniform nutrient distribution and waste removal, providing a more physiologically relevant environment for cell growth and tissue formation. The application of mechanical forces promotes cell alignment, differentiation, and tissue maturation, which are crucial for the development of functional tissue constructs (Gunduz et al., n.d.).

Recent advancements in bioreactor technology have focused on incorporating automated procedures and real-time monitoring of environmental factors such as pH, oxygen levels, and nutrient concentrations. These advancements are expected to further enhance the ability of bioreactors to mimic physiological pathways and improve outcomes in tissue engineering and regenerative medicine (Kaya, 2023). Research has shown that organoid bioreactors can successfully model complex tissue structures, like organogenesis in a dish, thereby providing valuable insights into disease mechanisms and treatment (Lancaster & Knoblich, 2014). Additionally, living organoid biobanks have been derived from colorectal cancer patients to facilitate personalized medicine approaches (Van De Wetering et al., 2015).

In conclusion, dynamic bioreactors are essential tools in tissue engineering, providing a controlled environment that promotes cell growth and tissue formation. Their ability to mimic in vivo conditions and provide mechanical stimulation makes them invaluable for developing functional tissue

constructs. As technology continues to advance, dynamic bioreactors are expected to play an increasingly important role in regenerative medicine.

5. *Project: Mini Air lift bioreactor*

This project contains unpublished data, data from Capuana et al., 2024 (Capuana et al., 2024) and data from Ferraro et al., 2024 (Ferraro et al., 2024), where I am the 2nd and 4th author, respectively. My contributions included scaffold fabrication, HA characterization and incorporation, scaffold characterizaion, bioreactor design and prototyping, cell culture. The mini air lift bioreactor project is the result of a collaboration between the Anatomy Institute of Paracelsus Medical University of Nurenberg (Germany), where I had the pleasure of passing my PhD period abroad, supervised by Prof. Gundula Schulze and Istituto Ortopedico Rizzoli with Dr. Angela De Luca and Dr. Gianluca Giavaresi. Furthermore a special thanks to Dr. Elisa Capuana for her precious help with CFD simulation.

5.1 Introduction

Osteochondral defects, involving damage to both articular cartilage and the subchondral bone, remain a significant challenge in regenerative medicine. These injuries often result from trauma, degenerative diseases, or congenital disorders and are particularly difficult to treat due to the limited regenerative capacity of cartilage and the structural complexity of the osteochondral interface. While surgical interventions such as microfracture and autologous osteochondral transplantation offer some relief, their long-term efficacy is often limited, with challenges such as insufficient integration, donor-site morbidity, and incomplete restoration of tissue functionality. These limitations underscore the need for innovative strategies to address osteochondral injuries (Middleton & Tipton, 2000; Mo et al., 2023).

Tissue engineering (TE) offers a promising alternative by combining scaffolds, cells, and bioactive signals to restore, maintain, or improve tissue function. A key component of TE is the use of porous scaffolds, which mimic the extracellular matrix (ECM) to support cell adhesion, proliferation, and differentiation. Unlike traditional two-dimensional (2D) cell cultures, these three-dimensional (3D) structures allow for the formation of functional tissues by fostering cell-cell and cell-matrix interactions and promoting the deposition of native-like extracellular matrix. Over the past few decades, bilayer scaffolds have emerged as an advanced strategy for osteochondral tissue engineering, as they enable the zonal regeneration of cartilage and bone through layers designed with specific pore architectures and properties tailored to each tissue type (H. W. Kim et al., 2004).

In this study, we investigated the potential of bilayer, i.e. two different pore size layer, scaffolds fabricated using Thermally Induced Phase Separation (TIPS) and filled with nanoparticles of Hydroxy Apatite (HA), a versatile technique for creating scaffolds with controlled pore size and porosity. These bilayer scaffolds were designed to replicate the native osteochondral interface, with a cartilage-mimetic layer featuring smaller pores to support chondrogenic regeneration and a bone-mimetic layer with larger pores to promote osteogenic differentiation. Recognizing the need to mimic the biomechanical environment of native tissues, dynamic culture systems were introduced as an alternative to static conditions. Dynamic culture systems, such as perfusion bioreactors, offer further advancements by providing controlled mechanical stimulation, uniform nutrient delivery, and enhanced oxygen transport, all of which are critical for achieving tissue maturation. However, the development and optimization of such systems remain a key challenge. This study contributes to the advancement of dynamic culture by exploring the scale-down and characterization of a custom-made "air-lift" bioreactor designed for efficient high-throughput analysis. An airlift bioreactor employs air or gas to circulate the culture medium within the vessel, ensuring efficient mixing and distribution of nutrients and oxygen. This low shear stress environment promotes the growth of microorganisms or cells, making it ideal for various bioprocess applications.

Building on previous research, which developed and characterized an external-loop airlift bioreactor, (De Luca et al., 2024) this research focuses on miniaturizing the system for improved scalability and cost-effectiveness. The redesigned bioreactor achieved a 70% reduction in height and an 80% reduction in the diameter of the perfusion chamber, while maintaining functional reliability. Computational Fluid Dynamics (CFD) simulations were employed to optimize the bioreactor's geometry, ensuring uniform fluid flow and efficient oxygen transfer. The scaled-down bioreactor also featured a scaffold support structure and a peristaltic pump for continuous nutrient perfusion.

This miniaturized system was designed to address challenges identified in earlier prototypes, such as non-uniform flow patterns, while aligning with the broader trends in tissue engineering toward miniaturization, scalability, and automation. These trends facilitate high-throughput testing of various cell types, scaffold designs, and culture conditions, enabling rapid evaluation of cellular responses and construct performance. The bioreactor allowed us to evaluate the performance of bilayer scaffolds under dynamic culture conditions, for the first evaluation a monoculture of L929 cells was used to asses the bioreactor fluid flow homogeneity. Then mesenchymal stromal cells (hMSCs) were cultured

for 7 days in dynamic and were monitored in terms of metabolic activity, colonization of the scaffold surface and section and histological analysis.
By combining advanced scaffold design with dynamic culture techniques, this project addresses key challenges in the field of osteochondral tissue engineering. It aims to offer a comprehensive solution for the regeneration of complex tissue interfaces, bridging the gap between experimental research and clinical applications. In future perspective a co.colture of hMSC and PACs will be evaluated.

5.2 Materials and Methods

Bilayer Scaffold Fabrication

The scaffolds were prepared starting from a ternary solution consisting of polymer /solvent /non-solvent. PLLA served as polymer, 1,4-dioxane (Sigma-Aldrich, Munich, Germany) represented the solvent and double distilled water was the non-solvent. The PLLA concentration was 6 wt% and the ratio of dioxane/water was 87/13 wt/wt for the unilayer scaffolds (100 µm pore size). The bilayer scaffolds were produced using 4 wt% PLLA. The weight ratio of the composite scaffold PLLA/Hydroxy Apatite (HA) was 95/5 wt/wt. First, the solution was sonicated at 60°C for 15 minutes at 35 kHz to evenly disperse the HA particles (10-100 µm). Subsequently, the solution was filled into cylindrical molds and submerged in a thermal bath with different TIPS time/temperature protocol:

1. PLLA-S (100 µm pore size, S=small) 15 min 25°C
2. PLLA-L (L=large, 250 µm pore size) 45 min 28°C
3. PLLA-HA 45 min at 28 °C (L, 250 µm pore size).

Then, a quench by pool immersion in an ethyl alcohol bath at a temperature of -20 °C for 15 minutes followed, freezing the structure. The bilayer structure was obtained by linking two disks of polymer matrices produced with different pore size and/or composition (PLLA-S and PLLA-L without/with HA) by gluing using dioxane. Finally, the foams were gently rinsed using deionized water for removal of any traces of dioxane and vacuum dried for 24 hours.

Scaffold Characterization

The morphology and thus, the size of the HA particles used were studied through an analysis made by MasterSizer2008 (Malvern Panalytical, Malvern, UK). Based on the measurements the distribution of particle diameters could be extrapolated.
Scaffold pore sizes, and particle distribution were observed using a scanning electron microscope (SEM, QUANTA 200F, FEI Company Philips, Thermo Fisher, Waltham, MA, USA) and a Micro-CT scanner (Skyscan 1272, Bruker). For SEM observation, the samples were longitudinally fixed on an aluminium stub. The samples were connected to the sample holding with conductive silver before gold-sputtered for 120 seconds under an argon atmosphere (Sputtering Scancoat Six, Edwards, Crawley, UK) and observed with an accelerating voltage of 10 kV. The average pore size was obtained by analysing 8-10 clearly visible pores for each SEM picture, by tracing a line between two points (opposite position) of a pore.
The final bilayer structure of the scaffolds and the particles distribution were observed via Micro CT analysis. The whole samples were inserted into the scan-chamber and an acquisition with a source voltage of 40 kV, a current of 250 mA, a rotating step of 0.1 and a pixel size of 4 μm was carried out. The reconstructions were carried out using the software NRecon (version1.6.10.2) starting from the acquired projection images. The 2D-images had a color depth of 8 bit with 255 grey level. After that, the whole set of raw images was displayed in a 3D space by a software CTVox.

Pycnometry was applied to determine overall porosity in the PLLA scaffolds. For porosity measurements via gas pycnometer (Pycnomatic ATC, Thermo Fisher Scientific, Waltham, Massachusetts, USA) helium gas was used as penetrating agent ("helium displacement method"). Using this technique, the material volume of a porous sample was estimated by subtracting the volume of the pores. The shaping of the specimens into a defined cylindrical shape was needed in order to evaluate the bulk volume of the samples. Measurements based on a scaffold mass of about 3.5 mg (neat PLLA scaffolds) and 5 mg (scaffolds supplemented with HA). The actual density of the substance under test is determined by the dry mass to volume ratio. Scaffolds were well dried before set into a measuring chamber with a known volume. In a reference chamber that has been calibrated, helium was initially charged at a known pressure before being inflated in the room with the sample. Scaffolds' porosity has been calculated using the following expression Eq 21:

$$POROSITY\ (\%)\ =\ 100\ *\ \left(1-\frac{V_{mes}}{V_{app}}\right)$$

Equation 21

Vmes is the real volume of the scaffolds measured by pycnometer and Vapp is the apparent volume calculated with the formula (volume of a cylinder). The amount of HA was calculated by thermal gravimetric analysis (TGA) (Labsys EVO, Setaram Instrumentation, Caluire-et-Cuire, France). Each sample was cut before the measurement chamber was loaded with the sample which was heated following a temperature profile of 10°C/minutes from 30°C up to 500 °C under continuous argon gas flow. The analysis of neat PLLA scaffolds served as control.

Bioreactor Miniaturization and Redesign

The scaled-down bioreactor was reengineered from the original glass prototype using stereolithographic 3D printing and printable resin, enabling a more adaptable and customizable design process facilitated by Autodesk's FUSION 360, a computer-aided design (CAD) software. The initial bioreactor had dimensions of 22.1 cm in height, a perfusion chamber diameter of 3.5 cm, and a riser diameter of 1 cm . In contrast, the modified version features a significantly reduced size, with a height of 6.5 cm, a perfusion chamber diameter of 1.8 cm, and a riser diameter of 0.3 cm.
To refine the fluid dynamics within the bioreactor, adjustments to its geometry were necessary. Flow homogenization grids were redesigned using Fusion 360, incorporating squared-hole patterns at varying distances (1 mm and 3 mm) from the liquid surface. Two grid configurations were created: one with a height of 0.4 cm and hole sizes of 1.5 mm, and another with a height of 2 mm and square holes measuring 0.653 mm per side. Both designs shared a grid diameter of 16 mm.

Mathematical modeling

The average bubble diameter (d_b) in the bubbly flow regime is determined using Miller's correlation (Eq. 22):

$$d_b = \left[\frac{6\sigma d_0}{g(\rho_l - \rho_g)}\right]^{\frac{1}{3}}$$

Equation 22

Where:

- σ: Surface tension of the liquid [N/m]
- d_0: Orifice diameter [m]
- g: Gravitational acceleration [m^2/s]
- $\rho_l and\ \rho_g$: Densities of the liquid and gas phases [kg/m3]

This formula assumes a uniform bubble size distribution enabled by the bubbly flow regime. The parameters reflect the interfacial forces, gravity, and density differences between the liquid and gas phases.

The terminal velocity (V_T) (Eq. 23) of bubbles in the riser is determined with a wall effect model, which accounts for the interaction between bubble size, column walls, and the Reynolds number Re_t^{∞}:

$$V_T = f(\lambda)V_T^{\infty}$$

Equation 23

Where:

- V_T^{∞} : Terminal velocity of a single bubble in an infinite, stagnant liquid.
- f(λ): Column wall factor.

The column wall factor f(λ) is calculated using Munroe's formula (Eq. 24):

$$f(\lambda) = 1 - \lambda^{1.5}$$

Equation 24

This formula applies to the range:

- $0.1 \leq \lambda \leq 0.80$

- $943 \leq Re_t^{\infty} \leq 11{,}000$

Here, λ is a dimensionless parameter related to the ratio of bubble size and column width, while Re_t^{∞} reflects the Reynolds number for the terminal velocity without wall effects.

Flow regime has to be considered:

- Viscous Regime ($Re_p < 1$): Terminal velocity depends on the bubble size and viscosity but not on inertial effects.
- Turbulent Regime (Re_p>100): Terminal velocity is dominated by inertial forces and is independent of Re_t^{∞}

This accounts for the interplay of viscous, inertial, and surface tension forces. By combining these approaches, the model comprehensively describes bubble dynamics in a bioreactor riser under a bubbly flow regime, enabling predictions of both bubble size and rise velocity.

Computational Fluid Dynamics (CFD) Simulations

Computational Fluid Dynamics (CFD) simulations were performed using Comsol Multiphysics software to analyze flow behavior and velocity distributions within the bioreactor. A 3D model incorporating axial symmetry was developed, reducing computational costs. The simulation assumed a constant air inlet velocity of 0.082 m/s, with the liquid phase treated as the continuous medium in a two-phase flow model. The simulations employed a bubbly flow model for transient analyses up to 120 seconds, ensuring the hydrodynamic solution reached steady-state conditions.
Key boundary conditions included an atmospheric pressure free surface at the outlet and a sliding condition for the liquid phase along the bioreactor walls. The simulations aimed to determine velocity fields and gas hold-up within the system, and the same boundary conditions were applied when testing the redesigned flow homogenization grids.

Oxygen Transfer Analysis

Oxygen transport from the gas to the liquid phase in the bioreactor was assessed using a global oxygen mass balance equation. The bioreactor retained the functional characteristics of an airlift system, with

the assumption of a fully mixed liquid phase. The governing equation for oxygen transfer is expressed as follows (Eq 25):

$$\frac{dC_l}{dt} = k_l a_l (C_l^* - C_l) - R_{O_2}$$

Equation 25

Where $k_l a_l$ is the overall mass transfer coefficient (s^{-1}), C_l^* presents the oxygen concentration at saturation (mg/L), and C_l is the bulk oxygen concentration (mg/L). The oxygen consumption rate (Eq 26), R_{O_2}, depends on the number of cells χ , the specific oxygen consumption rate q_0, and the liquid volume V as shown in:

$$R_{O_2} = \chi q_0 V$$

Equation 26

For the steady-state solution, the bioreactor model assumed a cell population of 360,000 cells, an initial oxygen concentration of zero, and an inlet air velocity of 0.082 m/s. The culture medium volume was set at 12 mL, with parameters tailored for mammalian cells ($q_0 = 96 \times 10^{-17} g/cell/s$) under standard incubator conditions (37°C, 1 atm). These values were calculated based on the two-resistance theory as described by (Capuana, Carfì Pavia, et al., 2022).
The transient solution tracked the evolution of oxygen concentration in the liquid phase, confirming that oxygen transfer from the gas phase exceeded cellular oxygen consumption, ensuring sufficient oxygen levels to sustain biological activity within the system.

Empirical inlet air flow rate

To characterize the airflow rate delivered by the peristaltic pump, since we used a gas and not a liquid, a system based on a “soap meniscus” method is used, as shown in Fig. 106.

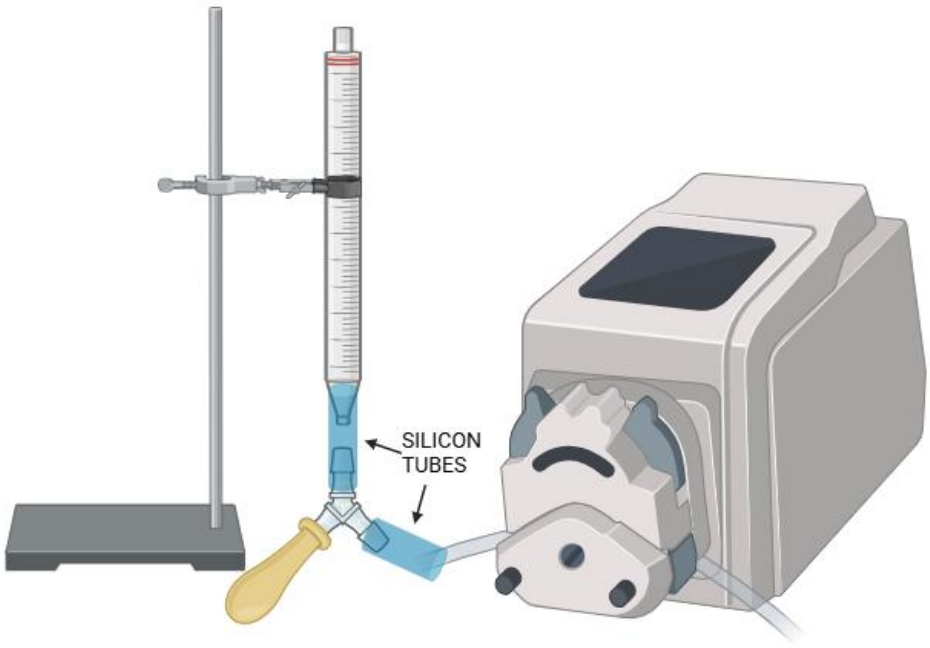

Figure 106: Experimental set up "soap -meniscus"

This system consists of a graduated pipette with a known diameter. A three-way connector is attached to the bottom of the graduated cylinder: one inlet is connected to the peristaltic pump, and the second is used to introduce a soap and water solution by a Pasteur pipette bulb. As air is introduced into the circuit, soap films form and rise within the glass column. A predefined path length within the cylinder is established for the soap films, and the travel time for each test is calculated by varying only the pump's flow setting. The rise velocity of the soap films is proportional to the airflow rate delivered by the pump. Tests were conducted using four different flow rates set by the pump (0.3, 0.6, 0.9, and 1.2 mL/min). For each setup, the rise times of the soap films to a specified height were measured, and the airflow rates were subsequently calculated as the volume traveled over time (m^3/sec) and then converted to mL/min.

Empirical liquid flow rate as function of air flow

To determine the liquid flow rate within the system as a function of the feeding airflow rate, a system was designed to evaluate fluid displacement under identical experimental conditions. Using Fusion 360, a bioreactor identical to the one used but connected to a much larger diameter container was designed, as shown in Fig. 107. This system maintains a constant liquid height within the riser (A);

water is drawn from the large cylinder (B), where the free surface level variation is negligible during the test.

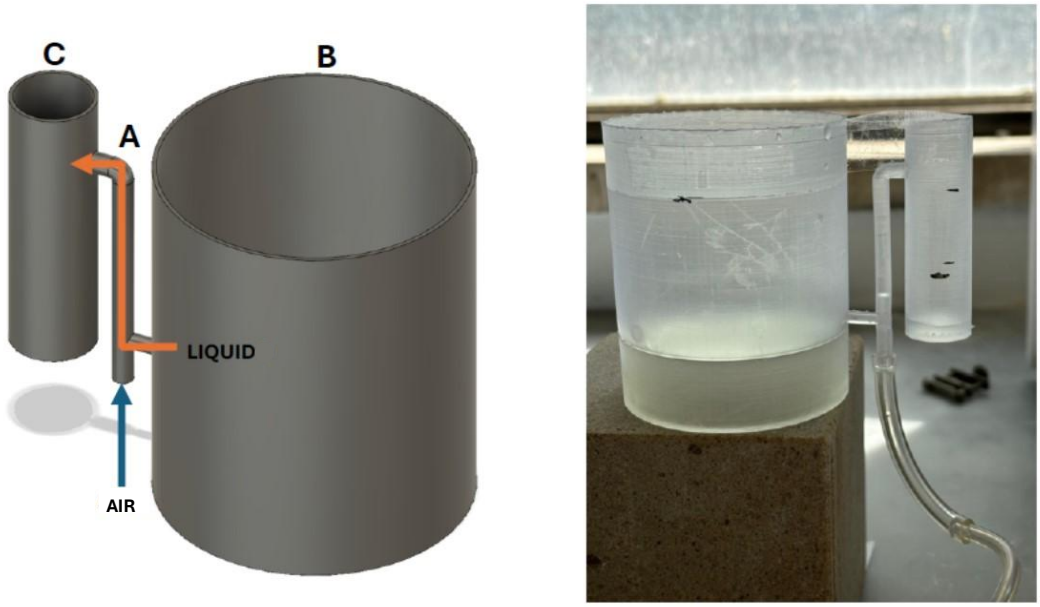

Figure 107: 3D printed system to evaluate liquid flow as a function of air flow inlet

During the tests, the time taken for the fluid to fill the bioreactor chamber (C) was measured as a function of the inlet airflow rate.

Biological evaluation

Nuremberg period

Cytotoxicity testing

For evaluation of cytotoxicity L929 mouse subcutaneous fibroblasts (strain C3H/An, Cell Line Services, Eppelheim, Germany), which are recommended by the international standard (ISO [international organization for standardization] 10993-5:2009 were cultured at an initial density of 1.0 x 104 cells/cm2 in cell culture flasks until 80-90 % confluence at 37 °C and 5 % CO2. In addition, hMSCs and pACs were used and seeded in a similar manner. The cytotoxicity testing procedure followed the respective ISO standard. Sterile extracts of all scaffold variants (PLLA without/with HA, 8 bilayer scaffolds per ml respective growth medium) were prepared by incubating them for 48 hours in growth medium to determine potential cytotoxic effects of the four scaffold types. L929

fibroblasts, hMSCs and pACs were seeded at 0.7-1 x 104 cells/cm2 in 96-well culture plates and allowed to adhere for 24 hours at 37 °C and 5 % CO2. Then, the supernatant was completely exchanged by scaffold extracts (volume 100 µL extract/well) or control solutions per each well for 24 hours at 37 °C and 5 % CO2. 10 % dimethyl sulfoxide (DMSO, Carl Roth GmbH and Ko.KG, Karlsruhe, Germany) diluted in the respective growth medium served as a positive control and pure growth medium as negative control. After 24 hours of incubation supernatants were discarded. Instead, 80 µL growth medium and 20 µL [3-(4,5-dimethylthiazol-2-yl)-5-(3-carboxymethoxyphenyl)-2-(4-sulfophenyl)-2H-tetrazolium, inner salt; MTS] solution (CellTiter 96® Aqueous One Solution Cell Proliferation Assay, Promega GmbH, Walldorf, Germany) were added to each well. After 2 hours incubation absorbance was measured photometrically at a wavelength of 490 nm (Tecan Austria GmbH, Grödig, Austria).

Seeding efficiency protocols

The first experiment conducted was to assess the ideal seeding protocol for our scaffolds, with a micropipette and different seeding volumes. For this experiment, cell seeding efficiency on scaffolds was assessed by maintaining a constant cell number (250,000 cells) while varying the seeding volume. The seeding efficiencies, calculated by the difference between the initial number of seeded cells and the cells remaining attached to the bottom of the well, showed a decrease with increasing volume.

hMSC isolation and culture

hMSCs derived from bone marrow of ten different healthy donors (mean age=25.03, 4x female, 6x male). Human bone marrow could be used in accordance with the ethical committee of Bavaria, Germany (Ethical approval number 17074 from 6. February 2018). In order to separate hMSCs from other cells, the following procedure was followed: bone marrow-derived blood was transferred into T175 culture flasks (6 ml of bone marrow for each flask), each containing 20 ml of hMSC growth medium (Dulbecco's modified eagle medium [DMEM], PAN-Biotech GmbH, Aidenbach, Germany, 5% platelet lysate [PL, BioScience, Aachen, Germany] solution, supplemented with 1% penicillin-streptomycin, 1% amphotericin B, 1% sodium pyruvate [all: PAN-Biotech GmbH] and 0.04% heparin [BioScience]). Bone marrow was cultured at 37 °C and 5% CO_2. Half of the liquid volume inside the culture flasks was replaced with new growth medium after 92 hours to partially remove

non-adhering cells different from hMSCs. After 7 days of incubation, the liquid volume was totally changed with fresh culture medium and, when cells were confluent, they were split or cryopreserved. For expansion hMSCs were detached with 0.05%/0.02% trypsin/EDTA solution (Merck KGaA, Darmstadt, Germany), rinsed with growth medium and seeded in T175 flasks at 1000 cells/cm^2. For scaffold seeding cells were counted with a Neubauer chamber or with a Luna II automated cell counter (logos biosystems, Anyang in Gyeonggi-do, South Korea) using 0.4% trypan blue dye in order to exclude dead cells from the count.

Bioreactor fluid-dynamic homogeneity evaluation L929

L929 fibroblast cells were cultured in standard conditions (37°C, 5% CO_2) using Dulbecco's Modified Eagle Medium (DMEM) supplemented with 10% fetal bovine serum (FBS) and 1% penicillin-streptomycin. For the experiment, 500,000 cells were seeded onto each scaffold (6 scaffolds per floor, 3 floors total) within a custom bioreactor system, resulting in a total of 18 scaffolds. The bioreactor was designed with three stacked levels, each containing six scaffolds (positions A–F). The system was operated under dynamic conditions to simulate physiological fluid flow. Cells were allowed to adhere and proliferate for the duration of the experiments. Cell viability and metabolic activity were quantified with 2 different experiments the first validation was carried for 48 hours the second one for 7 days. A CellTiter Blue- Assay and Live/dead were used to evaluate metabolic activity.

hMSC dynamic culture

Human mesenchymal stem cells (hMSCs) were seeded on two types of scaffolds:

1. Pure PLLA scaffolds
2. PLLA+HA scaffolds (poly(L-lactic acid) combined with hydroxyapatite)

Both scaffold types were tested under static conditions (no flow) and dynamic conditions (subjected to bioreactor fluid flow. Cell viability and metabolic activity were evaluated at 24 hours and 7 days using the CellTiter-Blue® Cell Viability Assay (Promega) and Live/dead assay. At day 7 Hisological analysis and Immunostaining were carried out.

Cell Titer Blue metabolic activity assay

The CellTiter-Blue assay was employed to assess cell viability and metabolic activity on the scaffolds. This assay relies on the reduction of resazurin, a cell-permeable dye, into resorufin, a fluorescent compound, by metabolically active cells. The fluorescence intensity is proportional to the number of viable cells. Scaffolds seeded with cells were cultured under static and dynamic conditions for selected time points (e.g., 1 and 7 days). At each time point, the culture medium was removed, and scaffolds were gently rinsed with phosphate-buffered saline (PBS) to remove any residual components. Following this, scaffolds were incubated with fresh medium containing 10% (v/v) CellTiter-Blue reagent (Promega, Madison, WI, USA) at 37 °C for 3 hours in a humidified incubator with 5% CO_2. After the incubation, 100 µL of the supernatant was collected and transferred to a black 96-well plate for fluorescence measurement (three times to have a triplicate of each salmple). The fluorescence intensity was recorded using a plate reader at an excitation wavelength of 560 nm and an emission wavelength of 590 nm. Cell viability was quantified by comparing the fluorescence intensity of test samples to that of negative controls (scaffolds without cells) and positive controls (scaffolds seeded with known cell numbers). The relative metabolic activity was calculated to evaluate the effect of scaffold composition (e.g., PLLA vs. PLLA+HA) and culture conditions (static vs. dynamic).Higher fluorescence intensity indicated greater metabolic activity, reflecting increased cell viability and proliferation. Dynamic culture conditions showed higher metabolic activity compared to static culture, suggesting improved nutrient and oxygen delivery in the perfusion system. Among scaffold compositions, PLLA+HA scaffolds exhibited superior cell viability, likely due to the osteoconductive properties of hydroxyapatite.

Live dead assay

One millilitre of PBS with Ca++, Mg++ was mixed with 5 µl of fluorescein diacetate (FDA) stock solution (5 mg/ml in acetone) and 1 µl of propidium iodide (PI) stock solution (2 mg/ml in PBS). The first dye labels living cells green, whereas the second stain labels dead cells red. 50 µl of the staining solution was placed on a thin glass slide, the sample (seeded scaffold segment or cover slip) immersed, another 50 µL drop was added to the sample and incubated. After 5 minutes` incubation, the sample was ready for the observation using a Leica Confocal Laser Scanning Microscope with Leica LASX software to take pictures. Results of the live/dead assay were used to calculate the area covered by vital cells using ImageJ1.48 v software. To assess cell penetration in unilayer scaffolds cross-sections of the live-dead stained scaffold were performed. In each microscopic field mean

values of minimum six measurements of the distance between the scaffold surface and the innermost cells visible within the scaffolds were were calculated. Bilayer scaffolds were cut longitudianally to check cell immigration into inner parts.

Immunostaining

To analyze cellular behavior and matrix production on the scaffolds, immunostaining was performed to detect collagen type I, collagen type II, and cell nuclei using DAPI. Scaffolds were cut in halves segments (~2 mm in diameter) were processed to ensure optimal staining quality.

The samples were first washed in Tris-buffered saline (TBS: 0.05 M Tris, 0.15 M NaCl, pH 7.6) to remove residual culture medium and debris. A blocking step followed, during which scaffolds were incubated for 20 minutes at room temperature (RT) in a solution containing 5% donkey serum and 0.1% Triton X-100, diluted in TBS. This step was critical to minimize nonspecific antibody binding. Following blocking, 50 µL of primary antibody solution was applied to each sample. The primary antibodies used included goat anti-human collagen type I and mouse anti-human collagen type II, diluted 1:50 in the blocking solution. The samples were incubated overnight at 4 °C in a humidified chamber to allow specific antigen-antibody binding. Controls were prepared by applying the blocking buffer without primary antibodies.

The next day, the samples were washed three times with TBS for five minutes each to remove unbound primary antibodies. Secondary antibodies were then applied, prepared as a 1:200 dilution in blocking buffer. Donkey-anti-goat Cy3-labeled antibodies were used for collagen type I detection, and donkey-anti-mouse AlexaFluor 488 antibodies were used for collagen type II detection. DAPI (10 µg/mL) was included in the secondary antibody solution to stain cell nuclei.

Samples were incubated for one hour at RT in a dark, humidified chamber to protect fluorophores from photobleaching. Afterward, the samples were washed three times with TBS to remove excess secondary antibodies. Finally, the stained samples were mounted on slides using Fluoromount G and covered with a glass coverslip.

The immunostained scaffolds were visualized using a fluorescence microscope. Collagen type I was detected using Cy3-labeled antibodies (red fluorescence), collagen type II using AlexaFluor 488 antibodies (green fluorescence), and nuclei were identified by DAPI staining (blue fluorescence). This combination allowed for a clear evaluation of the distribution of collagen types and cell nuclei, providing insights into matrix deposition and scaffold colonization.

5.3 Results

Hydroxyapatite powder was subjected to analysis by Mastersizer2000 with the aim of finding particles dimensions. Results are shown in Fig. 108. The majority of the particles presented a diameter less then 100 nm.

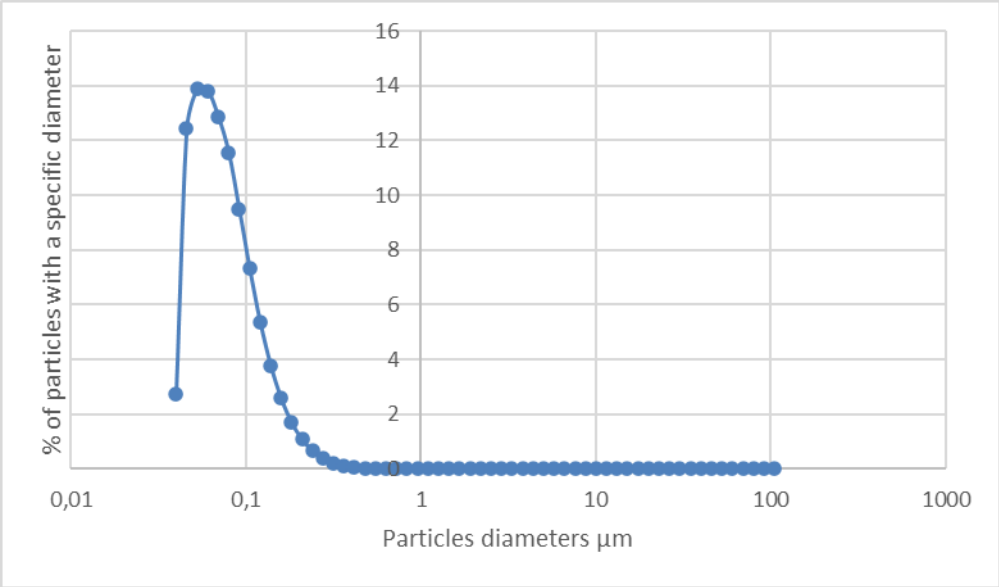

Figure 108: particles diameters distribution. Reproduced from Ferraro et al. 2024 (Ferraro et al., 2024)with permission.

Scaffold Characterization

PLLA and PLLA-HA matrices were produced starting from the same solutions with different TIPS protocol. Their morphology was then observed via SEM and, once the desired pore structure (different for each layer) was found, the relative protocol has been adopted to produce the samples to be used for *in vitro* tests.

A morphological analysis of the scaffolds was carried out by SEM. In Figs, it is possible to observe the pictures of the foams produced via TIPS testing different protocols. The TIPS protocol that has been chosen for the PLLA-L layer was 45 minutes - 28°C (Fig. 109 B). With these conditions the desired pore size of 250 µm was obtained. At low temperatures smaller pores were obtained (Fig. 109 A) .

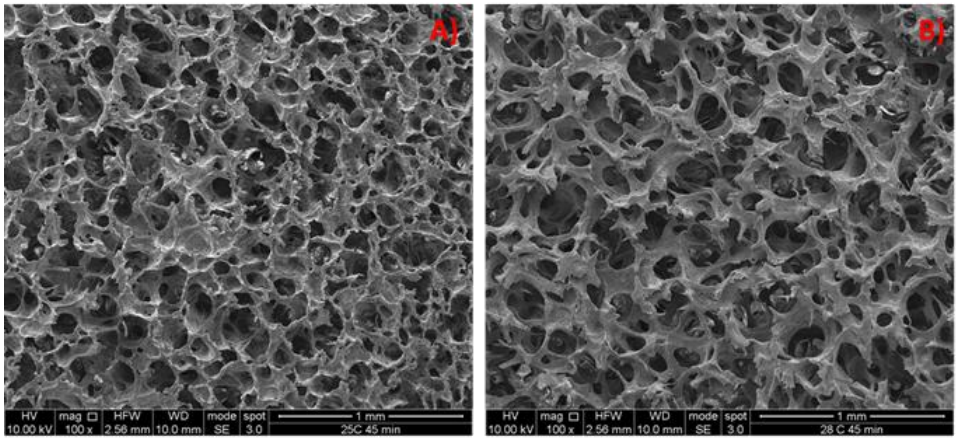

Figure 109: A) 25°C - 45 min; B) 28°C - 45 min; Reproduced from Ferraro et al. 2024 (Ferraro et al., 2024)with permission.

The required pore size for the layer PLLA-S was 100 µm, and it was obtained with the 15 minutes - 25° C TIPS protocol (Fig. 110).

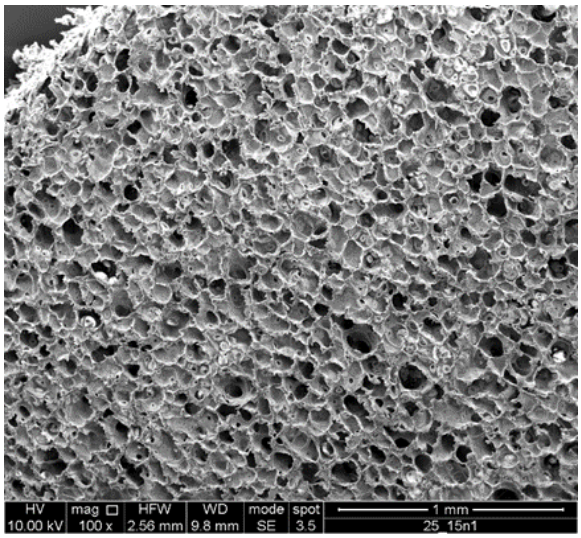

Figure 110: 25°C - 15 min Reproduced from Ferraro et al. 2024 (Ferraro et al., 2024)with permission.

The layer containing the HA (PLLA-HA-L) should have the same pore size of the PLLA-L ones, in order to reach comparable conditions to observe the effect of HA on cell differentiation. Therefore, for the solution filled with nHA particles, applying the same condition of the PLLA-L layer, the same avarege pore size (250 µm) was obtained (Figure 111).

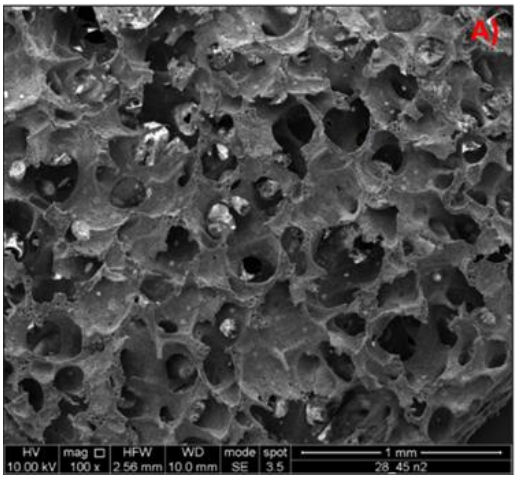

Figure 111: 28°C - 45 min; Adapted from Ferraro et al. 2024 (Ferraro et al., 2024)with permission.

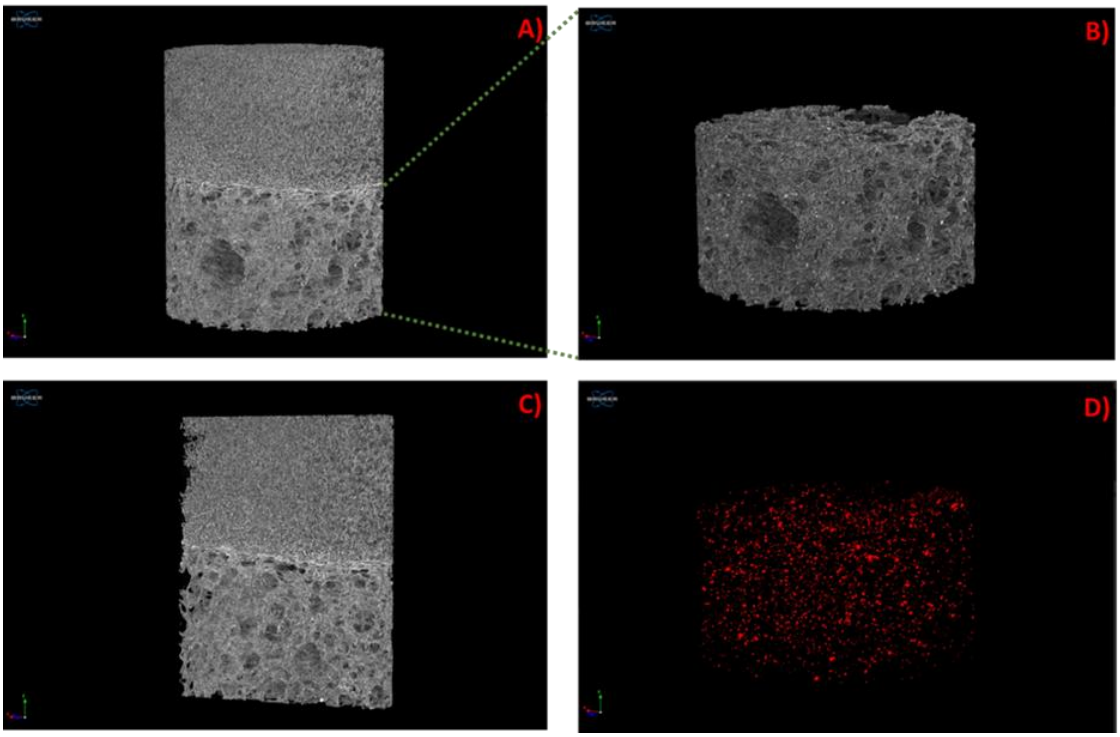

Figure 112: MicroCT PLLA-HA Scaffold; B) PLLA-HA-L layer; C) section of the scaffold; D) HA. Reproduced from Ferraro et al. 2024 (Ferraro et al., 2024)with permission.

Fig. 112 shows the micro CT images of bilayer scaffolds. It is easy to observe that the gluing process between the two sub-units has successfully carried out. As a matter of fact, the subunits appear well adhered each other, thus generating a continuous matrix. In Fig. 112D it is possible to observe the homogeneous distribution of HA into the matrix.

Bioreactor Miniaturization and Redesign

Building on the previous bioreactor design, the initial focus of the scaling-down process was on reducing dimensions, leading to a 70% decrease in the height and an 80% decrease in the diameter of the perfusion chamber. Fig. 113 shows the designs of the two tailored bioreactors.

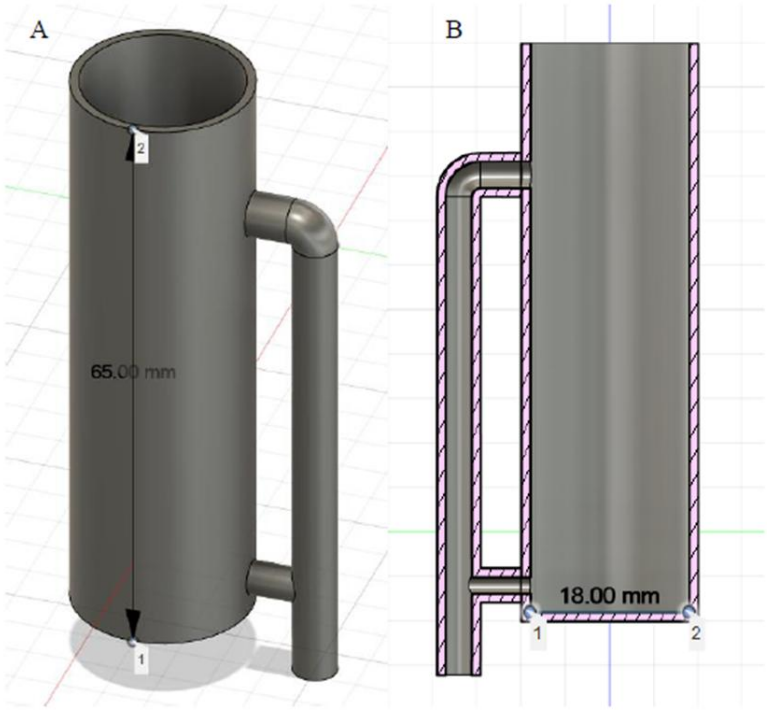

Figure 113: New prototype dimensions A) external view B)cross section

The bioreactor's dimensions were meticulously adjusted to keep a proportional relationship with the original design. This careful modification aimed to preserve the specific bubble flow regime, ensuring consistency between the two bioreactor versions. The bioreactor's operating regime remained consistent, creating a bubble column functioning as an external airlift reactor with two interconnected cylindrical tubes: a downcomer and a riser. The riser, which channels air bubbles, is connected to the peristaltic pump via a silicone tube and a sterile syringe filter. As the air bubbles rise through the riser, they draw in part of the culture medium, facilitating its circulation within the column. This promotes liquid-phase movement, enhances gas-liquid mass transfer, and ensures the oxygenation of the medium. With regard to the homogenization grids, the two designs are displayed in Fig. 114. Fig. 114C demonstrates the redesign of the distance from the free surface, taking into account that the

grids require handling. Therefore, they have been equipped with an upper solid section to facilitate gripping. This solid section may potentially influence the flow regime within the column.

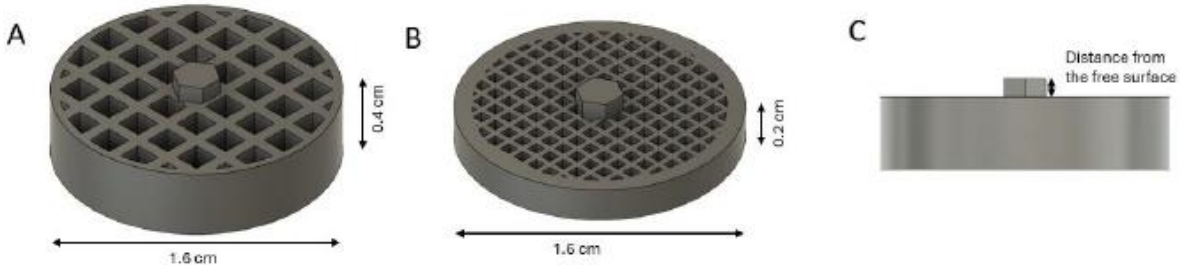

Figure 114: Liquid flow homogenization grid: A) coarse mesh grid (L=1.5mm), B) fine mesh grid (L=0.653 mm), C) frontal view of the grid with the upper solid part defining the distance from the free surface. Reproduced from Capuana et al., 2024 (Capuana et al., 2024), with permission.

The bioreactor by Capuana et al. (Capuana et al., 2023) features a double grid for scaffold accommodation. This configuration presented critical issues both in terms of maintaining sterility (excessive number of operations required by the operator for assembly) and the amount of culture medium used. The presence of numerous empty zones, i.e., without samples or printed supports, significantly increased the amount of medium needed to fill the entire bioreactor. Therefore, the sample holder was completely redesigned. After several attempts, the configuration shown in Fig. 115 was achieved.

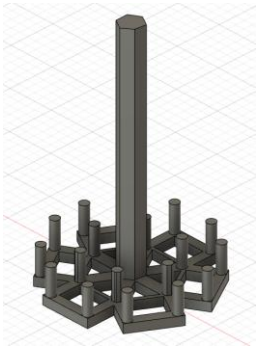

Figure 115: Hexagonal scaffold holder.

The scaffold holder is considerably less bulky and more versatile for sample insertion. The first detail noticed in the figure is the presence of a central hexagonal rod, with sides measuring 1.265 mm. From the rod extend 6 rectangular scaffold accommodations and 4 pins of 3 mm height. The latter serve to hold the sample in place. Simulation carried out demonstrated the necessity of grids to homogenize the fluid flow between each layer. To find a compromise between ease of operation and need of grids

we decided to place three grids, accommodating a total of 18 samples, 6 each floor. The distance between each grid and the top of pins is 5 mm as shown in Fig 116.

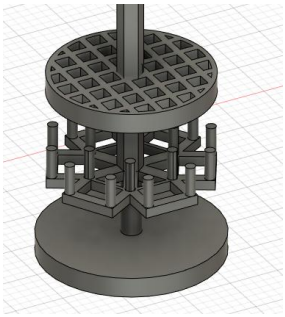

Figure 116: final design for scaffold holder and grid

The final prototype of the support with the grids is shown in Fig. 117.

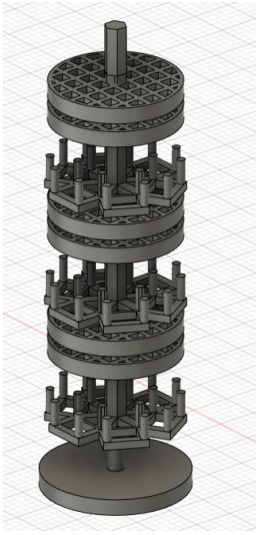

Figure 117: complete design of the scaffold holder

The final part of the scale-down involved the creation of a bubble breaker grid and the bioreactor cap. The grid was designed because the culture medium, composed of animal serum or human serum, tends to foam when recirculated. The foam could potentially compromise the sterility of the device. The design of the bubble breaker grid underwent several iterations. Initially, we considered making it part of the central rod to burst air bubbles forming near the free surface (Fig. 118).

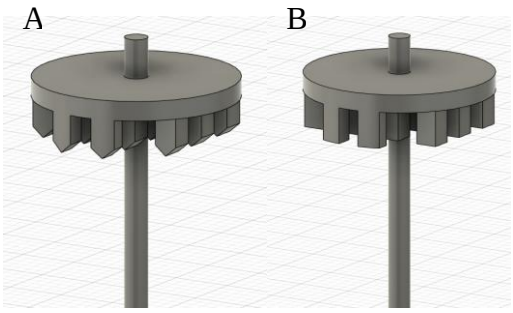

Figure 118: different bubble breaker projects

To avoid overloading the system's structure, we decided to discard these prototypes. The bubble breaker grid was integrated into the cap to prevent medium overflow from the bioreactor, as shown in the Fig. 119.

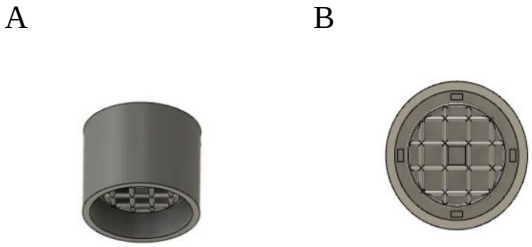

Figure 119: definitive bubble braker built into the lid

To test the actual stability of the scaffolds within the lattice, we conducted a test that also simulated the ease of working in a sterile environment. The scaffolds were hydrated to simulate sterile conditions and placed inside the bioreactor in their respective housings. The bioreactor was then connected to the peristaltic pump and operated at the desired flow rates as shown in Fig. 120.

Figure 120: bioreactor and scaffolds set up for dynamic testing

Computational Fluid Dynamics (CFD) Simulations

Computational fluid dynamics (CFD) simulations were used to determine gas holdup in the bioreactor (Figure 121A). The simulations revealed an absence of gas bubbles in the larger perfusion chamber, with air circulating through the upper orifice before exiting the bioreactor.

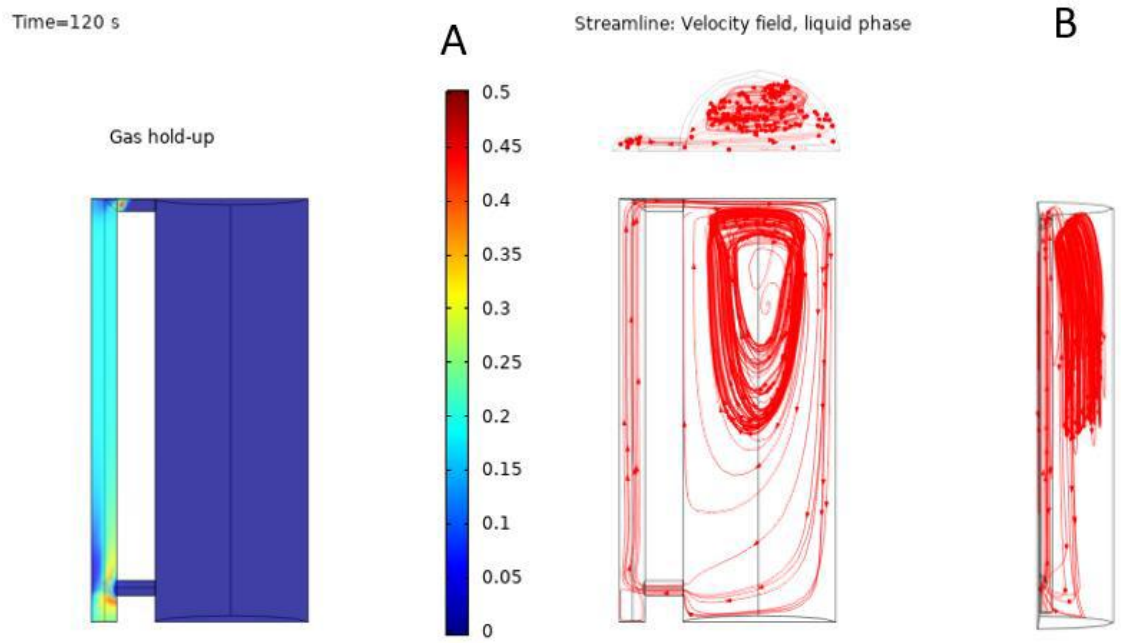

Figure 121: Results of the CFD simulation within the bioreactor: A) gas hold-up, B) streamline of the velocity field for the liquid phase.Time = 120s for the transient solution. Image reproduced from Capuana et al., 2024(Capuana et al., 2024) with permission.

The average gas holdup value in the riser, which was utilized in the mathematical model for oxygen transport and in calculating the specific gas-liquid interfacial area (a_l), was found to be 0.18 (Fig. 121). The image clearly demonstrates that bubble formation and entrainment occur solely within the riser. Thus, oxygen mass transport calculations between the two phases were exclusively focused on this region. The flow lines within the bioreactor, obtained from CFD analyses and depicted in Fig. 124B, highlight significant heterogeneity throughout the system's volume. To address this, a grid was introduced at the top to homogenize the flow. Two grids with different dimensions and distances from the free surface of the liquid phase were tested. This approach aims to determine whether a specific hole size or grid arrangement is more effective in achieving a uniform distribution of liquid flow within the bioreactor.

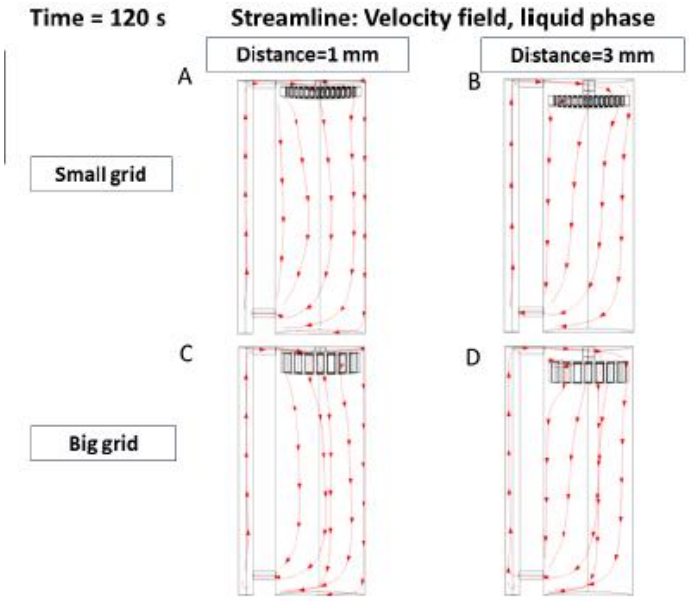

Figure 122: Streamline of the liquid velocity field within the bioreactor with different configurations: A) small grid at 1mm distance from the free surface, B) small grid at 3 mm distance from the free surface, C) big grid at 1mm distance from the free surface, D) big grid at 3 mm distance from the free surface Time = 120 s for the transient solution. Image reproduced from Capuana et al., 2024(Capuana et al., 2024) with permission.

In every scenario, the flow was more able to maintaining a homogeneous environment for scaffold culture under consistent stimuli, as opposed to the system without a grid. Ultimately, the configuration shown in Figure 122A was found to be the most optimal, exhibiting a more uniform liquid-phase velocity field.

Oxygen Transfer Analysis

The process of mass transfer in airlift bioreactors is essential for providing oxygen to cultured cells. This transfer occurs from a dispersed gas phase (air bubbles) to a continuous liquid phase (the culture medium). Given oxygen's critical role in cell survival, the miniaturization of the bioreactor raised concerns about whether the reduced culture medium volume could sufficiently sustain adequate oxygen levels for a high cell density and proper cellular metabolism. To address this, the mass transfer coefficient (k_l [m/s]) was calculated using the two-resistance theory, involving the determination of constants such as the Reynolds, Schmidt, and Sherwood numbers (Tab 17). The specific gas-liquid interfacial area (a_l) was estimated based on the bubble diameter and gas holdup.

Table 17: Parameter used for solving Eq. 1 from the two-resistance theory: the first column describes the parameters with their unit and the second one the calculated values. Table reproduced from Capuana et al., 2024(Capuana et al., 2024) with permission.

Parameters	**Calculated value**
Reynolds number	215.1
Equivalent bubble diameter	0.12 [cm]
Schmidt number	269.1
Sherwood number	414.5
k_l	0.001 [m/s]
a_l	3.6

Empirical inlet air flow rate

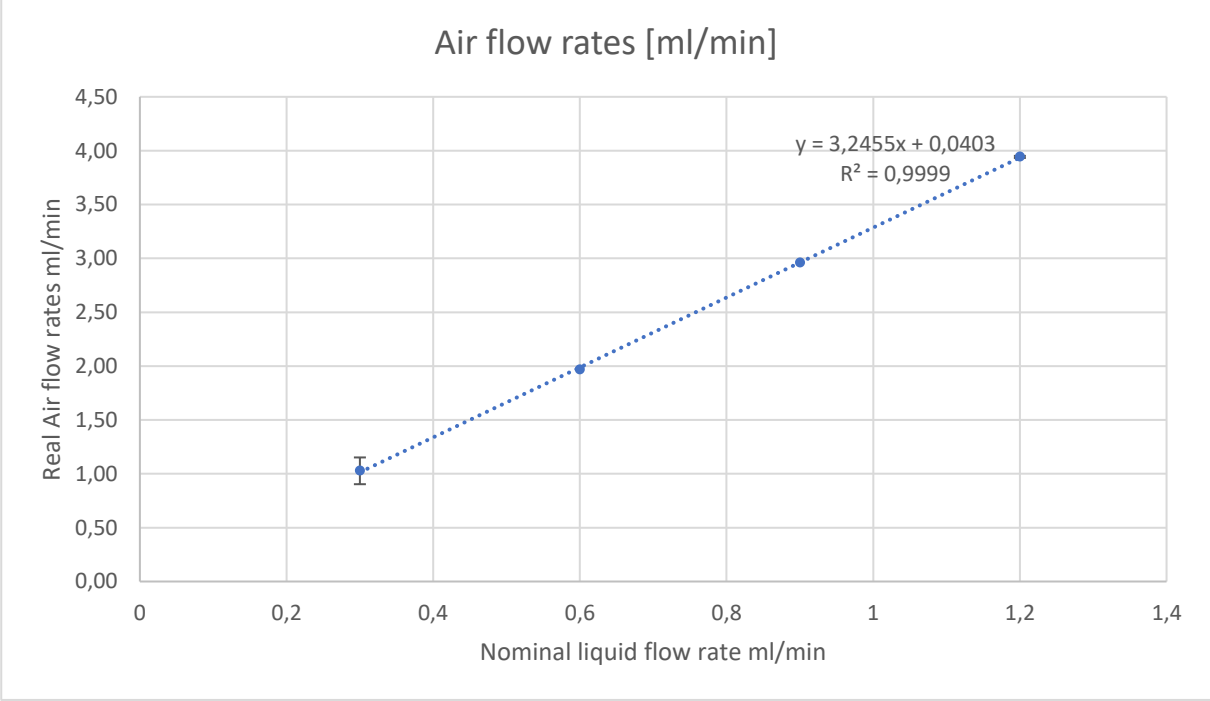

Figure 123: peristaltic pump characterization for air instead of a liquid

To ensure accurate and reliable data, all measurements were taken in triplicate, and the mean values were analyzed. From the data analysis and the graph (Fig. 123) , it can be observed that the air flow rate exhibits a linear trend as the nominal flow rate increases. Based on these data, a conversion coefficient was extrapolated from the slope of the trend line described by the equation $y =$

$3.2455x + 0.0403y = 3.2455x + 0.0403$, which relates the nominal pump flow rate to the actual gas flow rate.

This improved system, featuring the new peristaltic pump, has enabled us to work with lower air flow rates compared to previous studies.

Empirical liquid flow rate as function of air flow

The liquid flow rates, determined through the test described in Materials and Methods, were analyzed and plotted in an Excel graph. To ensure more accurate and reliable data, measurements were taken in triplicate, and the mean values were analyzed, as was done for the air flow rates. The relationship between the liquid flow rate and the air flow rate was graphed, as shown in the Fig. 124. The relationship is linear, with the liquid flow rates obtainable in the range of microliters per minute.

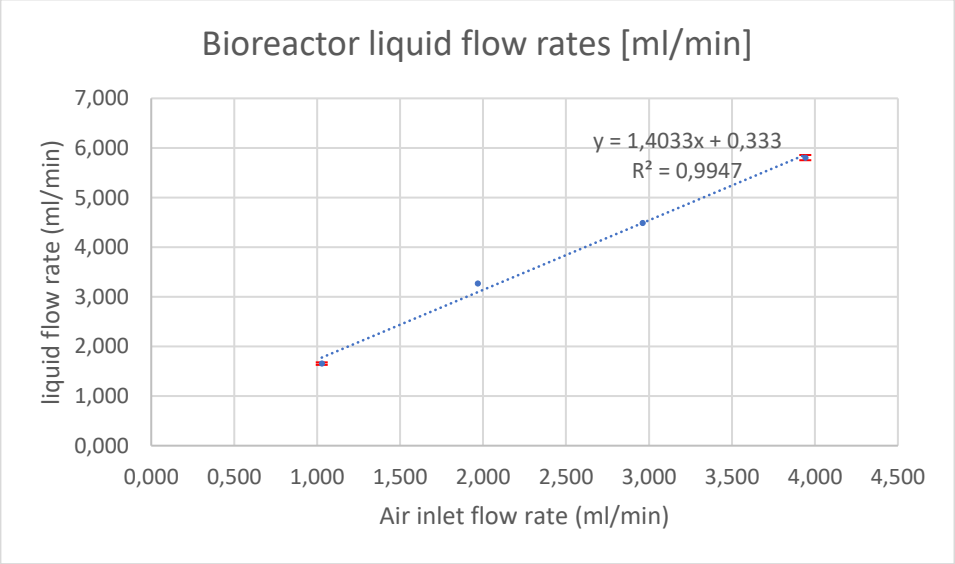

Figure 124: liquid flow rate induced by specific inlet air flow rates

Biological evaluation

Nuremberg period

Cytotoxicity testing

The cytotoxicity of biphasic pure PLLA and PLLA+HA scaffolds was evaluated. The tests showed no cytotoxicity for the extracts from both types of scaffolds, using the L929 cell line, which is commonly used for cytotoxicity assessments. Compared to the growth of L929 cells exposed to both

extracts, a slight reduction in the vitality of pACs and hMSCs was observed, but this reduction did not exceed the 70% cytotoxicity threshold as reported in Fig 125.

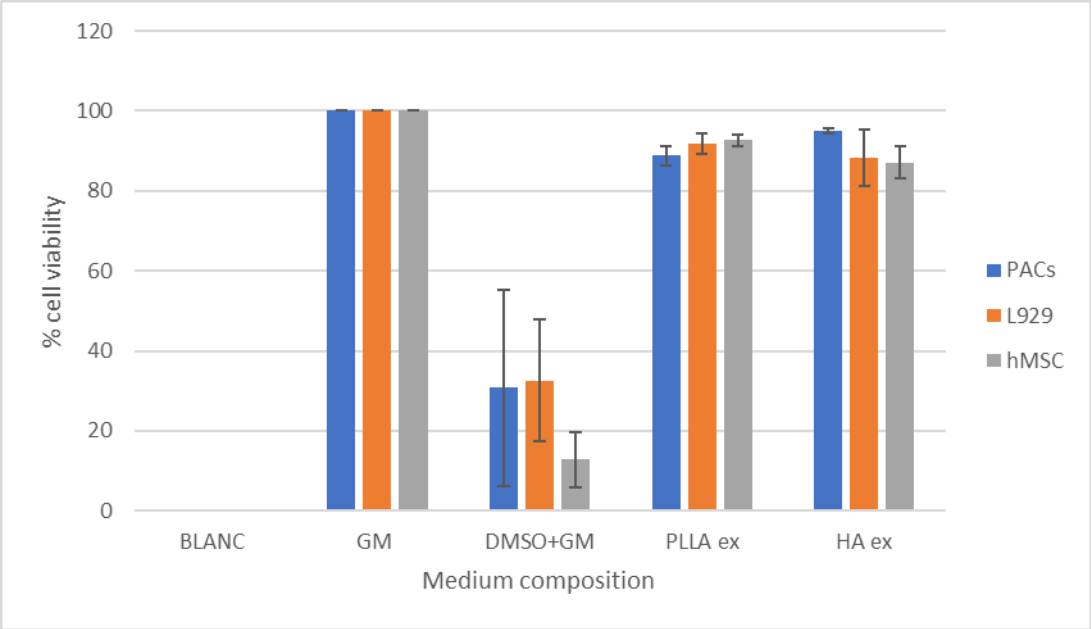

Figure 125: ***Cytotoxicity assay with bilayer PLLA scaffolds without/with HA supplementation****. L929 fibroblasts, human mesenchymal stem cells (hMSCs) and porcine articular chondrocytes (pACs) BLANC: control, DMSO: dimethyl sulfoxide, GM: growth medium, HA ex: hydroxyapatite extract, PLLA: poly-L-lactic acid extract. Mean values and standard deviations are shown.*

Seeding protocols and efficiency

The seeding efficiencies, calculated by the difference between the initial number of seeded cells and the cells remaining attached to the bottom of the well, showed a decrease with increasing volume Tab 18.

Table 18

Volume µl	Cells Seeded	Cells attached to the well	Well std dv %	Cells inside Scaffold	Efficiency %	MTS on scaffold	MTS std dv
20	250 000	14 300	10,00	235 700	94,28	47,21	2,73
40	250 000	48 000	15,00	202 000	80,80	43,80	3,18
80	250 000	175 000	17,00	75 000	30,00	35,74	11,49

Efficiency dropped from 94.28% at 20 µL to 30.00% at 80 µL, suggesting that higher volumes may reduce the efficiency of cell attachment to the scaffold, likely due to increased cell dispersion. The MTS assay confirmed cell viability on the scaffolds, with a decline in metabolic activity correlating with the reduced seeding efficiency. The minimal standard deviations in the MTS readings indicate consistent results across replicates

Bioreactor fluid-dynamic homogeneity evaluation L929

The experiment analyzed the viability of L929 cells within the bioreactor across three floors and six positional scaffolds (A–F). The overall cell viability exhibited a mean value of 29.36 with a standard deviation of 3.33, indicating moderate variability in cell growth across the entire system. When stratified by floor, the 3rd floor demonstrated the highest average cell viability (30.56 ± 4.34), while the 1st floor and 2nd floor had nearly identical averages (28.77 ± 2.23 and 28.75 ± 3.37, respectively). Despite slight differences in averages, the standard deviations across the floors remain relatively low, suggesting that the bioreactor maintains a reasonably homogeneous flow and nutrient distribution among the floors.

Analysis by position revealed scaffold A had the highest cell viability (32.03 ± 4.85), while B showed the lowest (27.42 ± 0.91). Scaffolds C, D, E, and F recorded intermediate values with limited variability (standard deviations ranging from 0.91 to 5.12). This further supports the hypothesis that flow conditions and environmental factors in the bioreactor are consistent across most positions, with minor localized variations.

These results (Tabs. 19-20-21) indicate that the bioreactor design promotes relatively uniform conditions for cell growth, as evidenced by the low standard deviations, while slight differences between positions and floors may be attributed to inherent system dynamics or scaffold-specific factors. Further optimization could reduce these residual differences to achieve complete uniformity.

Table 19: overall Cell Viability Results

Metric	**Average**	**Standard Deviation**
Overall Total	29.358	3.334

Table 20: Cell Viability Results by floors

Floor	Average	Standard Deviation
1st Floor	28.77	2.23
2nd Floor	28.75	3.37
3rd Floor	30.56	4.34

Table 21:Cell Viability Results by position

Position	Average	Standard Deviation
A	32.03	4.85
B	27.42	0.91
C	30.52	1.95
D	30.45	2.19
E	27.94	5.12
F	27.78	2.91

hMSC dynamic culture

The metabolic activity of hMSCs cultured on PLLA and PLLA+HA scaffolds under static and dynamic conditions was evaluated at 7 days using the CellTiter-Blue assay. The results (Tab 22) showed the following average fluorescence values (mean ± standard deviation):

Table 22: cell titer results

Scaffold type	Average	Std Dev
PLLA Static:	**53.17**	**1.76**
PLLA+HA Static:	**52.97**	**1.75**
PLLA Dynamic:	**58.12**	**2.33**
PLLA+HA Dynamic:	**57.90**	**2.32**

These results indicate that dynamic culture conditions resulted in higher metabolic activity compared to static conditions, regardless of the scaffold material. The PLLA and PLLA+HA scaffolds exhibited very similar values within each culture condition, with no substantial differences observed between the two materials. The low standard deviations across all groups suggest consistent metabolic activity among replicates, supporting the reproducibility of the results.

While hydroxyapatite (HA) did not significantly influence metabolic activity within the 7-day culture period, longer culture durations may be required to observe its potential effects on cell behavior, particularly in promoting hMSC differentiation. Extended experiments are necessary to assess HA's role in enhancing osteogenic differentiation and matrix mineralization over time.

Overall, the findings suggest that dynamic conditions enhance hMSC metabolic activity, likely due to improved nutrient and oxygen exchange in the bioreactor system. Further analysis through histological staining, live/dead assays, and immunostaining will provide additional insights into cell distribution, viability, and differentiation under these conditions

Live dead assay

The live/dead assay performed on hMSCs cultured on PLLA and PLLA+HA scaffolds under static and dynamic conditions reveals distinct differences in cell viability and distribution as shown in Figs. 126-127. On the outer surfaces, where static conditions led to a localized concentration of cells primarily on the superficial regions of the scaffold. However, under dynamic conditions, the cell viability and distribution improved markedly, with fluorescence indicating enhanced cellular interaction and integration with the scaffold material.

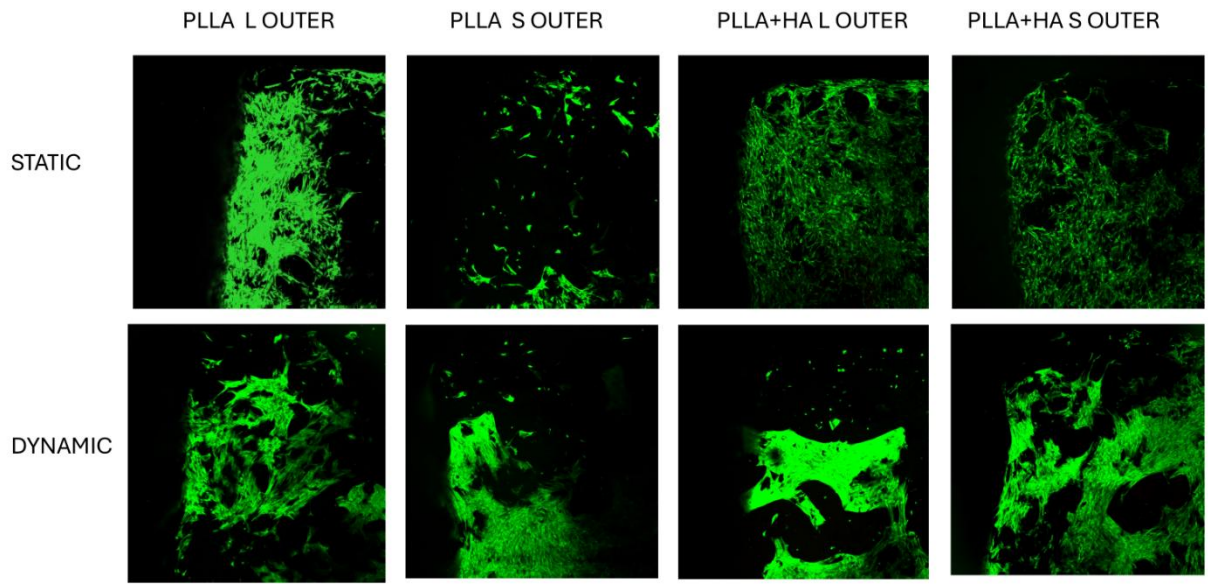

Figure 126: Live/Dead staining images of hMSCs seeded on PLLA and PLLA+HA scaffolds under static and dynamic conditions after 7 days of culture, OUTER SURFACES. Green fluorescence indicates live cells, while red fluorescence marks dead cells.

On the inner surfaces of the scaffolds, static conditions resulted in limited cell infiltration and sparse distribution of viable cells, as indicated by the faint green fluorescence. In contrast, dynamic culture conditions promoted a more homogeneous distribution and higher intensity of live-cell fluorescence, suggesting improved nutrient and oxygen exchange facilitated by the bioreactor system Across both PLLA and PLLA+HA scaffolds, no significant differences were observed in cell viability after 7 days of culture, suggesting that the presence of hydroxyapatite did not immediately influence metabolic activity or cell distribution within this timeframe. Nonetheless, these results underline the critical role of dynamic conditions in enhancing cellular behavior and scaffold colonization, demonstrating the potential of the bioreactor system to simulate a more physiologically relevant environment for tissue engineering applications.

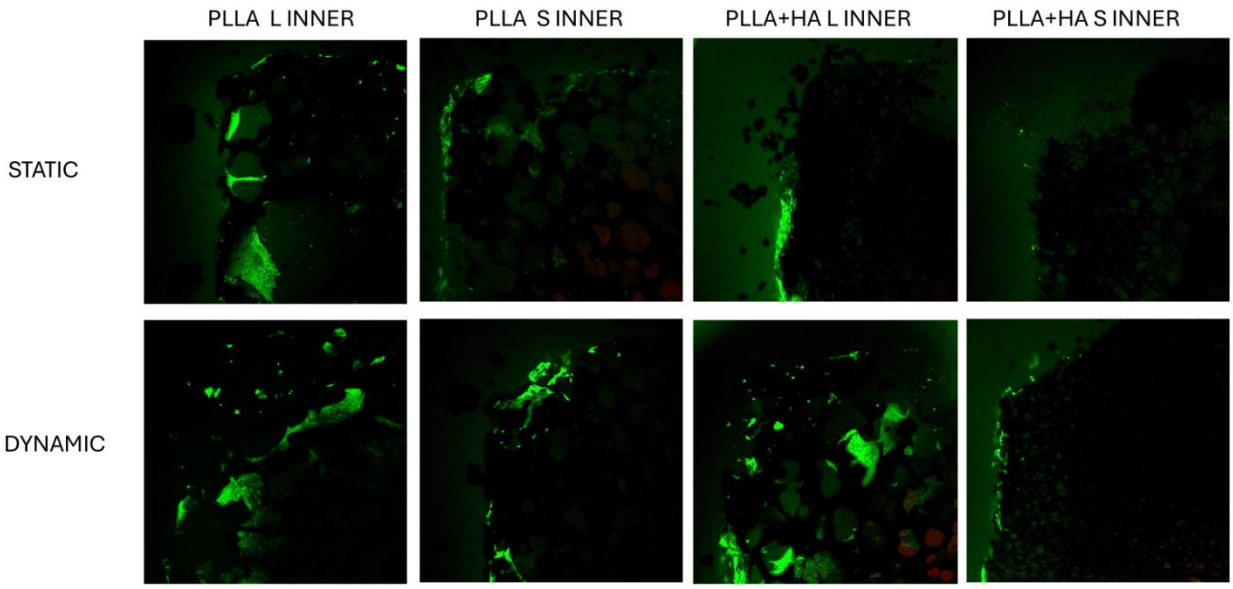

Figure 127: Live/Dead staining images of hMSCs seeded on PLLA and PLLA+HA scaffolds under static and dynamic conditions after 7 days of culture, INNER SURFACES. Green fluorescence indicates live cells, while red fluorescence marks dead cells.

Immunostaining

The immunostaining images (Fig. 128) provide insights into the extracellular matrix (ECM) production and cellular distribution within the PLLA and PLLA+HA scaffolds under static and dynamic conditions. Type I collagen (red) and type II collagen (green) were targeted to assess osteogenic and chondrogenic ECM production, respectively, while DAPI staining (blue) was used to visualize the cell nuclei and confirm cellular localization and density.

Under static conditions, both PLLA and PLLA+HA scaffolds display limited and uneven collagen deposition on both inner and outer surfaces, with type I collagen predominating. The cell nuclei, as indicated by DAPI staining, appear sparsely distributed, especially in the inner regions of the scaffolds, reflecting suboptimal cellular infiltration and ECM production likely due to restricted nutrient and waste exchange.

Dynamic culture conditions, on the other hand, demonstrate a marked improvement in ECM synthesis and cell distribution. Both type I and type II collagen are more abundantly and homogeneously produced, particularly on the inner surfaces of the scaffolds. The increased intensity of DAPI staining under dynamic conditions confirms enhanced cellular penetration and proliferation throughout the scaffold structure. Notably, the

PLLA+HA scaffolds show a pronounced increase in type I collagen production compared to PLLA alone, indicating the osteoconductive effect of hydroxyapatite, which supports osteogenic differentiation and mimics the native bone microenvironment.

These findings underscore the critical impact of dynamic culture in promoting cell infiltration, proliferation, and ECM production, particularly in scaffolds with osteoconductive properties such as PLLA+HA, thereby enhancing their suitability for bone tissue engineering applications.

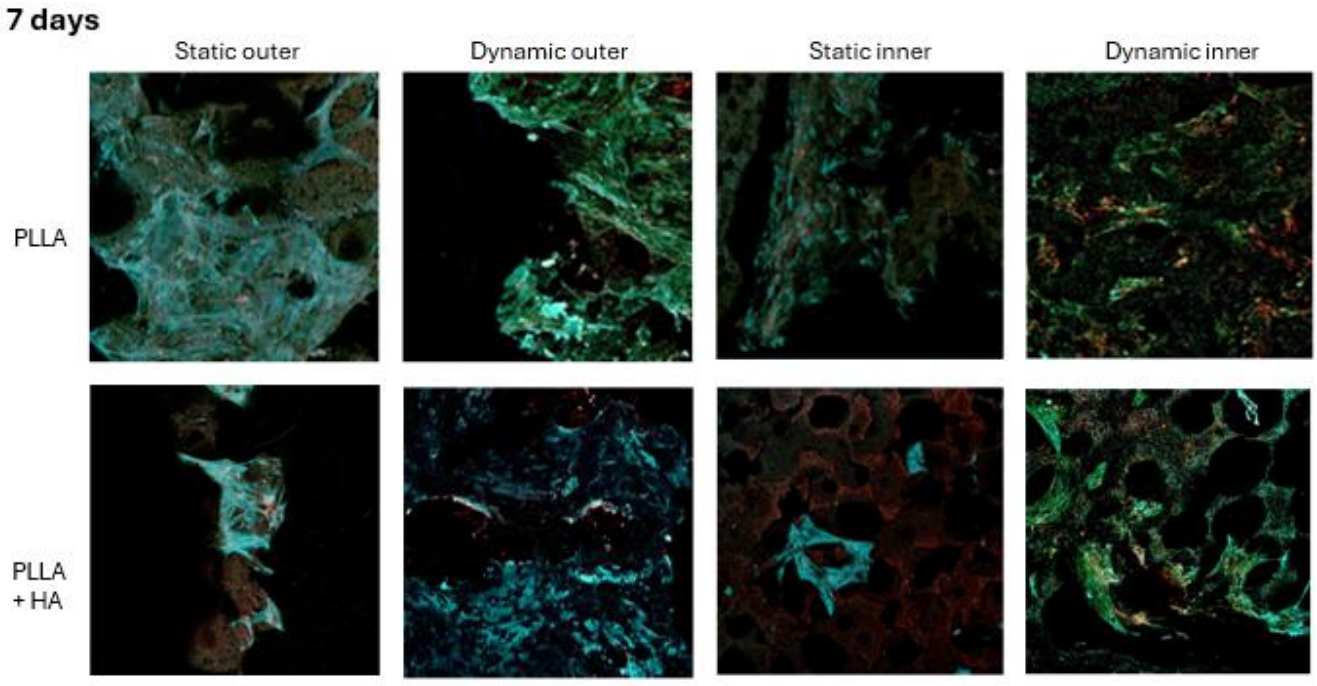

Figure 128: Immunostaining of PLLA and PLLA+HA scaffolds cultured with hMSCs for 7 days under static and dynamic conditions. Type I collagen (red) and type II collagen (green) deposition were visualized to assess extracellular matrix production, while DAPI staining (blue) highlights cell nuclei.

5.4 Discussion

This study focused on miniaturizing an airlift perfusion bioreactor for tissue engineering applications. The scaling-down process, which reduced the bioreactor's height by 70% and diameter by 80%, successfully preserved fluid dynamics, as evidenced by computational fluid dynamics (CFD) simulations. The CFD analysis showed a gas holdup value of 0.18 in the riser, indicating efficient gas-liquid mass transfer, and the use of homogenizing grids at 1 mm from the free surface improved liquid-phase flow, ensuring better oxygenation and nutrient distribution (Capuana et al., 2024). These

modifications are crucial for optimizing cell culture conditions, particularly for high-density cell cultures.

The scaffolds used in this study were bilayer poly-L-lactic acid (PLLA) scaffolds, with and without hydroxyapatite (HA). Micro-CT imaging confirmed that the gluing process between the two subunits of the scaffolds was successful, ensuring a continuous matrix and homogenous HA distribution. Biocompatibility tests showed that both PLLA and PLLA+HA scaffolds were non-toxic to L929 cells, porcine articular chondrocytes (pACs), and human mesenchymal stem cells (hMSCs), with no significant cytotoxicity observed. However, the presence of HA did not lead to significant changes in metabolic activity within the first 7 days of culture (Capuana et al., 2024)

The dynamic culture conditions in the miniaturized bioreactor significantly improved cell viability and extracellular matrix (ECM) production compared to static conditions. Live/Dead staining showed enhanced cell infiltration and distribution within the scaffolds, especially under dynamic conditions, indicating that the improved nutrient and oxygen exchange within the bioreactor promoted better cellular behavior. These findings align with previous studies suggesting that dynamic culture conditions more closely mimic in vivo environments and promote cellular proliferation and ECM deposition (Bostwick et al., 2022)

Immunostaining further demonstrated that dynamic conditions facilitated more abundant and homogenous deposition of type I and type II collagen, with the PLLA+HA scaffolds showing increased type I collagen production, indicating potential for osteogenic differentiation. This suggests that HA's presence may have an osteoconductive effect, supporting bone tissue engineering applications (Bhumiratana et al., 2011). Despite this, HA's impact on cell differentiation and matrix mineralization may require longer culture periods to be fully realized (Khoshbin et al., 2025).

The study also assessed the impact of scaffold volume on seeding efficiency. As the scaffold volume increased, seeding efficiency decreased, likely due to higher cell dispersion, which reduced the number of cells attaching to the scaffold. This trend emphasizes the need for optimized seeding protocols to ensure high efficiency, particularly in larger-scale bioreactors (Fabbri et al., 2016). The variability in cell viability across different positions and floors within the bioreactor, though minimal, suggests that there may still be room for further optimization in the bioreactor's design to ensure even distribution of cells and nutrients. In conclusion, the miniaturized bioreactor developed in this study provides an effective platform for dynamic cell culture, with potential applications in tissue engineering, especially for bone regeneration. While HA did not show immediate effects on cell

metabolism or distribution, its role in promoting osteogenic differentiation should be further explored over longer culture periods. The bioreactor's optimization for more uniform cell growth could further improve its suitability for high-density tissue engineering cultures.

5.5 Conclusion

This study demonstrated the successful miniaturization of an airlift perfusion bioreactor for tissue engineering, preserving essential fluid dynamics and enhancing gas-liquid mass transfer. The introduction of homogenizing grids improved oxygenation and nutrient distribution, crucial for high-density cell cultures.

The bilayer PLLA scaffolds, with and without HA, showed excellent biocompatibility, with no significant cytotoxicity. Despite the lack of immediate metabolic changes, HA's potential osteoconductive properties suggest value in bone tissue engineering.

Dynamic culture conditions in the miniaturized bioreactor significantly improved cell viability, ECM production, and collagen deposition, aligning with studies showing that dynamic conditions better mimic in vivo environments. Immunostaining confirmed enhanced type I collagen production in PLLA+HA scaffolds, indicating potential for osteogenic differentiation.

Scaffold volume impacted seeding efficiency, emphasizing the need for optimized protocols in larger bioreactors. Minimal variability in cell viability suggests room for further bioreactor design optimization.

In summary, the miniaturized bioreactor provides a promising platform for dynamic cell culture, with significant potential for tissue engineering, particularly bone regeneration. Further investigation into HA's role in promoting osteogenic differentiation and bioreactor optimization for uniform cell growth is warranted.

III. Conclusions

This thesis presents a comprehensive study on polymeric scaffolds and bioreactor systems as advanced tools for tissue engineering (TE) and 3D *in vitro* modeling, addressing critical challenges in regenerative medicine, drug development, and disease modeling. By integrating Poly(L-lactic acid) (PLLA) scaffolds fabricated using Thermally Induced Phase Separation (TIPS), stereolithographic (SLA) 3D printing for bioreactor prototyping, and dynamic bioreactor systems, this research advances the development of biomimetic environments capable of replicating native physiological conditions.

One of the major achievement of this work is the demonstration of a single biomaterial's versatility for multiple applications. PLLA scaffolds, were precisely tailored for different tissue engineering needs by adjusting pore size and architecture, ensuring optimal mechanical and biological properties. The incorporation of hydroxyapatite (HA) nanoparticles in some scaffold formulations further enhanced their osteoconductive capabilities, making them particularly suitable for bone tissue engineering. This modular approach improves scalability, reproducibility, and cost-effectiveness, which are essential for clinical translation and industrial applications.
The development of SLA 3D-printed bioreactors allowed for rapid prototyping and optimization of culture systems, ensuring precise control over bioreactor geometry for optimal fluid dynamics, sterility, and reproducibility. These perfusion and air-lift bioreactors significantly improved cell viability, nutrient diffusion, and extracellular matrix (ECM) deposition, demonstrating their critical role in advancing dynamic cell culture models. The biological relevance of these systems was confirmed through extensive cell culturing experiments, where different cell types were selected based on tissue-specific applications. Human mesenchymal stromal cells (hMSCs) were used to evaluate osteogenic differentiation, demonstrating increased cell adhesion, proliferation, and matrix mineralization on PLLA-HA scaffolds. In the context of cancer research, breast cancer cells were cultured within 3D tumor models, revealing a more physiologically relevant tumor microenvironment compared to conventional 2D cultures. These findings confirm that PLLA scaffolds and dynamic culture systems can serve as highly effective models for both tissue regeneration and disease research.

The study on the effect of thermal history on pore size architecture optimized PLLA scaffold fabrication using TIPS, demonstrating that precise thermal control can create gradient pore structures.

The ability to fine-tune pore size and interconnectivity provided a biomimetic osteochondral tissue and with bone and cartilage interface, improving mechanical stability and cellular infiltration.

The validation of PLLA porous scaffolds for 3D breast cancer models confirmed that breast cancer cells can proliferate and invade within porous structures, more closely mimicking in vivo tumor behavior. These results highlight the importance of 3D scaffolds in drug testing and cancer research, offering a potential alternative to traditional 2D cultures and animal models.

The air-liquid interface (ALI) bioreactor for respiratory models, developed using SLA 3D printing, successfully supported the culture of primary respiratory epithelial cells, demonstrating high potential for lung disease research and inhalation toxicity studies.

The study on air-lift perfusion bioreactor with PLLA-HA scaffolds confirmed that HA incorporation enhances hMSC adhesion, proliferation, and differentiation, making these scaffolds highly suitable for bone regeneration applications. The bilayer PLLA-HA scaffold for osteochondral regeneration provided a biomimetic approach to osteochondral defect repair, ensuring better mechanical integration and tissue compatibility.

A crucial contribution of this research is its potential to reduce reliance on animal experimentation in preclinical studies. Traditional animal models often fail to accurately predict human-specific responses due to species differences in metabolism, immune reactions, and tissue organization. Additionally, ethical concerns surrounding animal welfare have led to increased advocacy for the 3Rs principle (Replacement, Reduction, and Refinement) in biomedical research. The 3D in vitro models developed in this thesis provide a highly predictive and physiologically relevant alternative to animal testing. The ability to culture patient-derived cells on biomimetic scaffolds within dynamic bioreactors creates personalized, human-relevant platforms for studying disease progression, drug efficacy, and tissue regeneration. These models significantly improve predictive accuracy in preclinical testing, reducing the ethical and financial costs associated with animal research while ensuring more clinically relevant outcomes.

This research has significant implications for clinical and industrial applications, particularly in tissue engineering, regenerative medicine, and pharmaceutical development. The integration of TIPS-fabricated PLLA scaffolds, SLA 3D-printed bioreactors, and dynamic culture systems provides a scalable and reproducible platform for high-throughput drug screening, biomaterial testing, and tissue regeneration studies. The ability to tailor scaffolds and bioreactors to patient-specific conditions underscores the potential for personalized medicine, offering customized treatment strategies for

individual patients. By combining advanced scaffold fabrication, SLA 3D printing, and dynamic bioreactor technologies, this thesis establishes a new paradigm in bioengineering. The findings presented here pave the way for future research in tissue-on-chip systems, bioreactor automation, and microfluidic integration, all of which will further enhance the translational potential of these technologies. Moving forward, these advancements have the potential to revolutionize personalized medicine, improve drug screening reliability, and contribute to the global transition toward ethical, effective, and human-relevant biomedical research methodologies.

IV. Ringraziamenti Acknowledgements

Desidero esprimere la mia sincera gratitudine a tutte le persone che mi hanno accompagnato e supportato in questo percorso di dottorato.

Un grazie speciale al mio mentore e amico Francesco Carfì Pavia, che mi ha seguito giorno dopo giorno in questi tre anni di sangue, sudore e tanto divertimento scientifico. La tua guida e il tuo sostegno sono stati fondamentali per il mio successo.

Un sentito ringraziamento ai Prof. Valerio Brucato, Vincenzo La Carrubba e Fabio Bucchieri per la loro preziosa guida e supporto.

Grazie di cuore a tutte le colleghe, come Elisa, Maria Chiara e Veronica, mi siete state vicine in questo viaggio, la vostra amicizia, compagnia, e in alcuni tratti follia hanno reso tutto più semplice e piacevole.

Un grazie speciale ai miei amici di Pisa, Umbe, Alekos e Ire, mi avete sempre supportato, anche a distanza. La vostra presenza è stata un'ancora di salvezza in momenti difficili.

Un ringraziamento infinito alla mia famiglia: mamma e papà, grazie per il vostro amore incondizionato e il sostegno costante, e grazie alla mia fantastica sorella, grazie Bea che sei sempre pronta a darmi una mano, vincendo anche la paura dell'aereo per venire qui.

E infine, un ringraziamento enorme va al mio compagno di vita Nazareno. Amor, mi stai vicino nel bene e nel male da dieci anni, non so nemmeno come hai fatto, tutti se lo chiedono. Un po' di merito per questo dottorato va anche a te, per tutto quello che hai fatto e continui a fare per me ogni giorno che passa, per esserci sempre e per farmi crescere sempre, grazie grazie grazie.

I would like to express my deepest gratitude to Professor Gundula Schultze Tanzil for the warm hospitality I experienced in Nuremberg. Special thanks to my friends and colleagues with whom I

shared six wonderful months: Jacky, Toby, Clemens, Sandeep, Yasir, Christian and my roommate Emre. Your presence made this experience unforgettable.

V. References

Abolhassani, H., Eskandari, A., Saremi Poor, A., Zarrabi, A., Khodadadi, B., Karimifard, S., Sahrayi, H., Bourbour, M., & Tavakkoli Yaraki, M. (2024). Nanobiotechnological approaches for breast cancer management: Drug delivery systems and 3D in vitro models. *Coordination Chemistry Reviews, 508*, Article 215754. https://doi.org/10.1016/j.ccr.2024.215754

Ahmad, A. (Ed.). (2019). *Breast cancer metastasis and drug resistance* (2nd ed., Vol. 1152). Springer . https://doi.org/10.1007/978-3-030-20301-6

Al-Munajjed, A. A., Hien, M., Kujat, R., Gleeson, J. P., & Hammer, J. (2008). Influence of pore size on tensile strength, permeability and porosity of hyaluronan-collagen scaffolds. *Journal of Materials Science: Materials in Medicine, 19*(8), 2859–2864. https://doi.org/10.1007/s10856-008-3422-5

Alwahsh, M., Al-Doridee, A., Jasim, S., Awwad, O., Hergenröder, R., & Hamadneh, L. (2024). Cytotoxic and molecular differences of anticancer agents on 2D and 3D cell culture. *Molecular Biology Reports, 51*(1). https://doi.org/10.1007/s11033-024-09669-1

Al-Zyoud, W., Haddadin, D., Hasan, S. A., Jaradat, H., & Kanoun, O. (2023). Biocompatibility testing for implants: A novel tool for selection and characterization. *Materials, 16*(21). https://doi.org/10.3390/ma16216881

Anderson, N. M., & Simon, M. C. (2020). The tumor microenvironment. *Current Biology, 30*(16), 921–925. https://doi.org/10.1016/j.cub.2020.06.081

Antonelli, F. (2023). 3D cell models in radiobiology: Improving the predictive value of in vitro research. *International Journal of Molecular Sciences, 24*(13). https://doi.org/10.3390/ijms241310620

Rabbani, A. (2023). SEM image porosity and pore size. *MATLAB Central File Exchange*. https://it.mathworks.com/matlabcentral/fileexchange/70245-sem-image-porosity-and-pore-size

Arnason, G. (2020). The emergence and development of animal research ethics: A review with a focus on nonhuman primates. *Science and Engineering Ethics, 26*(4), 2277–2293. https://doi.org/10.1007/s11948-020-00219-z

Arnold, M., Morgan, E., Rumgay, H., Mafra, A., Singh, D., Laversanne, M., Vignat, J., Gralow, J. R., Cardoso, F., Siesling, S., & Soerjomataram, I. (2022). Current and future burden of breast

cancer: Global statistics for 2020 and 2040. *Breast, 66*, 15–23. https://doi.org/10.1016/j.breast.2022.08.010

Barcena, A. J. R., Dhal, K., Patel, P., Ravi, P., Kundu, S., & Tappa, K. (2024). Current biomedical applications of 3D-printed hydrogels. *Gels 10*(1). https://doi.org/10.3390/gels10010008

Barnes, P. J. (2008). Immunology of asthma and chronic obstructive pulmonary disease. *Nature Reviews Immunology, 8*(3), 183–192. https://doi.org/10.1038/nri2254

Benatti, A. C. B., Pattaro, A. F., Rodrigues, A. A., Xavier, M. V., Kaasi, A., Barbosa, M. I. R., Jardini, A. L., Filho, R. M., & Kharmandayan, P. (2019). Bioreabsorbable polymers for tissue engineering: PLA, PGA, and their copolymers. In A. M. Grumezescu & A. M. Holban (Eds.), *Materials for biomedical engineering: Hydrogels and polymer-based scaffolds* (pp. 83–116). Elsevier. https://doi.org/10.1016/B978-0-12-816901-8.00004-3

Beşkardeş, I. G., Aydın, G., Bektaş, Ş., Cengiz, A., & Gümüşderelioğlu, M. (2018). A systematic study for optimal cell seeding and culture conditions in a perfusion mode bone-tissue bioreactor. *Biochemical Engineering Journal, 132*, 100–111. https://doi.org/10.1016/j.bej.2018.01.006

Bhattacharya, R., Bose, D., Kaur, T., Patel, R., Renuka, O., & Rodriguez, R. V. (2024). Model organoids: Integrated frameworks for the next frontier of healthcare advancements. *Stem Cell Reviews and Reports*. https://doi.org/10.1007/s12015-024-10814-3

Bhumiratana, S., Grayson, W. L., Castaneda, A., Rockwood, D. N., Gil, E. S., Kaplan, D. L., & Vunjak-Novakovic, G. (2011). Nucleation and growth of mineralized bone matrix on silk-hydroxyapatite composite scaffolds. *Biomaterials, 32*(11), 2812–2820. https://doi.org/10.1016/j.biomaterials.2010.12.058

Bhuskute, H., Shende, P., & Prabhakar, B. (2022). 3D printed personalized medicine for cancer: Applications for betterment of diagnosis, prognosis and treatment. In *AAPS PharmSciTech 23*(1). https://doi.org/10.1208/s12249-021-02153-0

Bichat, F., Mouawad, R., Solis-Recendez, G., Khayat, D., & Bastian, G. (1997). Cytoskeleton alteration in MCF7R cells, a multidrug resistant human breast cancer cell line. *Anticancer Research, 17*(5A), 3393–3401. http://europepmc.org/abstract/MED/9413178

Bostwick, K. C. P., Martin, A. J., Collie, R. J., & Durksen, T. L. (2022). Motivation in context: A multilevel examination of growth orientation across one year. *Journal of Applied Developmental Psychology, 81*. https://doi.org/10.1016/j.appdev.2022.101435

Browe, D. C., Díaz-Payno, P. J., Freeman, F. E., Schipani, R., Burdis, R., Ahern, D. P., Nulty, J. M., Guler, S., Randall, L. D., Buckley, C. T., Brama, P. A. J., & Kelly, D. J. (2022). Bilayered extracellular matrix derived scaffolds with anisotropic pore architecture guide tissue organization during osteochondral defect repair. *Acta Biomaterialia*, *143*, 266–281. https://doi.org/10.1016/j.actbio.2022.03.009

Bucci-Muñoz, M., Gola, A. M., Rigalli, J. P., Ceballos, M. P., & Ruiz, M. L. (2023). Extracellular vesicles and cancer multidrug resistance: Undesirable intercellular messengers? *Life*, *13*(8). https://doi.org/10.3390/life13081633

Burney, P., Jarvis, D., & Perez-Padilla, R. (2015). The global burden of chronic respiratory disease in adults. *International Journal of Tuberculosis and Lung Disease*, *19*(1), 10–20. https://doi.org/10.5588/ijtld.14.0446

Caballero, D., Kundu, B., Abreu, C. M., Amorim, S., Fernandes, D. C., Pires, R. A., Oliveira, J. M., Correlo, V. M., Reis, R. L., & Kundu, S. C. (2022). Forecast cancer: The importance of biomimetic 3D in vitro models in cancer drug testing/discovery and therapy. *In Vitro Models*, *1*(2), 119–123. https://doi.org/10.1007/s44164-022-00014-z

Capuana, E., Campora, S., Catanzaro, G., Lopresti, F., Conoscenti, G., Ghersi, G., La Carrubba, V., Brucato, V., & Pavia, F. C. (2023). Computational modeling and experimental characterization of fluid dynamics in micro-CT scanned scaffolds within a multiple-sample airlift perfusion bioreactor. *Biochemical Engineering Journal*, *191*. https://doi.org/10.1016/j.bej.2022.108797

Capuana, E., Carbone, C., Pavia, F. C., Ghersi, G., La Carrubba, V., & Brucato, V. (2024). An airlift perfusion bioreactor for tissue engineering applications: From computational modeling to experimental validation. *Chemical Engineering Transactions*, *110*, 229–234. https://doi.org/10.3303/CET24110039

Capuana, E., Carfì Pavia, F., Lombardo, M. E., Rigogliuso, S., Ghersi, G., La Carrubba, V., & Brucato, V. (2022). Mathematical and numerical modeling of an airlift perfusion bioreactor for tissue engineering applications. *Biochemical Engineering Journal*, *178*, 108298. https://doi.org/10.1016/j.bej.2021.108298

Capuana, E., Lopresti, F., Carfì Pavia, F., Brucato, V., & La Carrubba, V. (2021). Solution-based processing for scaffold fabrication in tissue engineering applications: A brief review. *Polymers*, *13*(13). https://doi.org/10.3390/polym13132041

Capuana, E., Lopresti, F., Ceraulo, M., & La Carrubba, V. (2022). Poly-L-lactic acid (PLLA)-based biomaterials for regenerative medicine: A review on processing and applications. *Polymers, 14*(6). https://doi.org/10.3390/polym14061153

Carbone, C., Rigogliuso, S., Brucato, V. M. B., Cusimano, A., Labbozzetta, M., La Carrubba, V., Poma, P., Notarbartolo, M., & Carfì Pavia, F. (2024). PLLA porous scaffold as a 3D breast cancer model to investigate drug resistance. *Journal of Biomedical Materials Research Part A*. https://doi.org/10.1002/jbm.a.37836

Carfì Pavia, F., La Carrubba, V., Piccarolo, S., & Brucato, V. (2008). Polymeric scaffolds prepared via thermally induced phase separation: Tuning of structure and morphology. *Journal of Biomedical Materials Research Part A, 86*(2), 459–466. https://doi.org/10.1002/jbm.a.31621

Castro, N., Ribeiro, S., Fernandes, M. M., Ribeiro, C., Cardoso, V., Correia, V., Minguez, R., & Lanceros-Mendez, S. (2020). Physically active bioreactors for tissue engineering applications. *Advanced Biosystems, 4*(10). https://doi.org/10.1002/adbi.202000125

Chen, J. S., Tu, S. L., & Tsay, R. Y. (2010). A morphological study of porous polylactide scaffolds prepared by thermally induced phase separation. *Journal of the Taiwan Institute of Chemical Engineers, 41*(2), 229–238. https://doi.org/10.1016/j.jtice.2009.08.008

Chen, L., Wei, L., Su, X., Qin, L., Xu, Z., Huang, X., Chen, H., & Hu, N. (2023). Preparation and characterization of biomimetic functional scaffold with gradient structure for osteochondral defect repair. *Bioengineering, 10*(2). https://doi.org/10.3390/bioengineering10020213

Chew, S. A., Arriaga, M. A., & Hinojosa, V. A. (2016). Effects of surface area to volume ratio of PLGA scaffolds with different architectures on scaffold degradation characteristics and drug release kinetics. *Journal of Biomedical Materials Research Part A, 104*(5), 1202–1211. https://doi.org/10.1002/jbm.a.35657

Chinnasami, H., Gimble, J., & Devireddy, R. V. (2018). Structure–property relation of porous poly (l-lactic acid) scaffolds fabricated using organic solvent mixtures and controlled cooling rates and its bio-compatibility with human adipose stem cells. *Journal of Bioactive and Compatible Polymers, 33*(4), 397–415. https://doi.org/10.1177/0883911518758354

Choi, H., Choi, W.-S., & Jeong, J.-O. (2024). A review of advanced hydrogel applications for tissue engineering and drug delivery systems as biomaterials. *Gels, 10*(11), 693. https://doi.org/10.3390/gels10110693

Cifuentes, S. C., Saldaña, L., Gónzalez-Carrasco, J. L., Benavente, R., & García-Peñas, A. (2021). Effect of thermal processing on the dynamic/isothermal crystallization and cytocompatibility of polylactic acid for biomedical applications. *Macromolecular Chemistry and Physics, 222*(23). https://doi.org/10.1002/macp.202100274

Conoscenti, G., Carrubba, V. La, & Brucato, V. (2017). A versatile technique to produce porous polymeric scaffolds: The thermally induced phase separation (TIPS) method. *Archives in Chemical Research, 01*(02). https://doi.org/10.21767/2572-4657.100012

Conoscenti, G., Schneider, T., Stoelzel, K., Carfì Pavia, F., Brucato, V., Goegele, C., La Carrubba, V., & Schulze-Tanzil, G. (2017). PLLA scaffolds produced by thermally induced phase separation (TIPS) allow human chondrocyte growth and extracellular matrix formation dependent on pore size. *Materials Science and Engineering C, 80*, 449–459. https://doi.org/10.1016/j.msec.2017.06.011

Davis, S., Roldo, M., Blunn, G., Tozzi, G., & Roncada, T. (2021). Influence of the mechanical environment on the regeneration of osteochondral defects. *Frontiers in Bioengineering and Biotechnology, 9*. https://doi.org/10.3389/fbioe.2021.603408

De Luca, A., Capuana, E., Carbone, C., Raimondi, L., Carfì Pavia, F., Brucato, V., La Carrubba, V., & Giavaresi, G. (2024). Three-dimensional (3D) polylactic acid gradient scaffold to study the behavior of osteosarcoma cells under dynamic conditions. *Journal of Biomedical Materials Research Part A, 112*(6), 841–851. https://doi.org/10.1002/jbm.a.37665

De Marco, R., Pesce, G., Marcon, A., Accordini, S., Antonicelli, L., Bugiani, M., Casali, L., Ferrari, M., Nicolini, G., Panico, M. G., Pirina, P., Zanolin, M. E., Cerveri, I., & Verlato, G. (2013). The coexistence of asthma and chronic obstructive pulmonary disease (COPD): Prevalence and risk factors in young, middle-aged and elderly people from the general population. *PLoS ONE, 8*(5). https://doi.org/10.1371/journal.pone.0062985

Ding, Y., Liu, W., Yu, W., Lu, S., Liu, M., Kaplan, D. L., & Wang, X. (2018). Three-dimensional tissue culture model of human breast cancer for the evaluation of multidrug resistance. *Journal of Tissue Engineering and Regenerative Medicine, 12*(9), 1959–1971. https://doi.org/10.1002/term.2729

Eldeeb, A. E., Salah, S., & Elkasabgy, N. A. (2022). Biomaterials for tissue engineering applications and current updates in the field: A comprehensive review. *AAPS PharmSciTech, 23*(7). https://doi.org/10.1208/s12249-022-02419-1

Engel, N., Fechner, C., Voges, A., Ott, R., Stenzel, J., Siewert, S., Bergner, C., Khaimov, V., Liese, J., Schmitz, K.-P., Krause, B. J., & Frerich, B. (2021). An optimized 3D-printed perfusion bioreactor for homogeneous cell seeding in bone substitute scaffolds for future chairside applications. *Scientific Reports, 11*, 22228. https://doi.org/10.1038/s41598-021-01516-8

Engrácia, D. M., Pinto, C. I. G., & Mendes, F. (2023). Cancer 3D models for metallodrug preclinical testing. *International Journal of Molecular Sciences, 24*(15). https://doi.org/10.3390/ijms241511915

Fabbri, R., Macciocca, M., Vicenti, R., Pasquinelli, G., Caprara, G., Valente, S., Seracchioli, R., & Paradisi, R. (2016). Long-term storage does not impact the quality of cryopreserved human ovarian tissue. *Journal of Ovarian Research, 9*(1). https://doi.org/10.1186/s13048-016-0261-8

Faheed, N. K. (2024). Advantages of natural fiber composites for biomedical applications: A review of recent advances. *Emergent Materials, 7*(1), 63–75. https://doi.org/10.1007/s42247-023-00620-x

Fan, J., Abedi-Dorcheh, K., Vaziri, A. S., Kazemi-Aghdam, F., Rafieyan, S., Sohrabinejad, M., Ghorbani, M., Adib, F. R., Ghasemi, Z., Klavins, K., & Jahed, V. (2022). A review of recent advances in natural polymer-based scaffolds for musculoskeletal tissue engineering. *Polymers, 14*(10). https://doi.org/10.3390/polym14102097

Ferraro, W., Civilleri, A., Gögele, C., Carbone, C., Vitrano, I., Carfi Pavia, F., Brucato, V., La Carrubba, V., Werner, C., Schäfer-Eckart, K., & Schulze-Tanzil, G. (2024). The phenotype of mesenchymal stromal cell and articular chondrocyte cocultures on highly porous bilayer poly-L-lactic acid scaffolds produced by thermally induced phase separation and supplemented with hydroxyapatite. *Polymers, 16*(3). https://doi.org/10.3390/polym16030331

Fiume, E., Schiavi, A., Orlygsson, G., Bignardi, C., Verné, E., & Baino, F. (2021). Comprehensive assessment of bioactive glass and glass-ceramic scaffold permeability: Experimental measurements by pressure wave drop, modelling and computed tomography-based analysis. *Acta Biomaterialia, 119*, 405–418. https://doi.org/10.1016/j.actbio.2020.10.027

Ganguly, P. (2024). Organoids and 3D in vitro models as a platform for precision medicine (PM): An update. *Organoids, 3*(3), 165–173. https://doi.org/10.3390/organoids3030011

Garcia-Garcia, A., Muñana-González, S., Lanceros-Mendez, S., Ruiz-Rubio, L., Alvarez, L. P., & Vilas-Vilela, J. L. (2024). Biodegradable natural hydrogels for tissue engineering, controlled release, and soil remediation. *Polymers*, *16*(18). https://doi.org/10.3390/polym16182599

Garg, P., Malhotra, J., Kulkarni, P., Horne, D., Salgia, R., & Singhal, S. S. (2024). Emerging therapeutic strategies to overcome drug resistance in cancer cells. *Cancers*, *16*(13), 2478. https://doi.org/10.3390/cancers16132478

Grémare, A., Guduric, V., Bareille, R., Heroguez, V., Latour, S., L'heureux, N., Fricain, J. C., Catros, S., & Le Nihouannen, D. (2018). Characterization of printed PLA scaffolds for bone tissue engineering. *Journal of Biomedical Materials Research Part A*, *106*(4), 887–894. https://doi.org/10.1002/jbm.a.36289

Gu, Z., Wu, Q., Shang, B., Zhang, K., & Zhang, W. (2023). Organoid co-culture models of the tumor microenvironment promote precision medicine. *Cancer Innovation*.. https://doi.org/10.1002/cai2.101

Gunduz, O., Egles, C., Pérez, R. A., Ficai, D., & Ustundag, C. B. (Eds.). (2023). *Biomaterials and tissue engineering*. Springer.

Haider, A., Haider, S., Rao Kummara, M., Kamal, T., Alghyamah, A. A. A., Jan Iftikhar, F., Bano, B., Khan, N., Amjid Afridi, M., Soo Han, S., Alrahlah, A., & Khan, R. (2020). Advances in the scaffolds fabrication techniques using biocompatible polymers and their biomedical application: A technical and statistical review. *Journal of Saudi Chemical Society*, *24*(2), 186–215. https://doi.org/10.1016/j.jscs.2020.01.002

Halldin, C. N., Doney, B. C., & Hnizdo, E. (2015). Changes in prevalence of chronic obstructive pulmonary disease and asthma in the US population and associated risk factors. *Chronic Respiratory Disease*, *12*(1), 47–60. https://doi.org/10.1177/1479972314562409

Hartung, T. (2024). The (misleading) role of animal models in drug development. *Frontiers in Drug Discovery*, *4*. https://doi.org/10.3389/fddsv.2024.1355044

Hu, J., Sun, X., Ma, H., Xie, C., Chen, Y. E., & Ma, P. X. (2010). Porous nanofibrous PLLA scaffolds for vascular tissue engineering. *Biomaterials*, *31*(31), 7971–7977. https://doi.org/10.1016/j.biomaterials.2010.07.028

Hua, F. J., Nam, J. Do, & Lee, D. S. (2001). Preparation of a macroporous poly(L-lactide) scaffold by liquid-liquid phase separation of a PLLA/1,4-dioxane/water ternary system in the presence

of NaCl. *Macromolecular Rapid Communications*, *22*(13), 1053–1057. https://doi.org/10.1002/1521-3927(20010901)22:13<1053::AID-MARC1053>3.0.CO;2-5

Huang, R., Zhu, X., Tu, H., & Wan, A. (2014). The crystallization behavior of porous poly(lactic acid) prepared by modified solvent casting/particulate leaching technique for potential use of tissue engineering scaffold. *Materials Letters*, *136*, 126–129. https://doi.org/10.1016/j.matlet.2014.08.044

Huri, P. Y., Temple, J. P., Hung, B. P., Cook, C. A., & Grayson, W. L. (2015). Bioreactor technology for oral and craniofacial tissue engineering. In A. Vishwakarma, P. Sharpe, S. Shi, X.-P. Wang, & M. Ramalingam (Eds.), *Stem cell biology and tissue engineering in dental sciences* (pp. 117–130). Academic Press. https://doi.org/10.1016/B978-0-12-397157-9.00011-4

Imamura, Y., Mukohara, T., Shimono, Y., Funakoshi, Y., Chayahara, N., Toyoda, M., Kiyota, N., Takao, S., Kono, S., Nakatsura, T., & Minami, H. (2015). Comparison of 2D- and 3D-culture models as drug-testing platforms in breast cancer. *Oncology Reports*, *33*(4). https://doi.org/10.3892/or.2015.3767

Ivascu, A., & Kubbies, M. (2006). Rapid generation of single-tumor spheroids for high-throughput cell function and toxicity analysis. *Journal of Biomolecular Screening*, *11*(8), 922–932. https://doi.org/10.1177/1087057106292763

Jafari, M., Paknejad, Z., Rad, M. R., Motamedian, S. R., Eghbal, M. J., Nadjmi, N., & Khojasteh, A. (2017). Polymeric scaffolds in tissue engineering: A literature review. *Journal of Biomedical Materials Research - Part B Applied Biomaterials 105*(2) 431–459. https://doi.org/10.1002/jbm.b.33547

Jaiswal, C., & Mandal, B. B. (2024). A 3D in vitro triculture hybrid model recapitulating tumor stromal interaction of triple-negative breast cancer as a high throughput anticancer drug screening platform. *Advanced Therapeutics, 7*(5). https://doi.org/10.1002/adtp.202300450

Janik, H., & Marzec, M. (2015). A review: Fabrication of porous polyurethane scaffolds. *Materials Science and Engineering C 48,* 586–591. https://doi.org/10.1016/j.msec.2014.12.037

Jiang, X., Wang, J., Deng, X., Xiong, F., Zhang, S., Gong, Z., Li, X., Cao, K., Deng, H., He, Y., Liao, Q., Xiang, B., Zhou, M., Guo, C., Zeng, Z., Li, G., Li, X., & Xiong, W. (2020). The role of microenvironment in tumor angiogenesis. *Journal of Experimental and Clinical Cancer Research 39*(1). https://doi.org/10.1186/s13046-020-01709-5

Jin, S., Xia, X., Huang, J., Yuan, C., Zuo, Y., Li, Y., & Li, J. (2021). Recent advances in PLGA-based biomaterials for bone tissue regeneration. In *Acta Biomaterialia 127,* 56–79. https://doi.org/10.1016/j.actbio.2021.03.067

Kalirajan, C., Dukle, A., Nathanael, A. J., Oh, T. H., & Manivasagam, G. (2021). A critical review on polymeric biomaterials for biomedical applications. *Polymers 13*(17) https://doi.org/10.3390/polym13173015

Kapałczyńska, M., Kolenda, T., Przybyła, W., Zajączkowska, M., Teresiak, A., Filas, V., Ibbs, M., Bliźniak, R., Łuczewski, Ł., & Lamperska, K. (2018). 2D and 3D cell cultures – A comparison of different types of cancer cell cultures. *Archives of Medical Science, 14*(4), 910–919. https://doi.org/10.5114/aoms.2016.63743

Kaya, U. (2023). Advancements in Bioreactors: Revolutionizing Bioprocessing Technologies. *Pharmaceutical Bioprocessing 11(6),* 120-121. DOI: 10.37532/2048-9145.2023.11(6).

Khademhosseini, A., Karp, J. M., Gerecht-Nir, S., Ferreira, L., Annabi, N., Sirabella, D., Vunjak-Novakovic, G., & Langer, R. (2013). Embryonic stem cells as a cell source for tissue engineering. In R. Langer & J. P. Vacanti (Eds.), *Principles of tissue engineering* (4th ed., pp. 609–638). Academic Press. https://doi.org/10.1016/B978-0-12-398358-9.00032-X

Khoshbin, E., Karkehabadi, H., Salehi, R., Farmany, A., Najafi, R., & Abbasi, R. (2025). Comparative study of nanohydroxyapatite-emdogain effects on apical papilla stem cell survival and differentiation. *Biotechnology Letters, 47*(1), 24. https://doi.org/10.1007/s10529-024-03557-1

Kim, J. B., Stein, R., & O'Hare, M. J. (2004). Three-dimensional in vitro tissue culture models of breast cancer: A review. *Breast Cancer Research and Treatment, 85*(3), 281–291. https://doi.org/10.1023/B:BREA.0000025418.88785.2b

Kim, H. W., Knowles, J. C., & Kim, H. E. (2004). Hydroxyapatite/poly(ε-caprolactone) composite coatings on hydroxyapatite porous bone scaffold for drug delivery. *Biomaterials, 25*(7–8), 1279–1287. https://doi.org/10.1016/j.biomaterials.2003.07.003

Kolahi Azar, H., Gharibshahian, M., Rostami, M., Mansouri, V., Sabouri, L., Beheshtizadeh, N., & Rezaei, N. (2024). The progressive trend of modeling and drug screening systems of breast cancer bone metastasis. *Journal of Biological Engineering 18*(1). https://doi.org/10.1186/s13036-024-00408-5

Krishani, M., Shin, W. Y., Suhaimi, H., & Sambudi, N. S. (2023). Development of scaffolds from bio-based natural materials for tissue regeneration applications: A review. *Gels 9*(2). https://doi.org/10.3390/gels9020100

Kular, J. K., Basu, S., & Sharma, R. I. (2014). The extracellular matrix: Structure, composition, age-related differences, tools for analysis and applications for tissue engineering. *Journal of Tissue Engineering 5, 1-17*. https://doi.org/10.1177/2041731414557112

Kumar, A., & Jacob, A. (2022). Techniques in scaffold fabrication process for tissue engineering applications: A review. *Journal of Applied Biology and Biotechnology 10*(3), 163–176. https://doi.org/10.7324/JABB.2022.100321

La Carrubba, V., Pavia, F. C., Brucato, V., & Piccarolo, S. (2008). PLLA/PLA scaffolds prepared via thermally induced phase separation (TIPS): Tuning of properties and biodegradability. *International Journal of Material Forming, 1*(1), 619–622. https://doi.org/10.1007/s12289-008-0332-5

La Carrubba, V. La, & Brucato, V. (2018). Preparation of poly(l-lactic acid) scaffolds by thermally induced phase separation: Role of thermal history. *International Polymer Processing, 33*(3), 300–313. https://doi.org/10.3139/217.3511

Laino, G., Graziano, A., D'Aquino, R., Pirozzi, G., Lanza, V., Valiante, S., De Rosa, A., Naro, F., Vivarelli, E., & Papaccio, G. (2006). An approachable human adult stem cell source for hard-tissue engineering. *Journal of Cellular Physiology, 206*(3), 693–701. https://doi.org/10.1002/jcp.20526

Lakshmanan, M., Shewade, D. G., & Raj, G. M. (2022). *Introduction to basics of pharmacology and toxicology: Volume 3: Experimental pharmacology: Research methodology and biostatistics* (Vol. 3). Springer. https://doi.org/10.1007/978-981-19-5343-9

Lancaster, M. A., & Knoblich, J. A. (2014). Organogenesis in a dish: Modeling development and disease using organoid technologies. *Science, 345*(6194), 1247125. https://doi.org/10.1126/science.1247125

Langhans, S. A. (2018). Three-dimensional in vitro cell culture models in drug discovery and drug repositioning. *Frontiers in Pharmacology 9*(JAN), 6. https://doi.org/10.3389/fphar.2018.00006

Lanza, R. P., Langer, R., & Vacanti, J. (Eds.). (2000). *Principles of Tissue Engineering*. Elsevier. https://doi.org/10.1016/B978-0-12-436630-5.X5000-4

Li, R., Ting, Y. H., Youssef, S. H., Song, Y., & Garg, S. (2021). Three-dimensional printing for cancer applications: Research landscape and technologies. *Pharmaceuticals 14*(8). https://doi.org/10.3390/ph14080787

Lim, D., Renteria, E. S., Sime, D. S., Ju, Y. M., Kim, J. H., Criswell, T., Shupe, T. D., Atala, A., Marini, F. C., Gurcan, M. N., Soker, S., Hunsberger, J., & Yoo, J. J. (2022a). Bioreactor design and validation for manufacturing strategies in tissue engineering. *Bio-Design and Manufacturing 5*(1), 43–63. https://doi.org/10.1007/s42242-021-00154-3

Liu, C., Xia, Z., & Czernuszka, J. T. (2007). Design and development of three-dimensional scaffolds for tissue engineering. *Chemical Engineering Research and Design 85*(7 A), 1051–1064. https://doi.org/10.1205/cherd06196

Liu, D., Cheng, F., Pan, S., & Liu, Z. (2020). Stem cells: A potential treatment option for kidney diseases. *Stem Cell Research and Therapy 11*(1). https://doi.org/10.1186/s13287-020-01751-2

Liu, S., Yu, J. M., Gan, Y. C., Qiu, X. Z., Gao, Z. C., Wang, H., Chen, S. X., Xiong, Y., Liu, G. H., Lin, S. E., McCarthy, A., John, J. V., Wei, D. X., & Hou, H. H. (2023). Biomimetic natural biomaterials for tissue engineering and regenerative medicine: new biosynthesis methods, recent advances, and emerging applications. *Military Medical Research10*(1). https://doi.org/10.1186/s40779-023-00448-w

Liverani, C., De Vita, A., Minardi, S., Kang, Y., Mercatali, L., Amadori, D., Bongiovanni, A., La Manna, F., Ibrahim, T., & Tasciotti, E. (2019). A biomimetic 3D model of hypoxia-driven cancer progression. *Scientific Reports*, *9*(1). https://doi.org/10.1038/s41598-019-48701-4

Liverani, C., Mercatali, L., Cristofolini, L., Giordano, E., Minardi, S., Porta, G. Della, De Vita, A., Miserocchi, G., Spadazzi, C., Tasciotti, E., Amadori, D., & Ibrahim, T. (2017). Investigating the Mechanobiology of Cancer Cell–ECM Interaction Through Collagen-Based 3D Scaffolds. *Cellular and Molecular Bioengineering*, *10*(3), 223–234. https://doi.org/10.1007/s12195-017-0483-x

Loh, Q. L., & Choong, C. (2013). Three-dimensional scaffolds for tissue engineering applications: Role of porosity and pore size. *Tissue Engineering - Part B: Reviews 19*(6), 485–502. https://doi.org/10.1089/ten.teb.2012.0437

Lombardo, M. E., Carfì Pavia, F., Craparo, E. F., Capuana, E., Cavallaro, G., Brucato, V., & La Carrubba, V. (2021). Novel dual-flow perfusion bioreactor for in vitro pre-screening of

nanoparticles delivery: design, characterization and testing. *Bioprocess and Biosystems Engineering 44*(7), 1097–1108.. https://doi.org/10.1007/s00449-021-02609-4

Lombardo, M. E., Carfì Pavia, F., Vitrano, I., Ghersi, G., Brucato, V., Rosei, F., & La Carrubba, V. (2019). PLLA scaffolds with controlled architecture as potential microenvironment for in vitro tumor model. *Tissue and Cell, 58,* 12-20. https://doi.org/10.1016/j.tice.2019.04.004

Low, Y. J., Andriyana, A., Ang, B. C., & Zainal Abidin, N. I. (2020). Bioresorbable and degradable behaviors of PGA: Current state and future prospects. *Polymer Engineering and Science 60*(11), 2657–2675. https://doi.org/10.1002/pen.25508

Lu, T., Li, Y., & Chen, T. (2013). Techniques for fabrication and construction of three-dimensional scaffolds for tissue engineering. *International Journal of Nanomedicine 8*, 337–350. https://doi.org/10.2147/IJN.S38635

Luo, Y. S., Cheng, K. C., Huang, N. Du, Chiang, W. P., & Li, S. F. (2011). Preparation of porous crosslinked polymers with different surface morphologies via chemically induced phase separation. *Journal of Polymer Science, Part B: Polymer Physics, 49*(14), 1022–1030. https://doi.org/10.1002/polb.22274

Ma, H., Feng, C., Chang, J., & Wu, C. (2018). 3D-printed bioceramic scaffolds: From bone tissue engineering to tumor therapy. *Acta Biomaterialia 79*, 37–59. https://doi.org/10.1016/j.actbio.2018.08.026

Mabrouk, M., Beherei, H. H., & Das, D. B. (2020). Recent progress in the fabrication techniques of 3D scaffolds for tissue engineering. *Materials Science and Engineering C 110*, 110716. https://doi.org/10.1016/j.msec.2020.110716

MacDonald, R. A., Laurenzi, B. F., Viswanathan, G., Ajayan, P. M., & Stegemann, J. P. (2005). Collagen-carbon nanotube composite materials as scaffolds in tissue engineering. *Journal of Biomedical Materials Research - Part A, 74*(3), 489–496. https://doi.org/10.1002/jbm.a.30386

Marion, N. W., & Mao, J. J. (2006). Mesenchymal Stem Cells and Tissue Engineering. *Methods in Enzymology 420*, 339–361. https://doi.org/10.1016/S0076-6879(06)20016-8

Martin, I., Wendt, D., & Heberer, M. (2004). The role of bioreactors in tissue engineering. *Trends in Biotechnology 22*(2), 80–86. https://doi.org/10.1016/j.tibtech.2003.12.001

Mather, J. P. (2012). Concise review: Cancer stem cells: In vitro models. *Stem Cells 30*(2), 95–99). https://doi.org/10.1002/stem.774

Meneses, J., Silva, J. C., Fernandes, S. R., Datta, A., Ferreira, F. C., Moura, C., Amado, S., Alves, N., & Pascoal-Faria, P. (2020). A multimodal stimulation cell culture bioreactor for tissue engineering: A numerical modelling approach. *Polymers*, *12*(4). https://doi.org/10.3390/POLYM12040940

Micalet, A., Moeendarbary, E., & Cheema, U. (2023). 3D In Vitro Models for Investigating the Role of Stiffness in Cancer Invasion. In *ACS Biomaterials Science and Engineering 9*(7), 3729–3741. https://doi.org/10.1021/acsbiomaterials.0c01530

Middleton, J. C., & Tipton, A. J. (2000). Synthetic biodegradable polymers as orthopedic devices. *Biomaterials*, *21*(23), 2335–2346. https://doi.org/10.1016/S0142-9612(00)00225-9

Mo, X., Zhang, D., Liu, K., Zhao, X., Li, X., & Wang, W. (2023). Nano-Hydroxyapatite Composite Scaffolds Loaded with Bioactive Factors and Drugs for Bone Tissue Engineering. *International Journal of Molecular Sciences 24*(2). https://doi.org/10.3390/ijms24021291

Mondal, P., Bailey, K. L., Cartwright, S. B., Band, V., & Carlson, M. A. (2022). Large Animal Models of Breast Cancer. *Frontiers in Oncology 12*, 788038. https://doi.org/10.3389/fonc.2022.788038

Moran-Alvarez, A., Gonzalez-Menendez, P., Mayo, J. C., & Sainz, R. M. (2023). Reflections on the Biology of Cell Culture Models: Living on the Edge of Oxidative Metabolism in Cancer Cells. *International Journal of Molecular Sciences 24*(3). https://doi.org/10.3390/ijms24032717

Murphy, A. R., Laslett, A., O'Brien, C. M., & Cameron, N. R. (2017). Scaffolds for 3D in vitro culture of neural lineage cells. *Acta Biomaterialia 54*, 1–20. https://doi.org/10.1016/j.actbio.2017.02.046

Murphy, S. V., & Atala, A. (2014). 3D bioprinting of tissues and organs. *Nature Biotechnology 32*(8), 773–785. https://doi.org/10.1038/nbt.2958

Naahidi, S., Jafari, M., Logan, M., Wang, Y., Yuan, Y., Bae, H., Dixon, B., & Chen, P. (2017). Biocompatibility of hydrogel-based scaffolds for tissue engineering applications. *Biotechnology Advances 35*(5), 530–544. https://doi.org/10.1016/j.biotechadv.2017.05.006

Nam, Y. S., & Park, T. G. (1999). Porous biodegradable polymeric scaffolds prepared by thermally induced phase separation. *Journal of Biomedical Materials Research*, *47*(1), 8–17. https://doi.org/10.1002/(SICI)1097-4636(199910)47:1<8::AID-JBM2>3.0.CO;2-L

Nanou, A., Lorenzo-Moldero, I., Gazouleas, K. D., Cortese, B., & Moroni, L. (2022). 3D Culture Modeling of Metastatic Breast Cancer Cells in Additive Manufactured Scaffolds. *ACS Applied Materials and Interfaces*, *14*(24), 28389–28402. https://doi.org/10.1021/acsami.2c07492

Nardin, S., Mora, E., Varughese, F. M., D'Avanzo, F., Vachanaram, A. R., Rossi, V., Saggia, C., Rubinelli, S., & Gennari, A. (2020). Breast Cancer Survivorship, Quality of Life, and Late Toxicities. *Frontiers in Oncology 10*,864. https://doi.org/10.3389/fonc.2020.00864

Nasrollahzadeh, N., & Pioletti, D. P. (2016). Experimental method to characterize the strain dependent permeability of tissue engineering scaffolds. *Journal of Biomechanics*, *49*(15), 3749–3752. https://doi.org/10.1016/j.jbiomech.2016.09.021

Ndongo Sonfack, D. J., Tanguay Boivin, C., Touzel Deschênes, L., Maurand, T., Maguemoun, C., Berthod, F., Gros-Louis, F., & Champagne, P. O. (2024). Bioengineering Human Upper Respiratory Mucosa: A Systematic Review of the State of the Art of Cell Culture Techniques. *Bioengineering 11* (8). https://doi.org/10.3390/bioengineering11080826

Ngo, H. X., Bai, Y., Sha, J., Ishizuka, S., Toda, E., Osako, R., Kato, A., Morioka, R., Ramanathan, M., Tatsumi, H., Okui, T., & Kanno, T. (2022). A Narrative Review of u-HA/PLLA, a Bioactive Resorbable Reconstruction Material: Applications in Oral and Maxillofacial Surgery. *Materials 15* (1). https://doi.org/10.3390/ma15010150

Nguyen, H. T.-L., Nguyen, S. T., & Van Pham, P. (2016). Concise Review: 3D cell culture systems for anticancer drug screening. *Biomedical Research and Therapy*, *3*(5). https://doi.org/10.7603/s40730-016-0022-8

Noori, A., Ashrafi, S. J., Vaez-Ghaemi, R., Hatamian-Zaremi, A., & Webster, T. J. (2017). A review of fibrin and fibrin composites for bone tissue engineering. In *International Journal of Nanomedicine 12*, 4937–4961. https://doi.org/10.2147/IJN.S124671

Notarbartolo, M., Cervello, M., Poma, P., Dusonchet, L., Meli, M., & D'Alessandro, N. (2004). Expression of the IAPs in multidrug resistant tumor cells. *Oncology Reports 11*(2), 497–502.

O'byrne, P. M., & Postma, D. S. (1999). The Many Faces of Airway Inflammation The many faces of airway inflammation: Asthma and chronic obstructive pulmonary disease. *American Journal of Respiratory and Critical Care Medicine*, *159*(1), 1–17. https://www.atsjournals.org/doi/10.1164/ajrccm.159.1.9711035

Palladino, F., Marcelino, P. R. F., Schlogl, A. E., José, Á. H. M., Rodrigues, R. de C. L. B., Fabrino, D. L., Santos, I. J. B., & Rosa, C. A. (2024). Bioreactors: Applications and Innovations for a Sustainable and Healthy Future—A Critical Review. *Applied Sciences 14*(20) https://doi.org/10.3390/app14209346

Pampaloni, F., Reynaud, E. G., & Stelzer, E. H. K. (2007). The third dimension bridges the gap between cell culture and live tissue. *Nature Reviews Molecular Cell Biology*, *8*(10), 839–845. https://doi.org/10.1038/nrm2236

Panoskaltsis-Mortari, A. (2015). Bioreactor Development for Lung Tissue Engineering. *Current Transplantation Reports*, *2*(1), 90–97. https://doi.org/10.1007/s40472-014-0048-z

Parenteau-Bareil, R., Gauvin, R., & Berthod, F. (2010). Collagen-based biomaterials for tissue engineering applications. *Materials*, *3*(3), 1863–1887. https://doi.org/10.3390/ma3031863

Parisi, C., Salvatore, L., Veschini, L., Serra, M. P., Hobbs, C., Madaghiele, M., Sannino, A., & Di Silvio, L. (2020). Biomimetic gradient scaffold of collagen–hydroxyapatite for osteochondral regeneration. *Journal of Tissue Engineering*, *11*. https://doi.org/10.1177/2041731419896068

Parrish, J., Lim, K. S., Baer, K., Hooper, G. J., & Woodfield, T. B. F. (2018). A 96-well microplate bioreactor platform supporting individual dual perfusion and high-throughput assessment of simple or biofabricated 3D tissue models. *Lab on a Chip*, *18*(18), 2757–2775. https://doi.org/10.1039/c8lc00485d

Pattanayak, I., Alex, Y., & Mohanty, S. (2023). Advancing strategies towards the development of tissue engineering scaffolds: a review. In *Journal of Materials Science 58*(32), 12847–12898. https://doi.org/10.1007/s10853-023-08798-5

Pei, B., Hu, M., Wu, X., Lu, D., Zhang, S., Zhang, L., & Wu, S. (2023). Investigations into the effects of scaffold microstructure on slow-release system with bioactive factors for bone repair. *Frontiers in Bioengineering and Biotechnology 11*. https://doi.org/10.3389/fbioe.2023.1230682

Penderecka, K., Ibbs, M., Kaluzna, A., Lewandowska, A., Marszalek, A., Mackiewicz, A., & Dams-Kozlowska, H. (2020). Implementation of a dynamic culture condition to the heterotypic 3D breast cancer model. *Journal of Biomedical Materials Research - Part B Applied Biomaterials*, *108*(4), 1186–1197. https://doi.org/10.1002/jbm.b.34468

Pennella, F., Cerino, G., Massai, D., Gallo, D., Falvo D'Urso Labate, G., Schiavi, A., Deriu, M. A., Audenino, A., & Morbiducci, U. (2013). A Survey of Methods for the Evaluation of Tissue

Engineering Scaffold Permeability. *Annals of Biomedical Engineering*, *41*(10), 2027–2041. https://doi.org/10.1007/s10439-013-0815-5

Poma, P., Labbozzetta, M., & Notarbartolo, M. (2021). Patterns of Innate or Acquired Resistance to Anticancer Drugs: Our Experience to Overcome It. *Oncogenesis*, *26*(2), 27–37. www.begellhouse.com

Poma, P., Notarbartolo, M., Labbozzetta, M., Maurici, A., Carina, V., Alaimo, A., Rizzi, M., Simoni, D., & D'Alessandro, N. (2007). The antitumor activities of curcumin and of its isoxazole analogue are not affected by multiple gene expression changes in an MDR model of the MCF-7 breast cancer cell line: analysis of the possible molecular basis. *International Journal of Molecular Medicine*, *20*(3), 329–335.

Poma, P., Rigogliuso, S., Labbozzetta, M., Carfì Pavia, F., Carbone, C., Ma, J., Cusimano, A., & Notarbartolo, M. (2024). Antimigratory effects of a new NF-κB inhibitor, (S)-b-salicyloylamino-a-exo-methylene-γ-butyrolactone, in 2D and 3D breast cancer models. *Biomedicine and Pharmacotherapy*, *180*. https://doi.org/10.1016/j.biopha.2024.117552

Prince, E., Cruickshank, J., Ba-Alawi, W., Hodgson, K., Haight, J., Tobin, C., Wakeman, A., Avoulov, A., Topolskaia, V., Elliott, M. J., McGuigan, A. P., Berman, H. K., Haibe-Kains, B., Cescon, D. W., & Kumacheva, E. (2022). Biomimetic hydrogel supports initiation and growth of patient-derived breast tumor organoids. *Nature Communications*, *13*(1). https://doi.org/10.1038/s41467-022-28788-6

Radulescu, D. M., Neacsu, I. A., Grumezescu, A. M., & Andronescu, E. (2022). New Insights of Scaffolds Based on Hydrogels in Tissue Engineering. In *Polymers 14* (4). https://doi.org/10.3390/polym14040799

Rambhia, K. J., & Ma, P. X. (2015). Controlled drug release for tissue engineering. *Journal of Controlled Release*, *219*, 119–128. https://doi.org/10.1016/j.jconrel.2015.08.049

Ratner, B. D. (2011). The biocompatibility manifesto: Biocompatibility for the twenty-first century. In *Journal of Cardiovascular Translational Research 4*(5), 523–527. https://doi.org/10.1007/s12265-011-9287-x

Rodriguez-Cabello, J. C., Gonzalez De Torre, I., González-Pérez, M., González-Pérez, F., & Montequi, I. (2021). Fibrous Scaffolds From Elastin-Based Materials. *Frontiers in Bioengineering and Biotechnology 9*. https://doi.org/10.3389/fbioe.2021.652384

Roseti, L., Parisi, V., Petretta, M., Cavallo, C., Desando, G., Bartolotti, I., & Grigolo, B. (2017). Scaffolds for Bone Tissue Engineering: State of the art and new perspectives. *Materials Science and Engineering C 78*, 1246–1262. https://doi.org/10.1016/j.msec.2017.05.017

Roslan, M. R., Nasir, N. F. M., Cheng, E. M., & Amin, N. A. M. (2016). Tissue engineering scaffold based on starch: A review. *Proceedings of the 2016 International Conference on Electrical, Electronics, and Optimization Techniques (ICEEOT)*, 1857–1860. https://doi.org/10.1109/ICEEOT.2016.7755010

Sahoo, D. R., & Biswal, T. (2021). Alginate and its application to tissue engineering. *SN Applied Sciences 3* (1). https://doi.org/10.1007/s42452-020-04096-w

Sántha, M. (2020). Biologia futura: animal testing in drug development—the past, the present and the future. *Biologia Futura 71* (4), 443–452. https://doi.org/10.1007/s42977-020-00050-4

Sarparast, Z., Abdoli, R., Rahbari, A., Varmazyar, M., & Kashyzadeh, K. R. (2020). Experimental and Numerical Analysis of Permeability in Porous Media. *International Journal of Engineering, Transactions B: Applications*, *33*(11), 2408–2415. https://doi.org/10.5829/ije.2020.33.11b.31

Sarvazyan, N. (Ed.). (2020). *Tissue Engineering*. Springer International Publishing. https://doi.org/10.1007/978-3-030-39698-5

Schmid, R., Schmidt, S. K., Hazur, J., Detsch, R., Maurer, E., Boccaccini, A. R., Hauptstein, J., Teßmar, J., Blunk, T., Schrüfer, S., Schubert, D. W., Horch, R. E., Bosserhoff, A. K., Arkudas, A., & Kengelbach-Weigand, A. (2020). Comparison of hydrogels for the development of well-defined 3d cancer models of breast cancer and melanoma. *Cancers*, *12*(8), 1–21. https://doi.org/10.3390/cancers12082320

Selden, C., & Fuller, B. (2018). Role of bioreactor technology in tissue engineering for clinical use and therapeutic target design. *Bioengineering 5* (2). https://doi.org/10.3390/bioengineering5020032

Shanks, N., Greek, R., & Greek, J. (2009). Are animal models predictive for humans? In *Philosophy, Ethics, and Humanities in Medicine 4*(1). https://doi.org/10.1186/1747-5341-4-2

Sharma, K., Dey, S., Karmakar, R., & Rengan, A. K. (2023). A comprehensive review of 3D cancer models for drug screening and translational research. *Cancer Innovation*. https://doi.org/10.1002/cai2.102

Singh, V. K., Kalsan, M., Kumar, N., Saini, A., & Chandra, R. (2015). Induced pluripotent stem cells: Applications in regenerative medicine, disease modeling, and drug discovery. *Frontiers in Cell and Developmental Biology 3*(FEB). https://doi.org/10.3389/fcell.2015.00002

Smolarz, B., Zadrożna Nowak, A., & Romanowicz, H. (2022). Breast Cancer—Epidemiology, Classification, Pathogenesis and Treatment (Review of Literature). *Cancers 14*(10). https://doi.org/10.3390/cancers14102569

Soriano, J. B., Abajobir, A. A., Abate, K. H., Abera, S. F., Agrawal, A., Ahmed, M. B., Aichour, A. N., Aichour, I., Eddine Aichour, M. T., Alam, K., Alam, N., Alkaabi, J. M., Al-Maskari, F., Alvis-Guzman, N., Amberbir, A., Amoako, Y. A., Ansha, M. G., Antó, J. M., Asayesh, H., … Vos, T. (2017). Global, regional, and national deaths, prevalence, disability-adjusted life years, and years lived with disability for chronic obstructive pulmonary disease and asthma, 1990–2015: a systematic analysis for the Global Burden of Disease Study 2015. *The Lancet Respiratory Medicine*, *5*(9), 691–706. https://doi.org/10.1016/S2213-2600(17)30293-X

Subia, B., Kundu, J., & C., S. (2010). Biomaterial Scaffold Fabrication Techniques for Potential Tissue Engineering Applications. *Tissue Engineering 16*(6), 1597–1612. https://doi.org/10.5772/8581

Sztankovics, D., Moldvai, D., Petővári, G., Gelencsér, R., Krencz, I., Raffay, R., Dankó, T., & Sebestyén, A. (2023). 3D bioprinting and the revolution in experimental cancer model systems—A review of developing new models and experiences with in vitro 3D bioprinted breast cancer tissue-mimetic structures. *Pathology and Oncology Research*, *29*. https://doi.org/10.3389/pore.2023.1610996

Tandon, S., Kandasubramanian, B., & Ibrahim, S. M. (2020). Silk-Based Composite Scaffolds for Tissue Engineering Applications. *Industrial and Engineering Chemistry Research 59*(40), 17593–17611. https://doi.org/10.1021/acs.iecr.0c02195

Thangam, T., Parthasarathy, K., Supraja, K., Haribalaji, V., Sounderrajan, V., Rao, S. S., & Jayaraj, S. (2024). Lung Organoids: Systematic Review of Recent Advancements and its Future Perspectives. *Tissue Engineering and Regenerative Medicine 21*(5), 653–671. https://doi.org/10.1007/s13770-024-00628-2

Tosca, E. M., Ronchi, D., Facciolo, D., & Magni, P. (2023). Replacement, Reduction, and Refinement of Animal Experiments in Anticancer Drug Development: The Contribution of

3D In Vitro Cancer Models in the Drug Efficacy Assessment. *Biomedicines 11*(4). https://doi.org/10.3390/biomedicines11041058

Tratar, U. L., Horvat, S., & Cemazar, M. (2018). Transgenic mouse models in cancer research. In *Frontiers in Oncology 8*(JUL). https://doi.org/10.3389/fonc.2018.00268

Van De Wetering, M., Francies, H. E., Francis, J. M., Bounova, G., Iorio, F., Pronk, A., Van Houdt, W., Van Gorp, J., Taylor-Weiner, A., Kester, L., McLaren-Douglas, A., Blokker, J., Jaksani, S., Bartfeld, S., Volckman, R., Van Sluis, P., Li, V. S. W., Seepo, S., Sekhar Pedamallu, C., … Clevers, H. (2015). Prospective derivation of a living organoid biobank of colorectal cancer patients. *Cell*, *161*(4), 933–945. https://doi.org/10.1016/j.cell.2015.03.053

Viegi, G., Maio, S., Fasola, S., & Baldacci, S. (2020). Global Burden of Chronic Respiratory Diseases. *Journal of Aerosol Medicine and Pulmonary Drug Delivery*, *33*(4), 171–177. https://doi.org/10.1089/jamp.2019.1576

Vinci, M., Gowan, S., Boxall, F., Patterson, L., Zimmermann, M., Court, W., Lomas, C., Mendiola, M., Hardisson, D., & Eccles, S. A. (2012). Advances in establishment and analysis of three-dimensional tumor spheroid-based functional assays for target validation and drug evaluation. *BMC Biology*, *10*. https://doi.org/10.1186/1741-7007-10-29

Vunjak-Novakovic, Gordana., & Freshney, R. Ian. (2006). *Culture of cells for tissue engineering*. Wiley-Liss.

Wadman, M. (2023). FDA no longer has to require animal testing for new drugs. *Science*, *379*(6628), 127–128. https://doi.org/10.1126/science.adg6276

Wang, W., Deng, Q., Li, T., Liu, Y., Liu, Y., Sun, Y., Deng, C., Zhou, X., Ma, Z., Qiang, L., Wang, J., & Dai, K. (2021). Research Update on Bioreactors Used in Tissue Engineering. *Journal of Shanghai Jiaotong University (Science)*, *26*(3), 272–283. https://doi.org/10.1007/s12204-021-2293-5

Xie, M., Liu, X., Cao, X., Guo, M., & Li, X. (2020). Trends in prevalence and incidence of chronic respiratory diseases from 1990 to 2017. *Respiratory Research*, *21*(1). https://doi.org/10.1186/s12931-020-1291-8

Xin, H., & Naficy, S. (2022). Drug Delivery Based on Stimuli-Responsive Injectable Hydrogels for Breast Cancer Therapy: A Review. *Gels 8*(1). https://doi.org/10.3390/gels8010045

Yamada, K. M., & Cukierman, E. (2007). Modeling Tissue Morphogenesis and Cancer in 3D. In *Cell 130*(4), 601–610. https://doi.org/10.1016/j.cell.2007.08.006

Yang, C., Chen, R., Chen, C., Yang, F., Xiao, H., Geng, B., & Xia, Y. (2024). Tissue engineering strategies hold promise for the repair of articular cartilage injury. *BioMedical Engineering Online 23*(1). https://doi.org/10.1186/s12938-024-01260-w

Yang, F., Murugan, R., Ramakrishna, S., Wang, X., Ma, Y. X., & Wang, S. (2004). Fabrication of nano-structured porous PLLA scaffold intended for nerve tissue engineering. *Biomaterials*, *25*(10), 1891–1900. https://doi.org/10.1016/j.biomaterials.2003.08.062

Ye, B., Wu, B., Su, Y., Sun, T., & Guo, X. (2022). Recent Advances in the Application of Natural and Synthetic Polymer-Based Scaffolds in Musculoskeletal Regeneration. *Polymers 14*(21). https://doi.org/10.3390/polym14214566

Yu, H., Chong, S. K., Hassanbhai, A. M., Teng, Y., Balachander, G., Muthukumaran, P., Wen, F., & Teoh, S. H. (2020). Principles of bioreactor design for tissue engineering. In *R. Lanza, R. Langer, & J. Vacanti (Eds.), Principles of tissue engineering* (pp. 179–203). Academic Press. https://doi.org/10.1016/B978-0-12-818422-6.00012-5

Zarrintaj, P., Manouchehri, S., Ahmadi, Z., Saeb, M. R., Urbanska, A. M., Kaplan, D. L., & Mozafari, M. (2018). Agarose-based biomaterials for tissue engineering. *Carbohydrate Polymers 187*, 66–84. https://doi.org/10.1016/j.carbpol.2018.01.060

Zeinali, R., Franco, L., del Valle, L. J., & Puiggalí, J. (2022). Poly(butylene succinate) matrices obtained by thermally-induced phase separation: Pore shape and orientation affect drug release. *Polymer*, *252*. https://doi.org/10.1016/j.polymer.2022.124916

Zhang, B., Huang, J., & Narayan, R. J. (2020). Gradient scaffolds for osteochondral tissue engineering and regeneration. *Journal of Materials Chemistry B 8*(36), 8149–8170. https://doi.org/10.1039/d0tb00688b

Zhang, X., Yin, Z., Xiang, S., Yan, H., & Tian, H. (2024). Degradation of Polymer Materials in the Environment and Its Impact on the Health of Experimental Animals: A Review. In *Polymers 16*(19). https://doi.org/10.3390/polym16192807

Zhang, Y., & Habibovic, P. (2022). Delivering Mechanical Stimulation to Cells: State of the Art in Materials and Devices Design. *Advanced Materials 34*(32). https://doi.org/10.1002/adma.202110267

Zhao, F., & Ma, T. (2005). Perfusion bioreactor system for human mesenchymal stem cell tissue engineering: Dynamic cell seeding and construct development. *Biotechnology and Bioengineering*, *91*(4), 482–493. https://doi.org/10.1002/bit.20532

Zhao, J., Griffin, M., Cai, J., Li, S., Bulter, P. E. M., & Kalaskar, D. M. (2016a). Bioreactors for tissue engineering: An update. *Biochemical Engineering Journal 109*, 268–281. https://doi.org/10.1016/j.bej.2016.01.018

Zhou, J., Xiong, S., Liu, M., Yang, H., Wei, P., Yi, F., Ouyang, M., Xi, H., Long, Z., Liu, Y., Li, J., Ding, L., & Xiong, L. (2023). Study on the influence of scaffold morphology and structure on osteogenic performance. *Frontiers in Bioengineering and Biotechnology 11* https://doi.org/10.3389/fbioe.2023.1127162